Micro- and Nano-Electrode Arrays For Electroanalytical Sensing

A thesis submitted to the

Department of Electronics and Electrical Engineering

University of Glasgow

for the degree of

Doctor of Philosophy

by

Mairi Elizabeth Sandison

© M. E. Sandison, 2004

ABSTRACT

This thesis is primarily concerned with the fabrication and characterisation of nano- and micro- electrode arrays and with their application to electroanalytical sensing.

A systematic investigation of the electrochemical behaviour of two sets of microelectrode arrays, fabricated by standard photolithographic and reactive-ion etching techniques, is presented. The first set of microelectrode arrays had a constant relative centre-centre spacing of $10r$ (where r is the electrode radius). As the value of r was decreased, the cyclic voltammograms recorded from the array became increasingly peak-shaped, due to merging of the diffusion fields of the individual electrodes. Furthermore, it was shown that the peak current densities obtained were largest for the arrays with the smallest individual electrodes, as were the signal-to-noise ratios (SNRs). Electroplating the individual electrodes with platinum black was also shown to increase the peak currents and the SNRs, due to an increase in the effective surface area. Sigmoidal voltammograms, which are indicative of radial diffusion, were obtained for an individual electrode radius of 25 μm but not for arrays with smaller electrodes. To obtain radial diffusion for an array of 2.5 μm electrodes, it was shown (using a second set of microelectrode arrays) that a minimum relative centre-centre spacing of $40r$ is required.

Further enhancement of the peak current densities were obtained by decreasing the size of the individual electrodes. A series of nanoelectrode arrays were fabricated using electron-beam lithography (EBL). The voltammograms obtained from these arrays exhibited a continual increase in the recorded peak current as the individual electrodes radius was decreased to a value of 110 nm. Since EBL is a slow and costly technique, nanoimprint lithography (NIL) was investigated as an alternative method of fabricating nanoelectrode arrays and comparable results were obtained from arrays produced by EBL and NIL.

A dissolved oxygen and temperature sensor incorporating a working microelectrode array was also designed and fabricated. The sensor comprised a densely packed array of 2.5 μm radius electrodes and a micro-reference electrode, both of which were covered with an agarose electrolyte gel enclosed in an SU8 chamber. A thermal resistor was included for temperature compensation of the dissolved oxygen measurements. The Ag|AgCl micro-reference electrode was found to be stable for approximately 80 hours in 0.1 M KCl, with 100 nA of current passing through it. Linear calibration curves were obtained from both temperature and dissolved oxygen measurements.

Finally, preliminary work towards the integration of a series of sensors into the one platform was carried out. A system where sensors can be embedded into the base of a flow channel, which incorporates arrays of interdigitated microelectrodes, was designed and fabricated in poly(ethylene terephthalate). The electrodes enable the use of negative dielectrophoresis as an antifouling strategy, where foulants are repelled away from the sensing regions towards the centre of the flow channel. To illustrate the practical implementation of the dielectrophoretic antifouling strategy, preliminary simulation and experimental results were obtained using latex beads as model particles.

ACKNOWLEDGEMENTS

Firstly, I would like to thank Professor Jon Cooper for giving me the opportunity to pursue this PhD, for setting up the collaborations with Kodak and Unilever (who together with EPSRC funded this research) and for guidance and support throughout the past four years.

I would like to express my gratitude to Nic Green, Hywel Morgan and David Holmes for their guidance on the simulation and the DEP experimental work and for the use of equipment and software. Thanks also to the technical staff in the department of Electronics and Electrical Engineering, in particular Bill Monaghan and Mary Robertson, for all their advice on microfabrication and to the members of the Bioelectronics group for many interesting and helpful discussions.

To Mum and Dad, a huge big thank you for all your kindness, support and encouragement throughout my many years of studying (you can now tell anybody that asks that I am no longer a student!). Shona and Catriona, you will be glad to hear that I'm finally finished and will try much harder to keep in touch!

Thanks to all the friends in Bioelectronics that I have made over the years – the friendly, sociable atmosphere made the group a great place to work. Thanks to the footballers for many energetic games and to the beer drinkers for numerous happy nights in the pub (especially to Martin, Eishi, Cathy, Nigel, Paul and Chris). A special thank you to Erik and Aussie Dave for their friendship during the last five years. Thanks also to Kirstene and Anne for distracting me from my thesis with many fun nights out!

Finally, an extra special thank you to David for encouraging me along, for making me smile when I needed you too and for always being there.

CONTENTS

Title i
Abstract ii
Acknowledgements iv
Contents v

INTRODUCTION 1
1.1 Electrochemical Microsensors 1
1.1.1 Benefits of Miniaturisation 1
1.1.2 Microsensors Reported in the Literature 3
1.1.3 Industrial Interest 4
1.2 Development of Microfabrication Technologies 4
1.2.1 History of Photolithography 5
1.2.2 The Emergence of Micro-ElectroMechanical Systems (MEMs) and Micro Total Analysis Systems (μTAS) 5
1.3 Aims of Thesis 6
1.3.1 Organisation of Thesis 6

MICROFABRICATION AND NANOFABRICATION TECHNOLOGIES 8
2.1 Photolithography & Electron Beam Lithography 8
2.1.1 Photolithography 8
2.1.1.1 Spin Coating 11
2.1.1.2 Spray Coating 11
2.1.1.3 Laminating 11
2.1.1.4 Other Methods 12
2.1.1.5 Limits of Photolithography 12
2.1.2 Electron-beam lithography (EBL) 13
2.1.2.1 EBL Machines 13
2.1.2.2 Electron-Sensitive Resist 14
2.1.2.3 Electron-Solid Interactions 15
2.1.2.4 Software 16
2.2 Lift-off & Etching Techniques 16
2.2.1 Lift-off 16

2.2.2 Wet Chemical Etching 17
2.2.2.1 Isotropic Wet Chemical Etching 17
2.2.2.2 Anisotropic wet chemical etching 17
2.2.3 Reactive-Ion Etching (RIE) 18
2.3 Deposition of Thin-film Metal Layers and Insulation Materials 20
2.3.1 Physical Deposition: Evaporation and Sputtering 20
2.3.2 Electroplating 21
2.3.2.1 Electroplating "Black" Films 21
2.3.3 Chemical Vapour Deposition (CVD) 22
2.3.3.1 Plama Enhanced Chemical Vapour Deposition (PECVD) 23
2.3.4 Polyimide 23
2.4 Alternative Micromachining Technologies 23
2.4.1 Soft Lithography 24
2.4.1.1 Moulding 24
2.4.1.2 Microcontact Printing 25
2.4.1.3 Imprinting & Injection Moulding 25
2.4.2 High Resolution Micromachining Techniques 26
2.4.2.1 Nanoimprint Lithography (NIL) 26
2.4.2.2 LIGA 27
2.4.2.3 Laser Micromachining 28
2.5 Bonding Techniques 28
2.5.1 Anodic Bonding 28
2.5.2 Silicon Fusion Bonding and Thermal Bonding 29
2.5.3 Bonding Polymeric Materials 29
2.6 Conclusion 30

MATERIALS AND METHODS: MODELLING ENVIRONMENTS, MICROFABRICATION PROTOCOLS AND EXPERIMENTAL APPARATUS 31
3.1 Materials 31
3.2 Modelling Environments 32
3.2.1 Finite Element Simulations 33
3.3 Microfabrication Protocols 33
3.3.1 Standard Processes for Fabricating Silicon-Based Microdevices 34
3.3.1.1 Wafer Cleaning 34
3.3.1.2 Creating a Photoresist Mask 34
3.3.1.3 Anisotropic Etching of Silicon 34

3.3.1.4 Patterning Thin Film Metal Layers....35
3.3.1.5 Creating Patterned Insulation Layers....36
3.3.2 Alternative Resist Processing Methods....40
3.3.2.1 Resist Coating Techniques....40
3.3.2.2 Nanoimprint Lithography (NIL)....40
3.3.3 Electrochemical Deposition....41
3.3.3.1 Cleaning Electrodes....41
3.3.3.2 Electrochemical Deposition Processes....41
3.3.4 Polymer Microfabrication Processes....43
3.3.4.1 Thick-Film SU8....43
3.3.4.2 Polyimide....44
3.3.4.3 Poly(ethylene terephthalate) (PET) and Hot-Melt Adhesive Foils....45
3.4 Experimental Apparatus....46
3.4.1 Electrochemical Recordings....46
3.4.2 Reference Electrode Stability Measurements....48
3.4.3 Thermal Resistance Measurements....49
3.4.4 Experiments Using Dielectrophoresis (DEP)....50

THEORETICAL BEHAVIOUR OF MACROELECTRODES, MICROELECTRODES AND MICROELECTRODE ARRAYS....52
4.1 Electrochemical Systems....52
4.1.1 Equilibrium Conditions....53
4.1.2 Faradaic and Non-Faradaic Processes....54
4.2 The Electrode-Electrolyte Interface....55
4.2.1 The Interfacial Capacitance....56
4.2.1.1 The Helmoholtz-Perrin Model....56
4.2.1.2 The Gouy-Chapman Capacitance....57
4.2.1.3 The Stern Model....58
4.2.2 Resistive Mechanisms....60
4.2.3 Effects of the Electrode-Electrolyte Interface....61
4.3 The Rate Determining Step....62
4.4 Electrochemical Cell Configurations....64
4.4.1 The Three-Electrode System....65
4.5 Chronoamperometric & Voltammetric Techniques with Macroelectrodes....66
4.5.1 Chronoamperometry....66
4.5.2 Linear Sweep and Cyclic Voltammetry....69
4.5.2.1 Electrochemical Reversibility....71

4.6 Chronoamperometric and Voltammetric Techniques with Microelectrodes 72
4.6.1 Chronoamperometry 73
4.6.1.1 The Transition from Linear to Radial Diffusion 75
4.6.2 Linear Sweep and Cyclic Voltammetry 78
4.6.3 Faradaic-to-Capacitive Current and Signal-to-Noise Ratios 80
4.7 The Electrochemical Behaviour of Microelectrode Arrays 80
4.7.1 Loosely Packed Arrays 82
4.7.2 Intermediate Spacings 82
4.7.3 Densely Packed Arrays 82
4.7.4 Recent Investigations Concerning the Behaviour of Arrays of Electrodes 83
4.8 Finite Element Simulations of Microelectrode Array Diffusion Fields 84
4.8.1 Simulation Methods 84
4.8.2 Results 85
4.9 Conclusion 91

THE ELECTROCHEMICAL CHARACTERISATION OF MICROELECTRODE AND NANOELECTRODE ARRAYS 92
5.1 Microfabrication and Experimental Methods 92
5.1.1 Fabrication of Micro- and Nanoelectrode Arrays 92
5.1.1.1 Micro- and Nano-Electrode Array Geometries 93
5.1.2 Experimental Methods 94
5.2 Microfabrication & Experimental Considerations 94
5.2.1 Thin-film Insulation Layers 94
5.2.1.1 SU8 94
5.2.1.2 Normal and Low Stress SiN 96
5.2.1.3 Photoresist and Electron Beam Resists 97
5.2.2 Electrodeposition of Platinum Black 98
5.2.2.1 Electrode Porosity and the Edge Effect 98
5.2.3 Preparation of the Electrode Array Surfaces 100
5.3 Voltammetric Studies With Microelectrode Arrays 101
5.3.1 Microelectrode Arrays with Constant Relative Centre-Centre Spacing (Set A) 101
5.3.1.1 Gold Microelectrode Arrays 101
5.3.1.2 Platinum Black Microelectrode Arrays 106
5.3.2 Microelectrode Arrays with Constant Individual Electrode Radius (Set B) 107
5.3.2.1 Gold Microelectrode Arrays 107
5.4 Chronoamperometric Studies With Microelectrode Arrays 109

5.4.1 Microelectrode Arrays with Constant Relative Centre-Centre Spacing (Set A) 109
5.4.1.1 Comparison of Gold and Platinum Black Microelectrode Arrays ... 109
5.4.1.2 Signal-to-Noise Ratios (SNRs) and Detection Limits ... 112
5.4.2 Microelectrode Arrays with Constant Individual Electrode Radius (Set B) ... 114
5.5 Characterisation of Nanoelectrode Arrays ... 115
5.5.1 Nanoelectrode Arrays Fabricated by Direct-Write Electron Beam Lithography 116
5.5.1.1 Fabrication Considerations ... 116
5.5.1.2 Voltammetric Studies ... 116
5.5.2 Nanoelectrode Arrays Fabricated by Nanoimprint Lithography ... 117
5.5.2.1 Fabrication Considerations ... 117
5.5.2.2 Voltammetric Studies ... 120
5.6 Conclusion ... 121

DESIGN, FABRICATION AND CHARACTERISATION OF A DISSOLVED OXYGEN AND TEMPERATURE MICROSENSOR ... 123
6.1 Overview of Current Dissolved Oxygen Sensor Technologies ... 123
6.1.1 Electrochemical Microsensors ... 124
6.1.1.1 Micro-reference Electrodes ... 126
6.1.1.2 Biofouling ... 129
6.1.2 Optical Microsensors ... 130
6.1.3 Temperature Compensation ... 131
6.2 Microsensor Design and Experimental Methods ... 132
6.2.1 Microsensor Design ... 132
6.2.2 Experimental Methods ... 136
6.3 Microfabrication Considerations ... 137
6.3.1 Metal Electrodes and Thermal Resistor ... 137
6.3.2 Insulation Layer ... 137
6.3.3 SU8 Chamber ... 138
6.3.4 Electroplating ... 139
6.3.5 Electrolyte Gel ... 141
6.3.6 Completed Microsensor ... 142
6.4 Performance of Dissolved Oxygen and Temperature Sensor ... 143
6.4.1 Calibration of Thermal Resistor ... 143
6.4.2 Electrochemical Behaviour and Stability of Ag|AgCl Reference Electrode ... 144
6.4.3 Calibration of Dissolved Oxygen Sensor ... 149

6.5 Conclusion 151

THE DEVELOPMENT OF AN INTEGRATED MICROSENSOR PLATFORM: PRELIMINARY INVESTIGATIONS AND SUGGESTED FUTURE WORK 153
7.1 Overview..153
7.1.1 Integration of Microsensors 154
7.1.2 Particle Manipulation by Dielectrophoresis.......................................154
7.1.2.1 Dielectrophoresis in Microfluidic Channels 155
7.1.2.2 Inhibiting Adhesion of Cells and Colloids...157
7.2 Design of the Proposed Integrated Microsensor Platform 157
7.2.1 Protocols for Fabrication of the Integrated Microsensor Platform 160
7.3 Fabrication of the Integrated Microsensor Platform 160
7.3.1 Ceramic Substrates 160
7.3.1.1 Bonding of the Individual Layers 164
7.3.2 Poly(Ethylene Terephthalate) (PET) Substrates 165
7.3.3 Microsensor Interconnect Vias 167
7.3.3.1 Connection of the Microsensors to the Integrated Microsensor Platform 169
7.4 Simulation and Experimental Methods..170
7.4.1 Matlab Simulations 170
7.4.2 Experimental Methods...171
7.5 Preliminary Simulation and Experimental Results 172
7.5.1 Simulation of the Dielectrophoretic Antifouling Strategy..............................172
7.5.2 Experimental Results for the Dielectrophoretic Antifouling System 175
7.6 Conclusions and Suggestions for Future Investigations 177

CONCLUSION 180
8.1 Summary of Thesis 180
8.2 Suggestions for Future Work..181

REFERENCES 183
PUBLICATIONS ARISING FROM THIS WORK 202

CHAPTER 1

INTRODUCTION

In this chapter, the background and motivation for the research presented in this thesis is discussed. The research was primarily focussed on the study of microelectrode array geometries, the development of a dissolved oxygen microsensor and the integration of microsensors into a flow-through platform. Therefore, a review of recent literature concerning electrochemical microsensors will be presented and the historical development of analytical microsystems will be considered, with an emphasis on environmental and biomedical sensors. The aims of this thesis and the content of each chapter will also be outlined.

1.1 Electrochemical Microsensors

Electrochemical sensors have been employed for several decades in a variety of industrial, clinical and research environments. Early devices, which still influence the design of many modern electrochemical sensors, include those developed in the 1950s for monitoring blood gases (Clark, 1956) and the glucose enzyme electrode that was developed by Clark and Lyons in 1962 (Clark and Lyons, 1962), which was the first reported biosensor. In more recent decades, the emergence of microsensors – sensors with critical dimensions in the order of micrometers – has transformed the field of analytical electrochemistry. The majority of these microsensors have been constructed using the planar microfabrication techniques developed by the semiconductor industry for the production of integrated circuits, although innovative, non-traditional methods are increasingly being employed.

1.1.1 Benefits of Miniaturisation

Miniaturised sensors and systems often display several benefits over their macroscopic counterparts (Madou, 1997). For instance, when employing microelectrodes in place of

conventional macroelectrodes, mass transport to the surface of the electrode is significantly enhanced and the influence of convection is minimised (as will be discussed in Chapter 4). Noise levels and charging currents are also significantly lower for microelectrodes and faster response times may be obtained. Furthermore, the integration of controlling electronic circuitry and micromachined sensors is readily achievable and can markedly reduce the noise level of the overall system. In microfluidic systems, large surface-area-to-volume ratios and reproducible laminar flow profiles are often extremely beneficial, particularly for separation techniques, and substantially reduced volumes of reagents are generally required. High throughput analytical systems are also readily attainable and devices produced by standard microfabrication techniques are very reproducible. Furthermore, as the quantity of materials consumed when fabricating microsensors and microfluidic systems is often extremely low and as batch fabrication is frequently possible, there are powerful cost incentives for the miniaturisation of analytical systems.

In addition, the small size and weight of microsystems can be an advantage in itself. For example, biomedical applications can be readily envisaged for implantable sensors and ingestible devices (Johannessen *et al*, 2002; Frost and Meyerhoff, 2002), whilst remote analysis systems would be extremely useful for environmental analysis. When monitoring freshwater environments, for instance, it is necessary to ensure that representative samples are analysed. The stratification of rivers and lakes, which is affected by seasonal changes, river flow rates and chemical composition, obviously influences the acquisition of representative samples. By designing and manufacturing a small, low-cost microsensor system, it would be possible to place, unobtrusively, a series of devices at different depths throughout the water column and at different locations throughout a body of water (Arundell, 2000).

However, despite the substantial benefits, it should be noted that there are difficulties associated with microfabricated systems, particularly in the areas of device testing (where there is often no rapid assessment procedure), integration (where increased complexity often leads to low yields of fully functional devices) and interconnection to the "real world" (an area that is need of considerable research) (Madou, 1997). Nonetheless, with a modular approach to fabrication and testing, the benefits of miniaturisation for many analytical systems far outweigh any of the aforementioned disadvantages.

1.1.2 Microsensors Reported in the Literature

Numerous electrochemical microsensors, including ion selective electrodes (ISEs), biosensors and voltammetric sensors, have been reported in the literature, as illustrated by recent review papers (Fojta, 2002; Bakker and Telting-Diaz, 2002; Baldwin, 2000; Wang, 2002). For instance, microsensors have been employed to analyse the effluents of capillary electrophoresis and liquid chromatography systems, for in vivo detection of clinically important species, for monitoring DNA interactions and for gas sensing applications. In recent years, there has been increasing interest in exploiting electrochemical microsensors in the fields of clinical diagnostics and environmental analysis. In the case of the latter, microelectrode array based sensors have proved particularly successful in the detection of heavy metals in freshwater samples by stripping voltammetric techniques (Herdan *et al*, 1998; Uhlig *et al*, 1997; Tercier and Buffle, 1993), whilst several sensors have been developed to monitor dissolved oxygen levels and biological oxygen demand (as will be discussed in Chapter 6). Larger scale biosensors have also been developed for a variety of aquatic pollutants, including sulphites, alkylbenzene sulphonates and phenols (Nomura *et al*, 1998; Campanella *et al*, 1995; Kim and Lee, 2003).

Though there has been a great deal of research into sensors for many clinically relevant species (Wang, 1999; Wang, 2002), the most thoroughly investigated of these is undoubtedly the glucose sensor. The traditional approach to the electrochemical detection of glucose involves monitoring the oxidation of the hydrogen peroxide that is produced by the glucose oxidase catalysed reaction of glucose to gluconic acid (Wang, 2001). Methods for immobilising the glucose oxidase have included entrapment of the enzyme within a polymer or sol-gel layer and chemically bonding or electrodepositing it onto the surface of a microelectrode or microelectrode array (Chen *et al*, 2002; Jin *et al*, 2001; Frebel *et al*, 1997). Similar sensor designs have been employed to produce sensors for other physiologically important species, such as lactate and glutamate, whilst several studies have reported on the development of microsensors for the detection of neurotransmitters such as acetylcholine and the catecholamines (Strong *et al*, 2001; Neumann *et al*, 2000). Numerous other applications can be envisaged for miniaturised sensors and, as microfabrication techniques and sensor designs are further refined, it is likely that interest in microsensor technology will continue to rapidly grow.

1.1.3 Industrial Interest

There is strong industrial interest in miniaturised sensors and analytical systems, both in terms of manufacturing them as commercial products and in their application to areas such as process control, product testing and monitoring of waste products. One example of industrial interest in microsystems technology is provided by Kodak Analytical Services and Unilever, who have jointly funded this research.

Both Kodak and Unilever currently have extensive environmental analysis programmes and a strong interest in developing an "early-warning" remote monitoring system for freshwater environments local to their manufacturing plants. Such a system would generate fast, semi-continuous measurements that would be transmitted back to a central laboratory and would rapidly indicate any variation in local environmental conditions. Hence, the measurement of comprehensive freshwater parameters, such as dissolved oxygen, temperature and pH levels, is required, the degree of accuracy being adequate to detect any significant variation in conditions, though not necessarily more accurate than present laboratory techniques. Such a system may also be employed to monitor the level of common waste products, indicators of water hardness (for example Ca^{2+} and Mg^{2+}), potential toxins, including heavy metals, and any valuable reagents, such as silver compounds, which the company endeavours to recover from its effluent before it is discharged. An integrated microsensor array could be developed to fulfil the requirements of a remote environmental monitoring system and, for reasons outlined previously, would prove to be an extremely useful analytical tool. Thus, the research undertaken for this thesis aimed to contribute to the development of such an integrated microsensor system.

1.2 Development of Microfabrication Technologies

Microfabrication technologies, originally developed for use in the semiconductor industry, are central to the field of microanalytical systems. Throughout the later decades of the twentieth century, a wide range of microfabrication processing techniques were devised to meet the ever-increasing demands of the semiconductor industry. Today, these technologies are not only central to the production of integrated circuits, they are also fundamental to the development of miniaturised sensors, actuators and analytical systems. Photolithography is the process at the heart of current microfabrication technologies, although its development began in the early nineteenth century.

1.2.1 History of Photolithography

Photolithography is an optical process used to transfer an image written upon mask onto a radiation sensitive substrate (as described in Chapter 2). Its development began with the work of Joseph Nicephore Niépce. In the 1820s, he successfully copied a print etched on oil-paper onto a bitumen-coated plate by placing the print over the plate and exposing it to sunlight for several hours (Madou, 1997). The areas of bitumen exposed to sunlight were hardened and became less soluble in the solution of lavender oil and white petroleum that was used to develop the plate. This procedure, which is equivalent to the negative resist processes used to make printed circuit boards today, heralded the advent of both photography and photolithography.

Various more readily light-sensitive materials were investigated in the decades that followed, including dichromated gelatin systems. Such a system was patented by William Henry Fox Talbot in the 1850s and became the material of choice for over 100 years. However, all these photosensitive resists were negative acting and did not stand up to strong acid etchants (Wilson, 1994). In 1948, Eastman Kodak received a patent for the first synthetic photopolymer, poly(vinyl cinnamate), which was marketed under the name Kodak Photoresist, KPR (Arnost, 2000). However, significant adhesion problems were encountered with this polymer and, consequently, efforts were focussed on the development of a photosensitive rubber adhesive. A negative resist formulation comprising a low molecular weight rubber and a photoactive bis-azide compound was devised by Eastman Kodak and sold as Kodak Thin Film Resist, KTFR, from 1957 until around 1972, when its resolution of 2 μm was no longer satisfactory (Wilson *et al*, 1997). By this time, the market was dominated by a diazonaphthoquinone (DNQ)-novolac positive photoresist, sold by the company Azoplate who were the industry leaders for many years. In more recent years, continuing improvements in photoresist technology and the use of shorter ultraviolet wavelengths mean that a resolution of 0.2 μm may be routinely achieved today (Ito and Okazaki, 2000). Naturally, the advance of modern photoresists has been paralleled by the development of other essential microfabrication technologies, from continually evolving photolithographic exposure tools to a large variety of etching and deposition systems.

1.2.2 The Emergence of Micro-ElectroMechanical Systems (MEMs) and Micro Total Analysis Systems (μTAS)

As microfabrication technologies have matured, they have increasingly been applied to fields out with the traditional semiconductor industries. The field of micro-electromechanical

systems (MEMs), which was heralded by Richard Feynman in 1959 (Feynman, 1992), encompasses the microfabrication of all systems except for traditional integrated circuits (Judy, 2001) and includes the production of miniaturised biomedical and chemical devices. In 1990, Manz *et al* (Manz *et al*, 1990) proposed the concept of a miniaturised total analysis system (μTAS), which would enable the pre-treatment, separation and detection of a sample to be carried out within a single miniaturised system. Since then, much research has been directed towards the production of integrated micro-analytical systems and the field continues to grow rapidly (Reyes *et al*, 2002; Auroux *et al*, 2002).

1.3 Aims of Thesis

It has been well established that microelectrodes display significantly different electrochemical behaviour to conventional macroelectrodes (Bard and Zoski, 2000). When using a parallel array of microelectrodes, however, the characteristics of the array are strongly dependant upon its geometry and behaviour analogous to that of an individual microelectrode, macroelectrode or some intermediate response may be obtained. Therefore, a systematic investigation of a range of microelectrode array geometries has been undertaken to determine how electrochemical characteristics vary with array geometry, with a view to their use in an analytical microsensor. As little research into well-defined nanoelectrode arrays has been reported in the literature, these studies were extended into the sub-micron domain and a novel method of fabricating such arrays was investigated. A dissolved oxygen sensor incorporating a microelectrode array was then designed, with an internal reference electrode system and a thermal resistor for temperature compensation. Preliminary work on the integration of this microsensor into a flow-through platform was also undertaken.

1.3.1 Organisation of Thesis

An overview of the field of microfabrication is presented in Chapter 2, with a discussion of both the traditional procedures developed by the semiconductor industry and contemporary, non-traditional fabrication techniques. Chapter 3 details the central protocols for all the microfabrication and experimental work described in this thesis and will be referred to at relevant points in later chapters. The theory of conventional electrochemical cells, individual microelectrodes and microelectrode arrays is discussed in Chapter 4, along with the results from simulations of the microelectrode array geometries that were investigated empirically.

The results from the systematic investigation of a range of microelectrode and nanoelectrode arrays are presented in Chapter 5, where the fabrication of nanoelectrode arrays by nanoimprint lithography is also considered. In Chapter 6, a review of recent dissolved oxygen and biological oxygen demand microsensors is given and the design, fabrication and characterisation of a microelectrode array based dissolved oxygen sensor is described. Preliminary work on the integration of individual microsensors into a flow-through platform and the use of the electrokinetic technique, dielectrophoresis, for either antifouling or preconcentration purposes is reported in Chapter 7, which also considers future directions for this work. Finally, a review of the major results presented during this thesis is provided by Chapter 8.

CHAPTER

2

MICROFABRICATION AND NANOFABRICATION TECHNOLOGIES

As discussed in Chapter 1, rapid growth in the development of microsystems technologies has been witnessed in recent decades. The production of such microsystems involves a wide range of micro- and nanofabrication techniques and these will be considered in this chapter. An overview of conventional lithographic techniques will first be presented, followed by a review of alternative rapid fabrication technologies.

2.1 Photolithography & Electron Beam Lithography

Lithographic processes involve the transfer of a design onto a substrate that has been covered with a thin film of radiation sensitive material, known as resist. By exposing selective regions of this resist layer to a source of radiation and then developing it in an appropriate solution, a relief image will be formed in the resist. Several types of lithography (including x-ray, ion-beam and electron-beam) have been investigated by the semiconductor industry, but the most common, well-established lithographic technique is undoubtedly photolithography, which has been used almost exclusively in integrated circuit (IC) manufacturing.

2.1.1 Photolithography

Photolithography uses ultraviolet light to chemically modify the exposed areas of a photosensitive resist layer. A range of photolithographic equipment may be employed to expose a sample, depending upon the resolution, throughput and yield required. For example, the contact printer is a relatively simple system, with which a photoresist coated sample and a metal-patterned quartz mask are brought into direct contact with one and other (Sze, 2002). A beam of nearly-collimated, monochromatic, ultraviolet light is shone through

the transparent areas of the mask onto the resist below for a fixed length of time. The theoretical resolution, R, of such a system, that is the minimum resolvable feature size, is given by the following equation:

$$R = 3\sqrt{\tfrac{1}{2}\lambda z} \quad (2.01)$$

where λ is the wavelength of the ultraviolet light and z is the thickness of the photoresist layer (Madou, 1997). In practice, the resolution of a contact printer will be slightly larger than the theoretical resolution, as any imperfections in the hardware and processing conditions (such as swelling of the photoresist, mechanical instabilities and effects due to lens aberrations) will degrade the resolution of the process. The contrast of the photoresist employed is also critical to the minimum obtainable feature size. Furthermore, the sidewalls of the resulting resist pattern will never be entirely vertical, as the surface of the mask and substrate will never be completely flat and therefore very slight diffraction of the ultraviolet light will occur.

Nonetheless, due to the intimate contact of the mask and the resist layer, contact printing can generate very high-resolution pattern transfer. However, the principal drawback of contact printing is that contaminant particles can easily become imbedded into the photolithographic mask and, as a result of the hard contact between the mask and sample, permanent mask damage can occur. Therefore, the semiconductor industry favours projection photolithographic systems, where the pattern on the mask is projected onto the substrate using a high-resolution lens and thus no wafer contact is required. The theoretical resolution of a projection lithographic system is described by the Rayleigh criterion (Ito and Okazaki, 2000):

$$R = \frac{k\lambda}{NA} \quad (2.02)$$

where NA is the numerical aperture of the optical system and k is an experimental parameter (typically $0.5<k<1$) that is dependant upon the processing conditions and the specific photoresist employed.

Two types of photoresist exist: positive resist and negative resist. Positive photoresists are generally composed of three individual components (Sze, 2002): a resin base (an aromatic polymer of low molecular weight – typically a novolac resin – which may be dissolved in a

strong alkaline solution); a photoactive compound (an inhibitor to the dissolution of the resin base that is broken down by ultraviolet light) and an organic solvent (required for the liquid flow of the resist). Exposure to ultraviolet light breaks down the photoactive compound so that the dissolution rate of the resin base is greatly increased. For a typical novolac-diazonaphthoquinone (DNQ) photoresist system, the exposed areas of the photoresist may have a dissolution rate 1000 times larger than the unexposed areas. Thus, only the exposed regions of a positive photoresist layer will dissolve when immersed in an alkaline developer solution for a short period of time. Naturally, the reverse is the case for a negative photoresist, where exposure to ultraviolet light causes the photoactive compound to initiate the cross linking of a base polymer. Therefore, the exposed regions become significantly less soluble in developer solution. Hence, the exposure and development of a negative resist will produce a relief pattern that is the inverse of the original mask, whilst a positive photoresist produces a pattern corresponding to that of the mask (Figure 2.1). It should be noted, however, that exposure does not result in a distinct boundary between soluble and insoluble areas. Rather, a gradient of solubility will be produced in the boundary regions (Mack, 1994).

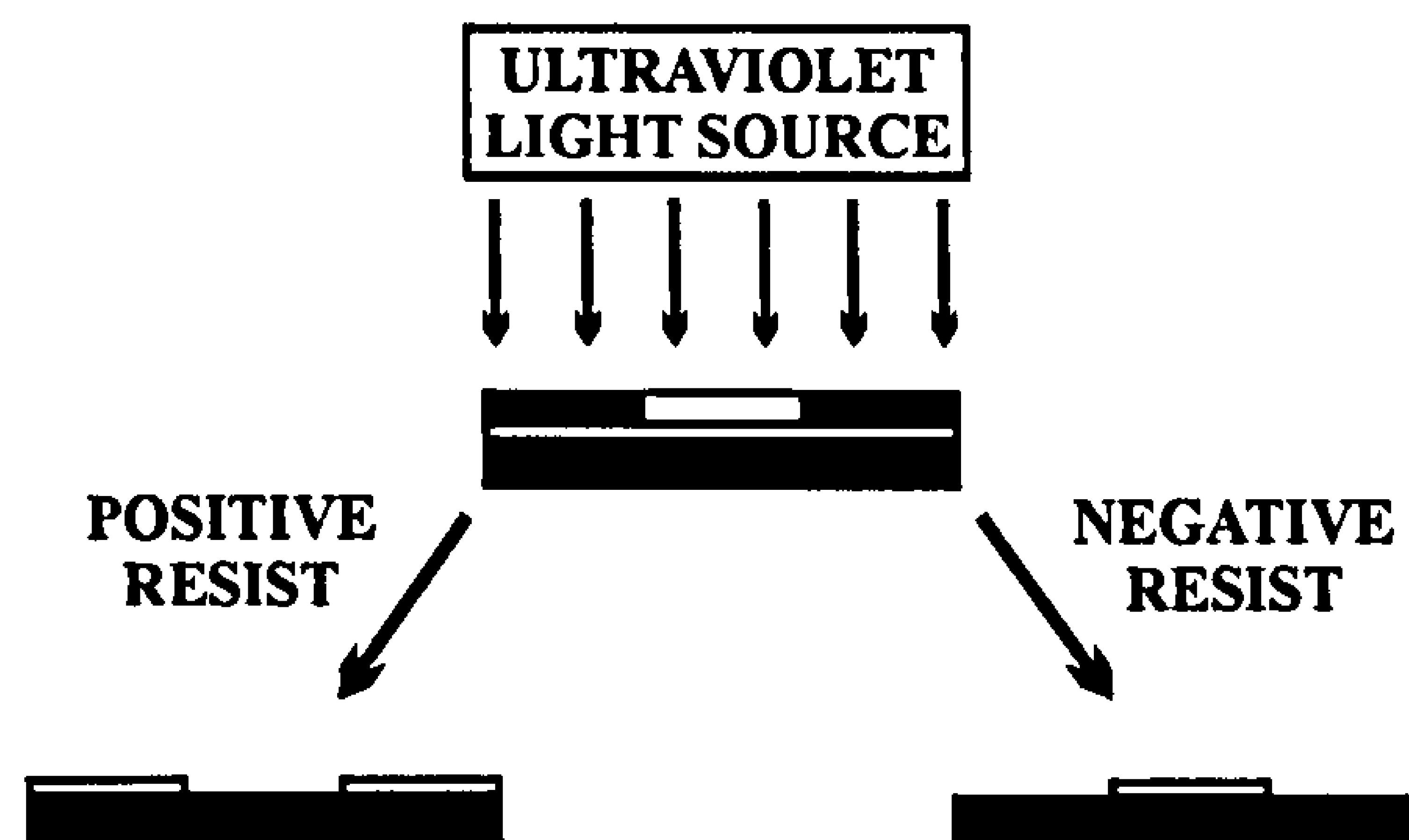

Figure 2.1 **Processing of Positive and Negative Resists Using a Contact Printer**

Illustration showing the different resist patterns obtained after the exposure and development of positive and negative resists. Dark grey represents the substrate, light grey represents the thin-film resist and black represents the metal-coated regions of the quartz mask.

A variety of techniques have been developed to deposit thin films of resist onto a substrate, including those outlined in the following sections. The procedure employed should be reproducible and produce a uniform film across the entire sample.

2.1.1.1 Spin Coating

To spin coat a layer of resist, a sample is first placed on a spinner chuck and held under vacuum. A quantity of resist is then dispensed to form a puddle in the centre of the sample, which is subsequently accelerated to a predetermined rotational speed. Typically, a substrate will be spun for 30-60 s at a rotational speed of 1000-5000 rpm. The thickness of the resulting film is determined by the solid content of the resist and the rotational speed employed (the thickness being inversely proportional to the square root of the latter and proportional to the square of the former) (Madou, 1997). Highly uniform films can be produced by spin coating but this is dependant upon the geometry of the sample. Optimum results will be obtained for circular substrates due to the balancing of the rotation-induced centrifugal force with the resisting viscous force of the resist (Li *et al*, 1998). Non-uniform areas occur when spinning non-circular substrates, which may be problematic depending upon the position of the pattern and the minimum feature size required. Furthermore, substrates that have significant variation in their surface topography, for example those patterned with steep channels or wells, cannot be successfully spin coated, as waves emanating from the corners of the surface features will be formed in the resist layer. Edge-beading is another a common problem, where a build-up of photoresist occurs at the sample edges due to surface tension. Nonetheless, spin coating remains the method of choice for resist deposition when coating planar silicon wafers.

2.1.1.2 Spray Coating

Substrates may also be spray coated with photoresist, using a fine aerosol dispensing mechanism. A range of equipment has been designed for this purpose, including a commercial system incorporating an ultrasonic spray nozzle (Luxbacher and Mirza, 1999). Spray coating has been investigated as a tool for depositing uniform films of resist onto substrates with pronounced surface topographies, as variations in height do not substantially affect the uniformity of the process (Pham *et al* 2001; Lee, 2002).

2.1.1.3 Laminating

Dry film photoresist technologies are well established in the printed circuit board (PCB) industry. Lamination involves placing thin sheets of photoresist that are covered with a protective Mylar® foil over a substrate and then passing the assembly through heated rollers at a controlled temperature and pressure (Lorentz *et al*, 1996). After lamination the Mylar

film, which prevents the photoresist from sticking to the rollers, is removed. At present, all commercial laminates are negative tone and typically produce resist films with a thickness of between 20 and 100 μm. Depending upon the surface topography and the position of the desired photoresist mask, lamination can be employed to pattern 3D microsystems. When a thick, high aspect ratio photoresist pattern is required, several layers of laminate may be coated onto a substrate and then patterned using techniques such as laser ablation and reactive-ion etching (see below) (Zhu *et al*, 1996).

2.1.1.4 Other Methods

Alternative methods for coating a substrate with photoresist include: dip-coating, where the substrate is completely immersed in a resist solution and then pulled out in a slow, controlled manner; meniscus-coating, where an inverted substrate is moved across a laminar resist flow; and electrophoretic coating, an isotropic electroplating process (see below) that requires an underlying conductive layer (Kutchoukov *et al*, 2000). Research into novel resist-coating methods continues to be reported in the literature (Zhou *et al*, 2000; Percin *et al*, 1998)

2.1.1.5 Limits of Photolithography

For a given NA, the maximum resolution obtainable from a photolithography system is ultimately restricted by the wavelength of the light source employed: the shorter the wavelength, the smaller the minimum feature size that may be patterned. The most advanced photoresists are optimised for use in the deep-ultraviolet wavelength range and industry is currently developing lithographic systems that employ 193 nm and 157 nm excimer lasers (Ito and Okazaki, 2000). However, at wavelengths below approximately 290 nm, conventional novolac photoresists become ineffective, due the large inherent absorption of the novolac base resin at lower wavelengths. Furthermore, as a result of diffraction, the depth of focus decreases along with the wavelength and consequently the photolithographic process becomes highly sensitive to variations in resist thickness. In addition, more complex and expensive optical systems are required, as the opacity of conventional optics becomes too large. Therefore, when structures with dimensions in the nanometre range are required, it is necessary to employ alternative lithographic technologies, such as electron beam lithography.

2.1.2 Electron-beam lithography (EBL)

Established in the late 1960s using modified scanning electron microscopes, electron beam lithography (EBL) is a high-resolution fabrication technique, which has been used to produce devices with linewidths as small as 3 nm (Cumming *et al*, 1996) (although 10-30 nm is the practical resolution of a typical EBL system). EBL involves the scanning of a focussed beam of electrons across specified areas of a substrate that has been coated with an electron-sensitive resist film. It is therefore dependant upon the complex interactions of the electron beam and the polymer resist (Kyser and Viswanathan, 1975). EBL is primarily used to produce photolithographic masks but also finds application in advanced prototyping of ICs and optoelectronic devices and in fundamental physical research, such as the study of quantum effects.

2.1.2.1 EBL Machines

The principal components of a typical EBL machine are outlined in Figure 2.2. Electrons may be emitted by heating a tungsten or LaB_6 filament to provide sufficient energy for electrons to overcome their work function barrier (a thermionic source); by applying a strong electric field to a sharp tungsten needle that enables electrons to tunnel through the barrier (a field emission source); or by combining these two methods to produce a thermal field emission source (otherwise known as Schottky emitter) (McCord and Rooks, 1997). In addition, the electron gun will normally incorporate two or more electrodes to control the emission properties of the electron source.

The diameter, profile and direction of the electron beam are precisely controlled by electron optics within the column, whilst accurate sample alignment is achieved by fine control of the stage positioning mechanism within the chamber. During operation, the vacuum system maintains a constant pressure throughout the column and at the gun assembly (approximately 10^{-7} Torr for the former and 10^{-8} Torr for the latter in the EPBG-5HR) and also controls the pressure changes required for loading and unloading samples. The supporting electronic systems supply power and transmit the signals that regulate various components throughout the EBL machine and the entire system is managed by a computer.

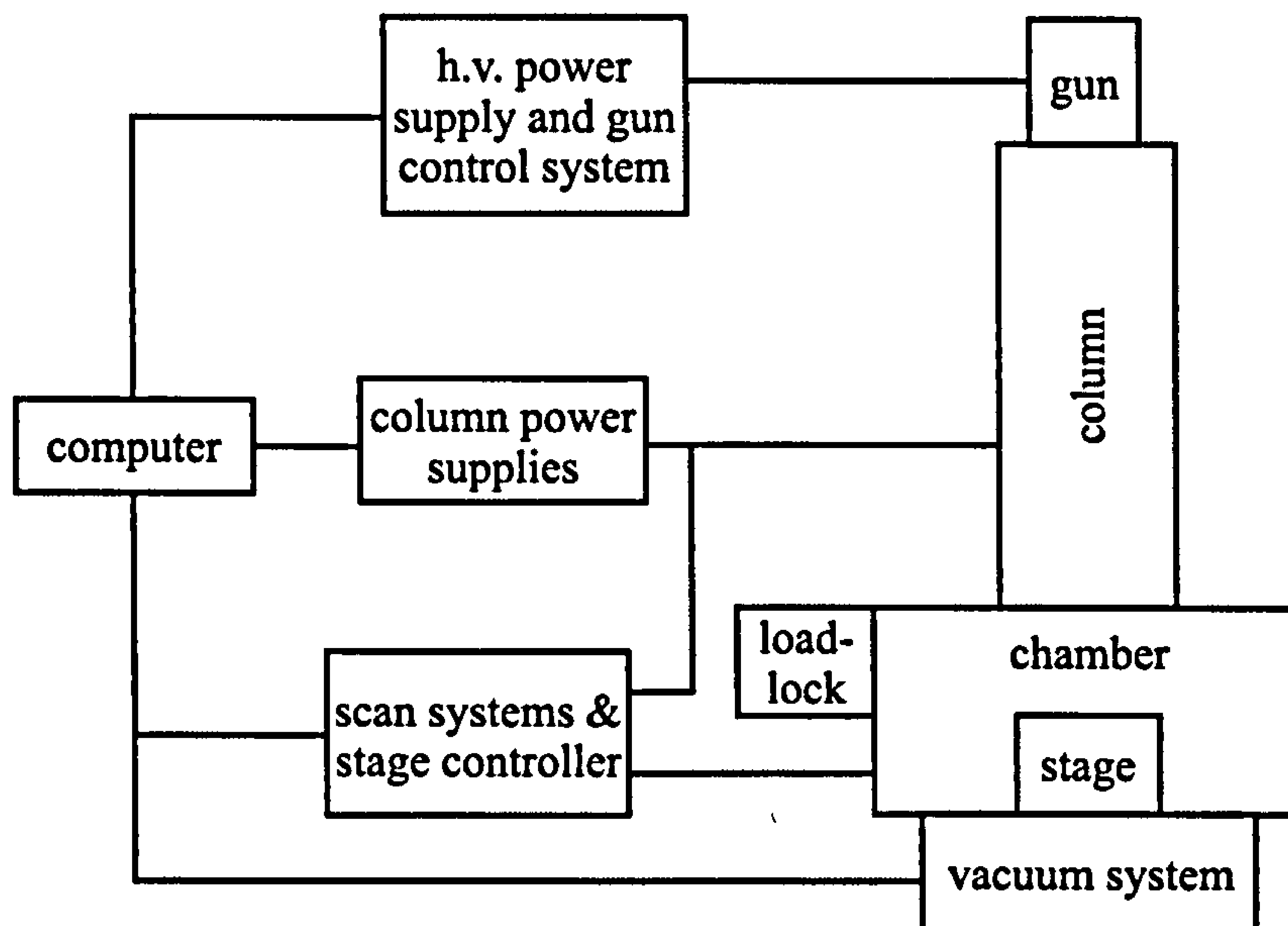

Figure 2.2 **An EBL Machine**
Schematic outlining the major components of a typical EBL machine.

Within the EBL column, a range of electron optics are necessary (FEI Company, Eindhoven). Lenses are required to focus the electron beam and a stigmator is necessary to compensate for any astigmatism arising from defects in the EBL column. Deflectors, which are driven by a pattern generator control unit, are employed to sweep the beam across specified areas of the sample surface. All of these functions can be achieved electrostatically or magnetically, the latter being most common. Apertures are also necessary for beam definition and for turning the beam on and off and an electron detector is required for locating alignment marks on the sample and for focussing.

2.1.2.2 Electron-Sensitive Resist

In the most common positive tone resists, electron beam irradiation initiates polymer chain scissions that produce fragments of lower molecular weight (Hoole *et al*, 1997). As with photoresist, a gradient of solubility results. An appropriate solvent can then be employed to develop the sample, as the lower molecular weight fragments will have a considerably higher dissolution rate than the primary molecule. One of the first materials to be used as an electron beam resist was poly(methyl methacrylate) (PMMA). It can be used to achieve extremely high-resolution pattern transfer and is still the most common resist in use today. When writing with very large doses, PMMA can also function as a negative resist, as

polymerisation of the polymer units will occur, creating a hard, insoluble material (Ziler *et al*, 1996).

A variety of polymeric materials have since been employed as electron sensitive resists, including several common photoresists. Multilayer resist systems have also been used in a variety of applications, most notably to produce an undercut profile for the lift-off procedure (see Section 2.2.1). For an overview of electron beam resists and their processing refer to the McCord and Rooks (1997).

2.1.2.3 Electron-Solid Interactions

Electron-solid interactions are fundamental to EBL technology. As the primary electrons (the electrons of the incident beam) penetrate the resist, the bulk of their energy is dissipated through the generation of a cascade of secondary electrons. The majority of the actual resist exposure is attributable to these so-called secondaries, which affect resist within a range of a few nanometres only.

However, many small angle scattering events occur as the primary electrons cross the resist interface (forward scattering), which tends to produce a significant broadening of the beam profile towards the bottom of the resist layer (McCord and Rooks, 1997). Furthermore, as the electrons permeate through the resist towards the substrate, large angle scattering events occasionally occur (backscattering). This gives rise to additional resist exposure, which is responsible for the proximity effect.

The proximity effect is the term for the nonuniform distribution of actual resist exposure across the patterned area that can be observed despite uniform electron beam irradiation (Chang, 1975). This can be a very significant effect depending upon the pattern geometry and the substrate material. Two types of non-uniform exposure can occur: variation between individual pattern elements, where the actual dose received by a specific feature depends upon its size and proximity to nearby features, and variation within a single pattern element, where the centre of an individual element receives a higher dose than the edges. Obviously, this has serious consequences for development procedures and the resulting pattern definition. Kyser and Viswanathan (1975) simulated the trajectories of forward-scattered and back-scattered electrons using a Monte Carlo technique. The results obtained for a point-source beam, incident at the origin, with an accelerating voltage of either 10 or 20 kV are shown in Figure 2.3.

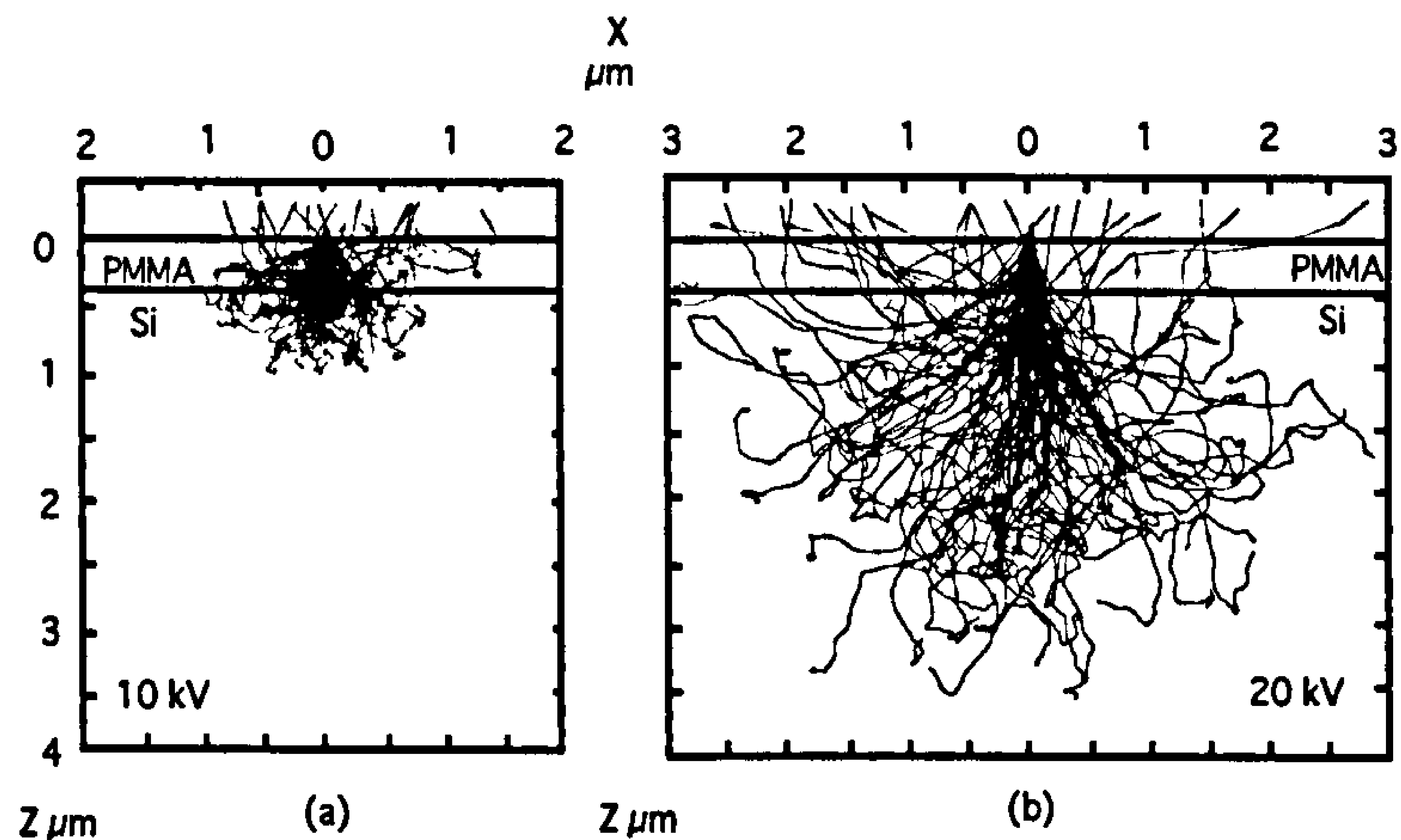

Figure 2.3 **Electron Trajectories**

Results from simulations by Kyser and Viswanathan (1975) of the trajectories of 100 forward- and back-scattered electrons, incident at the origin.

2.1.2.4 Software

EBL systems require a range of software to define the pattern geometry and to convert this information to an appropriate machine format. Pattern geometries can be prepared in a variety of ways but hierarchical design packages are generally employed, so that repeated objects may be modified quickly and simply. GDSII (Graphical Design System II), which supports a hierarchical system of structures, is the most widely used format for pattern definition. To convert a GDSII file to a machine-specific format, a transcription program is required and a dose modulation algorithm may also be employed to correct for the proximity effect, by assigning an optimised dose to the individual features of a pattern.

2.2 Lift-off & Etching Techniques

2.2.1 Lift-off

After patterning a resist layer, two standard techniques may be used to pattern an underlying or overlying thin-film metal layer. If the metal is deposited over a patterned resist layer, immersion in a solvent such as acetone will remove both the remaining photoresist and the overlying sections of metal, leaving behind a design that is the inverse of the initial resist

pattern. This technique is known as lift-off and will only be successful when the thickness of the metal film is significantly less than that of the resist layer. Ideally, the resist should also have an undercut profile to ease the process of lift-off. For positive photoresists, this can be achieved by a pre-exposure chlorobenzene soak, which causes hardening of the photoresist surface. In EBL, a PMMA bilayer is frequently employed for this purpose, with a high molecular weight PMMA being spun over a film of low molecular weight PMMA (McCord and Rooks, 1997). As the lower film has a greater sensitivity to electrons, an undercut profile will be obtained after development. With care, the lift-off technique is capable of generating high resolution pattern transfer and is the method of choice for patterning metal layers with nanoscale features.

2.2.2 Wet Chemical Etching

Should a layer of metal be deposited prior to the patterning of a resist film, the resist may then be used as a mask through which the exposed regions of metal can be etched. Wet chemical etching is a reactive process whereby solvated reactants diffuse towards the unprotected metal, react with the exposed surface and the products are transported away by diffusion. In general, the reaction at the metal surface is that of dissolution and both the agitation and the temperature of the system will affect the dissolution rate. Insulating materials and semiconductors may also be patterned by wet chemical etching, which can be either an isotropic (the etch rate is equal in all directions) or an anisotropic (the etch rate varies with crystallographic orientation) process.

2.2.2.1 Isotropic Wet Chemical Etching

Wet etching metals is an isotropic process, which leads to undercutting of the material beneath the photoresist mask. Consequently, wet chemical etching is normally only employed to pattern features that are relatively wide in relation to their depth, such as the majority of planar microstructures, and is not employed when fabricating nanoscale patterns.

2.2.2.2 Anisotropic wet chemical etching

The anisotropic wet etching of silicon is commonly referred to as bulk micromachining, as it entails etching away sections of the body of a silicon substrate, and is one of the fundamental techniques in the fabrication of microelectromechanical systems (MEMs). The anisotropic

nature of the etching process stems from the structure of crystalline silicon, wherein specific crystallographic planes etch significantly slower than others in certain etchant solutions (such as potassium hydroxide) (Elwenspoek and Jansen, 1999). The (111) planes have by far the slowest etch rate and it is therefore important to ascertain the angle they make with the wafer orientation. In the case of a Si(100) wafer, the angle of the (111) plane relative to the wafer surface is 54.74°, which, when etched through a mask layer with a square hole aligned to the <110> directed edges, will produce a pyramidal pit similar to that shown in Figure 2.4. A considerable variety of three-dimensional structures can created by the anisotropic etching of different crystalline forms of silicon, as described in detail by Elwenspoek and Jansen (1999).

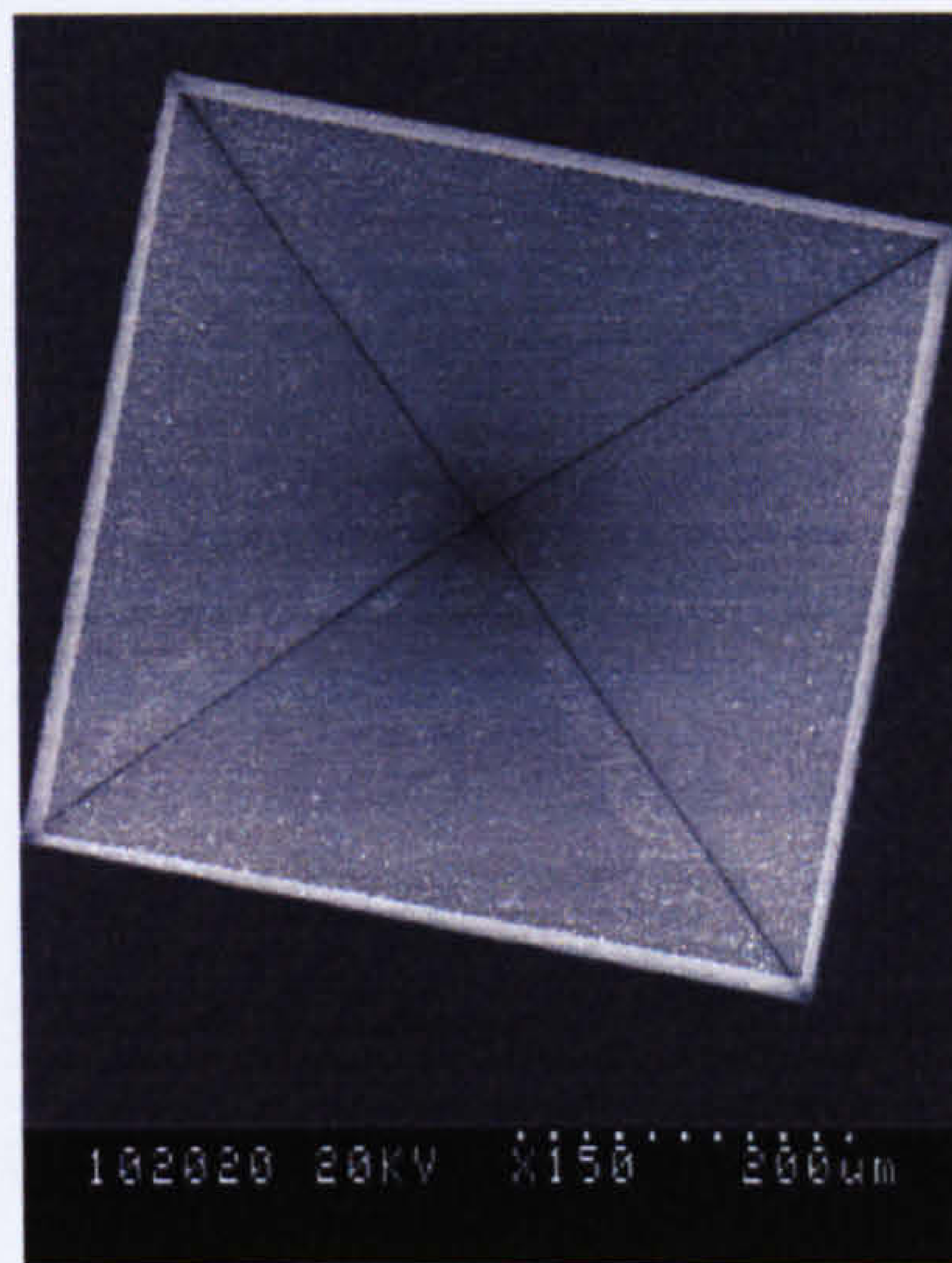

Figure 2.4 **Anisotropic Wet Etching**

SEM of a pyramidal pit produced by the anisotropic wet etching of a Si(100) substrate.

2.2.3 Reactive-Ion Etching (RIE)

The parameter of chemical etching known as anisotropy (A_f) may be defined as:

$$A_f = 1 - \frac{LateralEtchRate}{VerticalEtchRate} \tag{2.03}$$

Thus, to generate high fidelity pattern transfer, an A_f value in the region of one is required. Reactive-ion etching (RIE) procedures can provide this high degree of anisotropy, producing

structures with aspect ratios of up to 30:1 (Clerc *et al*, 1998), and therefore provide a high-resolution alternative to wet chemical etching (Figure 2.5).

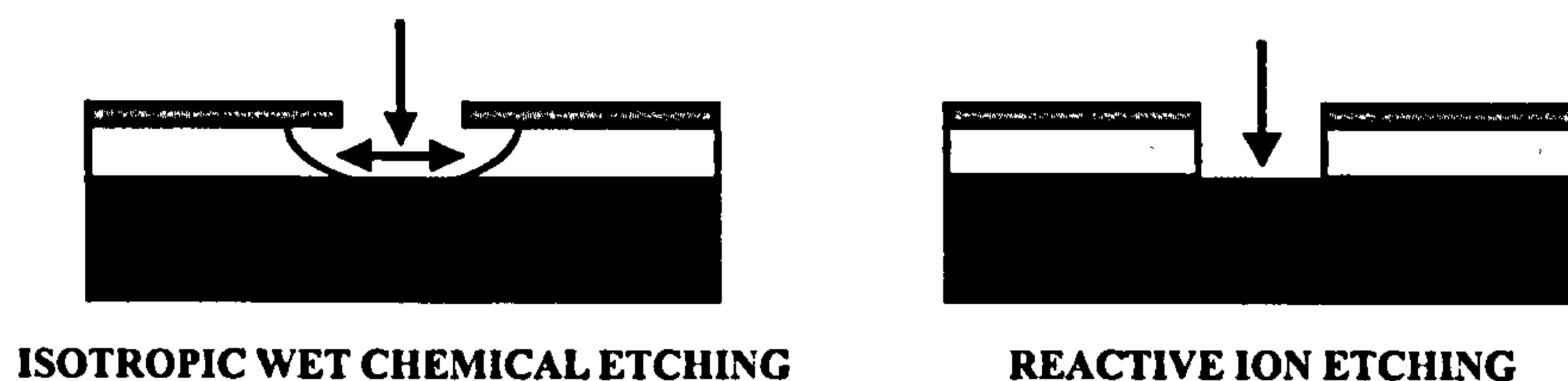

Figure 2.5 **Schematic Illustrating Typical Cross-Sectional Etched Profiles**
RIE is an anisotropic process where minimal undercutting of the material (light grey) occurs, whereas wet chemical etching is generally isotropic and therefore undercutting will take place.

RIE (see Figure 2.6) is a plasma-assisted dry etching technique that involves four distinct steps. Firstly, the etchant species is generated by rf glow discharge to create a plasma from an appropriate feed gas. Rectifying action within the plasma (due to the different mobilities of the constituent ions and electrons) then generates high-field sheath regions, the DC component of this accelerating the etchant across the dark space to the sample surface (Mucha *et al*, 1994). Surface adsorption of the etchant will occur and consequently chemical reactions will take place. The products of these chemical reactions are volatile and hence they desorb from the surface material, diffuse towards the plasma and are pumped away by a vacuum system.

In addition to the etching parameters employed (such as the d.c. bias voltage, chamber pressure, gas flow rates and r.f. power settings), the sample geometry can strongly affect the profile of the etched structures. For constant etching conditions, the characteristics of the etched profile will change as the spacing between individual structures increases or as the individual features are reduced in size. This was illustrated by Tsutsui *et al* (1993) who progressively increased the spacing in arrays of GaAs nanopillars and consequently observed a dramatic increase in the degree of undercut.

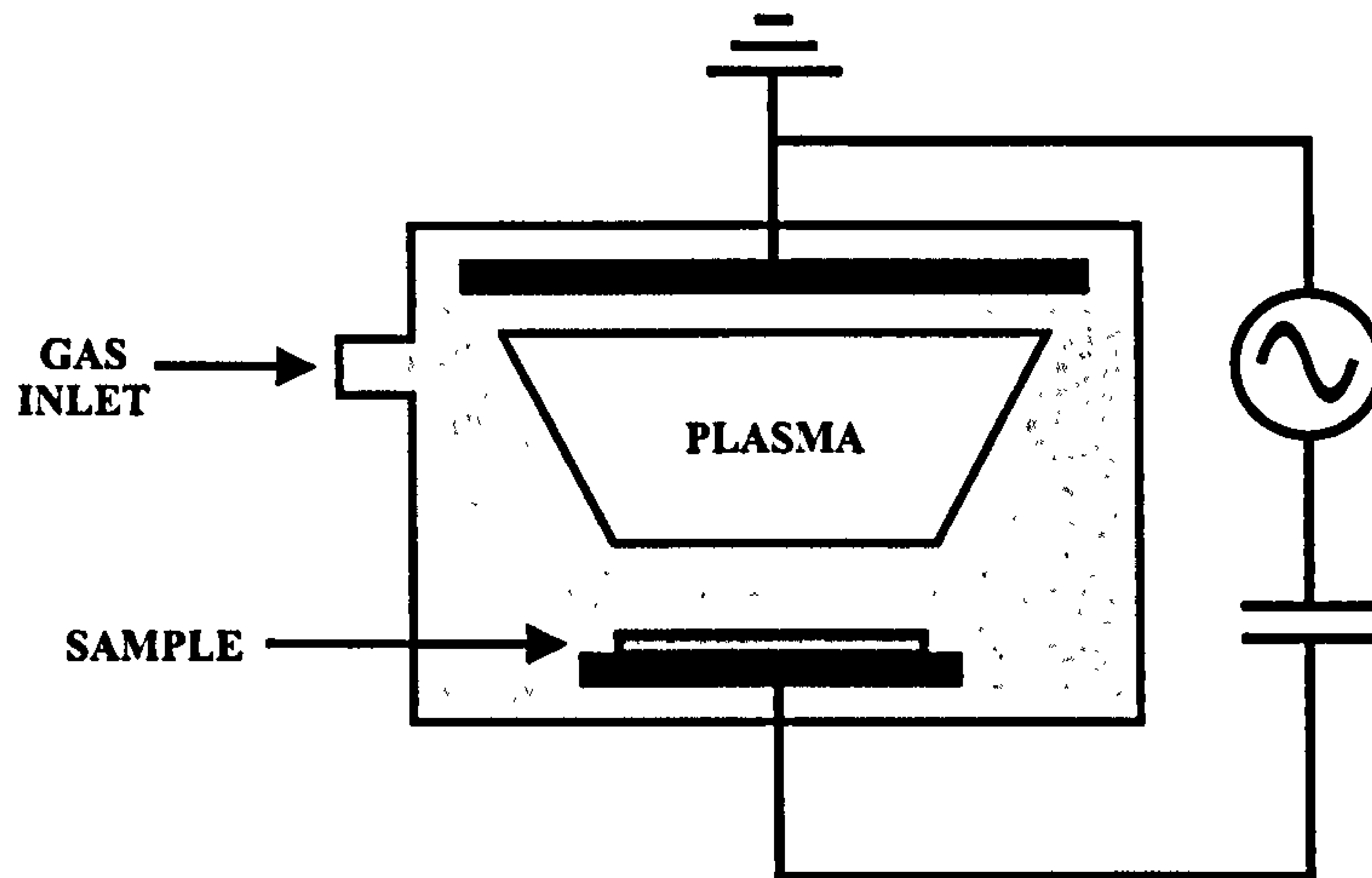

Figure 2.6 **Schematic of a Typical RIE Machine**
The plasma is a highly conductive gas, comprised of ions, electrons, neutrals and radicals, that, as a whole, is electrically neutral. A region known as the dark space is established between the plasma and the two electrodes, as the electrical-neutrality of the plasma cannot be maintained in close proximity to a metal surface (Handa, 1998)

For many applications, particularly in the fields of MEMs and microfluidics, it is desirable to anisotropically etch through large depths. In recent years, the production of advanced RIE machines and improvements in masking techniques have facilitated the development of suitable deep-RIE processes (Clerc *et al,* 1998) so that it is now possible to etch through several hundred microns of silicon, with a high degree of anisotropy.

2.3 Deposition of Thin-film Metal Layers and Insulation Materials

2.3.1 Physical Deposition: Evaporation and Sputtering

The deposition of thin-film metallic layers, either by evaporation or by sputtering, is fundamental to the production of microfabricated devices. In an evaporation system, a metal target is heated to boiling point under vacuum and the substrate is subsequently coated with the rising metal. The metal can either be heated resistively, inductively or by an electron-beam (Campbell, 1996). In the latter case, a tungsten filament is commonly employed to thermionically generate an electron beam, which is accelerated by an electric field and then steered by a "bending" magnet so that it is focussed upon the surface of the source metal. In

a sputtering system, the metal target is held at a high negative potential and bombarded with positive argon ions that, by transfer of momentum, sputter away the surface metal atoms, which then condense onto the substrate. Highly uniform films with precisely controlled thickness can be generated by both evaporation and sputtering and, hence, the choice of deposition method is often arbitrary (although sputtering can cause significant substrate damage, whilst the step coverage of evaporated films is generally poor).

2.3.2 Electroplating

Adherent metal films may also be deposited electrochemically, by reducing a dissociated metal salt onto a negatively biased electrode. Standard electroplating solutions exist for a range of metals, including all noble metals. The surface roughness of electroplated films is generally much greater than that of evaporated or sputtered films and the thickness, adhesion, porosity and uniformity of the films can be difficult to control. However, very thick layers of metal can be deposited and relatively simple, inexpensive equipment is required.

2.3.2.1 Electroplating "Black" Films

If the current density employed for electrodeposition is increased, dendritic growth will begin to occur due to the large reactant concentration gradient that subsequently develops. Higher field regions will surround the crystallites that extend the farthest outwards where higher rates of electrodeposition will consequently be favoured (Kovacs, 1998). At sufficiently high current densities, the resultant electroplated films will appear black and will have a large effective surface area that can generate greatly increased signals (see Figure 2.7). Platinum black films are regularly employed in neurophysiology and electrochemistry and can be electroplated from a hexachloroplatinate-lead acetate solution:

$$PtCl_6^{2-} + 4e^- \quad Pt_{(ad)} + 6Cl^- \qquad (2.04)$$

When electrodepositing a platinum black film, it is essential to introduce an additive such as lead into the electroplating bath. It has been proposed that these additives act as "psuedo-defects" (Layson & Columbia, 1997), encouraging electron transfer on smoother areas of the sample where nucleation centres would not otherwise form. It should be noted that platinum black microelectrodes generally exhibit large background currents and noise levels when

compared to smooth, metal electrodes (Niwa *et al*, 1996). Therefore, when deciding whether to electroplate a sensing electrode with platinum black, the relative increase in the signal and noise levels and the specific application of the system should be considered.

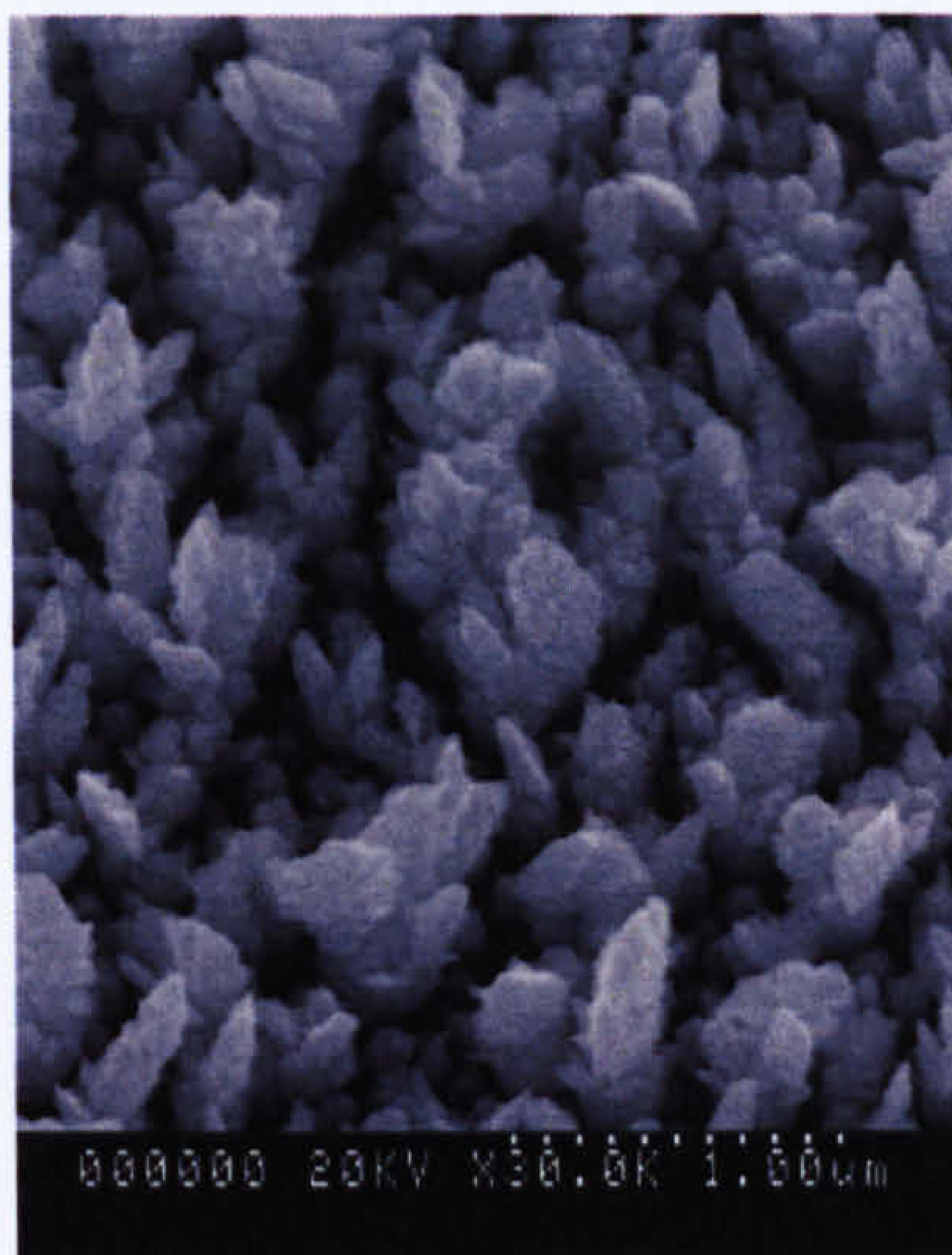

Figure 2.7 **Electrodeposited Platinum Black**

Platinum black films result from dendritic growth during electroplating.

2.3.3 Chemical Vapour Deposition (CVD)

Unlike evaporation and sputtering which involve solely physical processes, chemical vapour deposition (CVD) is a reactive technique where reactant gases adsorb onto a heated substrate, migrate towards energetically stable nucleation sites and undergo film-forming reactions, whilst gaseous by-products desorb from the surface and are pumped out of the reaction chamber (Madou, 1997). One of the products will be a solid component that is deposited onto the substrate whilst the remaining gaseous products are removed from the chamber together with a neutral carrier gas. CVD is most commonly employed to deposit thin dielectric and semiconductor layers.

The energy required for the CVD process may be delivered either by heating the substrate or by employing an rf plasma. If the sample is heated at atmospheric pressure (APCVD), the reaction process will generally be mass transport limited; whilst in a low pressure CVD system (LPCVD) the mass transport of reactants increases and so the process becomes reaction rate limited (Menz *et al*, 2001). In cases where the substrate material or surface features cannot withstand high temperatures, plasma enhanced CVD (PECVD) is employed.

2.3.3.1 Plama Enhanced Chemical Vapour Deposition (PECVD)

The dissociation energy required for the PECVD process, which employs similar equipment to a RIE system, is provided by the high-energy electrons or photons that are generated within the plasma (Campbell, 1996). A typical parallel-plate, PECVD reactor can, under optimum conditions, generate films that effectively correspond to the topography of the substrate material. Silicon nitride is commonly deposited by reacting silane and ammonia in a nitrogen carrier gas. PECVD silicon nitride, which is generally written as SiN, is not a stoichiometric material, rather it has the composition $Si_xN_yH_z$ (Sze, 2002). The precise composition and properties of the film depends strongly on the deposition conditions.

Both LPCVD and PECVD films suffer from intrinsic stresses, which are again dependent on the deposition conditions, that are often problematic when fabricating microsensors. These stresses, which can be either tensile or compressive and result from variation in the chemistry and porosity of the deposited material, are often very large and can lead to cracking and de-lamination of the film. However, recent research into CVD film properties has shown that by carefully controlling the reactor pressure, r.f. frequency and power, growth temperature and process gas flow, low-stress dielectric films can be produced (French *et al*, 1997; Bozeat *et al*, 1998).

2.3.4 Polyimide

Polyimide is an aromatic, heterocyclic polymer that is frequently employed as an interlayer dielectric and passivation material in the semiconductor industry, as a result of its low dielectric constant, high thermal stability and stress relief properties. Most commonly deposited by spin coating, polyimide is an excellent planarisation material, although its adhesive properties can be poor. Exposure to an oxygen plasma, which breaks open the surface imide rings increasing the hydrophilicity of the polymer (Nakamura *et al*, 1996), can significantly improve the adhesion of metals to polyimide films, whilst the silanisation of surfaces can promote the adhesion of polyimide to common substrates.

2.4 Alternative Micromachining Technologies

Although the microfabrication technologies discussed above are fundamental to the production of the vast majority of microsystems, they are, nonetheless, expensive and often

time-consuming techniques. As a result, novel materials and rapid fabrication techniques have been employed in recent years to produce cheaper devices. Furthermore, structures that may be replicated quickly, that are transparent to ultraviolet and visible light, and have surface chemistries that may be easily modified have been realised using non-traditional fabrication techniques. High-resolution procedures, such as LIGA (Lithographie, Galvanoformung, Abformung), laser micromachining and nanoimprint lithography, have also been employed to produce novel micro- and nano-structured devices.

2.4.1 Soft Lithography

Various research groups have developed microfabrication techniques that exploit the properties of elastomeric materials, most notably poly(dimethylsiloxane) (PDMS). PDMS has been employed for a vast range of applications, from microanalytical systems to MEMs, micro-optics and microelectronic devices as it is an inexpensive, chemically inert, silicone elastomer that is transparent to visible and ultraviolet light (Qin *et al*, 1998). A variety of techniques have been developed for structuring both PDMS and a range of other polymeric materials, including the techniques outlined below.

2.4.1.1 Moulding

The moulding of polymers against a rigid master is a well-established manufacturing technique that is commonly used to produce optical devices such as CDs and diffraction gratings. Similarly, a range of organic polymers and elastomeric materials have been moulded against a microfabricated master to create reproducible structures such as capillary electrophoresis systems (Duffy *et al*, 1998; Effenhauser *et al*, 1997) Once the initial cost of the microfabricated master has been met, numerous structures can be cast from the one device, making this simple procedure an attractive microfabrication technique. For details of a range of different moulding techniques (such as micromoulding in capillaries, microtransfer moulding and replica moulding) refer to the work of G. M. Whitesides' group at Harvard University (Xia *et al*, 1998; Xia *et al*, 1999).

Primary masters are typically fabricated by the photolithographic techniques described previously and can be created using a variety of materials, including silicon, glass, electroplated metals and photosensitive polymers, such as SU8. Factors such as the strength,

brittleness, rate of wearing and ease of cleaning all have a bearing on the choice of material employed for the master.

2.4.1.1.1 SU8

Several photosensitive polymeric materials have been employed in recent years for the production of lower cost, high aspect ratio moulds without the use of RIE. SU8, a negative photo-epoxy developed by IBM, has been used to create a wide variety of novel microstructures, both as part of a working device and as a mould. SU8 is reasonably chemically resistant and can produce tall structures with extremely high aspect ratios (Lorenz *et al*, 1997; Lee *et al*, 1995). It is therefore an attractive material for use in MEMs and microfluidic applications. However, as the adhesion of SU8 to common substrates can be relatively weak and un-developed residues can be somewhat difficult to remove, the optimisation of the processing conditions for each individual application is critical.

2.4.1.2 Microcontact Printing

Elastomeric structures produced by moulding may also act as stamps for the patterning of self-assembled monolayers (SAMs), films of functionalised long-chain molecules formed by chemisorption onto the surface of a suitable substrate (Qin *et al*, 1998). A PDMS stamp, moulded from a microfabricated master, is first inked with an alkanethiol solution (in the case of a gold coated substrate). The stamp is then pressed onto or rolled across a sample to produce a patterned SAM, which can be functionalised further or can act as a mask for wet etching. This technique can be employed to pattern both planar and curved substrates and feature sizes as small as 100 nm have been successfully reproduced (Michel *et al*, 2001). A promising application of this technology is in the production of DNA and protein arrays, which require the immobilization of large numbers of spatially separated biomolecular spots onto a planar substrate (Xiao *et al*, 2002).

2.4.1.3 Imprinting & Injection Moulding

Imprinting and injection moulding are common manufacturing techniques that have been successfully applied to high throughput commercial applications, such as the production of CDs, which normally involves the imprinting of a polycarbonate substrate using a Ni master (Xia and Whitesides, 1998). In more recent years, numerous microanalytical systems,

including microfluidic platforms with optical detection and micro-flow cytometers, have been produced by the imprinting or injection moulding of thermoplastics such as PMMA and polycarbonate (Becker and Heim, 2000; Martynova *et al*, 1997; Hulme *et al*, 2002; Madou *et* al, 2001). Interest in producing polymer microfluidic devices using these techniques is continually growing due the to low-cost, rapid nature of these procedures.

2.4.2 High Resolution Micromachining Techniques

2.4.2.1 Nanoimprint Lithography (NIL)

In 1996, the polymer imprinting procedure was re-examined by Chou *et al* who reported its use in the fabrication of sub-100 nm devices. This nanoimprint lithography (NIL) procedure shows great potential for the production of high-resolution structures, which are crucial to the future of ultra-large scale integrated semiconductor devices and to the commercialisation of nanodevices in general, including bioanalytical systems.

NIL is a relatively straightforward procedure (Faircloth *et al*, 2000). A nano-structured stamp is fabricated using a conventional technique such as EBL and is subsequently coated with a mould release agent. The sample that is to be imprinted is coated with a polymer film such as PMMA, which is heated to a point above the glass transition temperature of the polymer (approximately 120°C for PMMA), and the stamp is then pressed into this film (Figure 2.8a). Whilst maintaining a constant pressure, the whole system is cooled to a point well below the glass transition temperature of the polymer and the stamp is then removed (Figure 2.8b). A thin layer of polymer will normally remain in the bottom of the imprinted features and this can be removed by oxygen etching (Figure 2.8c). Provided an appropriate mould release agent is employed and minimal lateral pressure is applied, a NIL stamp can be re-used numerous times.

In recent years several research groups have investigated NIL as an alternative to the more expensive and time-consuming current nanofabrication techniques, such as EBL, x-ray lithography and focussed ion-beam technology (Hirai *et al*, 2001; Chen *et al*, 2002; Schulz *et al*, 2000). If suitable alignment systems can be developed, NIL may become a very valuable tool for the production of low-cost nanodevices.

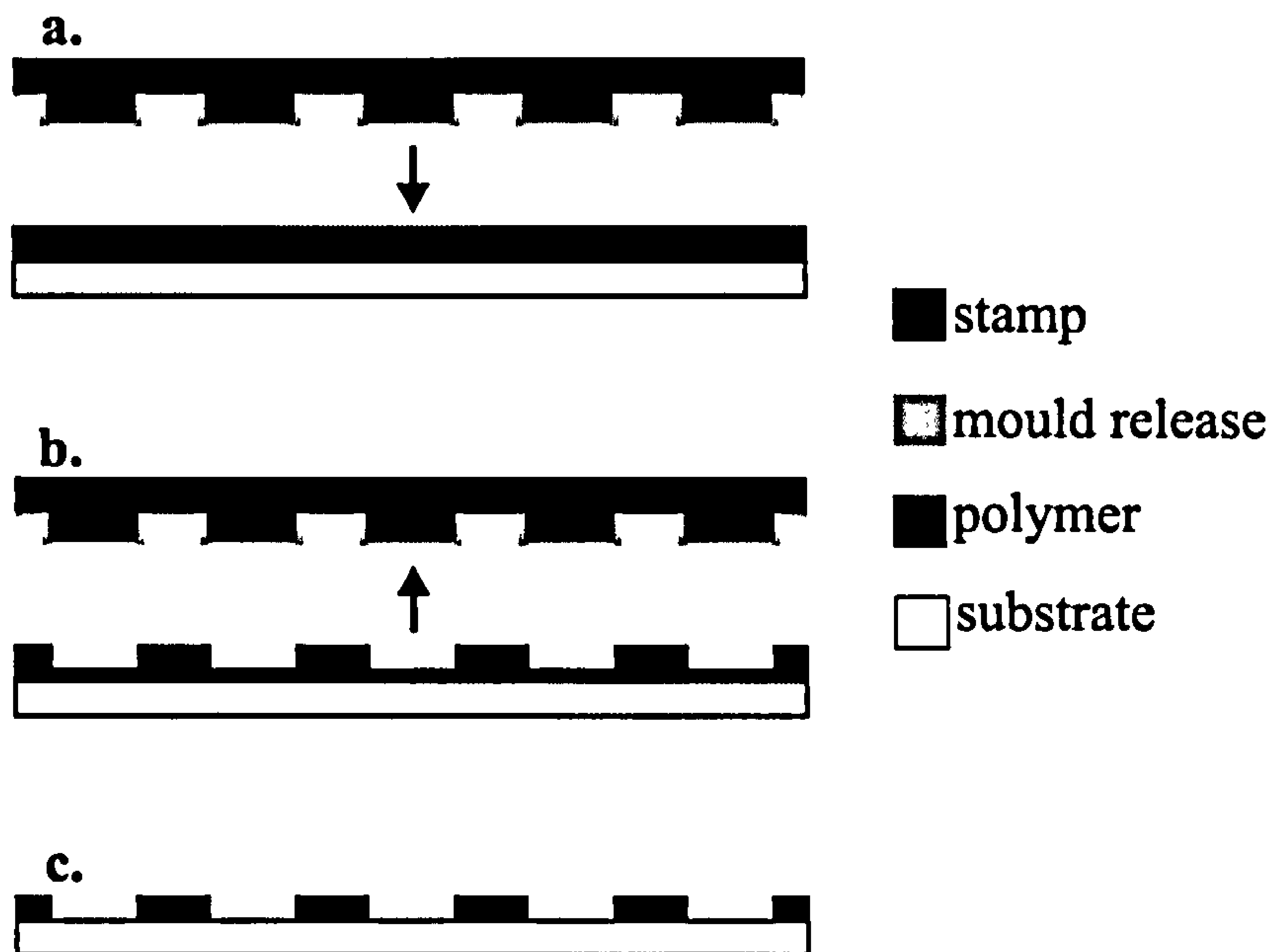

Figure 2.8 **Overview of the Nanoimprint Lithography (NIL) Process**
The NIL process as described in Section 2.4.2.1.

2.4.2.2 LIGA

LIGA is an acronym for "Lithographie, Galvanoformung, Abformung", the German for "lithography, electroforming, moulding". It is a technique for the production of high-resolution, three-dimensional microstructures, which was developed in the 1980s at the Karlsruhe Nuclear Research Centre (Becker *et al*, 1986). X-ray lithography employs wavelengths in the order of 1 nm and can generate extremely high aspect ratio structures in polymer films that are several hundred microns deep. In the case of LIGA, it is employed to produce a polymer template. This template is subsequently filled by electrodepositing a metal, which is then used as master for the moulding of another plastic structure. As with the moulding techniques described previously, numerous devices can be moulded from the one metal structure, each of which may subsequently be electroplated with metal to produce a structure that is virtually identical to the primary metal mould. A large range of microstructures, including accelerometers, micromotors and other MEMs devices, have been fabricated by LIGA. For an overview refer to Menz *et al.*

2.4.2.3 Laser Micromachining

A range of laser-based micromachining techniques have emerged in recent years, including excimer laser micromaching, which involves the direct ablation of a solid substrate by pulsed laser radiation (Holmes, 2001). Complex interactions arise between the laser radiation and the solid material but, as energy is only absorbed at the surface of the substrate, only a thin layer of material is removed during each pulse. If conditions are optimized, laser micromachining can create features with very large depths in virtually any solid material and minimum feature sizes are in the sub-10 μm range.

Alternative laser micromachining techniques include: pulsed-laser deposition, which is used to deposit a film of material over an entire sample; laser chemical vapour deposition (LCVD), where material is selectively deposited onto the sample; laser LIGA processes, in which laser ablation is employed in place of x-ray lithography; and stereolithography, which enables the creation of complex 3D structures by the laser induced solidification of a liquid polymer on a layer-by-layer basis (Bertsch *et al*, 1999).

2.5 Bonding Techniques

In the majority of microfluidic and MEMs devices, the bonding of two or more substrates will be required. This is often the most critical step in the fabrication of a device, particularly in microfluidic systems where a hermetic seal is required. Several strategies have been devised to successfully bond a variety of materials together, including the techniques described below.

2.5.1 Anodic Bonding

Anodic bonding is a well-established microfabrication technique, of particular importance to microfluidic systems where glass and silicon may be readily employed. First reported in 1969 as "Field assisted glass-metal sealing" (Wallis and Pomerantz, 1969), anodic bonding facilitates the formation of a strong, hermetic seal between a sodium-rich glass and a metal or semiconductor. Although the exact mechanism of bond formation is not yet fully known, it is understood that interfacial ionic flow governs the process.

Sodium is easily ionised at room temperature, these positive ions becoming considerably mobile at elevated temperatures. Therefore, if a sodium-rich glass and a semiconductor are clamped together and heated to a specific temperature, an applied dc electric field will initiate the migration of Na^+ towards the cathode (the cathode being in contact with the exposed glass surface). Consequently, a sodium depletion layer is formed at the interfacial glass surface, where the fixed negative charge remains, and a space charge region is created across the glass-semiconductor interface, which results in strong electrostatic forces that pull the two materials together. At this point atomic bond formation occurs, creating a completely hermetic seal (Choi *et al*, 1997; Nese and Hanneborg, 1993).

2.5.2 Silicon Fusion Bonding and Thermal Bonding

Silicon fusion bonding involves sealing two or more silicon substrates together. Prior to bonding, the native or grown oxide film on the surface of each substrate is made hydrophilic by a sequence of chemical processing steps. Once the two substrates are brought into contact with each other, they adhere together by van der Waal's bonding (Klaassen *et al*, 1996; Liu and DeVoe, 2001). To form a strong, stable bond, the sample is then heated to a temperature greater than 800°C. Although the bonding mechanism is not completely understood, the fundamental process in silicon fusion bonding is the formation of Si-O-Si bonds due to the polymerisation of the silanol groups present on the surface of the oxide films (Madou, 1997). The annealing temperature and the surface roughness of both substrates will strongly affect the quality of the bonding.

Glass, or glass-coated, substrates may be thermally bonded at a controlled temperature and pressure. The temperature required is dependant upon the composition of the glass employed. Certain glasses, such as phosphosilicate glasses, require high temperatures in the region of 1100°C, which will result in the degradation of most thin-film metal layers that may have been patterned on the surface of the substrates. However, commercial low-temperature sealing glasses that can be thermally bonded at temperatures in the range of 400-650°C are readily available (Madou, 1997).

2.5.3 Bonding Polymeric Materials

Numerous three-dimensional microsystems have been produced in recent years that have involved the bonding together of polymeric materials or their use as an intermediate layer in

the bonding of non-polymeric substrates. Lamination is one of the most common techniques employed in the fabrication of polymeric microfluidic devices. Metz *et al* (2001) produced a polyimide-based microfluidic device with embedded microelectrodes, the fabrication of which involved the lamination of a polyimide film over a polyimide channel wall that had been treated with a swelling agent. These devices exhibited high bond strengths with no visible interface between the constituent layers.

PDMS flow-channels can be hermetically sealed onto a glass, silicon, silicon nitride, silicon oxide, PDMS or other polymeric substrate by first modifying the PDMS surface using an oxygen plasma and then pressing it onto the substrate (Monaghan *et al*, 2000). Oxygen treatment renders the PDMS hydrophilic, due to the production of silanol groups at the surface, and bonding is thought to occur by a condensation reaction resulting in the formation of bridging covalent bonds (typically Si-O-Si) (Duffy *et al*, 1999). This bonding technique, which occurs at room temperature, is instantaneous and irreversible.

Common adhesives may be employed to bond two substrates together in an inexpensive and simple manner. In the capillary adhesive techniques, a small quantity of glue is dropped onto the interface of the two substrates that are to be bonded. Capillary forces subsequently draw the adhesive into the narrow gap between the adjoining surfaces (Menz *et al*, 2001). Hot melt adhesive foils can also be employed to bond two surfaces together. In this case, the substrates are clamped together and heated to an appropriate level (for low temperature adhesives the temperature required will be 70-100°C). As there is a wide range of adhesives available with varying chemical resistance, any adhesives employed must be checked for compatibility with the proposed application of the device.

2.6 Conclusion

A wide range of materials and methods have been employed in the fabrication of analytical sensors and microfluidic systems and the repertoire of micromachining techniques continues to grow as existing procedures are adapted to produce innovative structures. When devising a new fabrication protocol, optimisation of the procedures involved is critical, as is their careful selection from the range of available techniques (in terms of the materials required, reproducibility, complexity, production time and cost). Nonetheless, in the development of novel, efficient microsystems, the potential of the micro- and nanofabrication techniques outlined is huge.

CHAPTER 3

MATERIALS AND METHODS: MODELLING ENVIRONMENTS, MICROFABRICATION PROTOCOLS AND EXPERIMENTAL APPARATUS

This chapter details all the materials and methods employed during the research presented in this thesis. Firstly, the software tools employed for numerical simulation will be discussed. The microfabrication protocols for each individual stage in the production of the devices described in later chapters will then be presented. Lastly, the apparatus used for all the experimental work will be described (although the protocols employed for specific experiments will be presented during the relevant sections of future chapters).

3.1 Materials

All reagents employed for microfabrication and experimental work were purchased from Sigma-Aldrich (Poole, UK), unless otherwise stated. The materials used in the production of microfabricated devices were sourced from a variety of companies. Double-polished, silicon nitride coated, n-type Si(100) wafers were obtained from Edinburgh Microfabrication Facility (Edinburgh, UK), whilst virgin test Si(100) wafers, polished on one face only, were purchased from Compart Technology (Peterborough, UK). Ceramic substrates, pre-cut where necessary, were obtained from Coors-Tek (Fife, UK) and poly(ethylene terephthalate) (PET) sheets were purchased from Goodfellow (Cambridge, UK).

All lithographic materials were purchased from Chestech (Warwickshire, UK), except for a negative-tone laminate (Riston MM140), which was purchased from DuPont (Hertfordshire, UK), and an Electrolube photoresist aerosol, which was purchased from RS Components (Corby, UK) along with a two-part, clear silicone elastomer. Two different SU8 formulations were employed for microfabrication purposes: SU8 1040 from Sotec Microsystems (Renens,

Switzerland) and SU8 50 from MicroChem Corporation (imported by Chestech, Warwickshire, UK). The former was employed to create films with a thickness of 1-10 µm and the latter for films with a thickness of 100-400 µm. PI2545 polyimide precursor was purchased from HD Microsystems (Bad Homburg, Germany) and a silicone rubber (RTV Sealant 3145) was obtained from Dow Corning (Coventry, UK). A sample of VP108H hot-melt adhesive foil was supplied by Sika Werke (Leipzig, Germany)

An EG&G 273A potentiostat-galvanostat controlled by a computer with associated software (Princeton Applied Research, New Jersey, USA) was employed for all electrodeposition processes, whilst electrochemical recordings were made using a CV-37 Voltammograph from BAS Instruments (Cheshire, UK) that was controlled by an in-house data-handling programme and a PC26AT data acquisition card (Amplicon Liveline, Brighton, UK). A Ag|AgCl reference electrode and a coiled platinum auxiliary electrode were also obtained from BAS Instruments. Gas flow meters were purchased from Platon Instrumentation (Basingstoke, UK), whilst the associated tubing and fittings were sourced from both Swagelock (Irvine, UK) and Omnifit (Cambridge, UK). A Keithley 617 Electrometer meter was employed for voltage measurements and a Cole Parmer 74900 Syringe Pump was employed for dielectrophoresis experiments, along with a TG120 20 MHz signal generator from Thurlby Thandar Instrumenets, an in-house amplifier and a 54615B 500 MHz oscilloscope manufactured by Hewlett Packard. Polystyrene latex beads with carboxylated surfaces were purchased from Polysciences Europe (Germany).

Finally, various forms of microscopy were employed to image microfabricated devices. These included scanning electron microscopy (using either a Hitatchi S800 or S4700 microscope), atomic force microscopy (with a Dimension 3100 scanning probe microscope), optical microscopy (using a Nikon Microphot with either a JVC TK-C1380 or a Photometrics Coolsnap camera) and surface profiling (with a Dektat 3ST profilemeter).

3.2 Modelling Environments

The diffusion of electroactive species to the surface of a microelectrode or microelectrode array and the trajectories of particles in a flow-through analytical system were both modelled during the course of this research. The software packages FlexPDE version 2.22 (PDE Solutions, California, USA) and MATLAB® version 6.1 (MathWorks, Massachusetts, USA) were employed for this simulation work and were run on a personal computer with a 1 GHz

Intel Pentium III processor running the Microsoft Windows 2000 operating system. Details of the equations and boundary conditions employed to describe the systems being simulated are given in the relevant experimental chapters. Matlab was used when simulating systems described by algebraic equations, whilst the 3D version of FlexPDE was employed to investigate the behaviour of diffusion fields, which are described by partial differential equations (PDEs).

3.2.1 Finite Element Simulations

FlexPDE produces numerical solutions to systems of partial differential equations using the finite element method (Backstrom, 2002). This involves dividing the domain under study (for which boundary conditions are specified) into a mesh of elements; triangles in the case of 2D systems, tetrahedra in the case of 3D. Each element gives rise to a solution that is represented by a low-order polynomial function. The PDE is solved by determining the values of the dependent variables at all the nodes within the solution space, that is at the corners of each element and at the midpoints between these corners. To obtain the values for other points throughout the elements, FlexPDE applies an algorithm for interpolation between the nodes. For further details refer to the FlexPDE manuals in the "Help" section of the program.

3.3 Microfabrication Protocols

A range of micro- and nano-fabricated devices were produced during the course of this research, including microelectrode array structures, electrochemical sensors and microfluidic systems. These devices were fabricated using a variety of techniques and substrates (including silicon, glass, poly(ethylene terephthalate) (PET) and ceramic) and details of the protocols for the individual microfabrication steps employed are presented in the following sections. To fabricate a complete device, a sequence of these steps was performed, the sequence being determined by the design of the structure, as detailed in future chapters. Note that the parameter values given, such as exposure, development and etch times, are specific to the geometries employed and it may be necessary to modify their values when patterning alternative designs.

3.3.1 Standard Processes for Fabricating Silicon-Based Microdevices

3.3.1.1 Wafer Cleaning

All substrates were cleaned before subsequent processing. Silicon wafers and glass substrates were cleaned by ultrasonicating the sample for 5 minutes in Opticlear, then acetone and finally in methanol. The sample was then thoroughly rinsed in reverse osmosis (RO) water and blow-dried using nitrogen. When a substrate appeared particularly dirty, it was further cleaned by immersion in a 1:7 hydrogen peroxide:sulphuric acid solution at a temperature of approximately 80°C for 15 minutes. If any thin-film metal structures had previously been patterned on the substrate, the solution was cooled to below 50°C prior to immersion of the sample. For substrates that were damaged by immersion in acetone (for instance PET) the samples were ultrasonicated in a detergent solution (1:4 Decon 90:RO water), rinsed in RO water, then ultrasonicated in methanol and rinsed again.

3.3.1.2 Creating a Photoresist Mask

To pattern a photoresist layer, a puddle of resist was first dispensed onto the surface of the substrate. The sample was then spun for 30 s at a rotational speed dependant upon the required film thickness. A spin speed of 4000 rpm resulted in a film thickness of 1.8 μm when using S1818 resist. Decreasing the spin speed to 1000 rpm approximately doubled the thickness of the resulting film. After soft-baking the sample for 30 minutes at 90°C in a convection oven, the sample was aligned to the pattern on a quartz-chromium or acetate mask and exposed to 365 nm ultraviolet light (with an intensity of 5 mW cm^{-2}) for 11s using a Hybrid Technology Group SYS3 mask aligner. To remove the exposed resist, the sample was immersed in a 1:1 Microposit developer: RO water solution for approximately 60 s, during which time the sample was continuously agitated. After rinsing and blow-drying the sample, the photoresist mask was inspected under a microscope to ensure the pattern had been successfully developed.

3.3.1.3 Anisotropic Etching of Silicon

Anisotropic wet etching was employed to create pyrimidial holes through a silicon wafer. For a 380 μm thick silicon wafer, coated on both sides with silicon nitride, square holes with

a length greater than 537 μm[1] had to be etched into the upper silicon nitride layer (0.75 mm and 1 mm lengths were both used). This was achieved by patterning a photoresist film over the silicon nitride, to produce square holes with appropriate dimensions that were aligned to the <110> directed edges. The sample was then etched using a C_2F_6 plasma in an Oxford Plasma Technology BP80 system (Plasmatech, Bristol, UK) for 9 minutes at 100 W, 15 mT and 20 ml min^{-1} C_2F_6.

When wet-etching the sample, the wafer was enclosed in a stainless steel holder, which had been designed by a previous PhD student (Johannessen, 2001), so that only the patterned face of the wafer was exposed to the 4.5 M KOH etchant. A hot water bath and a reflux system were employed to maintain the temperature of the etchant at 80°C, and the sample was etched in the hot solution for approximately 8 hours. When the fragile silicon nitride membrane covering the backside of the wafer was required, it was necessary to handle the sample with care when removing it from the etchant and when rinsing and blow drying.

3.3.1.4 Patterning Thin Film Metal Layers

As discussed in Section 2.2, the two most common methods used to pattern thin-film metal layers are lift-off and wet-etching. Both methods were used when fabricating microsensors. Although lift-off is preferable for smaller patterns, and is essential when patterning sub-micron features, wet-etching was favoured for larger feature sizes, as it is a quicker procedure that does not involve the use of chlorobenzene.

3.3.1.4.1 Lift-off

When patterning a metal layer by lift-off, a photoresist structure that was the inverse of the desired pattern was first produced on the sample surface. So as to produce an under-cut profile, the sample was immersed in chlorobenzene for 15 minutes midway through the softbake period of the photoresist patterning procedure (Section 3.3.1.2). It was then carefully blow-dried and returned to the oven for a final 15 minute softbake. A thin-film metal layer was then evaporated over the photoresist structure and the sample was immersed

---

[1] A 537 μm hole in the mask layer would produce a pit through the entire silicon wafer, yet there would be no opening on the backside of the substrate. Any increase in the length of the mask hole would result in an opening on the backside of the wafer with dimensions equivalent to the increase in length.

in a warm acetone solution and agitated to "lift-off" the unwanted metal regions. If regions of the pattern did not lift-off satisfactorily, the sample was briefly ultrasonicated (for bursts of 10 s) to encourage the removal of the unwanted metal. After the lift-off process was complete, the sample was rinsed in acetone, methanol and RO water.

3.3.1.4.2 Wet-Etching

When wet-etching a sample, a metal layer was first evaporated onto the substrate. A photoresist film was then patterned over the metal layer (as described in Section 3.3.1.2) to produce a mask with features identical to the desired metallic structure. The unwanted metal was then removed by immersing the sample in an appropriate etchant. Table 3.1 describes the various etchant solutions employed and their approximate etch rates. Once the etching process was complete, the photoresist mask was removed by rinsing the sample in acetone, methanol and RO water.

Metal	Composition of Etchant	Approximate Etch Rate ($nm\ min^{-1}$)
NiCr	40:7:200 NH_4NO_3:CH_3COOH:RO water	100
Ni	5:5:2:12 HNO_3:CH_3COOH:H_2SO_4:RO water	300
Ti	1:26 HF:RO water	60
Pd	Transene Palladium Etchant at 50°C	600
Au	4:1:25 KI:I_2:RO water	100

Table 3.1 Solutions for Wet Etching Metallic Layers

3.3.1.5 Creating Patterned Insulation Layers

Both polymeric materials and plasma enhanced chemical vapour deposition (PECVD) silicon nitride (SiN) were employed as insulation layers for microsensor electrode arrays. As these materials were structured with a wide range of feature sizes, it was necessary to employ both photolithography and EBL when fabricating devices.

3.3.1.5.1 Electron-Beam Resist Insulation Layers

Both UVIII, a deep ultraviolet photoresist that is electron-sensitive, and Elvacite poly(methyl methacrylate) (PMMA), manufactured by DuPont, were employed to create the insulation layers of a range of nanoelectrode arrays. A layer of resist was first spun onto a gold-coated substrate at 5000 rpm for 60 s. Either a single layer of UVIII (from a 49% solution), a single layer of Elvacite 2010 PMMA (from an 8% solution), or an Elvacite 2010-2041 bilayer (from an 8% and 4% solution respectively) was employed. UVIII coated samples were then baked on a vacuum hot-plate at 135°C for one minute, whilst PMMA samples were baked in a oven at 180°C for one hour. In the case of a PMMA bilayer, the sample was baked both before and after deposition of the upper layer.

A Leica EBPG-5HR machine (with a LaB_6 thermionic emission source) was employed for all EBL procedures. In order to determine the optimum exposure dose for writing each of the electrode arrays, a range of exposure tests were carried out prior to fabricating the final devices. The array pattern was therefore written using four different exposure doses, with the sample being developed in either Microposit CD26 developer, in the case of UVIII, or in 1:2.5 methyl isobutyl ketone (MIBK):isopropyl alcohol (IPA), in the case of PMMA. After cleaning the samples in a Plasmafab 505 barrel asher for 30 s (at 70 W, 30 mT and 2 L min^{-1} oxygen[2]), the electrode radii resulting from each of the four doses were measured using an SEM and compared to the original design.

The results are displayed in Figure 3.1, which shows the electrode diameters that resulted from writing a 250 nm radius pattern in PMMA (the fourth dose of 200 $\mu C\ cm^{-1}$ did not expose the pattern adequately) and the optimum doses determined for four electrode patterns with varying radii written in UVIII. These doses were then used to fabricate nanoelectrode arrays, using the same procedure as employed for the exposure tests. It should be noted that, for UVIII, it was necessary to prime samples with a layer of hexamethyldisilazane (HDMS) prior to deposition of the resist layer. This was achieved by spin-coating the sample with HDMS at 3000 rpm for 60 s and then baking it in an oven at 80°C for 20 minutes.

[2] These parameters were employed whenever the barrel asher was used.

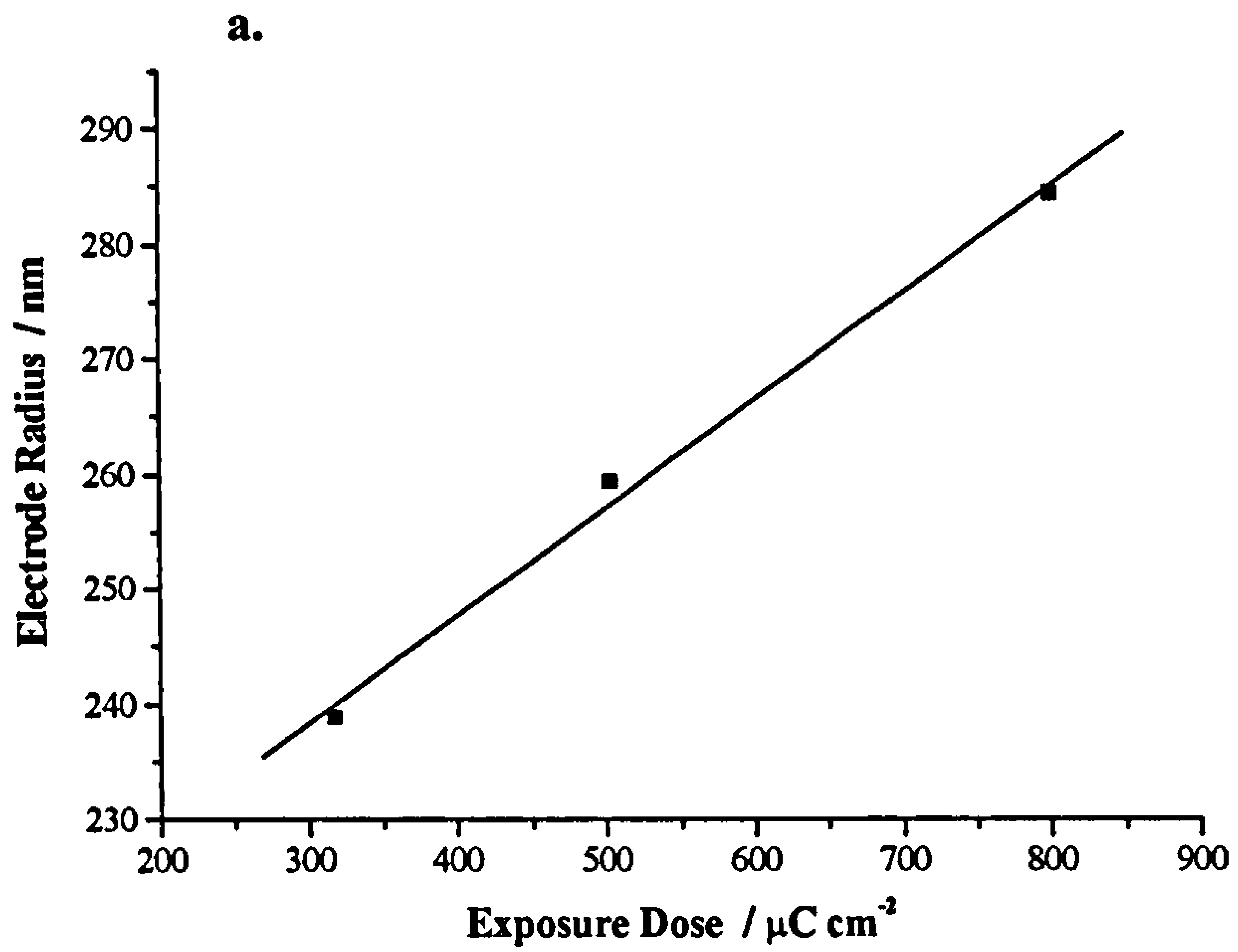

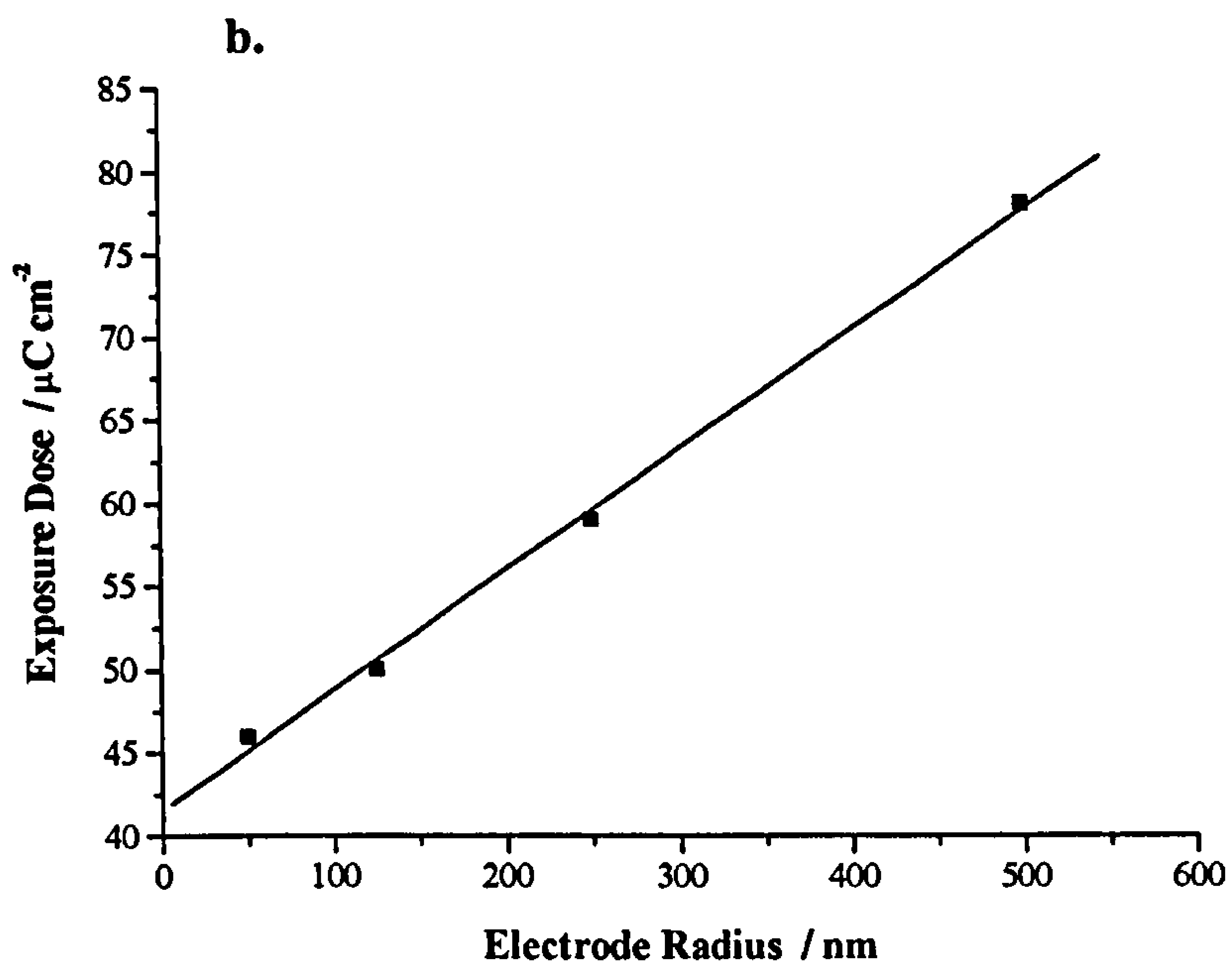

Figure 3.1 **Electron Beam Resist Exposure Tests**

a. The electrode radii resulting from various exposure doses when writing a 250 nm radius electrode array pattern in a PMMA film. b. The optimum exposure dose for a range of electrode radii when patterning a UVIII film.

3.3.1.5.2 SU8 Insulation Layers

When employing a thin SM1040 SU8 insulation layer, it was necessary to coat the sample with a thiol-based SAM prior to deposition of the SU8 solution to prevent any adhesion failures. Therefore, after de-hydration in a convection oven at 120°C, the sample was immersed into a 10mM mercaptoethanol solution (diluted with methanol) and left to soak for 1-2 hours. The sample was then rinsed with methanol, blow-dried and baked in an oven for 15 minutes at 100°C. After the sample had been allowed to cool to room temperature, a small quantity of SU8 was immediately deposited onto its surface. The sample was left to rest for a few minutes prior to spin-coating for the SU8 solution to settle.

Spin-coating a SU8 layer was a three step process. Firstly, the sample was spun for 5 s at a low rotational speed, in the region of 500 rpm, to cause the SU8 to spread across the entire sample surface. The sample was then accelerated over a period of approximately 5 s to a rotational speed dependant upon the desired film thickness (4000 rpm for 1 μm). This speed was then held for a further 30 s. After spin-coating, the sample was baked on a level hot-plate at 90°C for two minutes. Once the sample had cooled to room temperature, it was exposed to ultraviolet light for 5 s using a mask aligner and was then baked in an oven at 90°C for 20 minutes. So as to limit the extent of thermal stress, the sample was left to slowly cool to room temperature prior to development.

Great care had to be taken when developing the SU8 layer. The procedure employed was to pipette a drop of the concentrated propylene glycol monomethyl ether acetate (PGMEA) developer solution onto the sample and then immediately immerse it into a 1:1 developer:IPA solution for 5 s. The sample was then rinsed in an IPA bath for a further 5 s before being blow-dried. If any SU8 residue remained on the sample after development, it could normally be removed by RIE with a 9:1 O_2:CF_4 plasma for 10-20 minutes in the BP80 system at 50 W, 25 mT & 30 SCCM (Dentinger, 2002).

3.3.1.5.3 Silicon Nitride Insulation Layers

500–700 μm thick films of normal- and low-stress SiN were deposited by PECVD using an Oxford Plasma Technology 80 Plus system (Plasmatech, Bristol, UK). These films were patterned by RIE using a S1818 photoresist etch mask. A C_2F_6 plasma was again employed when etching the SiN (conditions as noted previously), with PECVD SiN having an etch rate

of approximately 50 nm min^{-1}. After etching, the photoresist mask was removed by rinsing the sample in acetone, methanol and RO water.

3.3.2 Alternative Resist Processing Methods

3.3.2.1 Resist Coating Techniques

When spin coating a substrate proved ineffective, alternative resist coating methods were investigated, namely spray coating, laminating and "pour coating". In the case of the former, a prototyping aerosol photoresist spray was used to coat the substrate, by spraying from a distance of approximately 20 cm using long, sweeping movements. The sample was then baked in an oven at 50°C for 20 minutes and subsequently exposed to ultraviolet light for 2 minutes using a contact box. After developing in a 0.3 M sodium hydroxide solution for 2-3 minutes, the sample was thoroughly rinsed with RO water. To laminate a sample with Riston MM140, a MegaElectronics A4 dry film laminator, set to 115°C, was employed. Samples were exposed for 25 s using the mask aligner and were then developed in a 0.08 M sodium carbonate solution for approximately 1 minute.

Before pour coating, a thiol-based SAM was formed on the surface of the sample (as described in Section 4.3.1.5.2), as this was found to improve the flow of the resist. A 2:1 S1805:EC solvent solution was then poured over the sample, which was left to settle for a short while before the majority of the resist was poured off. At this point, the sample was moved to an unheated, level hotplate and left to settle for approximately 15 minutes, covered with a petri dish. The temperature of the hotplate was then increased from room temperature to 90°C, with the sample remaining covered. Once the temperature had reached set-point, the petri dish was removed and the sample was baked for a further 2 minutes. The sample was then exposed for 20 s using the mask aligner, before being developed in a 1:1 Microposit developer:RO water solution for approximately 60 s.

3.3.2.2 Nanoimprint Lithography (NIL)

When employing the NIL process, it is first necessary to create a nanostructured stamping tool. For this application, a silicon master with an array of 250 nm radius pillars was required. To fabricate this, a PMMA bilayer was processed on the polished surface of a clean silicon substrate to produce an array of nano-holes. After oxygen cleaning the sample in the

barrel asher for 30 s, 100 nm of NiCr was evaporated onto the sample. Lift-off was then performed to produce an array of NiCr nano-dots that were to act as an etch mask when dry etching the silicon substrate. RIE was carried out in an Oxford Plasma Technology System 100 machine using a $SiCl_4$ plasma for 20 minutes at 12 mT and 160 W. The NiCr mask was then removed using the etchant solution detailed in Table 3.1. Prior to imprinting, the samples were spin coated at 5000 rpm for 60 s with a 0.5% solution of Dow Corning DC20 (a silicone based mould release agent), diluted with xylene, which was subsequently baked at 180°C for 10 minutes.

Samples were processed using an Obducat Nanoimprinter. After spin-coating a sample with a layer of resist, the stamping tool was placed on top of the sample and a square of PDMS was then placed over both (to help ensure a uniform pressure distribution). As the nanoimprinter is computer controlled, the desired time, pressure and temperature parameters were entered into the control software before running the NIL process. When using PMMA, samples were imprinted at 170-190°C and 15-30 Bar for 5 minutes, whilst S1805 photoresist was imprinted at 120-140°C and 5-15 Bar for 5 minutes. All samples were cooled to 50-70°C before the pressure was released. Once the imprinting cycle had finished, the sample and tool was gently eased apart with tweezers. The samples were then progressively etched in the barrel asher for bursts of 2-5 minutes to remove the resist that remained in the bottom of the resulting nano-holes.

3.3.3 Electrochemical Deposition

3.3.3.1 Cleaning Electrodes

Both electrochemical cleaning and oxygen plasma etching were employed to prepare electrodes for electrodeposition. In the case of the former, electrodes were cycled between 0.3 and 1.3 V in a 1 M sulphuric acid solution at a scan rate of 100 mV s^{-1}, until a stable signal was obtained. For the latter, samples were rinsed in acetone, methanol and RO water before being oxygen cleaned in the barrel asher for 2 minutes.

3.3.3.2 Electrochemical Deposition Processes

After connecting wires were soldered to the electrode or electrode array that was to be electroplated, the solder joints were insulated with silicone rubber and the sample was

cleaned. An EG&G potentiostat and a commercial reference and counter electrode were employed for the electrodeposition process, which was carried out within a Faraday cage. Platinum black was electroplated from a 24 mM hydrogen hexachloroplatinate, 2.1 mM lead acetate solution; silver from a 0.2 M silver nitrate, 2.0 M potassium iodide, 0.5 mM sodium thiosulphate solution; silver chloride from a 0.1 M hydrochloric acid solution and gold from an Enthone-Omi (Surrey, UK) plating recipe[3], the temperature of which was maintained at 50°C whilst the solution was stirred.

Electroplated Material	Chronopotentiometry		Chronoamperometry	
	Time (s)	Current (μA)	Time (s)	Voltage (mV)
Ag	300, 300, 600	-2, -5, -10	300, 900	-300, -550
AgCl	300, 900	1.5, 5	300, 900	100, 300
Au	300, 600, 900, 1800, 1800	-20, -30, -35, -50, -75	-	-

Individual Electrode Radius *(μm)*	Chronopotentiometry		Chronoamperometry	
	Time *(s)*	Current *(μA)*	Time *(s)*	Voltage *(V)*
50	180	-10.0	180	-1.50
25	150	-11.0	150	-1.40
12.5	120	-12.5	120	-1.30
5	90	-15.0	90	-1.25
2.5	75	-18.0	75	-1.20
1.25	60	-20.0	60	-1.15

Table 3.2 **Parameters for Electrodeposition of Metallic Layers**
a. (Top) When electroplating Ag|AgCl and gold the applied current or voltage was progressively increased. b. (Bottom) The optimised parameters for the deposition of platinum black onto a range of microelectrode arrays

Both chronoamperometry and chronopotentiometry were employed when electroplating and typical parameters used for the deposition of both gold and Ag|AgCl films are given in Table 3.2a. Platinum black was electroplated onto arrays of microelectrodes (whose geometries are

[3] The solution employed comprised 30% BDT 'B' unit concentrate, 25% BDT 'A' gold complex and 0.52% brightener solution.

detailed in Section 5.1.1.1) and the optimum deposition currents or voltages, determined empirically for each array, are detailed in Table 3.2b.

3.3.4 Polymer Microfabrication Processes

3.3.4.1 Thick-Film SU8

SU8-50 was employed to create thick polymer films. As this formulation is a highly viscous material, a small quantity was deposited onto the centre of the sample, which was then heated gently on a hot-plate until the resist began to flow more readily. Complete coverage of the sample was obtained by tilting it slowly backwards and forwards. The sample was then covered and left to settle for approximately two hours. A three-step process was again employed when spinning the sample; rotating it at 300 rpm for 5 s, ramping the spin speed up to approximately 750 rpm over a period of 5 s (for a 250 μm thick layer) and then maintaining this speed for a further 30 s. The sample was then covered and left to settle for an additional two hours.

Prior to exposing the sample, all the solvent in the SU8 film had to be removed and so the sample was placed on a flat surface in a convection oven at 50°C. The temperature was then increased to 95°C and the sample was baked overnight at this temperature. Before removing the sample from the oven, the temperature was decreased to 50°C. The total exposure time required for a 250 μm film, using the mask aligner, was 9 minutes. This was broken down into three exposure periods with a three minute rest between each, so as to prevent over-heating of the sample. The sample was then baked at 95°C for 45 minutes, again ramping from 50°C to 95°C at the beginning of the bake cycle and from 95°C to 50°C at the end. When developing the SU8 film, the sample was first immersed in γ-butyrolactone (GBL) for 1-2 minutes, prior to immersion in the propylene glycol monomethyl ether acetate (PGMEA) developer. When agitating the sample, development time was approximately 15 minutes for a 250 μm film, though the sample was periodically rinsed in a 1:1 IPA:developer solution and inspected to ascertain how the development was progressing. Once the development process was complete, the sample was rinsed with IPA and blow-dried. RIE with a 9:1 O_2:CF_4 plasma could again be employed to remove small amounts of SU8 residue.

3.3.4.2 Polyimide

Polyimide was employed as a both a planarising and an insulating material. To improve the adhesion of the polyimide to the ceramic substrates employed, the surface of the sample was silanised prior to application of the polyimide. This was achieved by immersion in a 2% 3-aminopropyltriethoxysilane solution, diluted with acetone, for 1-2 hours. The samples were then blow-dried, baked in oven at 120°C for 15 minutes and left to cool to room temperature, prior to deposition of the polyimide precursor. After depositing a small quantity of the PI2545 solution onto the substrate, the sample was left to settle for approximately 30 minutes. It was then spin-coated at 300 rpm or 500 rpm for 5 s, accelerated to 750 rpm or 6000 rpm and then held at this speed for a further 30 s - the latter values being for a film thickness of approximately 1 μm, the former values for a film thickness of approximately 5 μm. Afterwards, the sample was baked in an oven at 100°C for one hour and was then left to cool to room temperature.

At this stage, the PI2545 film could be patterned by employing a standard positive photoresist, such as S1818. The process previously described (see Section 3.3.1.2) for a creating a photoresist mask was employed, the only alterations being the softbake stage, which was carried out on a hotplate at 90°C for 2 minutes, and the development stage, during which both the exposed S1818 and the underlying PI2545 were removed by the Microposit developer. The remaining photoresist was then stripped using n-butyl acetate instead of acetone, which would have attacked the uncured polyimide precursor. To cure the polyimide layer, the sample was baked in a convection oven, which was continuously purged with nitrogen. The initial oven temperature was 100°C but this was immediately ramped to 200°C once the sample had been placed in the oven. The temperature was then held at 200°C for 30 minutes, ramped up to 350°C and finally held at this value for a further hour. The temperature was then left to fall to below 100°C before removing the sample from the oven. If small regions of polyimide residue remained on the sample after the development stage, these could again be removed by RIE with a 9:1 O_2:CF_4 gas mixture. Finally, if a metal film was to be evaporated over the polyimide layer, the sample was treated by oxygen plasma etching for 3 minutes, using an Oxford Plasma Technology RIE80 system (Plasmatech, Bristol) at 290 mT and 50 W rf power.

Polyimide was also used to bond two ceramic substrates together, whilst simultaneously patterning the exposed areas of polyimide. The process employed when bonding a planar base plate to an upper plate into which a series of holes had been machined is illustrated in

Figure 3.2. It should be noted that, rather than coating the entire structure, small quantities of resist were pipetted into the recessed areas alone when spinning the photoresist layer.

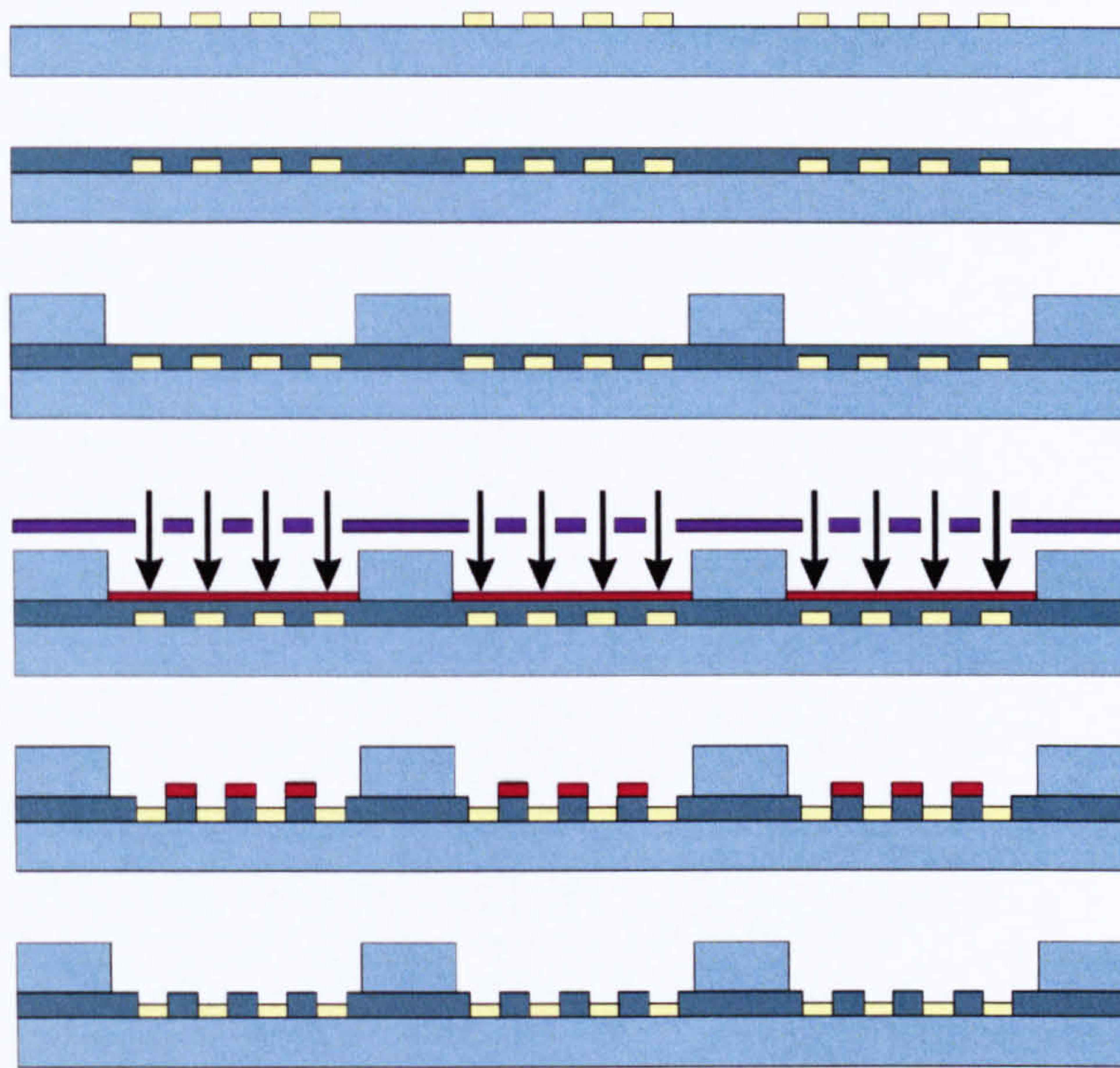

Figure 3.2 **Schematic Illustrating the Polyimide Bonding Process**

After spin-coating the patterned base plate (blue and yellow) with a thin layer of polyimide precursor (green), the two plates were clamped together and softbaked. The recessed areas were then spin-coated with photoresist (red) and exposed to ultraviolet light through a chrome-patterned mask (purple). After developing and wet-etching the sample and removing the remaining photoresist layer, the polyimide was then cured in the oven.

3.3.4.3 Poly(ethylene terephthalate) (PET) and Hot-Melt Adhesive Foils

Sheets of PET, which could be readily cut using a sharp scalpel blade, were employed as both substrates and flow-channels. When bonding, the two components were simply positioned between two sheets of mylar foil and pressed together using an aluminium clamp. They were then thermally bonded in a convection oven at a temperature of approximately 115°C for 30 minutes. Before removing the PET structure, the clamp was left to cool to room temperature. Sheets of hot-melt adhesive foil were also employed to form flow-channels. A

section of foil, shaped using a scalpel blade, was positioned between the substrate and a sheet of waxed non-stick paper. A glass slide was then placed over the paper and the entire assembly was clamped and baked in an oven at 100°C for 10 minutes. Once the device had cooled to room temperature, further layers of hot-melt adhesive foil could be bonded over the initial layer – three layers were required for a flow-channel depth of approximately 450 μm – before a glass or ceramic lid was bonded to the adhesive foil structure.

3.4 Experimental Apparatus

The apparatus employed for all the experimental work undertaken is described in the following sections. Details of the protocols employed for specific experiments can be found within the relevant experimental chapters. The theoretical background for the electrochemical experiments is presented in Chapter 4, whilst an overview of dielectrophoresis (an AC electrokinetic technique) is presented in Chapter 7.

3.4.1 Electrochemical Recordings

All electrochemical experiments were performed within a Faraday cage and all external cables were shielded. A test rig was constructed within the Faraday cage so that the dissolved oxygen level of an aqueous solution could be regulated by flowing nitrogen, oxygen, or a mixture of both through the solution, as described in Figure 3.3. An aquarium pump could also be connected to one of the flow-meters so that air could be pumped through the solution. When acquiring electrochemical measurements, the laboratory temperature, which was controlled by an air-conditioning system, was 24°C ±1°C. Furthermore, measurements were obtained, as far as was possible, when the laboratory was quiet, so as to reduce the occurrence of environmentally induced transients (Long and Webber, 1988).

All voltammetric measurements were made in triplicate and any corresponding calculations and graphs employ mean values, with error bars calculated as three standard deviations. For cyclic voltammograms, oxidative (anodic) and reductive (cathodic) peak currents were measured as illustrated in Figure 3.4. For chronoamperometric recordings, all results are quoted as time-averaged values, averaged over a period of 10 s unless otherwise stated. The results of all electrochemical experiments were plotted and analysed using Origin version 6.0 (Microcal Software, Massachusetts, USA).

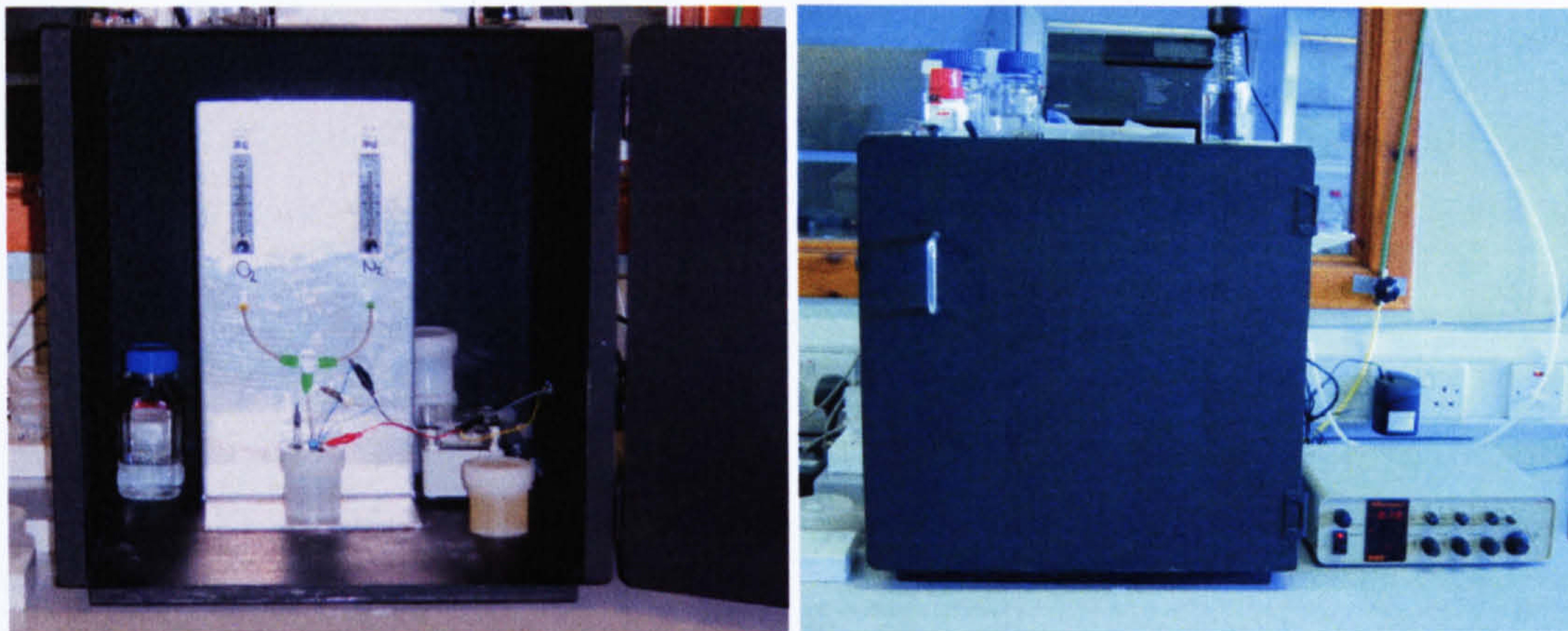

Figure 3.3 **The Electrochemical Measurement Setup and Dissolved Oxygen Test Rig**

The test rig incorporated an oxygen and a nitrogen gas line, which were merged using a T-connector before being passed through the sample solution. Both lines were directed through a flow meter (0-250 cc min^{-1}) so that, by controlling the relative flow-rates of nitrogen and oxygen, a range of dissolved oxygen concentrations could be obtained. A potentiostat was connected to the three-electrode cell within the Faraday cage by a shielded cable that was fed through a hole in the side of the cage.

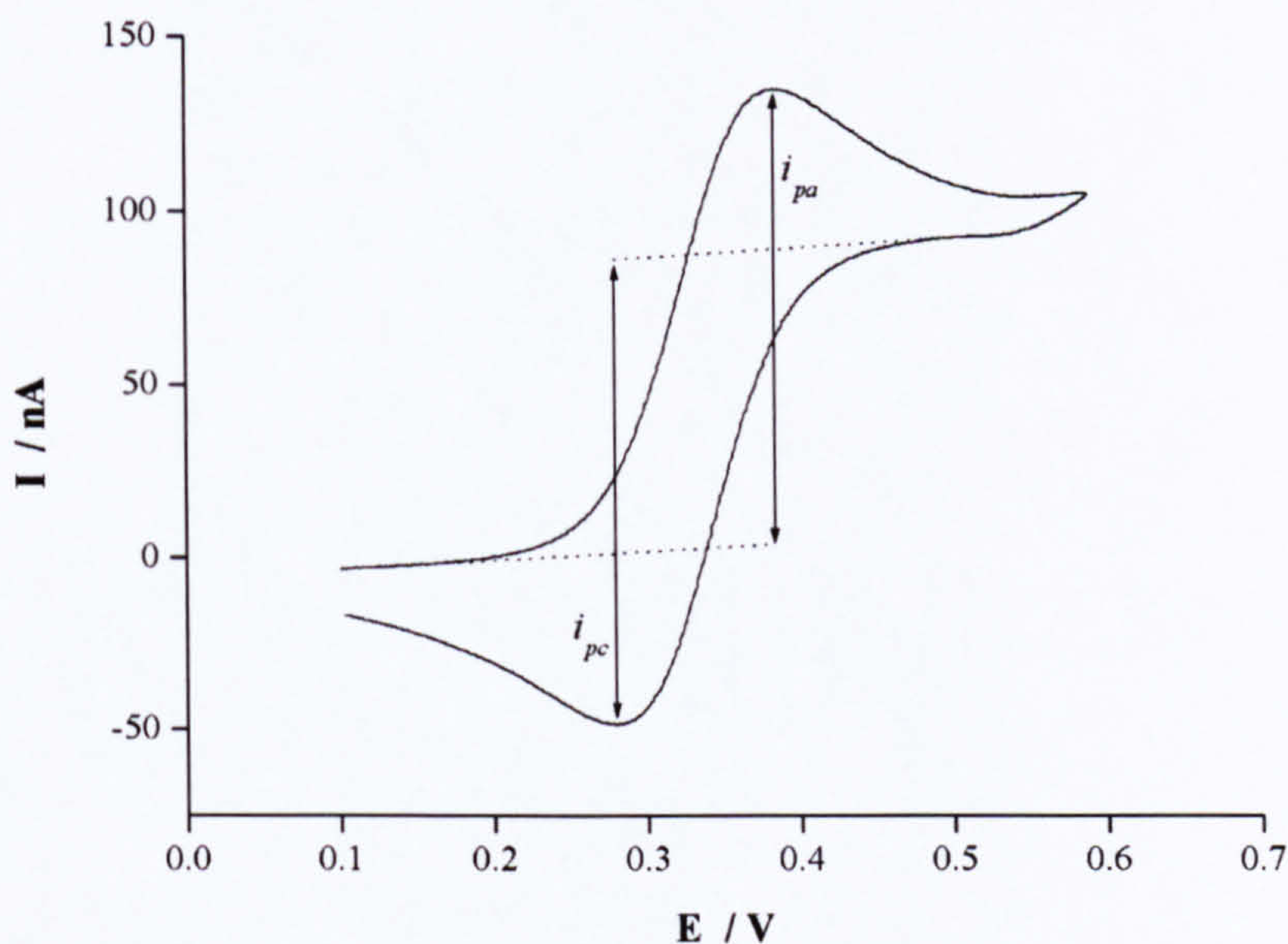

Figure 3.4 **Measurement of Oxidative and Reductive Peak Currents**

i_{pa} is the anodic (oxidative) peak current, whilst i_{pc} is the cathodic (reductive) peak current.

3.4.2 Reference Electrode Stability Measurements

The apparatus employed to monitor the potential stability of a micro-reference electrode with respect to a commercial Ag|AgCl electrode is shown in Figure 3.5. To maintain a constant current through the reference electrode, a 1 MΩ resistor was connected in series with the micro-reference electrode. Therefore, when a voltage of ±0.1 V was applied with the potentiostat, the resulting current was 100 nA. It should be noted that the presence of a buffer at the reference electrode input on the potentiostat prevents any current flow along this branch of the circuit. Hence, current only flows through the resistor, through the two reference electrodes and through the counter electrode input on the potentiostat. Furthermore, in order to avoid any current being drawn from the circuit when measuring the potential difference between the two electrodes, an INA114 instrumentation amplifier was employed. Two unity gain buffers at the inputs prevent current from flowing into the amplifier, while the voltage output is simply the difference in potential between the two inputs, that is the potential difference between the micro- and macro-reference electrodes.

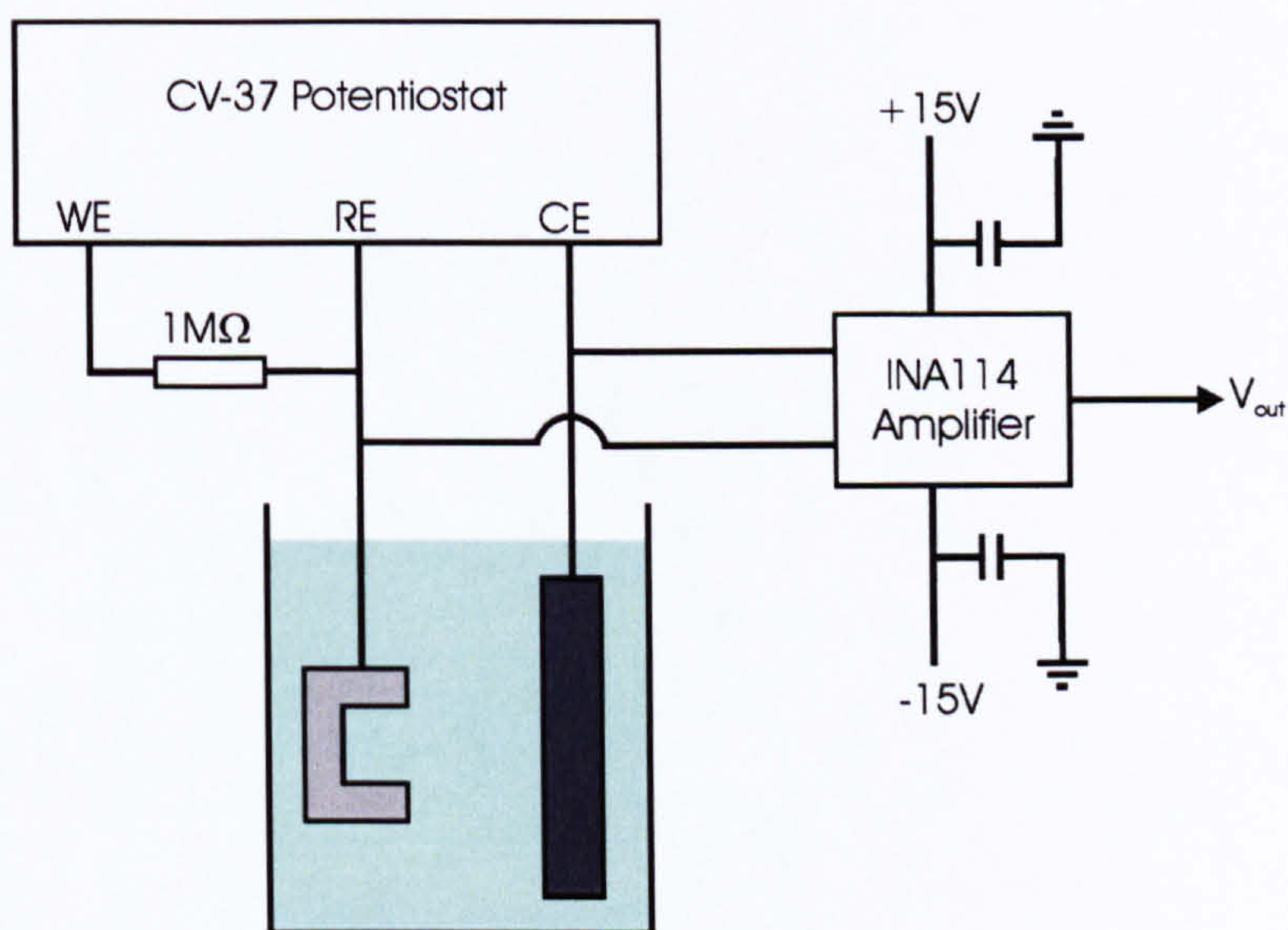

Figure 3.5 **Apparatus for Monitoring the Stability of Micro-Reference Electrodes**

Both the micro-reference electrode (light grey) and the macro-reference electrode (dark grey) were immersed in the test solution. The WE, RE and CE labels on the potentiostat represent the working, reference and counter electrode inputs respectively.

3.4.3 Thermal Resistance Measurements

Variation in resistance with temperature was measured by constructing a potential divider circuit, as shown in Figure 3.6. The voltage, *V2*, supplied by the power source is divided between a fixed resistance, *R*, which is held at a constant temperature, and the resistance to be measured, R_t, which is immersed in a solution whose temperature can be varied. Thus, the voltage across R_t is:

$$V_1 = V_2\left(\frac{R_t}{R_t + R}\right) \tag{3.01}$$

which can be re-organised to obtain the following expression for the value of R_t:

$$R_t = \frac{R\frac{V_1}{V_2}}{1 - \frac{V_1}{V_2}} \tag{3.02}$$

The value of *R* employed was 4.3 kΩ and two 9 V batteries were used as the power source.

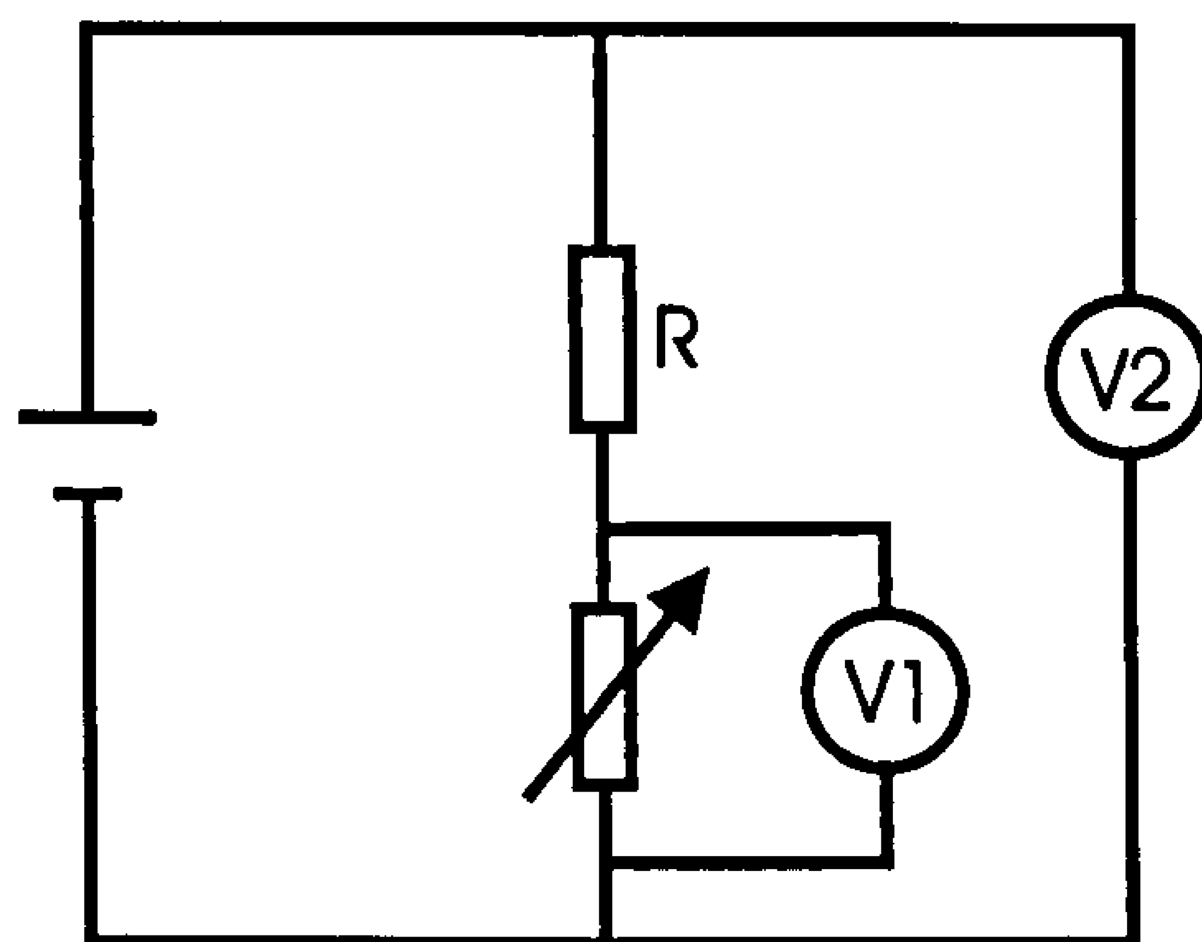

Figure 3.6 Potential Divider Circuit for Resistance Measurements

The device being calibrated is represented by the variable resistor.

The experimental setup employed when measuring the variation in the resistance of a device with temperature is described in Figure 3.7. Using heatshrink paste, the measurement junction of a commercial thermocouple temperature measurement system, *T1*, was fixed to the backside of the device being calibrated, so that its temperature could be accurately measured. A digital thermometer, *T2*, was also immersed in the beaker to confirm the temperature measurements from *T1*. By varying the temperature of the test solution using the

combined magnetic stirrer and hotplate and noting the values of *T1*, *T2*, *V1* and *V2* at various point in time, a calibration chart for the variation of resistance with temperature could be obtained by employing Equation 3.02.

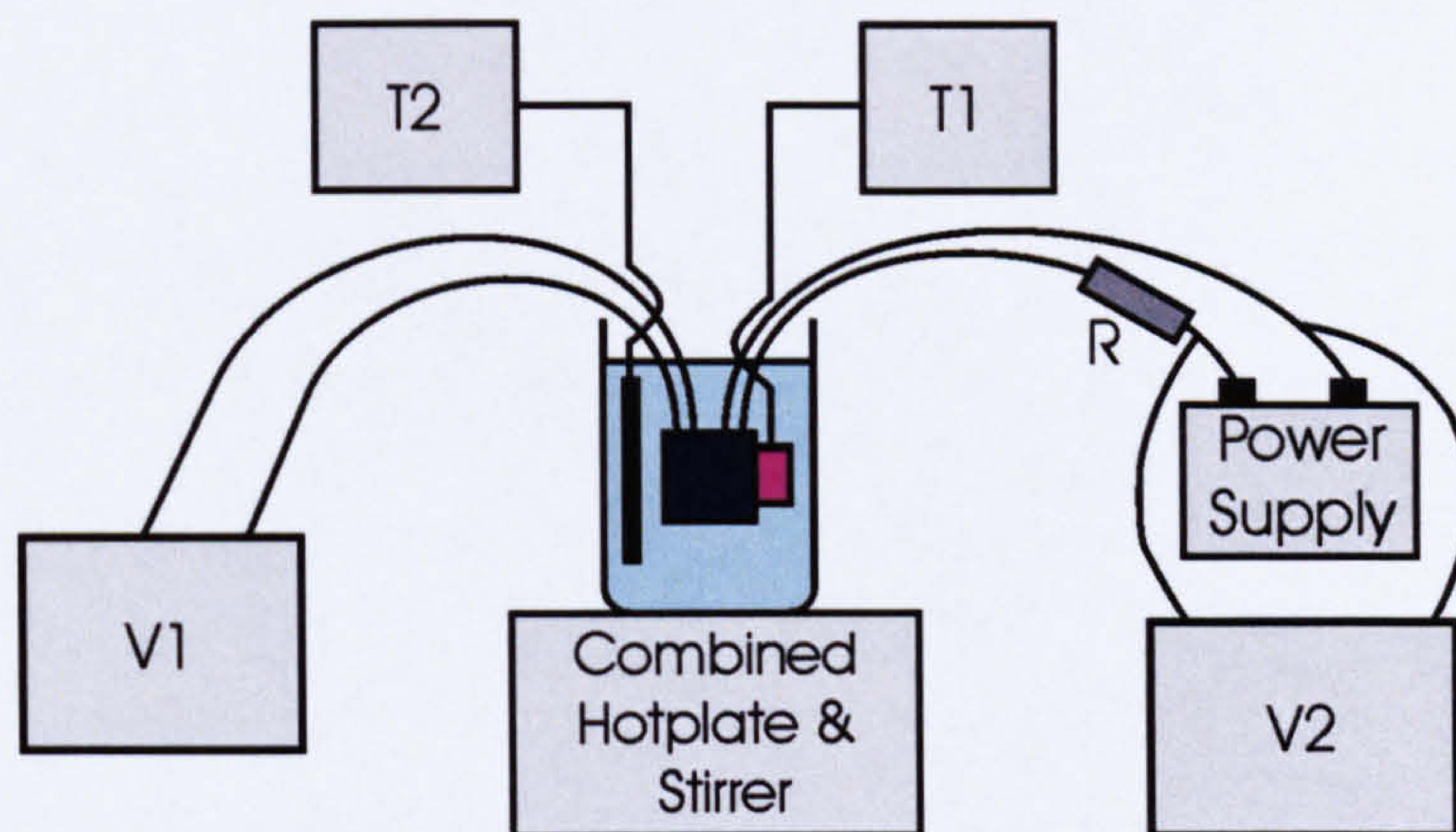

Figure 3.7 Experimental Apparatus for Thermal Resistor Measurements
T1 was a thermocouple measurement system, the sensing junction (purple) being fixed to the back of the thermal resistor (dark blue), whilst *T2* was a digital thermometer. *V1* and *V2* were digital multimeters.

3.4.4 Experiments Using Dielectrophoresis (DEP)

The apparatus employed for dielectrophoresis experiments is described in Figure 3.8. The flow of a sample solution through the microfabricated device was controlled by a syringe pump, whilst an a.c. voltage, which was monitored by an oscilloscope, was applied to the electrodes within the device using a signal generator and amplifier. A CCD camera was employed to record the image seen through the microscope onto a video tape and also to enable the progress of the experiment to be viewed on a monitor.

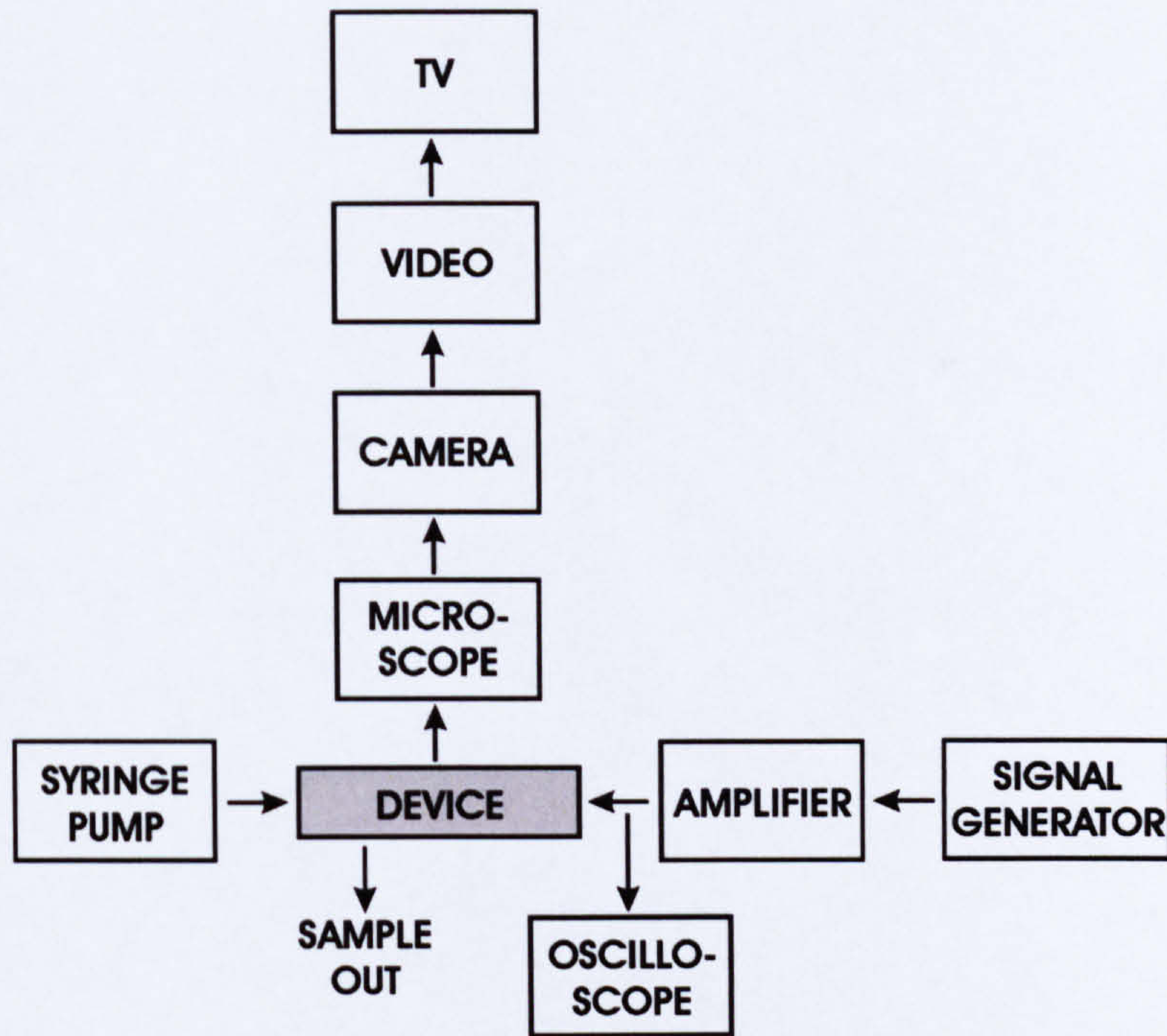

Figure 3.8 **Experimental Setup for DEP Experiments**

The arrows indicate the connections between individual pieces of equipment.

CHAPTER 4

THEORETICAL BEHAVIOUR OF MACROELECTRODES, MICRO-ELECTRODES AND MICROELECTRODE ARRAYS

An electrochemical reaction may be described as a heterogeneous chemical process that involves a net electron transfer across the interface between an electronic and an ionic conductor, for instance between a metallic electrode and an electrolyte (Bard and Faulkner, 2001). As discussed in Section 1.1.2, electrochemical detectors have been successfully employed in a numerous bioanalytical and environmental microsystems. Therefore, after outlining the basic theory of an electrochemical cell and presenting an overview of relevant potential step and potential sweep techniques, this chapter explores the electrochemical behaviour of both individual microelectrodes and microelectrode arrays. Graphs produced using Matlab and Origin are employed to illustrate the behaviour described by various theoretical equations. In the penultimate section of the chapter, results from finite element simulations showing the diffusion profiles for both individual microelectrodes and of arrays of microelectrodes with varying geometries are presented.

It should be noted at the outset of this chapter that, whilst it was endeavoured to use common symbols, there are differences in the syntax that chemists and physicists use. For instance, the parameter η can refer to both viscosity and overpotential, whilst *E(x)* generally refers to an electric field in physics but is often used to denote potential profiles by electrochemists. Furthermore, the terms *kT/q* and *RT/F* are equivalent but, when formulating equations, physicists tend to employ the former whilst chemists employ the latter. Equations given in this chapter are written in the form that was found in the majority of sources.

4.1 Electrochemical Systems

As described by Bockris and Reddy (1970), almost all interfaces are electrified, with the surfaces of a material carrying excess charges. For instance, when a metal surface is brought into contact with an ionic solution, electron transfer processes ensue, such as the dissolution of the surface metal. As the charge transfer process continues, excess electrons will accumulate at the metal surface and a potential difference will develop across the electrode-electrolyte interface, which consequently reduces the energy barrier for the reverse reaction (the re-formation of the metal, in this instance). An equilibrium state, where both the forward and backward electron transfer processes proceed at an equal rate, will subsequently be reached, at which point a net flow of electrons will have occurred in one direction. As a consequence, the interface will have become charged and a potential difference will have been established between the two phases. This potential difference occurs almost entirely at the interface, giving rise to extremely high electric fields (Kovacs, 1994).

To determine the potential difference across an electrode-electrolyte interface, a complete electrical circuit is necessary and therefore a minimum of two electrodes is required. Such an assembly is known as an electrochemical cell. Obviously, a potential difference will develop at the interface of both these electrodes and so, to monitor the potential drop across the electrode of interest only, a standardised reference electrode is commonly employed as the auxiliary electrode (Fisher, 1996). A reference electrode maintains a stable and fixed potential difference across its electrode-electrolyte interface (although, when there is an applied, external potential, this constancy will only be sustained within a limited potential range). Therefore, any variation in the measured potential of the cell can be attributed to the electrode of interest, the so-called working electrode. By convention, an absolute potential of zero is assigned to the standard hydrogen electrode (SHE), the internationally acknowledged principal reference system, which comprises a platinum electrode saturated with hydrogen gas that is immersed in a solution with unit activity of hydrogen ions. All standard electrode potentials (E^0) are measured relative to the SHE and are defined as the equilibrium potential for a redox couple when all its potential determining ions have unit activity. As the SHE is relatively difficult to prepare, alternative reference systems are commonly employed, such as a Ag|AgCl electrode immersed in a saturated potassium chloride solution, which has a potential of 0.197 V vs. SHE at room temperature (Bard and Faulkner, 2001).

4.1.1 Equilibrium Conditions

Provided there is no net current flow and no overall chemical change in the cell composition, the working electrode will remain at equilibrium and the magnitude of the electron transfer

current across the electrode-electrolyte interface will be equal in both directions and is known as the exchange current density (Bockris and Reddy, 1970). The potential of an electrode under such equilibrium conditions (E_e) is given by the Nernst equation:

$$E_e = E^0 + \frac{RT}{nF} ln\left(\frac{C_O}{C_R}\right)_{x=0} \tag{4.01}$$

where R is the molar gas constant, T is the absolute temperature, n is the number of electrons exchanged, F is the Faraday constant, and C_O and C_R are the concentrations at the electrode surface of the oxidised and reduced species respectively (assuming unit activity).

4.1.2 Faradaic and Non-Faradaic Processes

An electrochemical cell, however, is normally operated under conditions where a net current does flow, although a net electrochemical reaction will only proceed spontaneously if the free energy change for the overall cell reaction is negative, as is the case for galvanic cells. Even when the thermodynamics of an electrochemical cell are favourable, the rate of electrolysis will be dependant upon the reaction kinetics for both electrodes (Greef *et al*, 1985). Under thermodynamically or kinetically unfavourable conditions, an externally applied potential can be employed as a driving force to induce electron transfer between the electrodes and the solution phase species (an electrolytic cell). The magnitude of the difference in potential between the applied voltage and the equilibrium potential ($E\text{-}E_e$) is commonly termed the overpotential (η). As the electroneutrality of the overall system must be maintained, the rate of electron transfer at the cathode (the electron source) is equal to the rate at the anode (the electron sink).

Faraday's law implies that the flow of current across an electrode-electrolyte interface is stoichiometrically related to the extent of the chemical reaction (Bard and Faulkner, 2001). Such a charge transfer reaction is classed as a faradaic process and the resulting current flow, i, is expressed by:

$$i = -nFAJ(0,t) \tag{4.02}$$

where A is the surface area of the electrode and $J(0,t)$ is the time-dependant flux of the ionic species at the electrode surface. In addition to faradaic processes, other non-faradaic phenomenon will occur in an electrochemical cell. For instance, adsorption and desorption

processes may take place and changes in potentials or solution composition can alter the structure of the electrode-electrolyte interface. Although interfacial charge transfer does not occur as a result of these processes, transient external currents can nonetheless flow.

4.2 The Electrode-Electrolyte Interface

It is also necessary to consider the influence of the electrode-electrolyte interface and what bearing it has on the behaviour of an electrochemical system. As previously discussed, a space charge layer becomes established at the surface of an electrode immersed in an ionic solution (illustrated in Figure 4.1). It is assumed that the charge on the electrode resides in an extremely thin layer (<0.01 nm) at the metal surface, whilst the charge in solution is comprised of several layers (Bard and Faulkner, 2001). Lining the surface of the metal is a layer of oriented solvent molecules, occasionally incorporating other specifically adsorbed species.

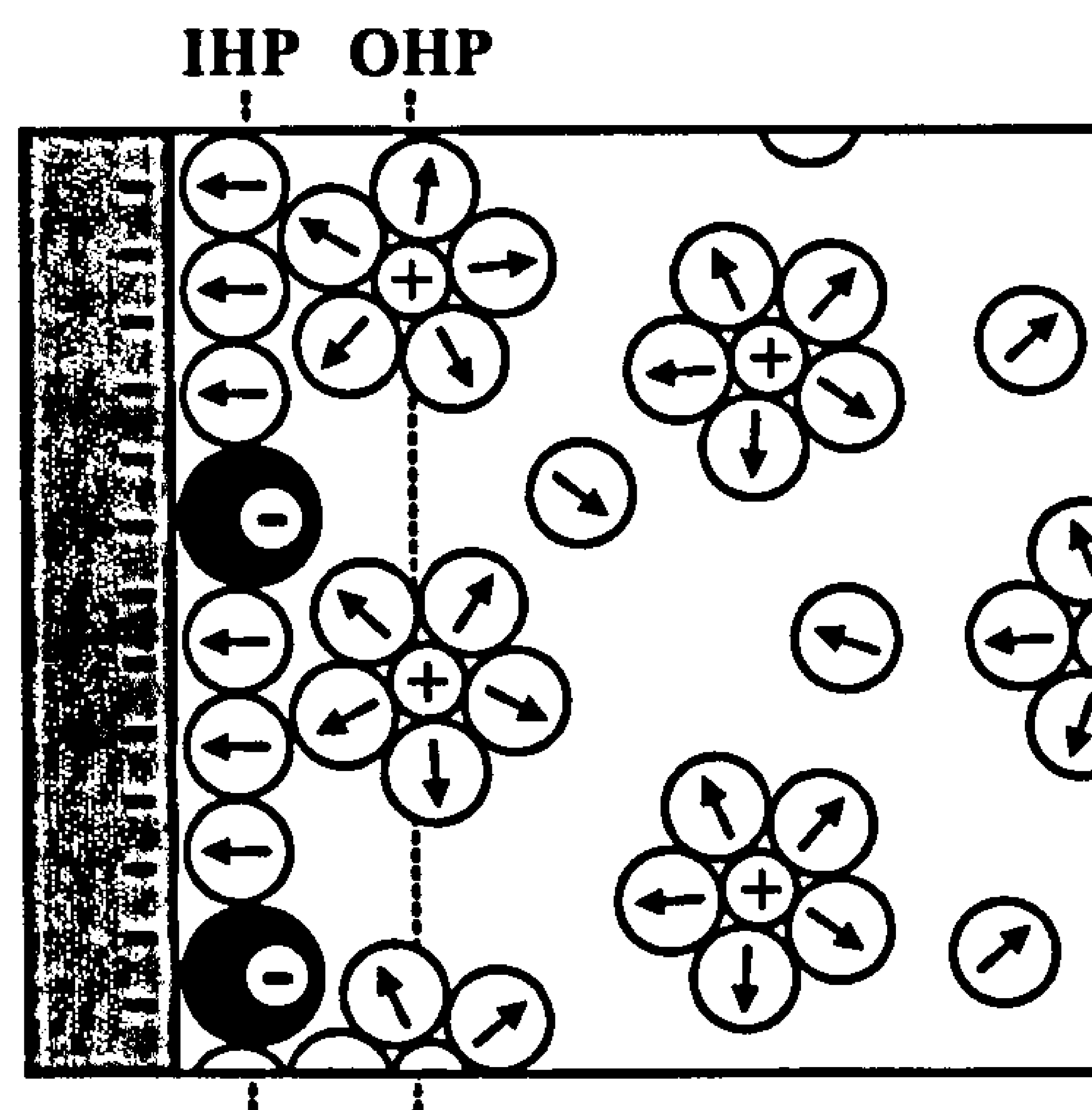

Figure 4.1 Schematic Diagram Illustrating the Structure of the Electrode-Electrolyte Interface

The electrode surface is represented by the grey region to the left, the black circles represent specifically adsorbed ions, the light grey circles positive ions and the white circles the solvent molecules (with the arrowheads pointing toward the positive region of the dipole).

The locus of the electrical centres of this layer, which limits the approach to the electrode surface of any solvated ions, is known as the inner Helmholtz plane (IHP), whilst the locus of the closest solvated ions is known as the outer Helmholtz plane (OHP). Together, these

two layers are commonly referred to as the double layer. The behaviour of the solvated ions, which are described as being non-specifically adsorbed, is governed by long-range electrostatic forces. Due to thermal agitation, these non-specifically adsorbed ions are distributed in a three-dimensional region of the space known as the diffuse layer, which extends from the OHP to the bulk solution.

4.2.1 The Interfacial Capacitance

The structure of the electrode-electrolyte interface outlined in the previous section resembles that of a capacitive device and, therefore, several models have been constructed to describe the capacitance of the interfacial region. The earliest of these is the Helmholtz-Perrin model, which was proposed at the end of the nineteenth century (Kovacs, 1994).

4.2.1.1 The Helmoholtz-Perrin Model

Helmholtz and Perrin proposed a simple mathematical model for the interface, which assumed that the charge in the solution was comprised of a two-dimensional sheet at the OHP. Such a structure can be described by the parallel-plate capacitor equation:

$$C_H = \frac{\varepsilon_0 \varepsilon_r A}{d} \tag{4.03}$$

where A is the surface area of the electrode, d is the thickness of the double layer, ε_o is the permittivity of free space and ε_r is the dielectric constant of the solvent (which for water has a value of 78.5 at room temperature, though it may be as low as 6 at the electrode interface [1]). However, there are considerable inconsistencies between experimental observations and the Helmholtz-Perrin model. Most significantly the capacitance varies with potential, as the thickness of the space charge layer decreases at higher potentials when the ions become more compacted at the electrode surface. Thus, the capacitance increases with potential and, similarly, with electrolyte concentration.

---

[1] As the permittivity of water is dependant upon the degree of orientation of the water molecules, the dielectric constant of water is influenced by the electric field strength of the local environment (Bockris and Reddy, 1970). For instance at the surface of a sufficiently charged electrode, the water molecules will be fully oriented and a dielectric constant of approximately 6 will result.

4.2.1.2 The Gouy-Chapman Capacitance

A diffuse charge layer of finite thickness arises at the electrode-electrolyte interface as a result of the interaction between the charge on the metal electrode, which will either attract or repel the charge carriers, and thermal processes, which will tend to randomise them. Hence, Gouy and Chapman independently (in 1910 and 1913 respectively) proposed a model of the electrode-electrolyte interface incorporating a diffuse charge region, that assumed neither a fixed layer of hydrated ions at the OHP nor a linear voltage drop extending outwards towards the bulk solution. The derivation of their model is described in detail by Bard and Faulkner (Bard and Faulkner, 2001) and yields the following formulae for the differential diffuse layer capacitance (in Fm^{-2}):

$$C_D = \sqrt{\frac{2\varepsilon_0\varepsilon_r n^2 q^2 N_A C^*}{kT}} \cosh\frac{nqV_0}{2kT} \tag{4.04}$$

where q is the elementary charge, N_A is Avogadro's number, C^* is the bulk concentration of the electrolyte, k is the Boltzmann constant, T is the temperature in Kelvin and V_0 is the potential at the electrode. It should be noted that the hyperbolic cosine function in this expression accounts for the mobility of the charges, whilst the square root function is equivalent to the parallel plate capacitor equation for a capacitor with a interlayer dielectric thickness of L_D, the Debye length (the distance over which the applied potential decays to $1/e$ of its maximum value):

$$C_D = \frac{\varepsilon_0\varepsilon_r}{L_D} \cosh\frac{nqV_0}{2kT} \tag{4.05}$$

where:

$$L_D = \sqrt{\frac{\varepsilon_0\varepsilon_r kT}{2N_A C^* n^2 q^2}} \tag{4.06}$$

Figure 4.2 demonstrates the variation in the diffuse layer capacitance with applied potential for three different electrolyte concentrations. Although these capacitance curves approximate the observed behaviour of typical electrochemical systems at low potentials and low electrolyte concentrations, experimental capacitance measurements do not increase as

rapidly with applied potential (Bard and Faulkner, 2001). Furthermore, real systems exhibit a flattening in capacitance at higher potentials. One of the reasons for these discrepancies in the Gouy-Chapman model is that the finite size of the solvated ions in the electrolyte was not taken into account.

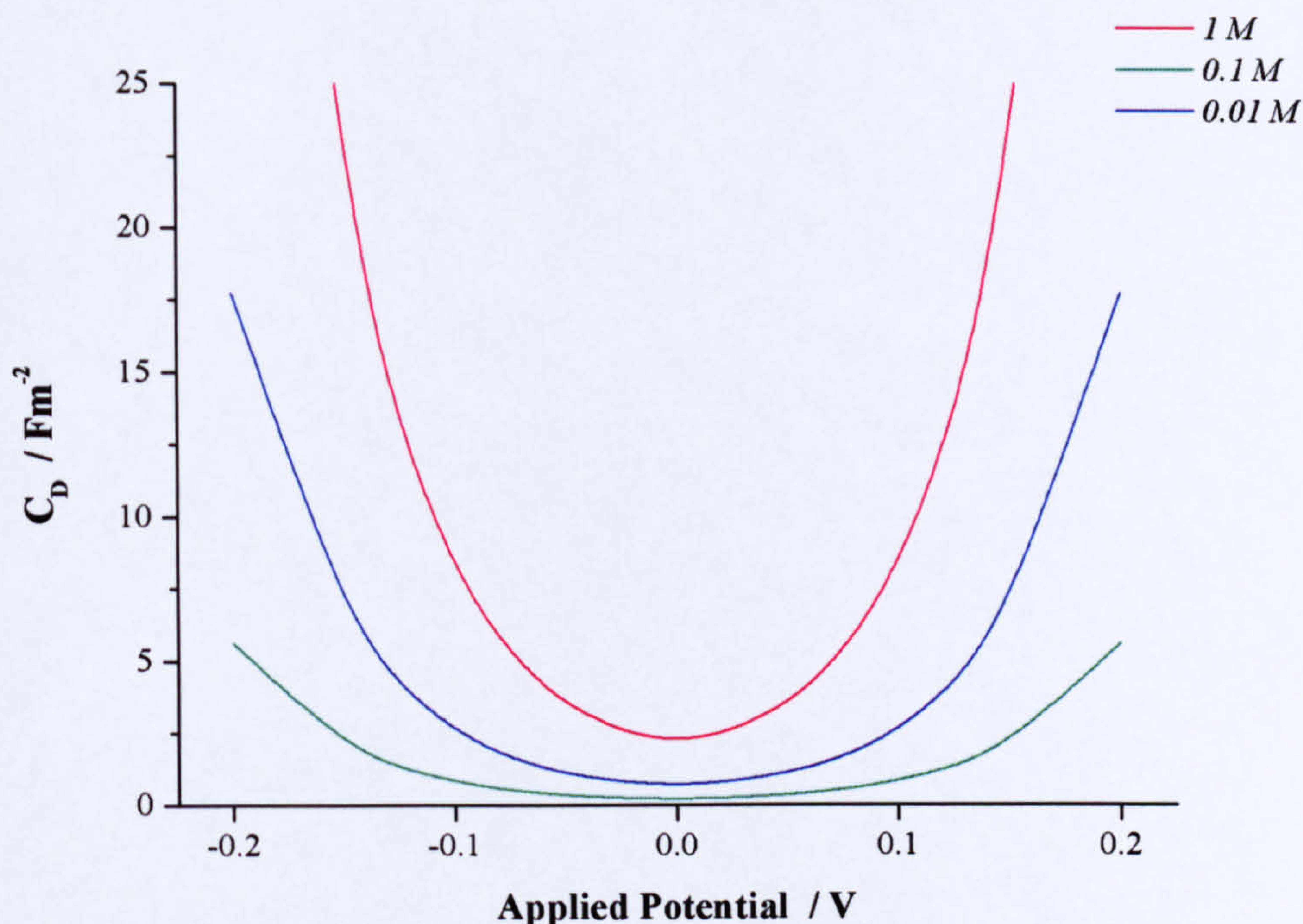

Figure 4.2 **Variation in the Diffuse Layer Capacitance with Applied Potential & Electrolyte Concentration**

Curves calculated using Equations 4.05 and 4.06, assuming a temperature of 298 K and a one-electron transfer process.

4.2.1.3 The Stern Model

In the derivation of the Gouy-Chapman model, a point charge approximation was employed (Bockris and Reddy, 1970). However, solvated ions cannot unlimitedly approach the electrode surface, as their advance is hindered by the finite size of the ionic radius, the thickness of the surrounding solvent layer and the thickness of the hydration layer at the electrode surface. Thus, the plane of closest approach for the electrical centres of ions is located at the OHP. At low potentials and electrolyte concentrations, when the diffuse layer thickness is large compared to the thickness of the double layer, the point charge approximation does not significantly affect the predicted capacitance values. However, at

larger potentials or electrolyte concentrations, the behaviour of the solution charge tends towards the behaviour of the Helmholtz model.

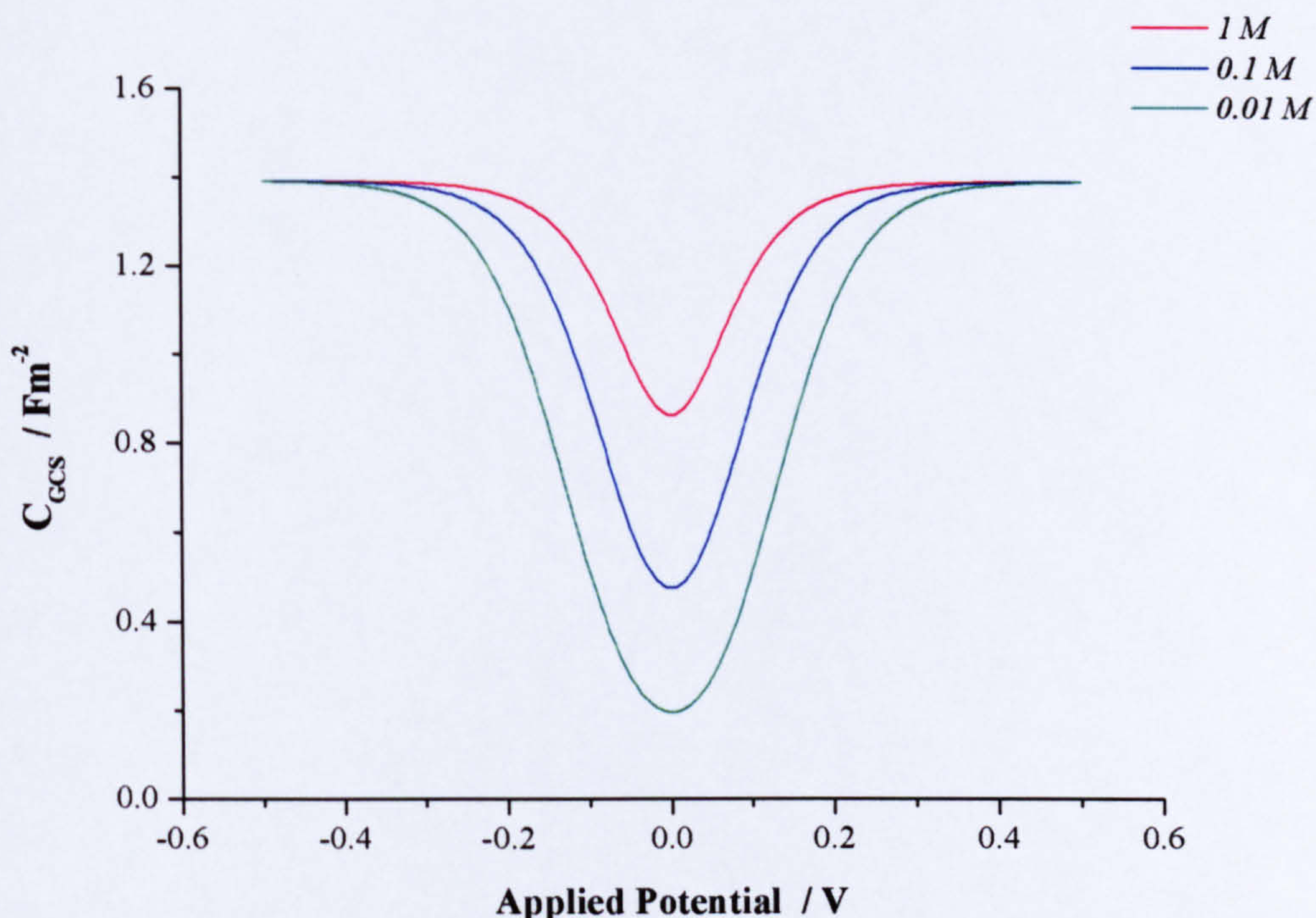

Figure 4.3 **Variation in the Gouy-Chapman-Stern Capacitance with Applied Potential**

Curves calculated using Equation 4.07. A value of 0.5 nm was employed for the double layer thickness and a one-electron transfer process and a temperature of 298 K were assumed.

Thus, Stern (in 1924) suggested refining the Gouy-Chapman model by altering the boundary conditions employed to independently describe the two distinct regions of the space charge layer, the double layer and the diffuse layer (Kovacs, 1994). The reciprocal of the differential capacitance yielded by employing these conditions is:

$$\frac{1}{C_{GCS}} = \frac{d}{\varepsilon_o \varepsilon_r} + \frac{1}{\frac{\varepsilon_0 \varepsilon_r}{L_D} \cosh \frac{nqV_0}{2kT}} \tag{4.07}$$

It can be seen that this capacitance (the Gouy-Chapman-Stern capacitance) is equivalent to two capacitors in series; that of the Helmholtz capacitance, which corresponds to the charges

held at the OHP, and the diffuse layer capacitance, which describes the behaviour of the wholly diffuse charges:

$$\frac{1}{C_{GCS}} = \frac{1}{C_H} + \frac{1}{C_D} \tag{4.08}$$

Figure 4.3 demonstrates the behaviour of this composite capacitance, which is dominated by the smallest component. Although this model satisfactorily predicts the general behaviour of real electrochemical systems and is suitable for modelling the electrode-electrolyte interface of most electroanalytical sensors, certain discrepancies are still apparent. Thus, refinements to the Gouy-Chapman-Stern model continue to be made (for details refer to Morgan and Green, 2003).

4.2.2 Resistive Mechanisms

In addition to the double layer capacitance, a circuit model for the electrode-electrolyte interface must also incorporate a parallel, non-linear resistive element to account for charge transfer processes across the electrode-electrolyte interface. Kovacs (1994) demonstrates how the resistance due to charge transfer, R_{ct}, may be expressed as:

$$R_{ct} = \frac{RT}{nFj_0 A \cosh\left(\frac{nF\eta_t}{2RT}\right)} \tag{4.09}$$

where j_0 is the exchange current density (Am^{-2}) and η_t is the overpotential due to charge transfer. Therefore, at higher overpotentials, R_{ct} will decrease exponentially as the applied potential is increased.

A further resistance, R_d, must also be incorporated as a consequence of the diffusion of the electroactive species. When the time variation of the electrolytic current is sufficiently slow (that is near d.c. conditions apply), this diffusion resistance is given by (Cobbold, 1974):

$$R_d = \frac{RT}{nFA}\left(\frac{1}{j_s - j}\right) \tag{4.10}$$

where j_s is the saturation current density, which corresponds to the maximum rate at which the electroactive species can be transported to the electrode surface (see Section 4.5). Combining Equations 4.9 and 4.10, it can be seen that, for conditions close to equilibrium, the total resistance will be effectively constant but, as the electrode current increases with the applied potential, the resistance will rapidly decrease. It should be noted, however, that when the applied potential varies significantly with time, the resistance will vary inversely with the frequency and a Warburg impedance model will be required to describe the resistance due to diffusion. For details refer to Kovacs (1994).

Furthermore, there will be a net resistance, R_s, encountered by the charge flowing through the solution between the working electrode and the reference electrode (Bard and Faulkner, 2001). Unlike the previous terms, this resistance is proportional to the geometric area of the electrode surface, as opposed to the actual surface area. The working electrode is normally significantly smaller than the reference electrode and, therefore, R_s is largely determined by the resistance of the solution in the vicinity of the working electrode (as resistance is inversely proportional to area). For a working electrode with spherical symmetry, the solution resistance may be expressed as (Koster *et al*, 2001):

$$R_s = \frac{1}{4\pi\sigma r}\left(1 - \frac{r}{L}\right) \tag{4.11}$$

where σ is the conductivity of the solution, r the geometric radius of the electrode and L the distance between the reference electrode and the working electrode.

4.2.3 Effects of the Electrode-Electrolyte Interface

All these equivalent circuit elements can be combined to produce a theoretical model for the electrode-electrolyte interface that can be used to predict the behaviour of simple electrochemical systems and to interpret experimental results (Figure 4.4). Indeed, the space charge layer can significantly impact the results of an electrochemical experiment. Notably, the double layer capacitance gives rise to a charging current, which flows when a potential is applied to the system and which is superimposed onto the recorded faradaic current. For instance, the charging current that results from the application of a potential step of magnitude E is (Bard and Faulkner, 2001):

$$i = \frac{E}{R_s} e^{-\frac{t}{R_s C_{dl}}} \tag{4.12}$$

where C_{dl} is the double layer capacitance (either calculated as AC_{GCS} or determined empirically). Thus, the charging current decays exponentially with a time constant, τ, of R_sC_{dl}.

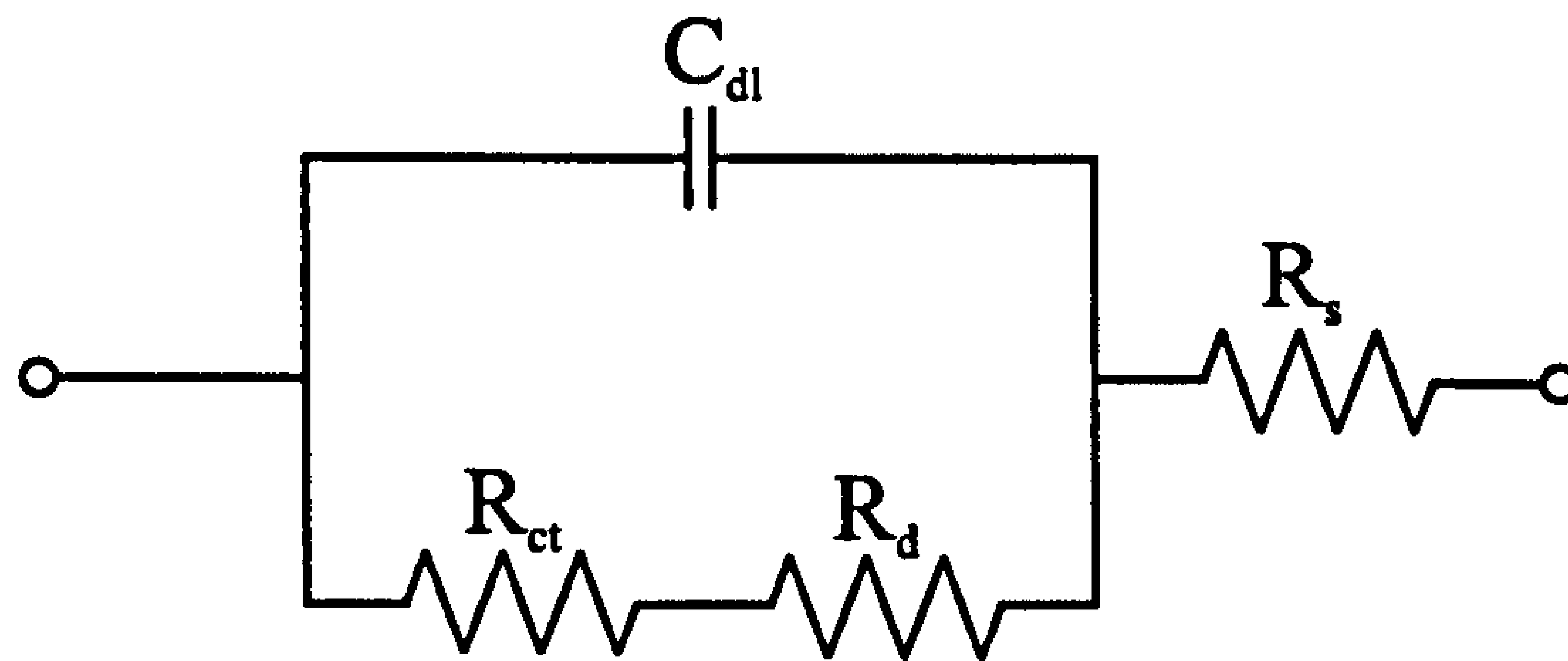

Figure 4.4 **An Equivalent Circuit Model of the Electrode-Electrolyte Interface**

Furthermore, electrode kinetics can also be influenced by double-layer effects and by the specific adsorption of ions, which was first recognized by Frumkin in 1933 (Bockris and Reddy, 1970). As previously discussed, the double layer thickness and the concentration of the electroactive species at the OHP are altered by variation in both the potential and the nature and concentration of the supporting electrolyte. These variations in the structure of the electrode-electrode interface will affect the electron transfer rate constant, the exchange current density and, consequently, the charge-transfer characteristics of the electrochemical system.

4.3 The Rate Determining Step

As charge passes through an electrochemical cell, the quantity of the reactant species at the electrode interface will be depleted and a concentration gradient will therefore be established. The volume of solution adjacent to the electrode surface where this concentration gradient occurs, known as the diffusion layer, extends further outwards into the bulk solution with time. Hence, the magnitude of the electrolytic current will be determined either by the rate of the electron transfer across the electrode-electrolyte interface

or by the transport of the reactants to (and products from) the electrode surface. In the former case, the electrode kinetics are governed by the potential dependant heterogeneous rate constant for the electron transfer process and the behaviour of the electrolytic current is described by the well known Butler-Volmer formulation (Bard and Faulkner, 2001):

$$i = i_0 \left[\frac{C_{O(x=0)}}{C_O^*} e^{-\frac{\alpha F}{RT}\eta} - \frac{C_{R(x=0)}}{C_R^*} e^{\frac{(1-\alpha)F}{RT}\eta} \right] \tag{4.13}$$

where i_0 is the exchange current density, which is proportional to the standard heterogeneous rate constant, k_0, α is the transfer coefficient (a measure of the symmetry of the energy barrier to the forward and reverse reactions) and η is the applied overpotential. Therefore, the larger the magnitude of the overpotential, the greater the resulting electrolytic current.

However, a potential will be eventually be reached where the electron-transfer kinetics become so rapid that the reactant molecules reaching the electrode surface are consumed more quickly than they are replenished from the bulk solution. The electrolytic current will therefore be mass-transfer limited and further increases in the applied potential will no longer increase the magnitude of the current. The flux of the reactant species to the electrode surface can be described by the Nernst-Plank equation (Bard and Faulkner, 2001), which for the one-dimensional case is expressed as:

$$J(x) = -D\frac{\partial C(x)}{\partial x} - \frac{nF}{RT}DC\frac{\partial E(x)}{\partial x} + Cv(x) \tag{4.14}$$

where D is the diffusion coefficient, $E(x)$ is the potential profile within the solution and $v(x)$ is the velocity profile. The three terms on the right hand side of the equation describe the flux due to diffusion, migration and convection respectively. To simplify analysis, electrochemical systems are commonly designed so that the contribution from one or two of these mass transfer processes is negligible. For example, convection can be minimised by using an unstirred solution in a vibration free environment and migrational effects can be made negligible by the incorporation of a large concentration of a supporting electrolyte (relative to the concentration of the electroactive species).

4.4 Electrochemical Cell Configurations

In a traditional electrochemical cell, the electrodes employed typically have dimensions in the millimetre range. In recent years, however, electrodes with significantly smaller dimensions have been increasingly employed. Although the definition of a microelectrode is somewhat ambiguous, it is conventionally assumed that a microelectrode has a radius (in the case of a disc electrode) of 25 μm or less (Bard and Faulkner, 2001). The behaviour of an electrochemical system is strongly influenced by the dimensions of the electrodes employed and in many respects microelectrode behaviour is quite different to conventional macroelectrode behaviour. One of the most significant differences is the increased rate of mass transport to the surface of a microelectrode, which will be discussed in Section 4.6. Another dissimilarity concerns the suitability of micro- and macroelectrodes for use in a simple two-electrode electrochemical cell.

The two-electrode configuration described previously is the simplest design for an electrochemical measurement system. Provided that a suitable reference electrode is employed and only minute currents are allowed to pass through the circuit, it should be possible to accurately define the potential across the electrode-electrolyte interface. However, when more substantial currents flow, it may not be possible to obtain a precise value for the working electrode potential, as the finite resistance of the electrolyte solution will no longer be negligible. The potential across the electrochemical cell, E, may then be defined as (Koryta *et al*, 1993):

$$E = E_{WE} - E_{RE} + iR_s \tag{4.15}$$

where E_{WE} is the working electrode potential and E_{RE} is the reference electrode potential. The value of E_{RE} is determined by the chemical composition of the reference electrode and should remain constant, although very large or rapidly changing current levels can alter the chemical composition of the electrode and result in fluctuations of E_{RE}. The third term, iR_s, expresses the voltage drop that results from the passage of current through the electrolyte solution. This is normally considered negligible for microelectrode systems, as the currents concerned are small and, when the working and reference electrodes are situated close together on a single substrate, the value of the solution resistance is low. Therefore, the two-electrode system is generally sufficient for microelectrode experiments.

4.4.1 The Three-Electrode System

However, when larger electrodes are employed, iR_s is no longer negligible and will vary with the magnitude of the current. Consequently, it would not be possible to measure the current at a known potential using a two-electrode electrochemical cell. Instead, a three-electrode system is employed in conventional macroelectrode experiments, where a counter electrode is used in addition to the working and reference electrodes.

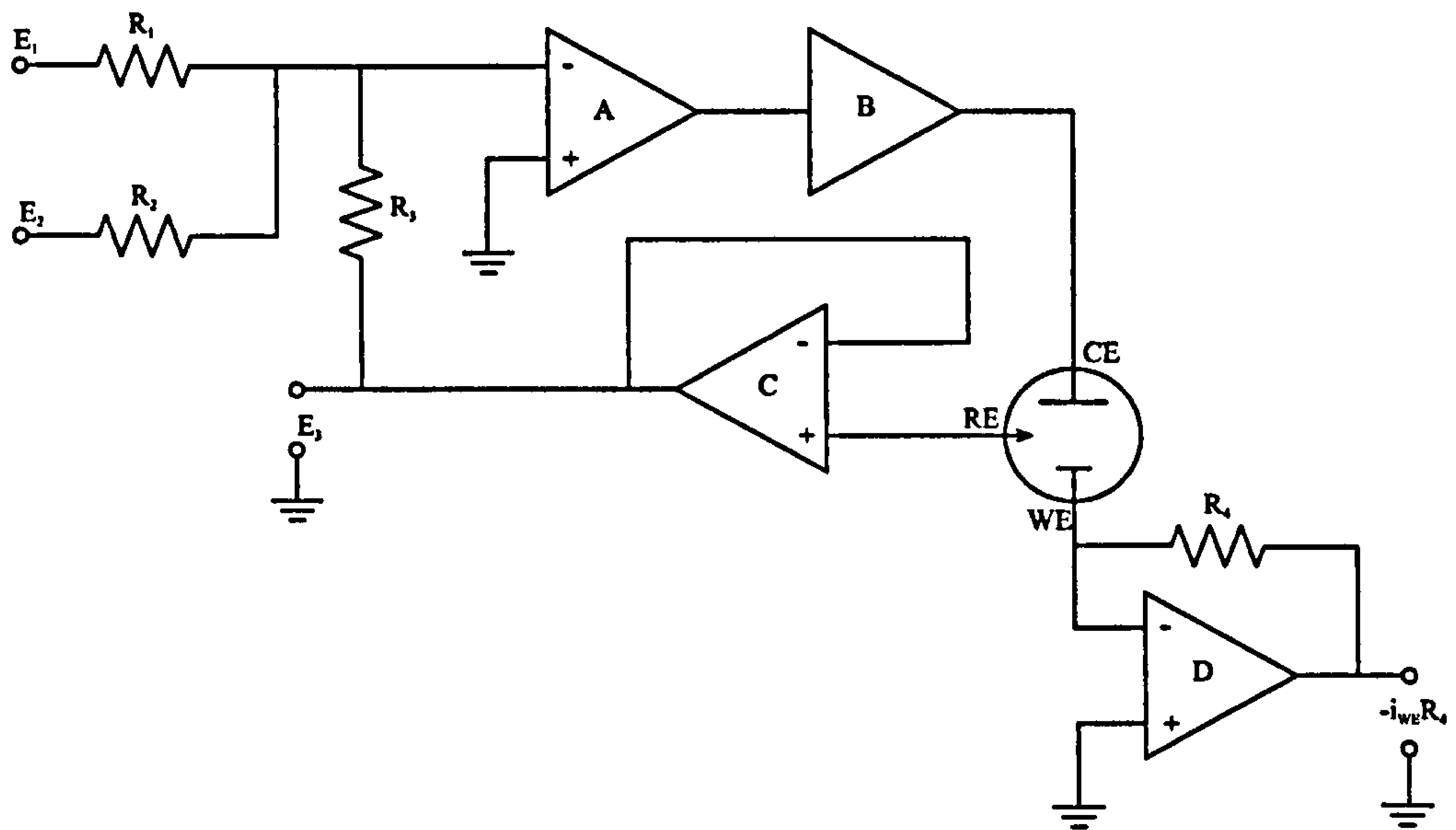

Figure 4.5 **Schematic of a Three-Electrode Potentiostatic System as Described by Bard and Faulkner (2001)**

In this arrangement, the control amplifier, A, (which is followed by a booster amplifier, B, that increases the gain of the system) adjusts its output so that the sum of the inputs E_1 and E_2, weighted by R_3/R_1 and R_3/R_2 respectively, is the potential of the reference electrode. (Various input signals can be summed together to create the complex waveforms often required for voltametric experiments.) As the working electrode is held at virtual ground, the potential across it will be the same as that at the reference electrode (though there will be a small drop across the uncompensated resistance of the solution between the two electrodes). The current flowing through the working electrode is measured by recording the output from the current follower, $-i_{WE}R_4$, that the working electrode feeds, which is proportional to the current flowing through the electrode. The potential at the output of the voltage follower, C, which presents a very high impedance to the reference electrode and therefore draws negligible current from it, is measured to determine the working electrode potential.

The system is controlled by a potentiostat, which ensures that virtually no current passes through the reference arm of the circuit and only flows between the working and counter electrodes (Bone and Zaba, 1992). The potential at the counter electrode is adjusted by the potentiostat so that a constant potential is maintained at the working electrode with respect to the stable reference electrode potential and the current passing through the working electrode is measured simultaneously. So that no serious polarisation of the counter electrode occurs, which would influence the response of the electrochemical cell, the counter electrode is generally chosen to have a much larger surface area than the working electrode. A typical three-electrode potentiostat system is illustrated in Figure 4.5.

4.5 Chronoamperometric & Voltammetric Techniques with Macroelectrodes

In the most widely practised electrochemical techniques, the process occurring at the working electrode are probed by stepping or sweeping the applied potential. A great deal of information can be obtained by electrically perturbing the system and then observing the resulting changes to the system.

4.5.1 Chronoamperometry

Chronoamperometry is a basic potential step experimental technique where, at a given time, the potential is stepped from a value where no faradaic processes occur to a value where a faradaic current does flow (Bard and Faulkner, 2001). If the potential step is sufficiently large, the reactant concentration at the electrode surface will decrease to zero and the current flow will be limited by the rate of mass-transfer. Assuming that the mass-transfer is independent of convection (as the solution is unstirred) and migration (due to a large supporting electrolyte concentration), the flux of the electroactive species to the electrode will depend solely on diffusion. As determined by Fick in 1855, mass transfer due to diffusion is proportional to the concentration gradient of the species (previously noted as the first term of the Nernst-Plank equation):

$$J(x,t) = -D\frac{\partial C(x,t)}{\partial x} \tag{4.16}$$

The diffusion coefficient is normally determined empirically and, in liquids, has a typical value of 10^{-8}–10^{-10} $m^2\ s^{-1}$. As diffusion is driven by Brownian motion, mathematical models describing the diffusion coefficient have been constructed from random walk theory, beginning with the work of Einstein in 1905. This approach resulted in an expression, known as Einstein's equation, that relates the diffusion coefficient to molecular fluctuations within the medium (Morgan and Green, 2003):

$$D = \frac{kT}{q}\mu = \frac{kT}{6\pi r\eta} \tag{4.17}$$

where μ is the mobility of the electroactive species, r is the radius of the electroactive species and η is the viscosity of the solution. Similarly, the thickness of the diffusion layer, δ, at time t can be estimated by the Einstein-Smoluchowski equation, which for the one-dimensional case is (Bockris and Reddy, 1970):

$$\delta = \sqrt{2Dt} \tag{4.18}$$

In the majority of electrochemical experiments, non-steady state conditions apply to the diffusion of the electroactive species; that is the rate of diffusion is not constant but instead varies with time. Non-steady state diffusion is formulated by Fick's second law:

$$\frac{\partial C(x,t)}{\partial t} = D\frac{\partial^2 C(x,t)}{\partial x^2} \tag{4.19}$$

which can be solved by Laplace transformation. As this partial differential equation is first order with respect to time and second order with respect to distance, its solution requires one initial condition and two spatial boundary conditions to describe the particular problem of interest. When employing macroelectrodes, mass transport to the electrode surface in a chrono amperometric experiment may be approximated as linear diffusion to a horizontal plane (a one dimensional problem) and the following boundary conditions may be applied (Bard and Faulkner, 2001):

$$C(x,0) = C^* \tag{4.20}$$

$$C(0,t) = 0 \qquad (t>0) \tag{4.21}$$

$$\lim_{x\to\infty} C(x,t) = C^* \tag{4.22}$$

The initial condition (4.20) simply states that, prior to the application of the potential step, the concentration of the electroactive species is constant throughout the solution with a value of C^*. Once the potential has been stepped, however, the concentration at the electrode surface will decrease to zero (4.21), although in regions far from the electrode surface the concentration will remain unperturbed by events at the electrode (4.22, the semi-infinite condition). Application of these boundary conditions to the Laplace transform of Fick's second law of diffusion yields (for details refer to Bard and Faulkner, 2001):

$$C(x,s) = \frac{C^*}{s} - \frac{C^*}{s} e^{-\sqrt{\frac{s}{D}}x} \tag{4.23}$$

By combining expressions 4.02 and 4.16 and then taking the Laplace transform, the following expression for the current flow is obtained:

$$i(s) = nFAD\left(\frac{\partial C(x,s)}{\partial x}\right)_{x=0} \tag{4.24}$$

Substitution of the derivate of Equation 4.23 for $x=0$ gives:

$$i(s) = nFAC^*\sqrt{\frac{D}{s}} \tag{4.25}$$

the inverse transform of which produces the current-time response:

$$i(t) = nFAC^*\sqrt{\frac{D}{\pi t}} \tag{4.26}$$

This expression, known as the Cottrell equation (after F.G. Cottrell who first derived it in 1902), demonstrates how mass-transfer limited electrolytic current is directly proportional to the surface area of the electrode and varies inversely with the square root of time (Figure 4.6), thus the recorded current never reaches a steady state.

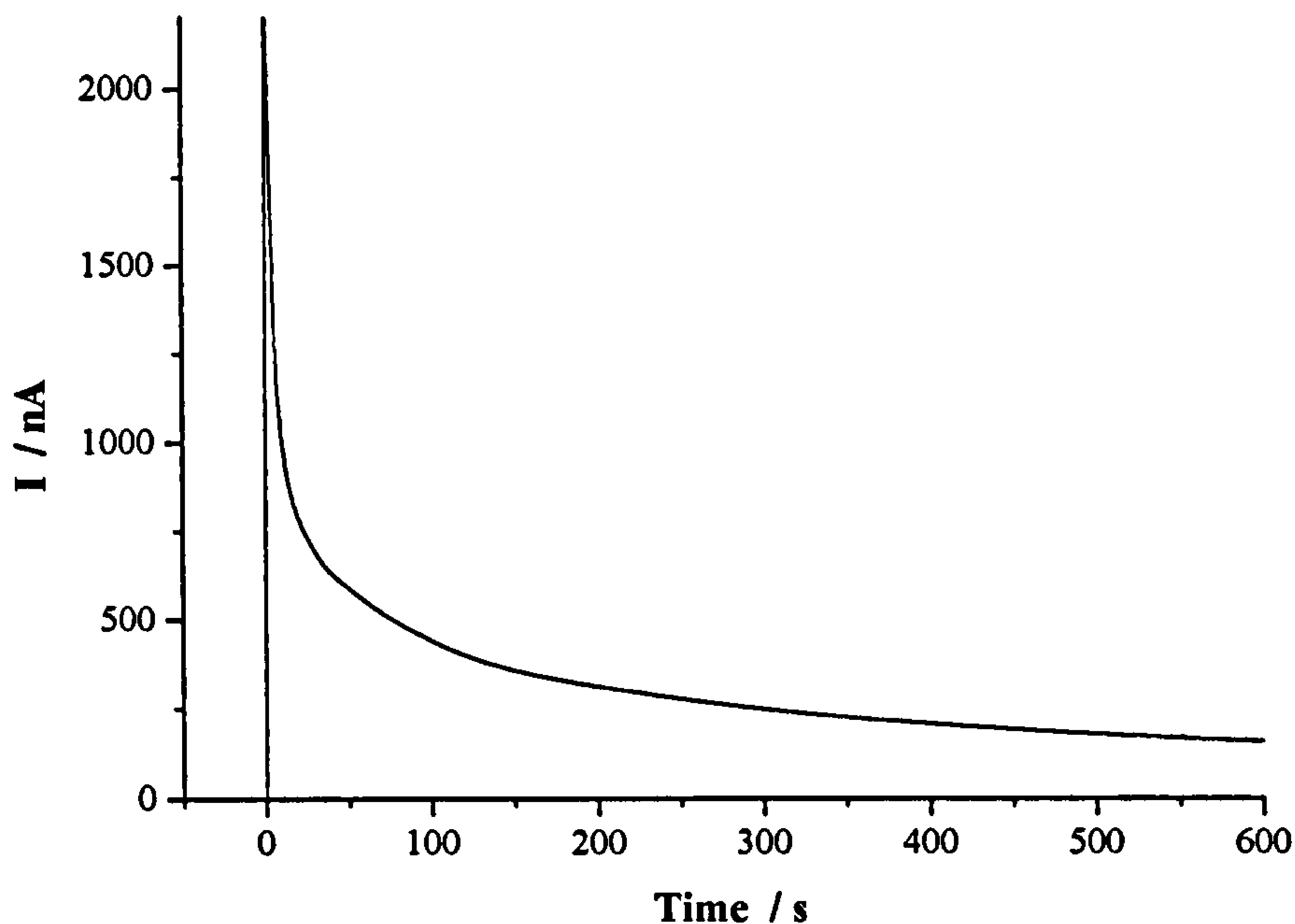

Figure 4.6 **Chronoamperometric Recording from a Macroelectrode**
Trace recorded using a 0.8 mm radius gold disc electrode in a 1 mM ferrocene monocarboxylic acid (FMCA) solution with a 10 mM phosphate buffered saline (PBS) supporting electrolyte.

4.5.2 Linear Sweep and Cyclic Voltammetry

In linear sweep voltammetry the electrode potential is swept at a constant rate from an initial value that is not large enough to induce an electron transfer reaction to a level where the redox reaction is driven rapidly. In cyclic voltammetry, the potential is then swept back again to the initial value and, in both cases, the results are plotted as a current-voltage curve, as shown in Figure 4.7.

Initially, no electron transfer reactions occur, as the potential that is the driving force for the reaction is too small. However, as the potential is increased, the current begins to rise, due to an increase in the electron transfer rate constant, and the surface concentration of the electroactive species decreases. Eventually, the surface concentration will fall to zero and the rate of mass transport of the electroactive species to the electrode, which limits the net flow of current, will reach its maximum value. Thus, the peaked shape of the voltammogram stems from the combination of the increasing heterogeneous rate constant and the increasing consumption of the electroactive species, the latter resulting in a steadily increasing diffusion

layer thickness (Fisher, 1996). The current recorded after the peak is simply dependant upon the rate of mass transport to the electrode surface, whilst the current recorded prior to the peak is controlled by electrode kinetics.

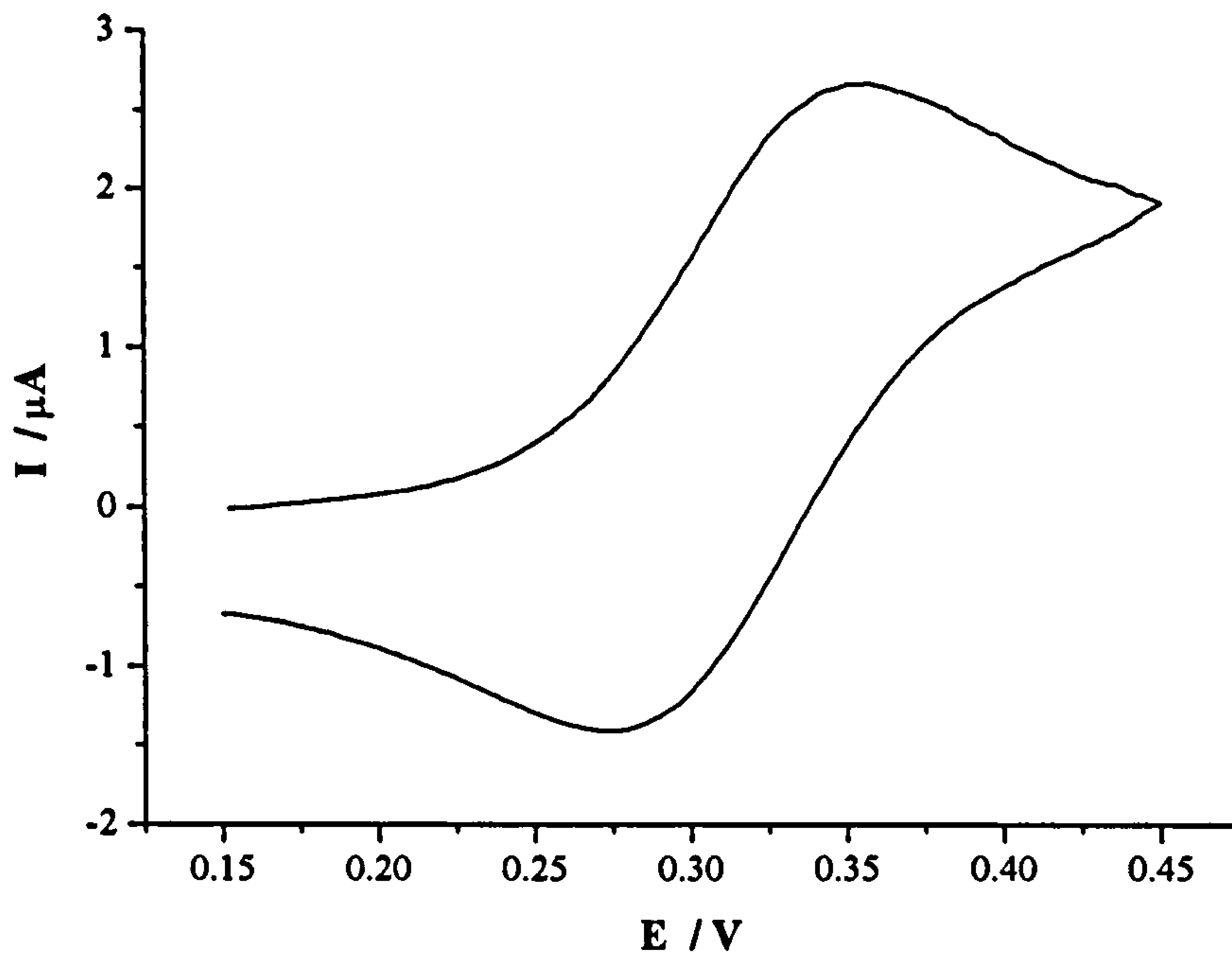

Figure 4.7 **A Cyclic Voltammogram**

Voltammogram recorded using a 0.9 mm radius platinum disc electrode in a 1 mM FMCA solution, with a 10 mM PBS supporting electrolyte, at a scan rate of 20 mV s^{-1}

In cyclic voltammetry, the direction of the sweep is reversed at a certain potential after the peak and the shape of the current-voltage curve during the backward sweep is determined by the reverse redox reaction. When the potential is switched, there will be a large concentration of the product from the forward reaction in the vicinity of the electrode surface that is available for consumption in the reverse electron transfer reaction and, thus, the backward sweep will proceed in the same manner as the forward sweep.

As well as the faradaic response, real voltammograms will include a non-faradaic component (as discussed in Section 4.1.2). An approximately constant charging current will be superimposed on the faradaic response, forming a baseline (Bard and Faulkner, 2001). Assuming the time constant is small compared to the scan rate, v, the charging current will rise from its initial value to an approximate steady state value of:

$$|i_c| = C_{dl}\nu \quad (4.27)$$

Peak current measurements must therefore be corrected accordingly, although their measurement is often imprecise due to uncertainty in the correction term for the charging current. Hence, whilst voltammetry is not the most attractive technique for the quantitative evaluation of a system, the extraction and interpretation of mechanistic and semi-quantitative information is its real strength. Indeed, cyclic voltammetry is an extremely powerful technique that is frequently performed to yield qualitative information about an electrochemical system, such as information concerning the reversibility of a redox couple.

4.5.2.1 Electrochemical Reversibility

A system is said to be electrochemically reversible, or Nernstian, if the electrode potential and the surface concentrations of the oxidised and reduced species appear to be in equilibrium with each other at all times, owing to fast charge-transfer processes. Thus, after any perturbation in the electrode potential, the surface concentrations rapidly adjust to the ratio dictated by the Nernst equation (4.01) and, as the interfacial redox kinetics are so fast, no experimental manifestations of this adjustment will be observed. By contrast, if disequilibrium is observed at the electrode interface, the system is said to be irreversible. However, the reversibility of a given system is dependant upon the time scale of the experiment and the demands that are made of the charge-transfer kinetics and, therefore, any system may appear reversible in one particular situation and quasi-reversible or totally irreversible in another (Bard and Faulkner, 2001).

In a reversible system, the peak potential, E_p, does not vary with the scan rate, whilst, for an irreversible system, E_p will occur further from E_e at faster scan rates. For the same voltage sweep parameters, the peak current, i_p, is also smaller for an irreversible couple than for a reversible couple. However, for any system, i_p will increase as the scan rate is increased, since i_p reflects the concentration gradient at the electrode surface, which is steeper for thinner diffusion layers. The thickness of the latter is influenced by the variation of the electrode potential – the more rapidly the electrode potential is swept, the less time there is available for electron transfer reactions to occur, and, consequently, the thinner the resulting diffusion layer will be.

For a reversible system (at 25°C), the peak current generated during the forward sweep of the first cycle is expressed by the Randals-Sevcik equation (Kissinger and Heineman, 1983):

$$i_p = 268714\left(n^{\frac{3}{2}} AC^{*}(Dv)^{\frac{1}{2}}\right) \qquad (4.28)$$

In the derivation of this equation, it was assumed that mass-transport was driven by diffusion only and so i_p is proportional to the square root of the scan rate, which is indicative of diffusion control in the same manner that the diffusion limited current in a chronoamperomteric experiment is inversely proportional to the square root of time.

The ratio of the peak currents, i_{pa}/i_{pc}, and the peak-peak separation, $E_{pa}-E_{pc} = \Delta E_{pk}$, are convenient tests of the reversibility of a system. The value of the former is always equal to one for a Nernstian wave with stable reaction products. In the case of the latter, although it is dependant upon the switching potential, the value of ΔE_{pk} is always near to $2.3RT/nF$ for a reversible system:

$$\left|E_{pc} - E_{pa}\right| \approx \frac{59}{n} \quad (mV\ at\ 25°C) \qquad (4.29)$$

4.6 Chronoamperometric and Voltammetric Techniques with Microelectrodes

So far, the discussions concerning potential step and potential sweep techniques have focused on electrochemical systems employing macroelectrodes. However, the use of microelectrode-based systems in electrochemical analysis has increased dramatically since the late 1970s, when the group of M. Fleischmann at the University of Southampton confirmed that the electrochemical behaviour of an electrode changed significantly as its surface area was reduced (Heinze, 1993). As a direct consequence of their small size, the response of a microelectrode to a variation in applied potential is significantly different to that of a macroelectrode.

As the surface area of an electrode is decreased (and therefore its circumference-to-area ratio increases) the electrode can no longer be approximated as a semi-infinite planar electrode; rather, the electrode will increasingly adopt the characteristics of a point source or drain.

Hence, as the size of the electrode is decreased, the diffusion field, which is essentially linear for a macroscopic electrode, becomes increasingly non-linear. Therefore, mass-transport of the electroactive species to the electrode surface is greatly enhanced. Furthermore, after the application of a potential step, a steady-state current that is essentially convection independent is rapidly reached. This characteristic results from the increasing surface area of the boundary of the diffusion layer with an increasing diffusion layer thickness, which leads to a constant flux of the reactant towards the electrode surface. The signal-to-noise ratio (SNR) is also significantly improved by employing microelectrodes, as is the faradaic-to-capacitive current ratio, which means that extremely fast scan rates may be employed (see Section 4.6.3) (Stulik *et al*, 2000).

4.6.1 Chronoamperometry

As discussed previously, the Cottrell equation is derived by solving Fick's second law assuming semi-infinite, linear diffusion to a horizontal plane. Therefore, it is not applicable to microelectrode behaviour. Instead, a time independent correction term must be incorporated into the equation to express the current profile of a microelectrode after the application of a potential step. The derivation of an expression that describes the current profile of a microelectrode is simplest in the case of a spherical or hemispherical geometry, where (Bard and Faulkner, 2001):

$$i(t) = nFAC^{*}\left(\sqrt{\frac{D}{\pi t}} + \frac{D}{r}\right) \tag{4.30}$$

It can be seen that the first term in this expression is equivalent to the current profile obtained when mass transport to the electrode surface is linear. At very short times, when the diffusion layer thickness is much smaller than the electrode radius and the diffusion field is essentially linear, this term will dominate. However, as the experiment progresses, radial diffusion will become increasingly significant and the second term will become more influential. As the diffusion layer continues to grow, becoming significantly larger than the electrode radius, the diffusion field will become radial and a steady-state limiting current, i_L, will be reached, which for a hemispherical microelectrode has a value of:

$$i_L = 2\pi nFC^{*}Dr \tag{4.31}$$

As the limiting current varies with radius rather than area, the current density will be significantly larger than that produced by a macroelectrode and, the smaller the microelectrode employed, the greater the current density obtained.

A similar expression may be employed to describe the current profile at a disk microelectrode, although its derivation is slightly more complicated as diffusion of the electroactive species occurs both normal to the electrode surface and radially with respect to the axis of symmetry (Bard and Faulkner, 2001). Hence, for a microdisk geometry, the current density varies across the plane of the electrode, with the greatest current density occurring at the perimeter of the electrode (the closest point of arrival for the electroactive species diffusing radially from the surrounding volume). Equation 3.32 describes the current generated by a disk microelectrode, where the factor b ($\pi^{1/2}<b<4\pi^{-1/2}$) changes during the transition from the planar diffusion regime to the radial diffusion regime (Heinze, 1993).

$$i = nFAC^{*}\left(\sqrt{\frac{D}{\pi t}} + b\frac{D}{\pi^{\frac{1}{2}} r}\right) \tag{4.32}$$

Again, the first term is equivalent to the Cottrell equation and dominates the initial current response, whilst the second term prevails at longer times, leading to a limiting current of:

$$i_L = 4nFDC^{*}r \tag{4.33}$$

If a microelectrode is recessed, as is typical for a thin-film microelectrode structure, the diffusion profile is slightly different to that of an inlaid microelectrode and mass transport to the electrode surface is reduced by an amount dependent upon the height, h, of the recess. Figure 4.8 shows a typical current-time trace for a single recessed microelectrode, the limiting current for which may be expressed as (Lenigk *et al*, 1999):

$$i_L = nFAD\frac{C^{*}}{r+h} \tag{4.34}$$

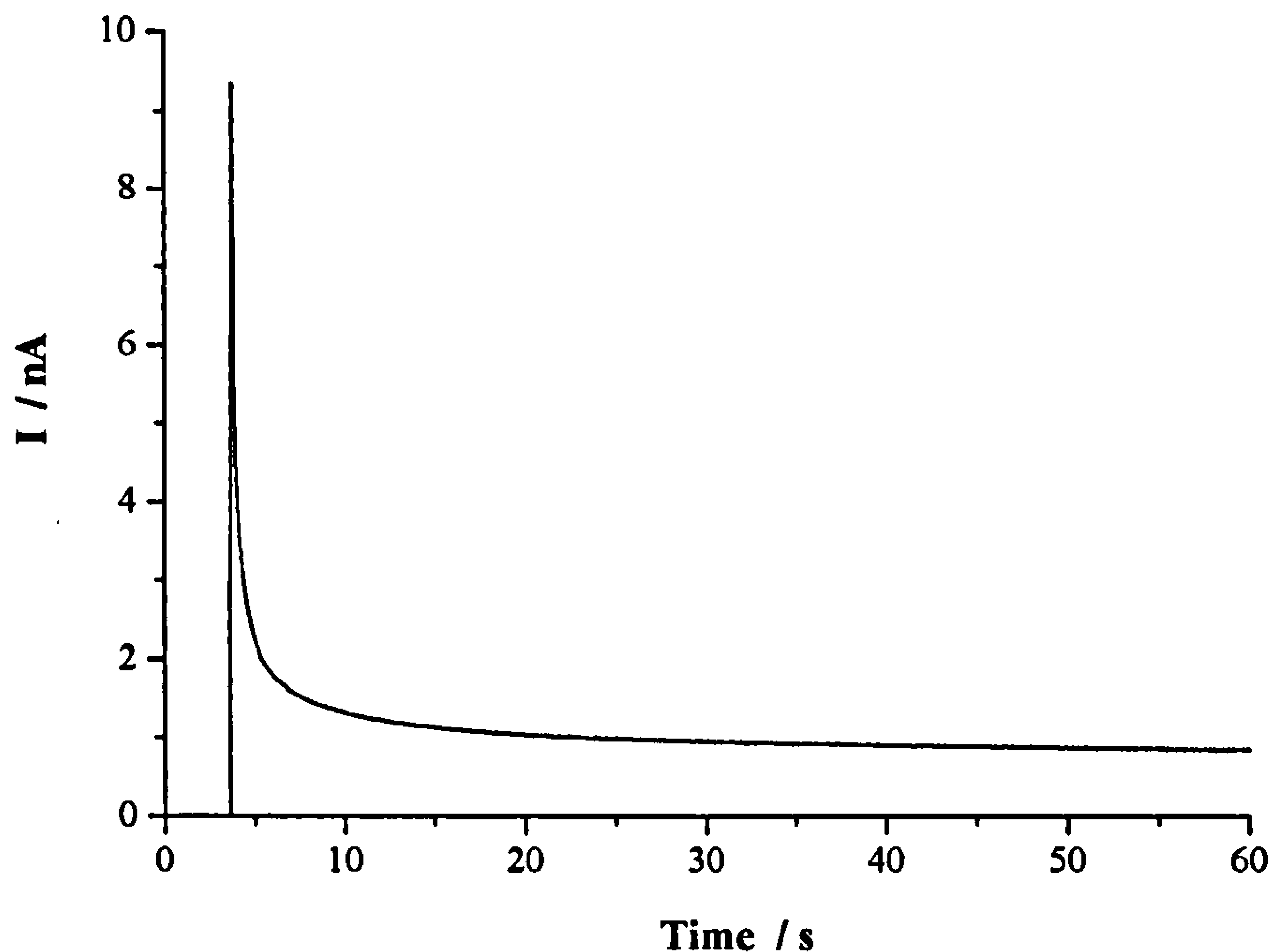

Figure 4.8 **A Current-Time Trace for a Recessed Microelectrode**
Recorded at 0.45 V in a 1 mM FMCA solution, with a 10 mM PBS supporting electrolyte, using a 2.5 μm radius gold disc electrode, recessed by height of 500 nm.

4.6.1.1 The Transition from Linear to Radial Diffusion

From the previous discussion, it is clear the characteristics of the diffusion field vary with both radius and time. Immediately after the application of a potential step, the diffusion field will be linear, even for the smallest microelectrode. The evolution of the diffusion field from this initial linear state to a fully radial state is dependant upon the electrode radius, the smaller the electrode, the shorter the time required to reach a steady-state. This is illustrated by Figure 4.9, which shows current-time curves calculated for four different electrode radii, and by the finite element simulation results presented in Section 4.8.

The ratio $i_r/(i_r + i_l)$ may be employed to characterise the extent of the non-linearity of the diffusion field, where i_l and i_r are the first and second terms respectively in either Equation 4.30, for a spherical or hemispherical microelectrode, or Equation 4.32, for a disk microelectrode. In the case of the former, the ratio may be expressed as:

$$\frac{i_r}{i_r + i_l} = \frac{1}{1 + \frac{r}{\sqrt{\pi D t}}} = \frac{1}{1 + \frac{r}{\delta}} \tag{4.35}$$

where δ is the linear diffusion layer thickness for a chronoamperometric experiment (Freund and Brajtertoth, 1991).

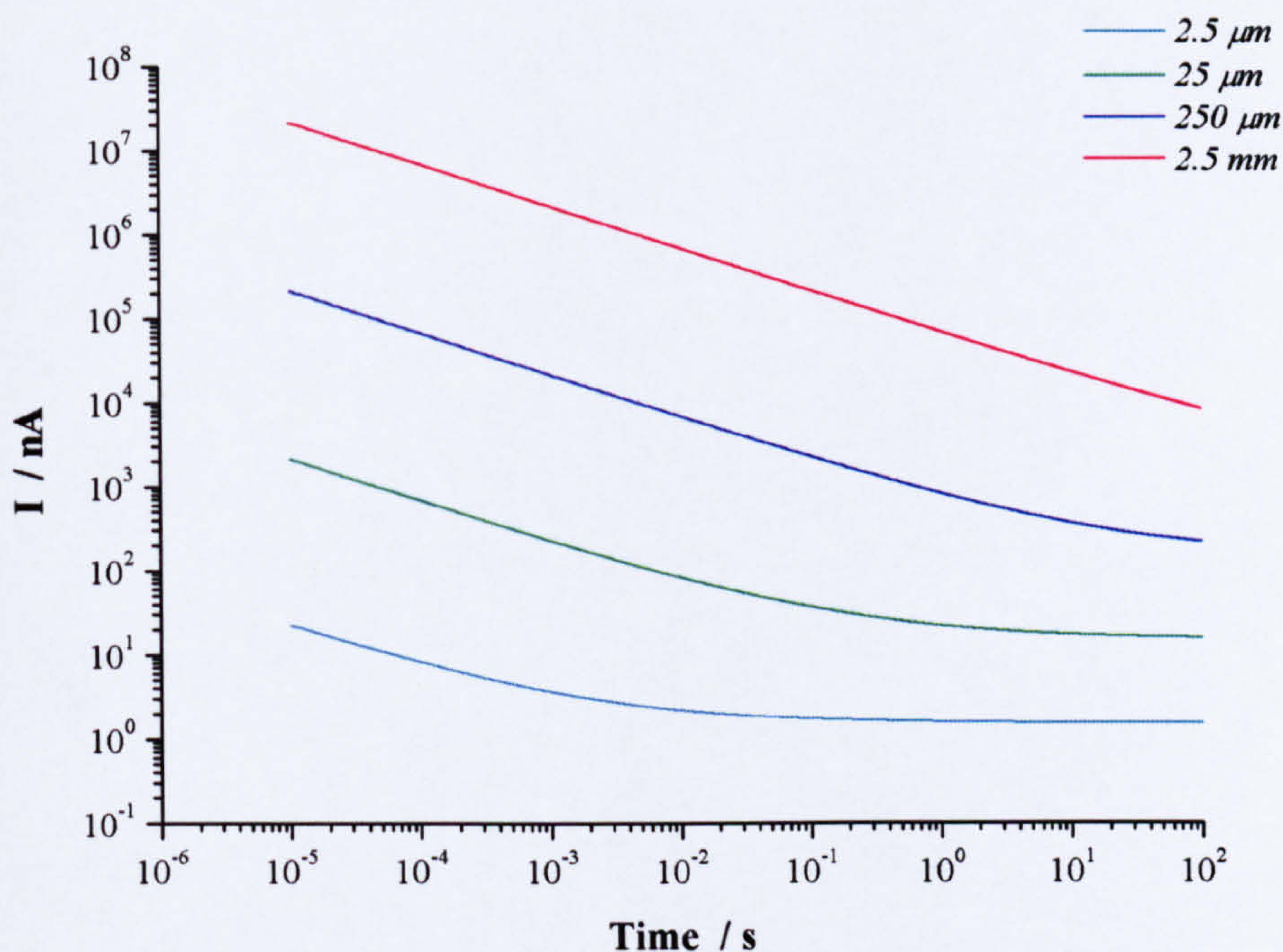

Figure 4.9 **Predicted Current-Time Evolution for Four Hemispherical Electrodes**

Equation 4.30 was employed to calculate current time profiles for four different electrode radii, assuming a concentration of 1 mM, a diffusion coefficient of 10^{-9} m^2s^{-1} and a one-electron transfer process. The electrode radius corresponding to each of the curves is given in the legend.

Equation 4.35 clearly demonstrates the importance of the diffusion layer thickness relative to the electrode radius. When $\delta >> r$, the value of the ratio tends towards one and diffusion towards the electrode surface will be fully radial, whereas the ratio will tend towards a value of zero when $\delta << r$ and, therefore, diffusion will be linear. Figure 4.10 illustrates the variation in the value of Equation 4.35 with radius and time, showing the increase in the non-

linearity of the diffusion field with decreasing electrode radius and increasing diffusion layer thickness.

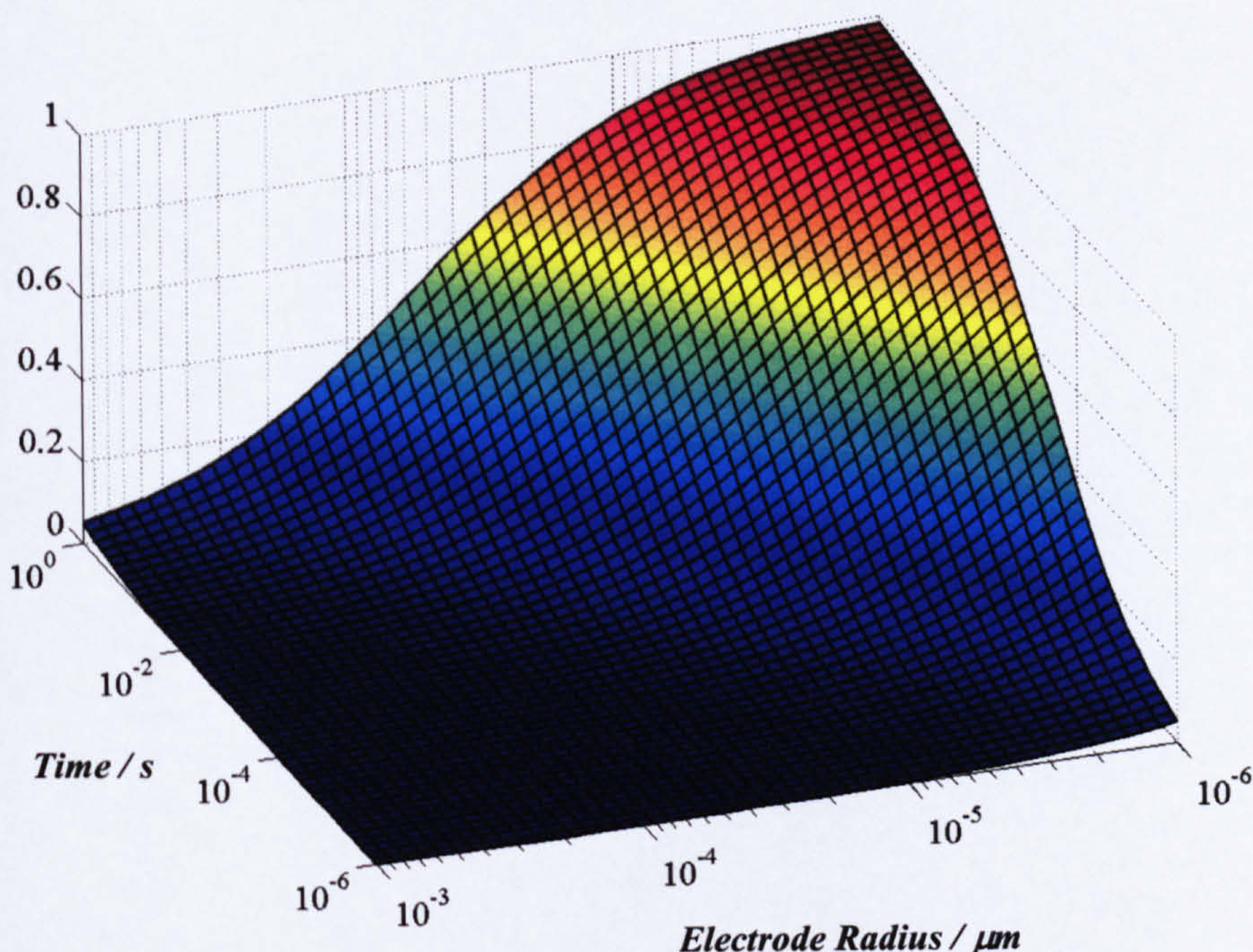

Figure 4.10 **Variation in the Extent of Radial Diffusion with Microelectrode Radius and Experimental Timescale**

Equation 4.35 was solved for a range of electrode radii and timescales, assuming a diffusion coefficient of 10^{-9} m^2s^{-1}.

Radius (μm)	1	2	5	10	20	50	100	200	500
Time (s)	0.029	0.115	0.718	2.87	11.5	71.8	287	1149	7182

Table 4.1: **Time Required for the Current to Reach a Steady State for Hemispherical Electrodes of Varying Radii**

Times were calculated using Equation 4.35, assuming that a ratio of greater than 0.95 indicated radial diffusion. A diffusion coefficient of 10^{-9} m^2s^{-1} was employed.

If a $i_r/(i_r+i_l)$ ratio of 0.95 or a larger is assumed to indicate fully radial diffusion, Table 4.1 gives the time required to reach this steady state for a range of electrode radii. It should

be mentioned here that Heinze (1993) employs a dimensionless parameter $\eta = \sqrt{Dt/r^2}$ to characterise the non-linearity of the diffusion field, with a value of 6 or larger indicating that a steady state current has been reached. This would correspond to a value of 0.914 for a hemispherical electrode and 0.931 for a disk microelectrode for Equation 4.35.

4.6.2 Linear Sweep and Cyclic Voltammetry

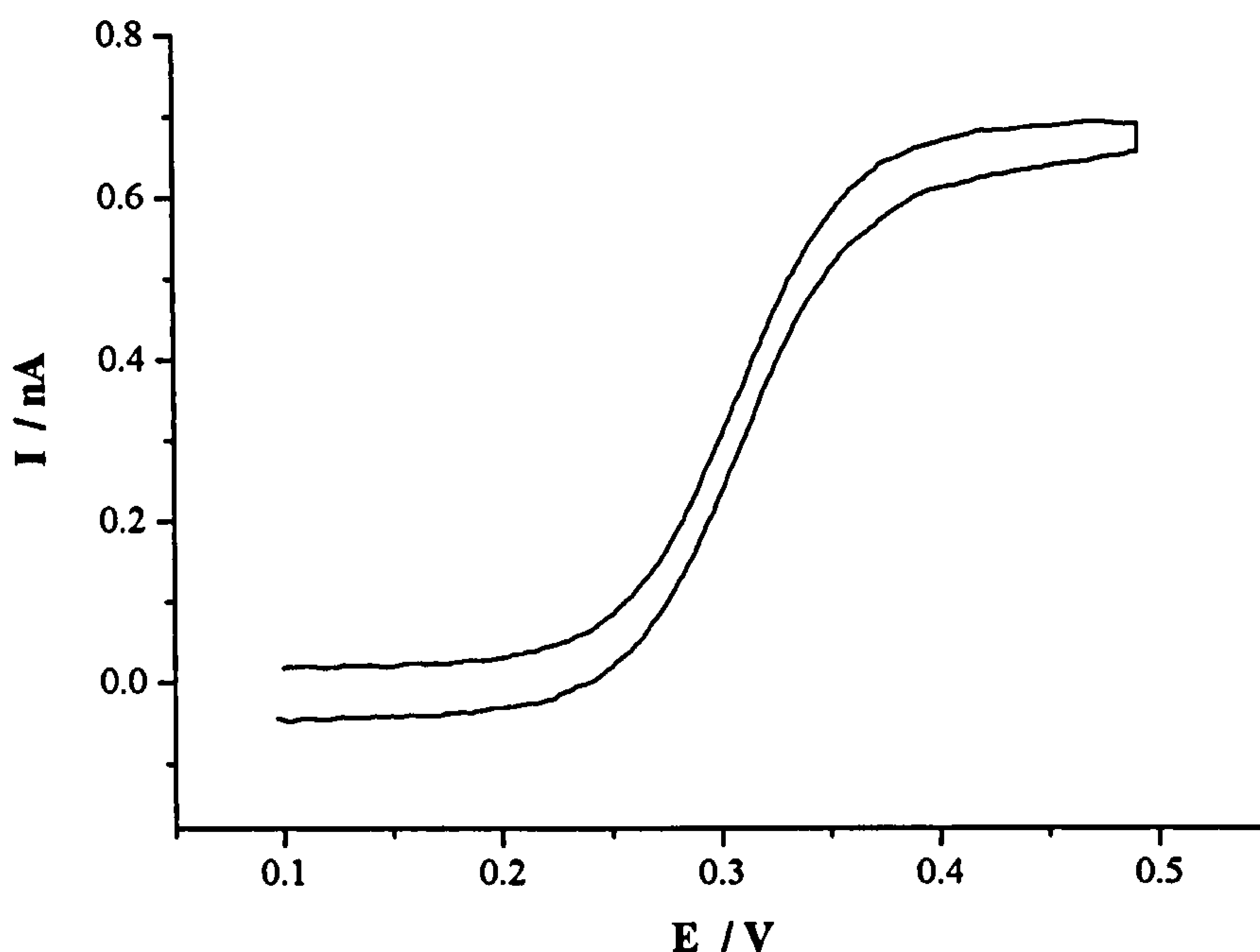

Figure 4.11 **A Cyclic Voltammogram for a Recessed Microelectrode**
Recorded in a 1 mM FMCA solution, with a 10 mM PBS supporting electrolyte, at a scan rate of 10 mV s^{-1} using a 3 μm radius gold electrode, recessed by height of 500 nm.

As discussed in Section 4.5.2, the peaked shape of a cyclic voltammogram recorded using a macroelectrode stems from the increasing diffusion layer thickness and the consequent decrease in the concentration gradient at the electrode surface. However, as in the case of chronoamperometry, this increasing diffusion layer thickness does not alter the overall rate of mass transport to a microelectrode whose diffusion field is effectively radial, as occurs at sufficiently long-time scales. Hence, a cyclic voltammogram for a microelectrode structure will be sigmoidal in shape rather than peaked (Figure 4.11), with a steady state current

equivalent to the limiting current for chronoamperometry. Furthermore, no reverse wave will be present, as the product of the forward reaction will rapidly diffuse away from the electrode surface and will therefore not be available for the backward reaction (Dayton *et al*, 1980).

Theoretical expressions describing the complete voltammetric wave cannot be obtained analytically, except when employing a spherical microelectrode, for which current-voltage characteristics are described by the incorporation of a spherical correction factor into the expression for semi-infinite linear diffusion to a planar electrode. The extent of the non-linearity of the diffusion field is again dependent upon both the characteristic radius of the electrode and the timescale of the experiment, in other words the potential scan rate. Increasingly non-linear diffusion fields can be generated by either decreasing the electrode radius or decreasing the scan rate and, the smaller the electrode radius, the faster the scan rate that may be employed whilst still achieving a sigmoidal profile.

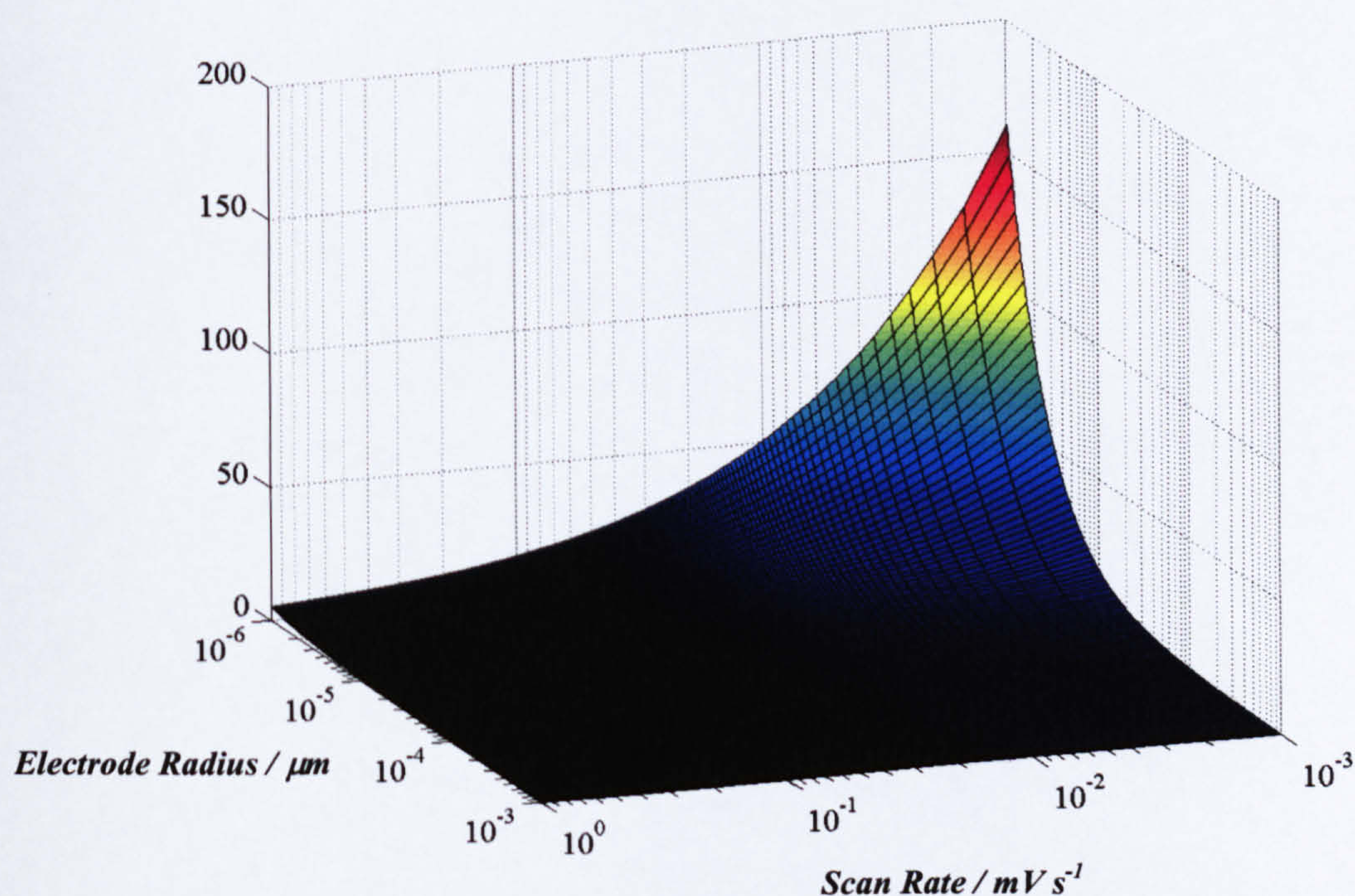

Figure 4.12 Variation in the Sphericity of the Diffusion Field at a Spherical Microelectrode

The variation in sphericity with scan rate and electrode radius was calculated using Equation 4.36. A diffusion coefficient of 10^{-9} m^2 s^{-1}, a temperature of 298 K and a one-electron process were assumed.

The sphericity variable, σ_{cf}, analogous to η for chronoamperometry, characterises the degree of radial diffusion to a spherical microelectrode, where $\sigma_{cf}>1$ indicates that a steady state current will be achieved (Heinze, 1993).

$$\sigma_{cf} = \sqrt{\frac{RDT}{nFvr^2}} \tag{4.36}$$

Figure 4.12 illustrates the variation in σ_{cf} with electrode radius and potential scan rate.

4.6.3 Faradaic-to-Capacitive Current and Signal-to-Noise Ratios

The charging current generated during a voltammetric experiment governs the minimum detectable analyte concentration, that is the concentration below which separation of the faradaic and capacitive currents is no longer feasible. As the double layer capacitance employed in Equation 4.27 varies with r^2, whilst the steady-state faradaic current for a microelectrode varies with r, the faradaic to capacitive current ratio, i_f/i_c, improves significantly as the electrode radius decreases. This increasing ratio enables the recording of voltammograms in solutions with progressively lower analyte concentrations. Faster scan rates may also be employed when using microelectrodes, as, by reducing the double layer capacitance, the minimum tolerable i_f/i_c ratio will be reached at proportionally higher scan rates for a specific concentration of analyte. Furthermore, as electrochemical noise is proportional to the electrode area, the signal-to-noise ratio (SNR) for a microelectrode is proportional to $1/r$, thus, the smaller the electrode radius, the greater the SNR.

4.7 The Electrochemical Behaviour of Microelectrode Arrays

Although microelectrodes can yield extremely large current densities, their absolute current output is relatively small. Thus, parallel arrays of microelectrodes have been employed to produce sensors, such as those mentioned in Section 1.1.2, which combine the benefits of microelectrodes with satisfactory output signals, by summing the currents from several elements.

Various microelectrode array structures have been investigated but the most common design is that illustrated in Figure 4.13. The adhesive properties and structural integrity of the

insulation layer employed in such a device are critical to its performance and longevity, particularly when the device is operating in a strong electrolytic media. As the insulation properties of traditional passivation materials have been optimised to a greater extent than their corrosion resistance, several failure mechanisms may be encountered with the most common employed materials. Faßbender *et al* (2000) examined a range of both inorganic and organic passivation layers to determine their durability and eventual failure mechanisms. When using inorganic materials, a combination of hydrolytic degradation and intrinsic stresses is thought to result in the formation of microvoids and fractures within the insulation layer, whilst swelling due to water absorption, resulting in the delamination of the insulation layer, is the foremost problem when using organic materials. Thus, the selection of an appropriate insulation material and the tailoring of its properties (such as its intrinsic stress levels, porosity and interfacial chemistry) should be carefully considered when fabricating a microelectrode array structure.

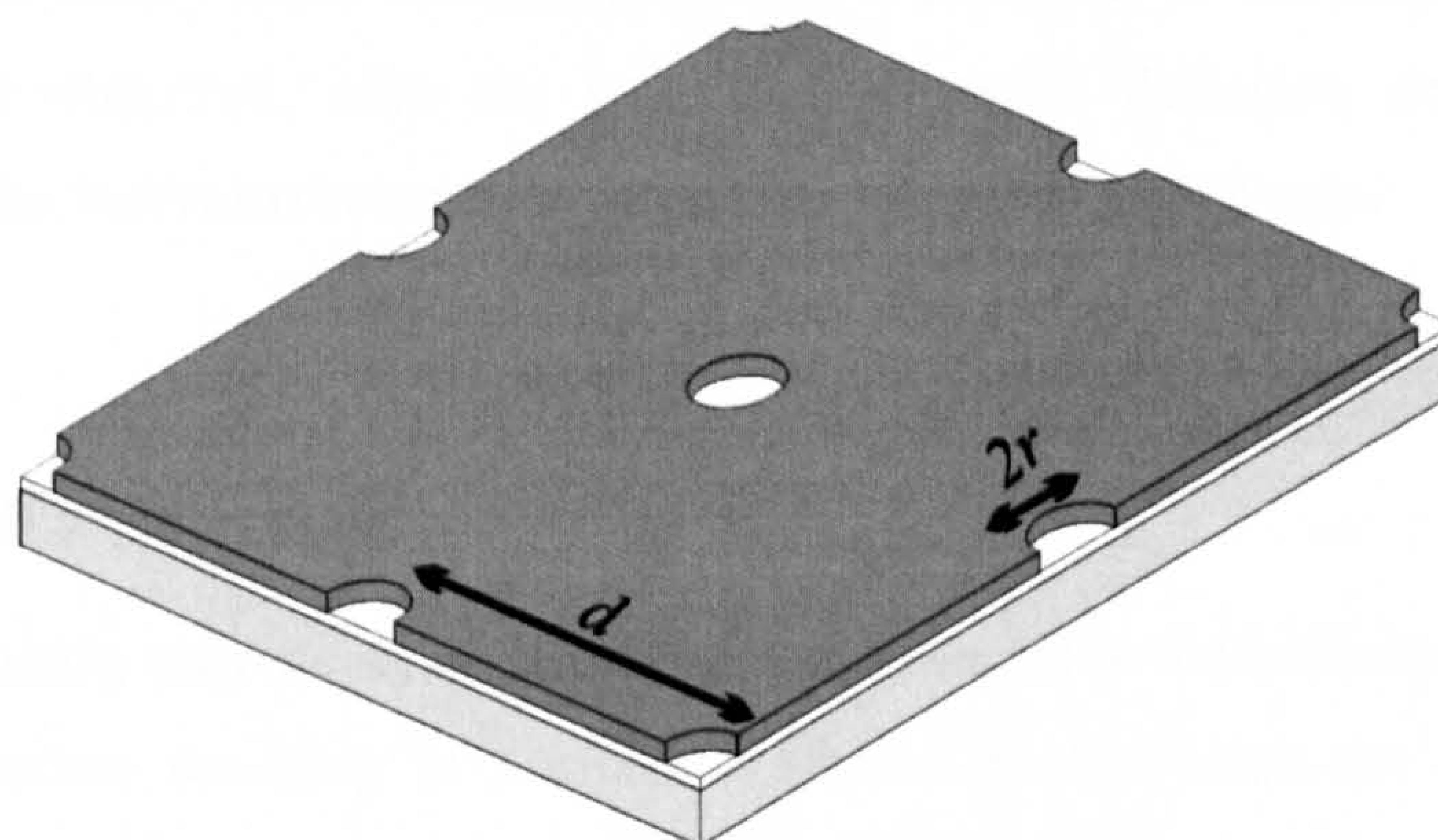

Figure 4.13 **A Parallel Array of Recessed Microelectrodes**
A thin-film metal electrode (white) is lithographically patterned on a planar substrate (light grey). An insulating material (dark grey) is then deposited over the electrode and an array of holes is subsequently etched through it to produce an array of microelectrodes.

Both microelectrodes and microelectrode arrays may be electroplated with platinum black to increase their effective surface area and therefore enhance their current output (Elliot *et al*, 1999). However, this will also increase the level of any background or charging currents and the resulting electrochemical properties of the array will be strongly influenced by the porosity of electroplated film (with the latter being highly dependent upon the microelectrode array geometry and deposition parameters, such as the charge density and the plating time).

Naturally, the geometry of a microelectrode array is fundamental in determining its electrochemical characteristics, with the centre-centre spacing, *d*, between individual microelectrodes significantly affecting the time-dependant diffusion profile of the electroactive species. For a constant individual electrode radius, variation in the relative centre-centre spacing, *d/r*, will alter the non-linearity of the diffusion profile as follows (Feeney and Kounaves, 2000; Morf, 1996; Wittstock *et al*, 1998).

4.7.1 Loosely Packed Arrays

If the centre-centre distance is sufficiently large, that is if the diffusion layer thickness is smaller than *d/2*, the microelectrode array will behave as multiple single electrodes in parallel and produce a limiting current of $i_L m$, where *m* is the number of electrodes in the array. Thus, immediately after the application of a potential to the electrode array, linear diffusion will be observed, with the transition to radial diffusion occurring at a time dependent upon the individual electrode radius, as discussed previously.

4.7.2 Intermediate Spacings

However, the spacing may be such that at longer timescales the individual diffusion fields will begin to overlap, resulting in a mixed diffusion profile, with the degree of merging dependant upon both the spacing and time-scale of the experiment. For this intermediate case, diffusion is assumed to be radial close to the surface of the microelectrodes but planar as it extends further outwards. It should also be noted here that, although deep recesses reduce the rate of mass transport to the electrode surface (Zhu *et al*, 1998), it has been shown that the overlap between the diffusion fields of the individual electrodes will occur to a lesser degree for recessed electrodes than for planar electrodes, with the initial linear diffusion period being prolonged by a time dependant upon the height of the recesses (Wittstock *et al*, 1998).

4.7.3 Densely Packed Arrays

As the electrode spacing is further decreased, such that the diffusion layer thickness becomes significantly larger than *d/2*, the diffusion fields of the individual electrodes will totally overlap and diffusion to the electrode array will become essentially linear. Thus, the

favourable characteristics of microelectrodes, such as the achievement of steady-state currents, will not be obtained and the current profile observed will be described by the expressions for macroelectrodes given previously. However, the current generated (which will obviously increase as the interelectrode spacing is decreased) will be proportional to the geometric area of the array, A_{geom}, that is the sum of both the active and the inactive area, whilst noise and capacitive currents will proportional to the active area, A_{act}, alone. Therefore, very high SNRs and i_f/i_c ratios may be obtained, with an increase of A_{geom}/A_{act} over the value for a conventional electrode with the same geometric area.

4.7.4 Recent Investigations Concerning the Behaviour of Arrays of Electrodes

Several papers discussing the theoretical behaviour of microelectrode arrays have been published (Morf and de Rooij, 1997; Morf, 1997; Lee *et al*, 2001, Beriet *et al*, 2000), along with a small number of experimental studies (including those by Le Drogoff *et al* (2001) and Kudera *et al* (2001) who examined the behaviour of mercury-plated microband arrays and gold microdisk arrays respectively). However, an electrochemical investigation detailing the systematic variation of *r* and *d/r* could not found in the literature.

In order to extend the existing literature, the electrochemical behaviour of a system of microfabricated electrode arrays (consisting of sets of arrays with either varying individual electrode radii or varying *d/r* ratios, both with and without electroplated platinum black) will be described within this thesis (Chapter 5). Such a study should be of value when designing an analytical sensor, particularly with regard to the optimisation of the current response and the SNR of the sensor.

In recent years, various groups have reported research into the fabrication and characterisation of nanoelectrode ensembles. Menon and Martin (1995) presented a template method for the fabrication of such ensembles, where a gold electroless deposition process was employed to fill the pores within a nanoporous filtration membrane, thereby producing an ensemble of nanoelectrodes with an individual electrode diameter as small as 10 nm. Nanoelectrode ensembles have also been fabricated by incorporating redox-molecule based nanoelectrode sites into a passivating film that covers an underlying electrode (Creagar and Radford, 2001). However, the only literature found that reported an ordered nanoelectrode array was from the group of Irina Kleps (Kleps *et al*, 2002), who described the fabrication of a pyramidal nanostructured device, where a sequence of standard microfabrication processes was employed to produce tip electrodes with a diameter in the range of 10-250 nm.

4.8 Finite Element Simulations of Microelectrode Array Diffusion Fields

To further investigate the behaviour of individual microelectrodes and microelectrode arrays, the finite element solver FlexPDE was employed to simulate the diffusion fields that develop at a range of electrode geometries after the application of a diffusion-limiting potential step (as discussed in Section 4.5.1).

4.8.1 Simulation Methods

To represent the microelectrode structures it was necessary to employ a three-dimensional model, which entailed extruding the features defined on the $Z=0$ plane. As discussed in Section 4.5.1, the diffusion profile of a non-steady state system is described by Fick's second law (Equation 4.19). The initial condition and the boundary conditions noted previously (Equations 4.20 to 4.22) were adapted to describe the structures being simulated. The uppermost surface of the solution space, which was extruded to a height greater than the estimated diffusion layer thickness, was assigned a fixed value equal to the bulk concentration (1 mM). A zero flux condition was applied to the extruded sides of the solution space and the conditions assigned to the lowest surface were dependant upon the geometry of the system being simulated.

To simulate semi-infinite linear diffusion, a fixed value boundary condition was applied to the entire lower surface, whilst for a disc microelectrode the condition was applied to a circular segment of the surface. In the case of the latter, a zero flux boundary condition was applied to the remainder of the lower surface and no conditions were assigned to the extruded walls of the circular segment, as the electroactive species should be able to diffuse freely throughout the solution space. As an instantaneous change in the value of the surface concentration generated strong transient signals in the system, the fixed value boundary condition was specified as a linear ramp which fell from 1 mM to zero over a period of 1 μs.

As well as increasing the accuracy of the solution by modifying both the number of mesh rows in each dimension and the error limit value, intermediate surfaces with no boundary conditions were employed to force a finer mesh in regions of instability. To assess the reliability of the results, time-dependant concentrations obtained when using the linear diffusion model were compared to the values predicted by the theoretical concentration profile, which can be expressed as (Bard and Faulkner, 2001):

$$C(x,t) = C^{*} erf\left(\frac{x}{2\sqrt{Dt}}\right) \tag{4.37}$$

where x is the distance from the electrode surface.

4.8.2 Results

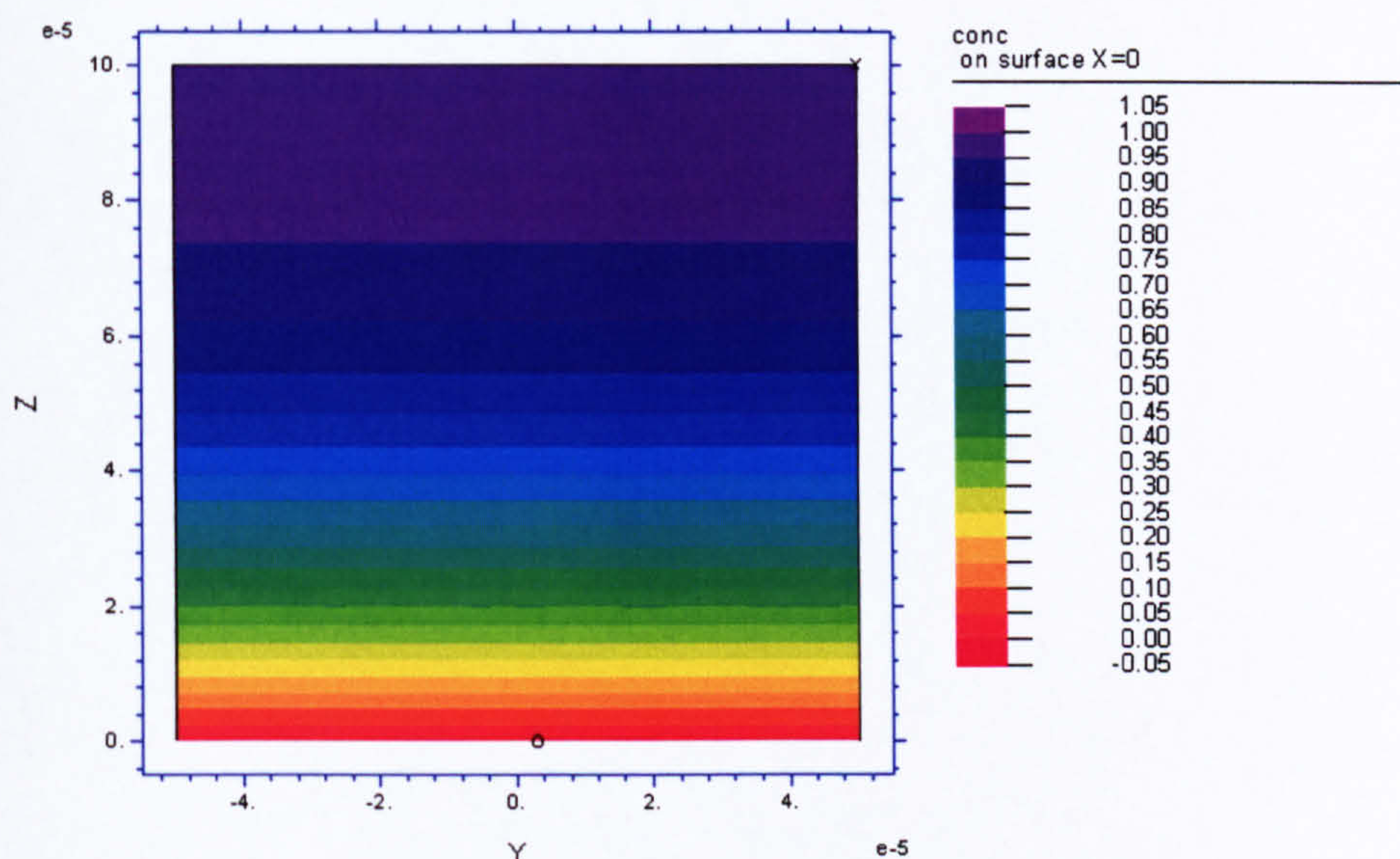

Figure 4.14 **Linear Diffusion to a Horizontal Plane**

A cross section of the diffusion field (at X=0) obtained when simulating for a period of 1 s using a diffusion coefficient of 7.2^{-10} m^2s^{-1} and a bulk concentration of 1 mM. The axis scales are in metres.

Figure 4.14 shows a cross section of the diffusion field, obtained 1 s after the application of a potential step, when simulating linear diffusion to a horizontal plane. Clearly, the simulated diffusion profile has a linear structure. The time-dependant variation of the concentrations at 10 nm, 100 nm and 1 μm above the electrode surface is displayed in Figure 4.15, along with the theoretical concentration profiles calculated for these heights using Equation 4.37. It can be seen that the theoretical and the simulated concentration-time profiles are comparable.

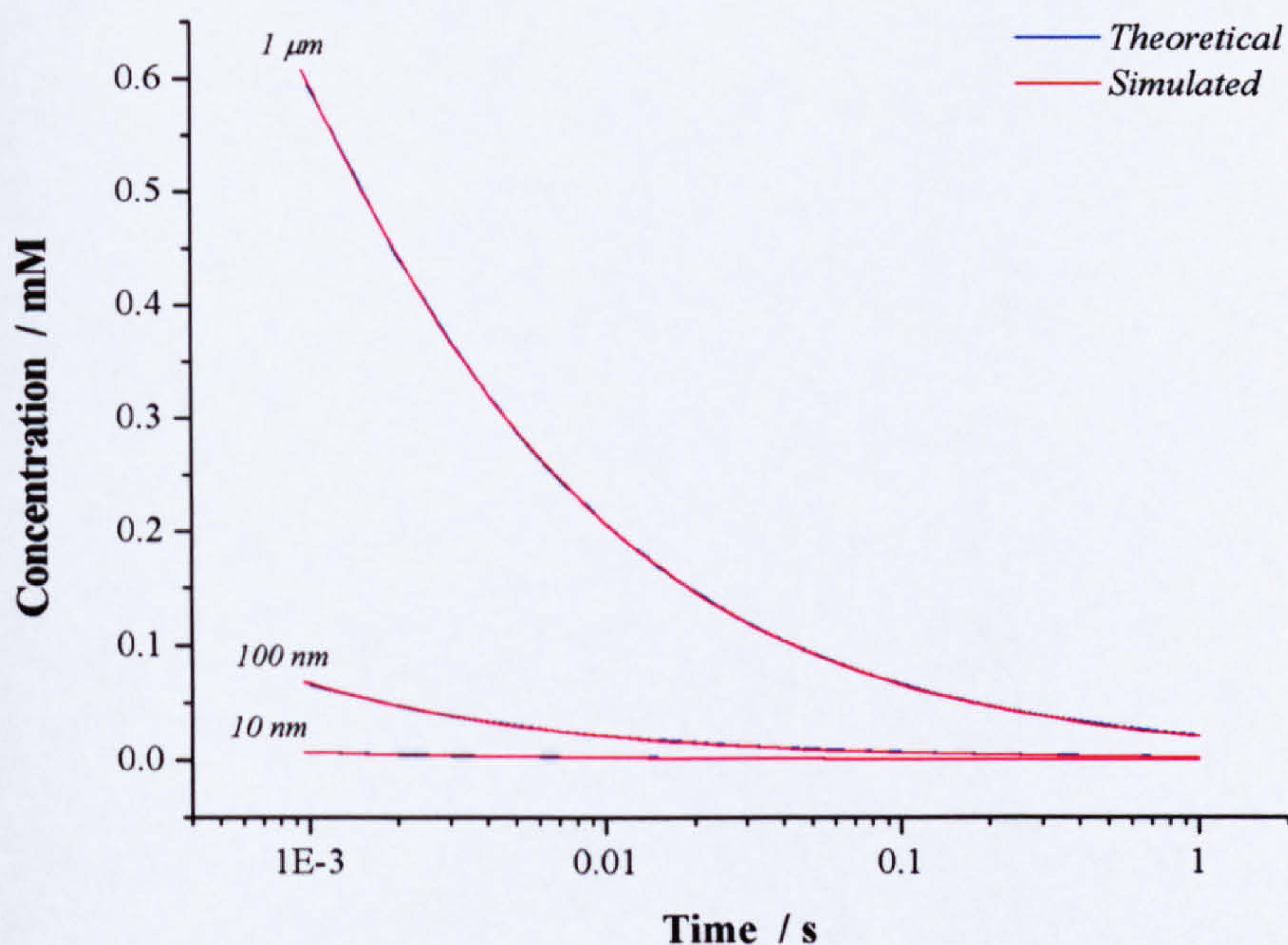

Figure 4.15 **Concentration-Time Profiles at Various Heights Above the Surface of a Planar Macroelectrode**

The theoretical profiles calculated using Equation 4.37 and the results from a FlexPDE simulation are shown. Both used a diffusion coefficient of 7.2^{-10} m^2s^{-1} and a bulk concentration of 1 mM.

As discussed in Section 4.6.1.1, the characteristics of the diffusion field at the surface of a microelectrode vary with time. Figure 4.16 shows a cross-section of a simulated diffusion field, for a 2.5 μm radius electrode, at 0.1 ms, 10 ms and 1 s after the application of a potential step. It illustrates how the diffusion field at a microelectrode surface evolves from being largely linear in nature to being effectively radial. It should be noted that some instability was observed in the returned values during the early stages of the simulations (the overshoot seen around the edges of Figure 4.16a is a consequence of this). However, when simulating the diffusion fields for times greater than 1 ms, these instabilities vanished and the results obtained were comparable with theory. If an investigation is undertaken into the behaviour of diffusion fields at short times after the application of the potential, a smaller error limit value and a greater number of mesh rows should be employed (although to achieve reasonable computation times a more powerful computer would be required).

a.

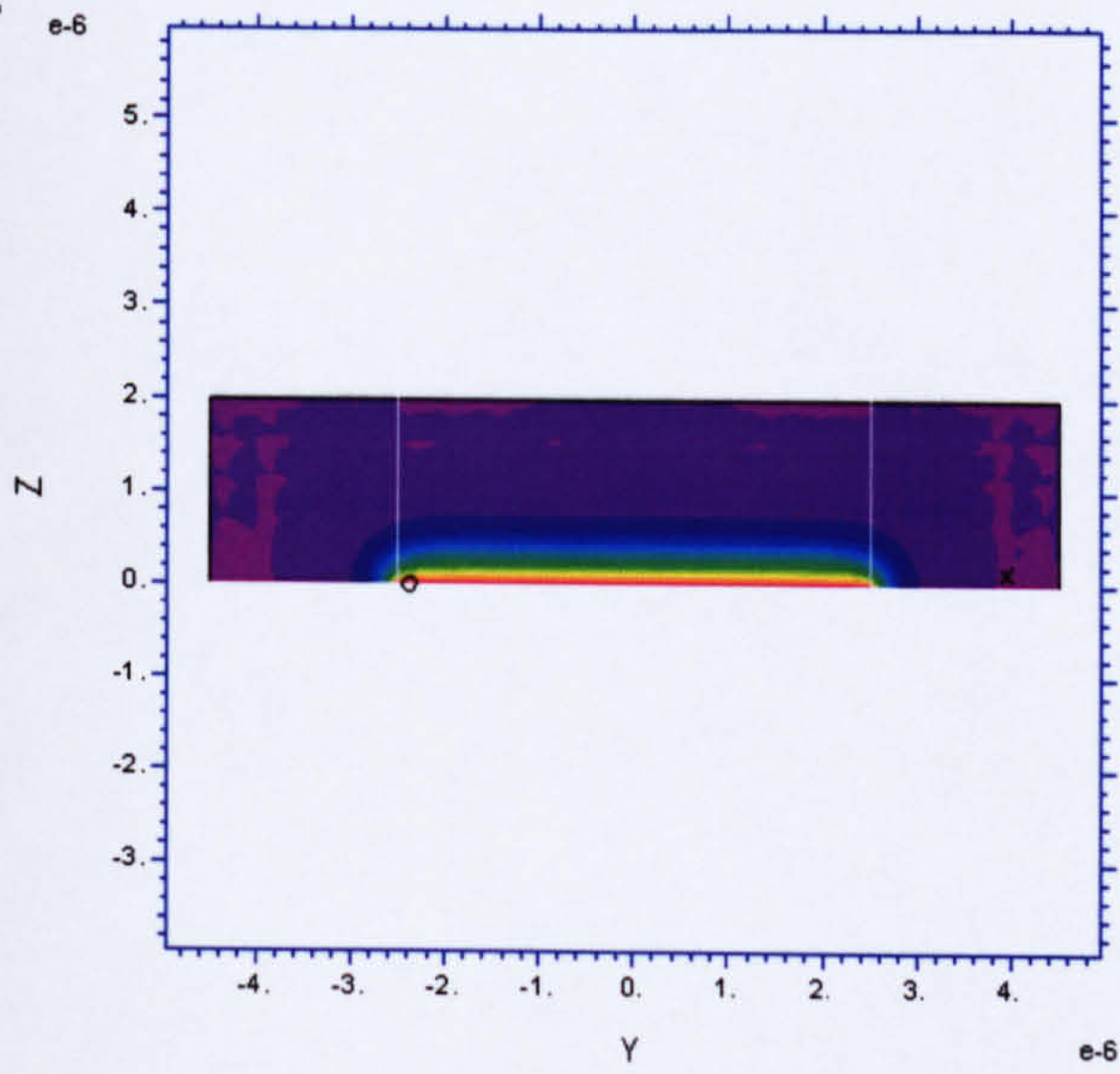

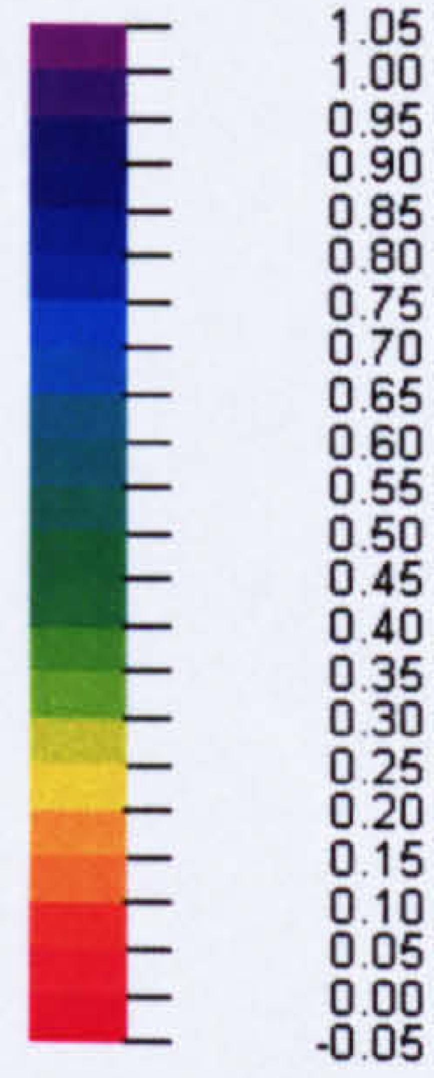

b.

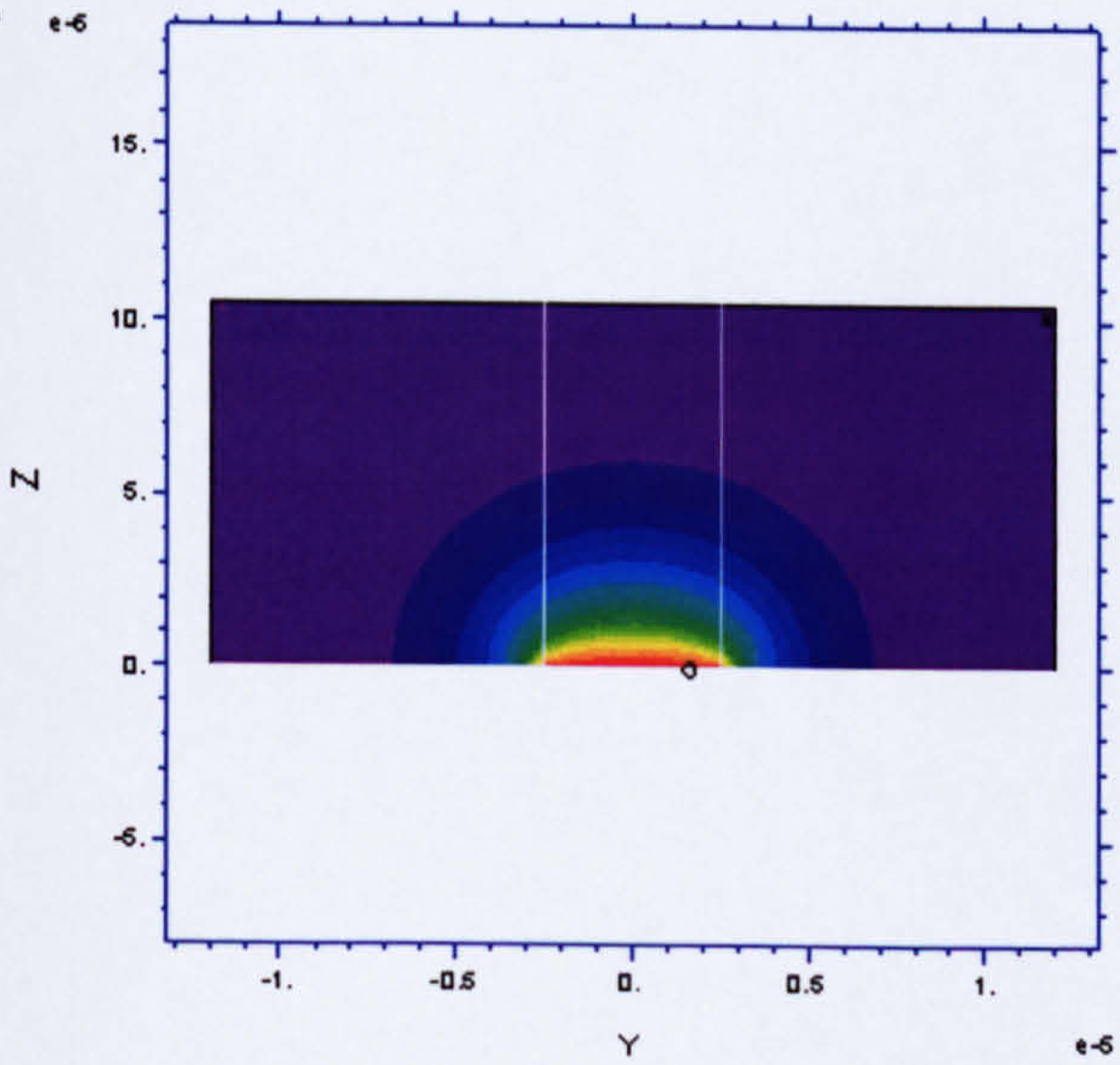

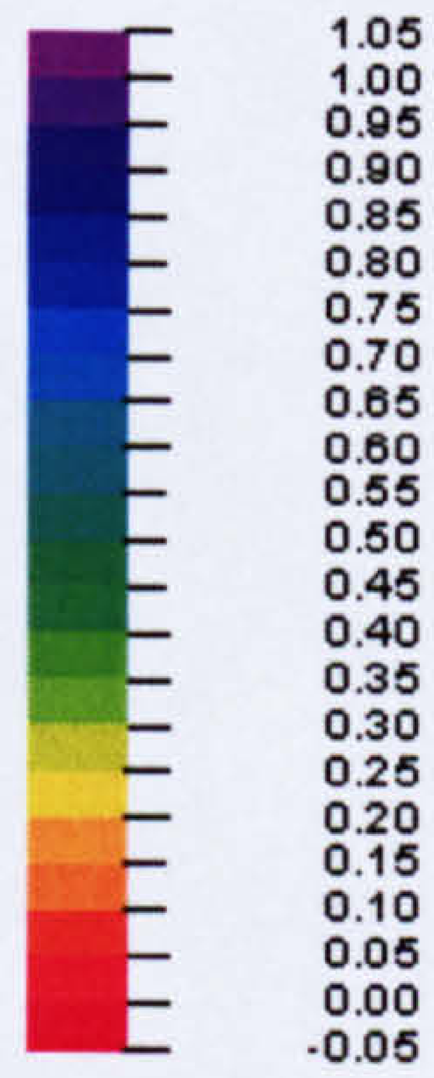

c.

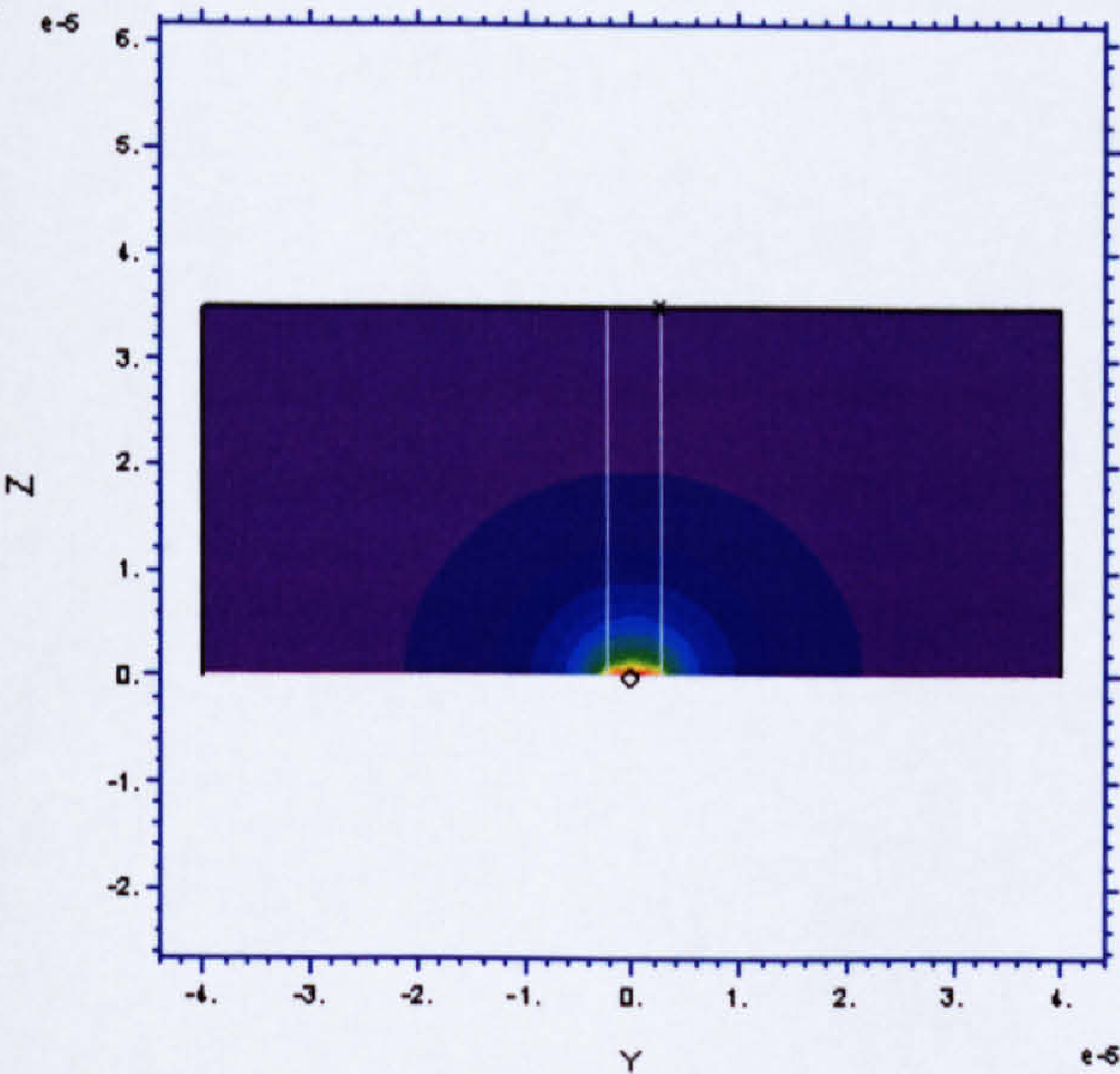

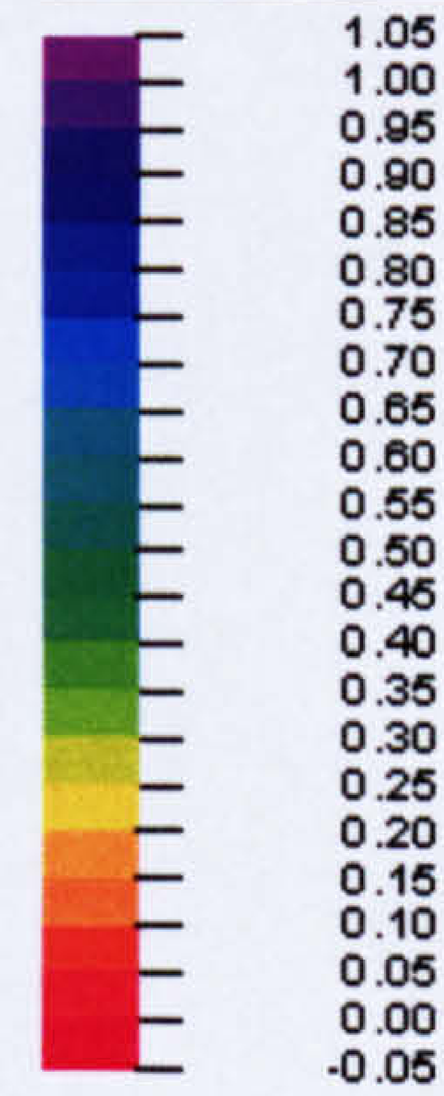

Figure 4.16 **A Cross-Section of the Diffusion Field at the Surface of a Microelectrode at Various Times**

(Previous page) The simulated diffusion field at a 2.5 μm radius electrode are displayed at 0.1 ms (a), 10 ms (b) and 1s (c) after the application of a potential step. Note that the Y and Z scales (in m) vary from graph to graph, whilst the white lines extend outwards from the edges of microelectrode in each cross-section. A diffusion coefficient of 7.2^{-10} m^2 s^{-1} and a bulk concentration of 1 mM were employed.

Diffusion fields were also simulated for a series of microelectrode arrays which had been studied experimentally (see Chapter 5) and the results from these simulations are presented in Figure 4.17. The diffusion field obtained 4 s after the application of a potential step for an array of 25 μm radius electrodes with a centre-centre spacing of 250 μm is shown in Figure 4.17a. It can be seen that the diffusion field for each microelectrode is independent and essentially radial. In Figures 4.17b to 4.17e, the ratio of the radius to the inter-electrode spacing is maintained at a value of 10, but the electrode radius is progressively decreased. For a 12.5 μm electrode radius (Figure 4.17b), the simulated diffusion fields begin to overlap, although the characteristics of the diffusion field around each individual electrode remains largely radial. As the electrode radius is decreased further, the diffusion fields merge increasingly and their radial component is progressively reduced (Figures 4.17c and 4.17d). When the initial radius is decreased by a factor of 10 to 2.5 μm, the diffusion profile obtained was primarily linear. These results are in agreement with the predicted behaviour of microelectrode arrays (Section 4.7) and, as will be seen in Chapter 5, they are also in agreement with experimental findings.

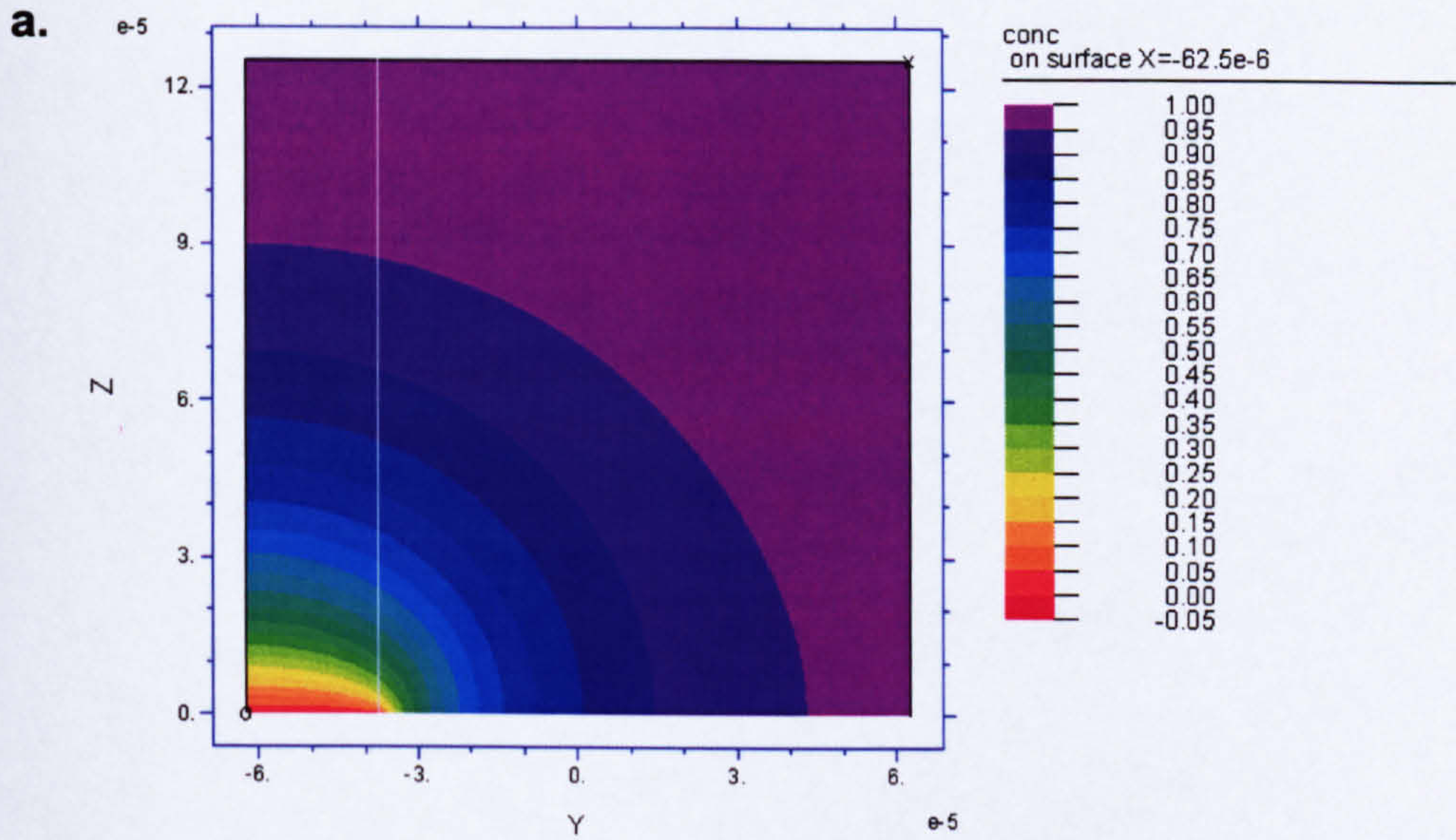
a.
conc
on surface X=-62.5e-6
1.00
0.95
0.90
0.85
0.80
0.75
0.70
0.65
0.60
0.55
0.50
0.45
0.40
0.35
0.30
0.25
0.20
0.15
0.10
0.05
0.00
-0.05
Z
Y
e-5

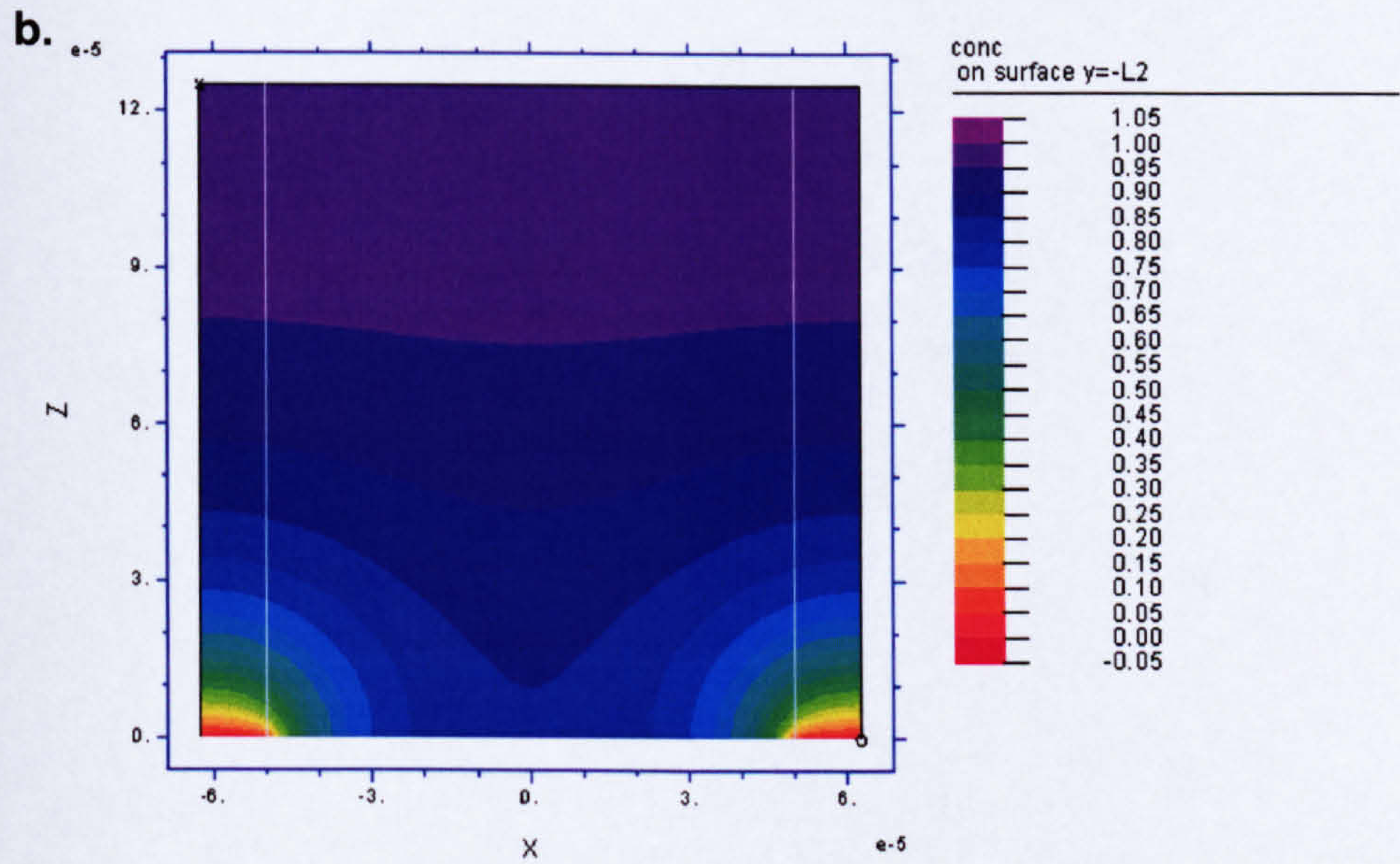
b.
conc
on surface y=-L2
1.05
1.00
0.95
0.90
0.85
0.80
0.75
0.70
0.65
0.60
0.55
0.50
0.45
0.40
0.35
0.30
0.25
0.20
0.15
0.10
0.05
0.00
-0.05
Z
X
e-5

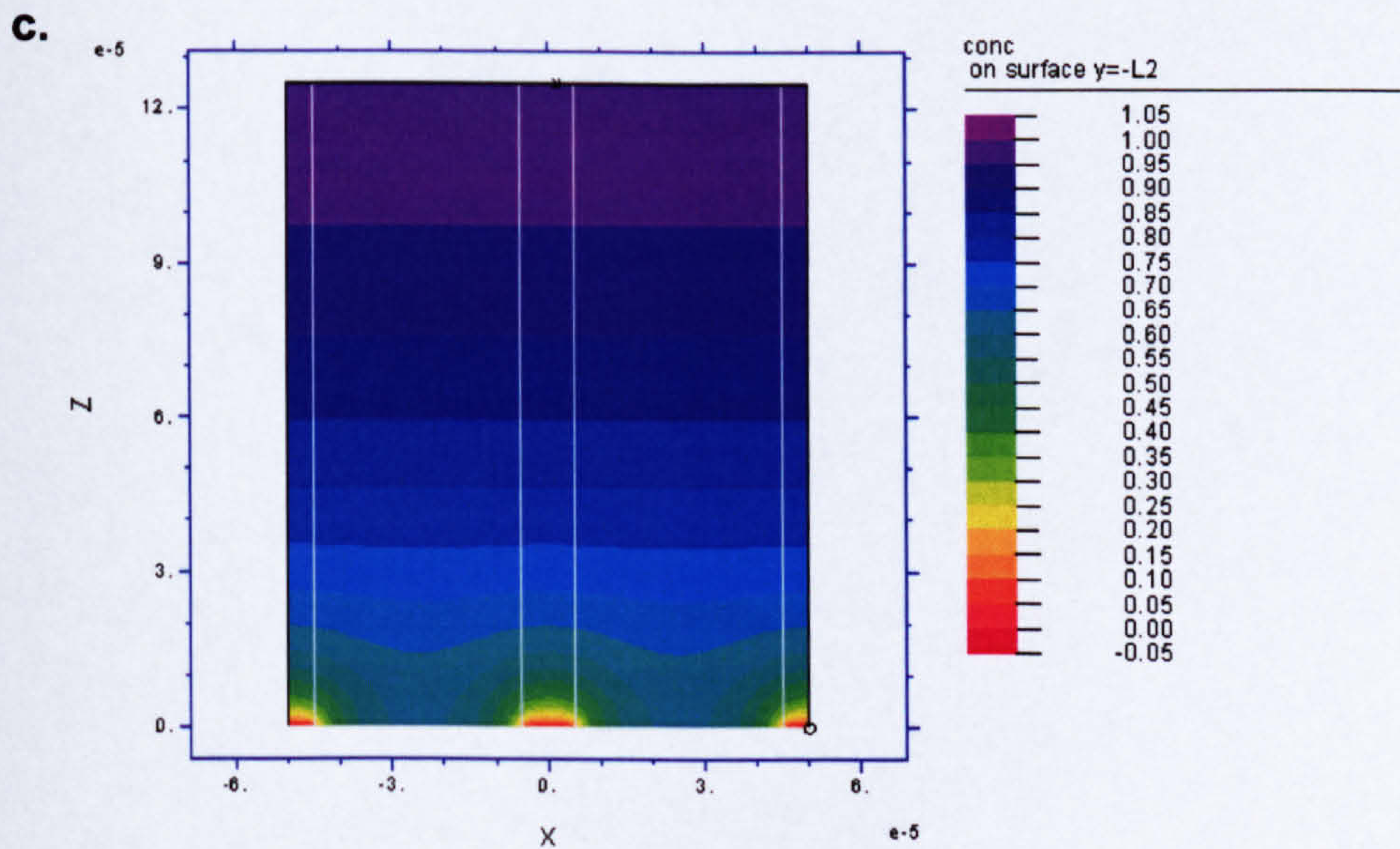
c.
conc
on surface y=-L2
1.05
1.00
0.95
0.90
0.85
0.80
0.75
0.70
0.65
0.60
0.55
0.50
0.45
0.40
0.35
0.30
0.25
0.20
0.15
0.10
0.05
0.00
-0.05
Z
X
e-5

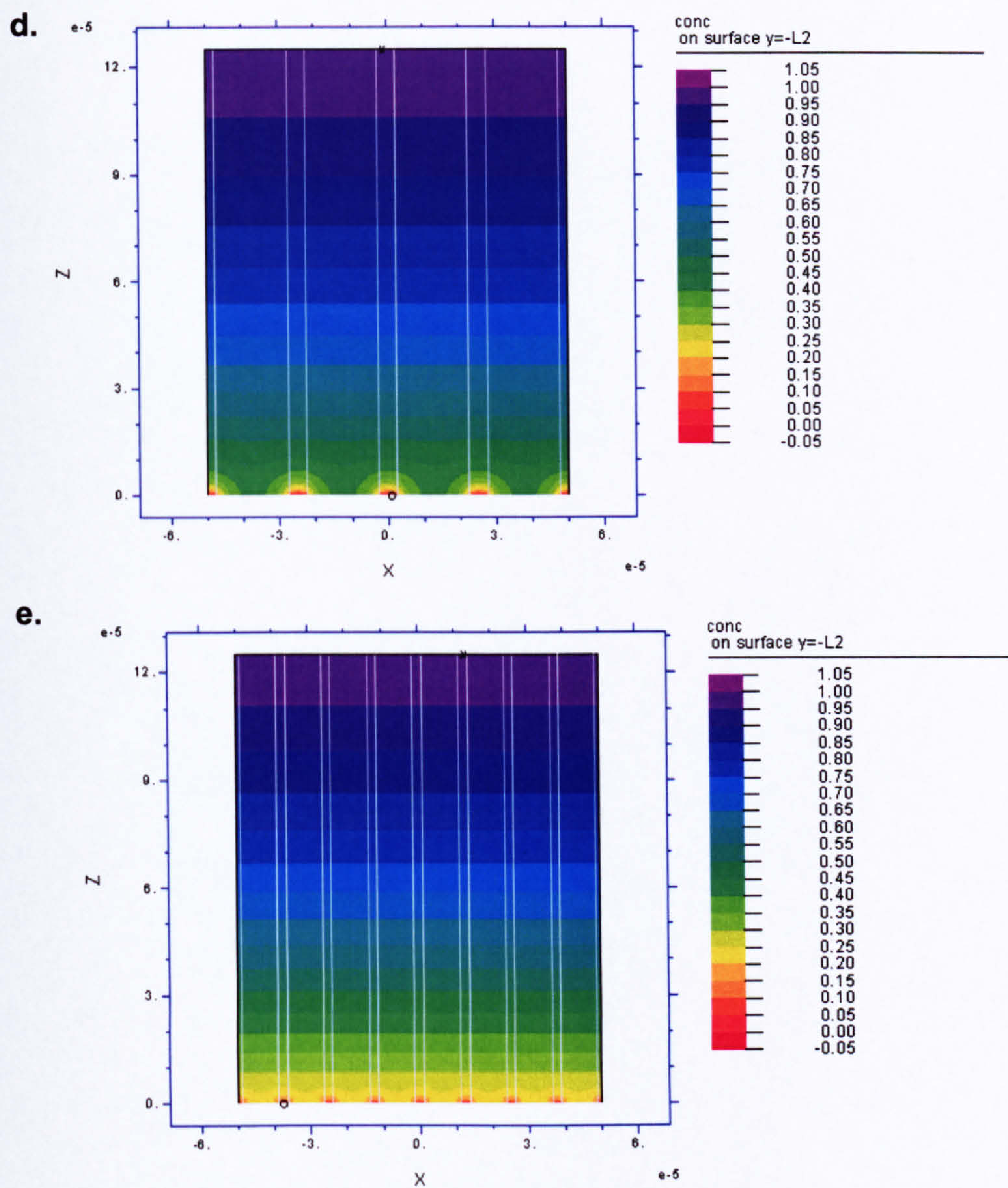

Figure 4.17 Cross-Sectional Profiles of the Diffusion Field at the Surface of a Range of Microelectrode Arrays

Diffusion fields were simulated for a period of 4 s, assuming a diffusion coefficient of 7.2^{-10} m^2 s^{-1} and a bulk concentration of 1 mM. The resulting diffusion fields are symmetrical about the left and right boundaries and the white lines indicate an electrode edge. The axis scales are in metres and remain constant from one graph to the next. The individual electrode radius decreases from 25 μm to 2.5 μm.

4.9 Conclusion

Electrochemical microsensors are increasingly being employed for analytical investigations due their high sensitivity and the wide range of applications for which they are suitable. However, the behaviour of an electrochemical system is complex and an understanding of its performance is important for both experimental design and the interpretation of results. Significantly, microelectrode structures exhibit radically different behaviour to conventional macroelectrodes, with steady-state currents, large current densities and high i_f/i_c ratios being readily observed.

Recently, many electroanaytical sensors have employed arrays of microelectrodes; the behaviour of which is dependent upon the geometric area of the array, the interelectrode spacing, the timescale of the experiment and the individual electrode radius. Finite element simulations may be employed to explore the variation in microelectrode array behaviour as these parameters are modified. The investigations of the diffusion profiles presented in this chapter demonstrate that finite element simulations are a useful tool for furthering the understanding of time-varying diffusion fields at the surface of microelectrodes and microelectrode arrays.

CHAPTER 5

THE ELECTROCHEMICAL CHARACTERISATION OF MICRO-ELECTRODE AND NANOELECTRODE ARRAYS

In this chapter, the results from an experimental investigation into the behaviour of a system of microelectrode arrays are presented, the relevant theory having been discussed in Chapter 4. The effects of varying the microelectrode array geometry and the electrode porosity are discussed, as is the optimisation of the geometry for electroanalytical sensor applications. Furthermore, the fabrication and electrochemical characterisation of arrays of nanoelectrode with a well defined geometry is described, as the favourable characteristics of microelectrode arrays should be enhanced by further decreasing the size of the individual electrodes.

5.1 Microfabrication and Experimental Methods

5.1.1 Fabrication of Micro- and Nanoelectrode Arrays

The generic structure of the micro- and nanoelectrode arrays investigated has been described in Figure 4.13. These parallel arrays of electrodes were fabricated by various lithographic and reactive-ion etching (RIE) techniques, protocols for which were detailed in Chapter 3. When fabricating a series of microelectrode arrays, a 380 μm thick Si(100) wafer, coated on both sides with 200 nm silicon nitride, was employed as the substrate. A number of 1 mm^2 working electrodes with a connecting wire and a bonding pad were patterned by either lifting-off (Section 3.3.1.4.1) or wet-etching (Section 3.3.1.4.2) a 10 nm Ti, 10 nm Pd, 100 nm Au film that was deposited by electron beam evaporation (with the Ti functioning as an adhesive layer (Vogt *et al*, 1994) and the Pd preventing Ti diffusion along the Au grain boundaries (Sharp, 1979)). After oxygen cleaning the surface in a barrel asher (Section 3.3.1.5.1), a SM1040 SU8 or SiN insulation layer was deposited over the entire wafer. This was then patterned to produce an array of micro-holes over the cathode and to expose the bonding pad. SiN was deposited by PECVD and patterned by RIE (Section 3.3.1.5.3), whilst

SM1040 SU8 was patterned as described in Section 3.3.1.5.2. Finally, the wafer was diced, connecting wires were soldered to the individual electrode arrays and the solder joints were insulated with a silicone rubber. Nanoelectrode arrays were fabricated similarly, the only difference being that the insulation layer was created from a UVIII or PMMA electron-beam resist, either by EBL (Section 3.3.1.5.1) or NIL (Section 3.3.2.2).

5.1.1.1 Micro- and Nano-Electrode Array Geometries

	Individual Electrode Radius *(μm)*	**Number Of Electrodes In Array**	**Total Area Of Array** *(10^{-9} m^2)*
Set A Micro-Electrode Arrays	50	4	31.4
	25	9	17.7
	12.5	25	12.3
	5	121	9.50
	2.5	441	8.66
	1.25	1681	8.25
Nano-Electrode Arrays	0.5	10201	8.01
	0.25	40401	7.93
	0.125	160801	7.89
	0.05	1002001	7.87
Set B Micro-Electrode Arrays	***d/r* Ratio**		
	150	9	0.177
	30	121	2.38
	12	676	13.3
	6	2601	51.1

Table 5.1 Geometries of the Micro- and Nanoelectrode Arrays Investigated

Two sets of rectangular arrays of microdisc electrodes were investigated, one with a constant relative centre-centre spacing (Set A) and another with a constant individual electrode radius (Set B). In the case of Set A, the centre-centre distance from one corner electrode to the next, l, was 500 μm and the centre-centre distance between an individual electrode and its row and column neighbours, d, was $10r$, where r is the electrode radius. Thus, the arrays had a

constant relative centre-centre spacing, *d/r*, of 10. For Set B, *l* was 750 μm and *r* was 2.5 μm. The set of nanoelectrode arrays simply continued the series of the Set A microelectrode arrays. All the electrode array geometries that were investigated are detailed in Table 5.1.

5.1.2 Experimental Methods

The apparatus described in Section 3.4.1 was employed for all electrochemical recordings, as were a commercial Ag|AgCl reference electrode and a coiled platinum counter electrode. Cyclic voltammograms were recorded in a 1 mM ferrocene monocarboxylic acid (FMCA), 10 mM phosphate buffered saline (PBS) solution and linear voltammograms were recorded in air-saturated water (produced by pumping air through the water before the start of the recording and over the surface of the water during the recording). Chronoamperometric traces were recorded in water that had been equilibrated to room temperature and oxygen level for several hours. Gold electrode arrays were polarised for 10 minutes and platinum black electrode arrays for 15 minutes prior to measuring time-averaged currents. Background traces were recorded in either 10 mM PBS, for experiments using an FMCA solution, or in a saturated sodium sulphite solution[1], for experiments involving dissolved oxygen measurements.

5.2 Microfabrication & Experimental Considerations

5.2.1 Thin-film Insulation Layers

As discussed in Section 4.7, the properties of the insulation layer are critical to the performance and longevity of a microelectrode array (Schmitt *et al*, 1999; Feeney and Kounaves, 2000). In this work, SU8 photoepoxy, PECVD SiN, photoresist and electron beam resist were all employed with varying degrees of success.

5.2.1.1 SU8

In order to avoid the use of CVD materials, the insulation layer was initially created from SM1040, an SU8 formulation that can be spun to produce films with a minimum thickness of approximately 1μm. However, the adhesion of SM1040 to evaporated gold proved to be

extremely poor and the SU8 layer would frequently become detached from the surface. Therefore, the evaporated gold surface was coated with a thiol surface-assembled monolayer (SAM) prior to the deposition of the SM1040 layer. Adhesion was significantly improved by use of 2-mercaptoethanol, as the thiol group binds strongly to the gold surface whilst the ethanol tail interacts with the SM1040 epoxy groups.

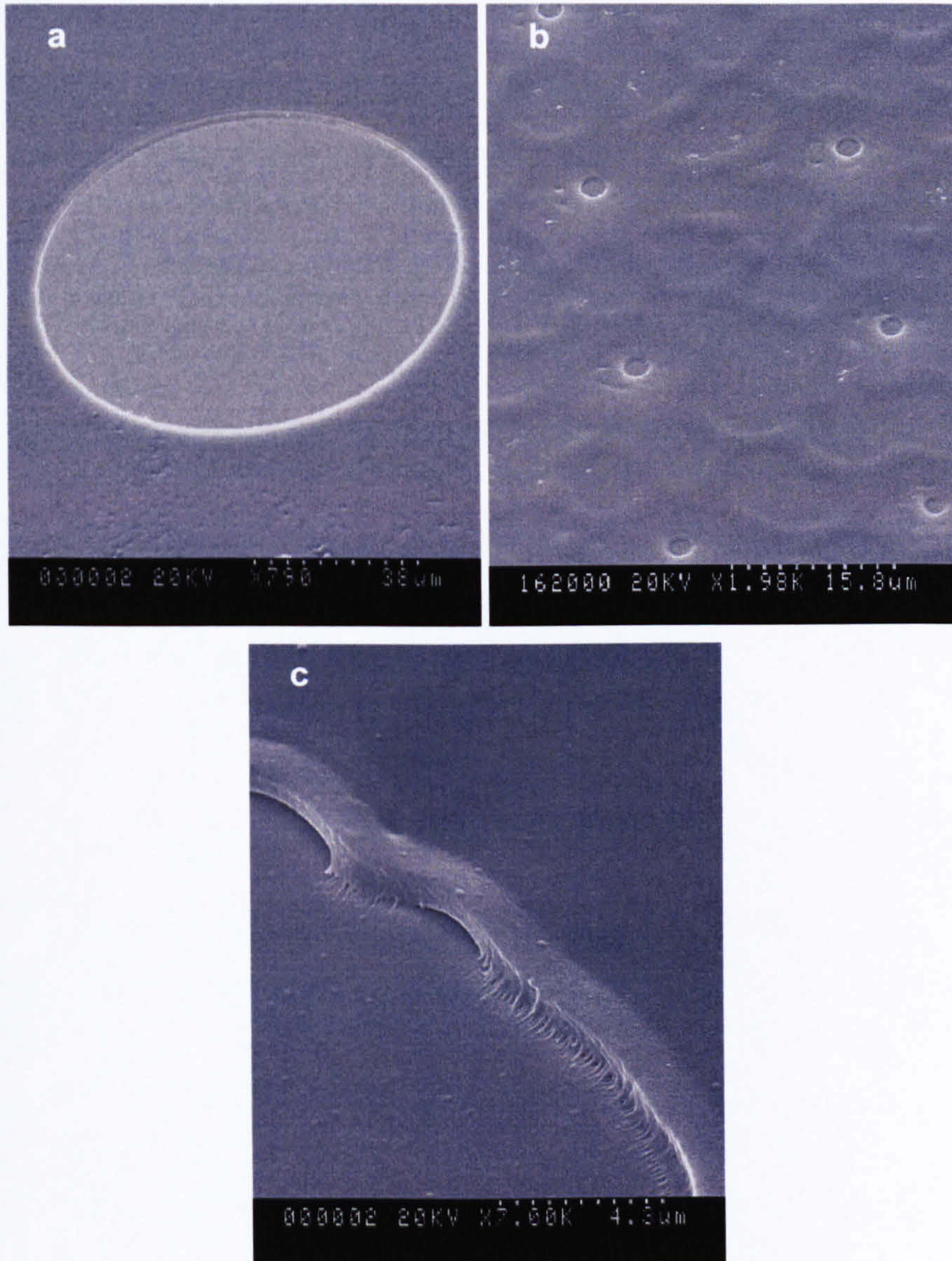

Figure 5.1 **SU8 Microelectrode Array Insulation Layers**

a: A successfully fabricated SM1040 insulation layer. b: An overdeveloped sample with a weakly adhered insulation layer. c:

---

[1] Sodium sulphite is an effective oxygen scavenger.

The edge of a microhole starting to raise up from the electrode surface.

However, although satisfactory devices could be produced by employing a SAM (Figure 5.1a), the results were not particularly reproducible. This was partly attributable to the precise timing required when developing a sample, as the optimised process involved pipetting a small drop of the developer solution onto the sample, immediately immersing it in a 1:1 developer-IPA solution for 5 s and then rinsing it in an IPA bath. Poor adhesion (Fig 5.1b) generally resulted from any over-development of a sample, either by pipetting on too much developer, by not immediately immersing it into the developer-IPA solution or by leaving it immersed for any longer than 5 s.

Furthermore, the edges of the microholes occasionally rose up from the substrate surface (Fig 5.1c), even when the overall adhesion of the SU8 layer appeared satisfactory. This was generally exacerbated by performing electrochemical experiments in solution and by rinsing the device afterwards. Therefore, it was necessary to employ an alternative passivation material and, consequently, PECVD SiN was employed as the insulation material for all the microelectrode arrays characterised.

5.2.1.2 Normal and Low Stress SiN

No difficulties were encountered when patterning a normal stress PECVD SiN insulation layer. However, the resulting devices proved unreliable for electrochemical experiments, due to the high tensile stress of the films, which frequently resulted in delamination and fracturing of the SiN layer, particularly at the edges of the microholes (Figures 5.1a-5.1c). Therefore, it was necessary to employ a low-stress PECVD material instead. This greatly improved the durability of the insulation layer and no delamination or fracturing of the dielectric was observed in devices employing low-stress SiN. By oxygen cleaning the devices prior to each experiment, they proved effective for repeated electrochemical trials.

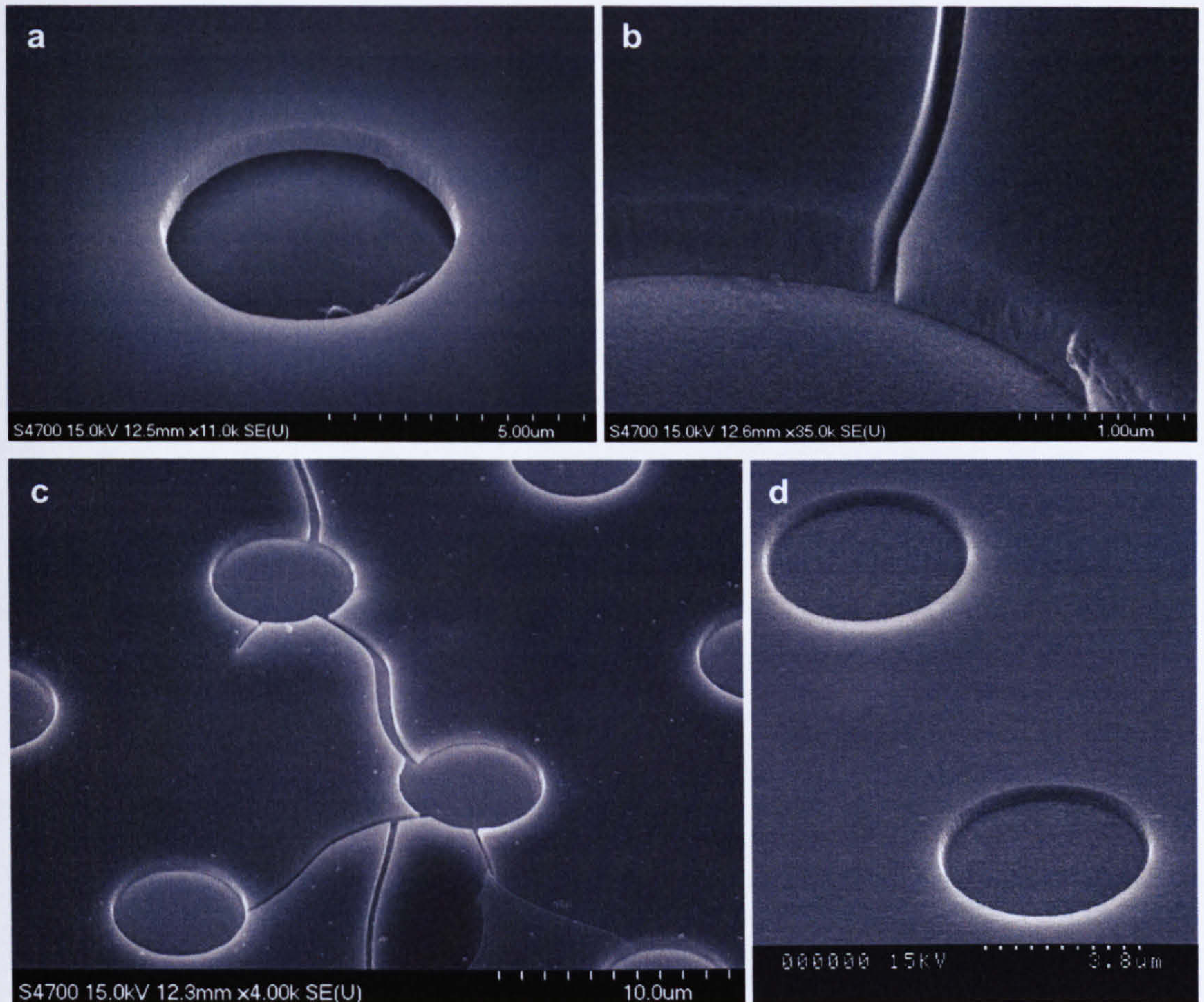

Figure 5.2 **SiN Microelectrode Array Insulation Layers**

a: Delamination around the edges of a microhole in a normal stress SiN layer. b and c: Extensive fracturing of a normal-stress SiN layer. d: A strongly adhered low-stress SiN layer.

5.2.1.3 Photoresist and Electron Beam Resists

Creating the insulation layer from a lithographic resist can be both simple and rapid. However, the chemical resistance of most resist materials is poor. For instance, many standard cleaning agents will simply strip the entire resist layer and, consequently, they are not suitable for the production of the majority of microsensors. Nonetheless, they were used to produce the nanoelectrode array structures, as processing samples using RIE is more complicated when creating sub-micron features[2]. PMMA, UVIII and S1805 resists were all employed to produce nanoelectrode arrays.

[2] When densely packed features are to be patterned, the etch rate will not be constant for all feature sizes. Furthermore, the thinner resist layers required to produce nanometre scale features do not

5.2.2 Electrodeposition of Platinum Black

5.2.2.1 Electrode Porosity and the Edge Effect

A comparison of signals from the gold and platinum black microelectrode arrays requires some consideration of the morphology of the electroplated films, particularly with respect to any increase observed in the resulting geometric radii of the individual microelectrodes. The radius of the largest microelectrodes was not significantly altered by electroplating platinum black, as any growth outwards over the SiN layer was not significant when compared to the microelectrode dimensions. However, if the plating current was not carefully limited, the smallest gold electrodes frequently more than doubled in size during electrodeposition and became hemispherical in shape and highly porous (Figure 5.3a).

Furthermore, it should be noted that the microelectrodes at the edge of the arrays always experienced the greatest increase in size. This phenomenon can be explained by the so-called edge-effect, which is displayed by finite arrays of densely packed microelectrodes (Lee *et al*, 2001; Beriet *et al*, 2000). The current density generated by microelectrodes at the perimeter of such an array will be noticeably larger than that generated by the internal electrodes, as radial diffusion towards the outer areas of the perimeter electrodes will occur.

The edge-effect is clearly demonstrated in Figure 5.3b, which shows the corner of a highly overplated microelectrode array. From measurements of the average radius of these plated microelectrodes (Figure 5.4), it can be seen that the radius of the cornermost electrode may become almost double that of an internal electrode.

---

survive for long when the sample is being etched in a RIE machine. Therefore, a metal mask layer is required, which must be stripped after etching.

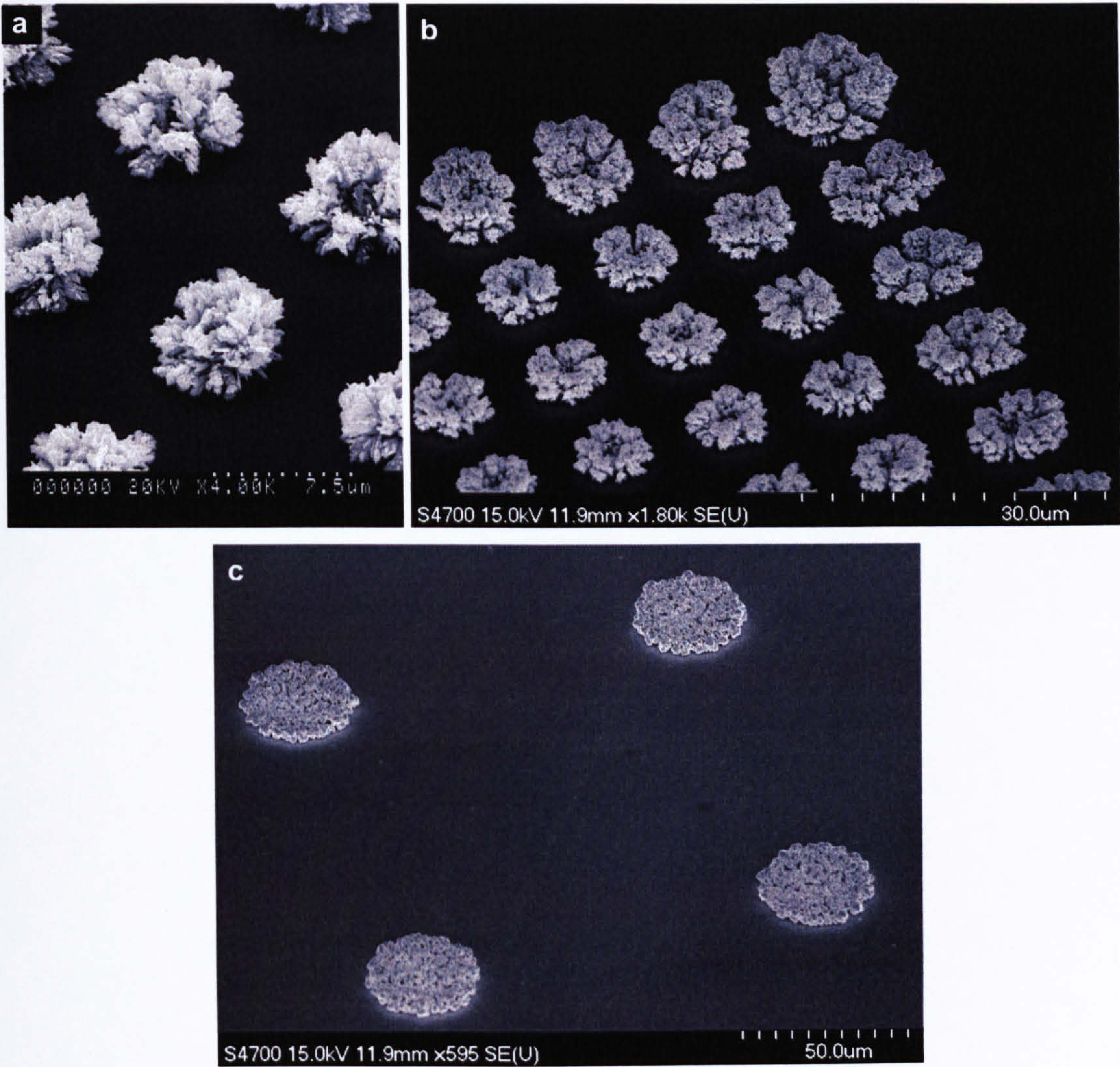

Figure 5.3 **Platinum Black Microelectrode Arrays**

a: Highly porous platinum black microelectrodes plated onto a 1.25 μm gold electrode array. b: The corner of a highly overplated microelectrode array that illustrates the influence of the edge effect. c: 12.5 μm platinum black microelectrodes of lower porosity.

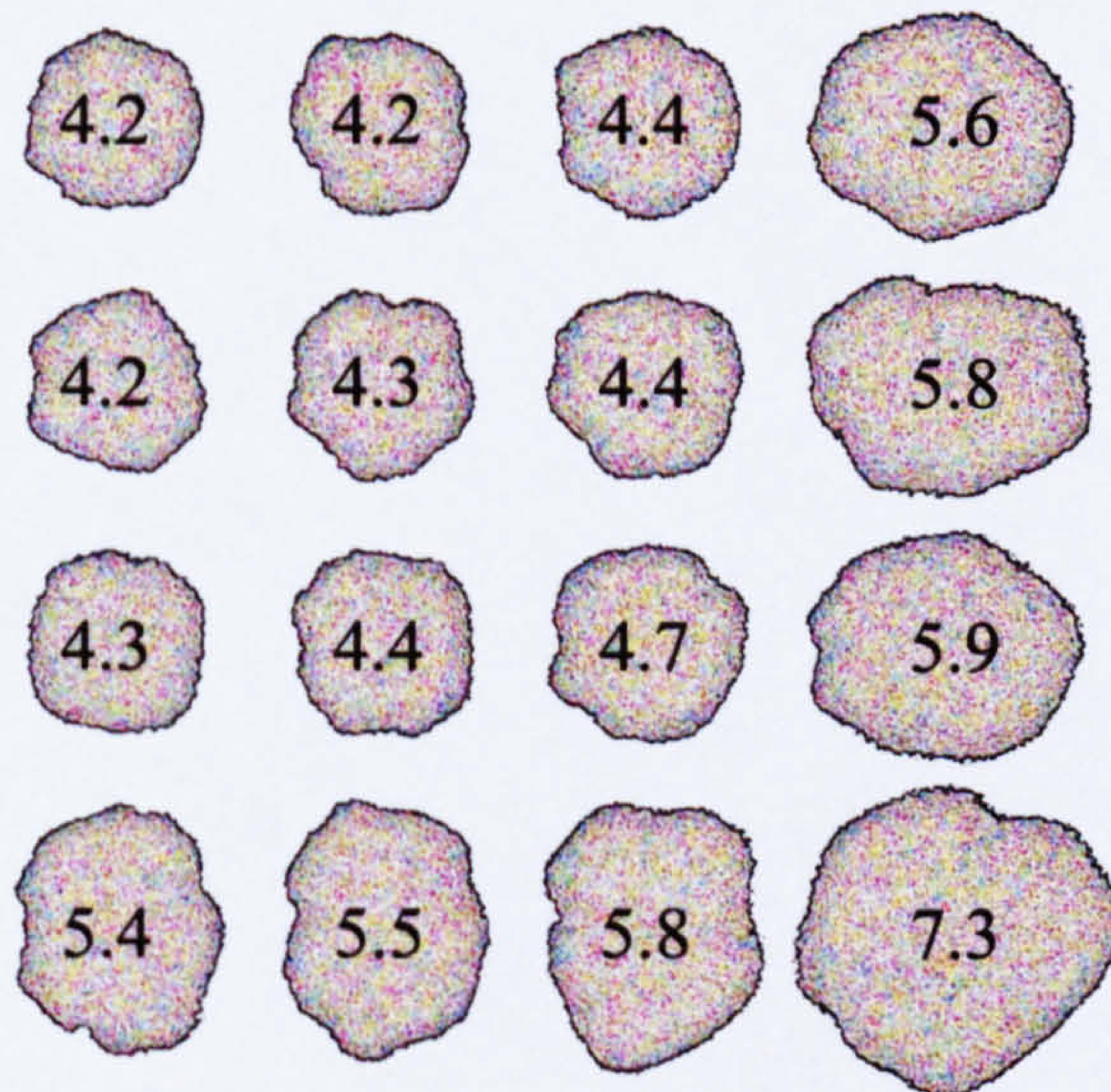

Figure 5.4 **Influence of the Edge Effect on Electroplated Microelectrode Arrays**

The average radius of the base of each electrode is marked in μm.

Rigorous attempts were therefore made to produce a constant electrode morphology and to control the individual electrode radius and porosity, as this study required comparable microelectrode arrays. However, even with careful control of the process some outward electroplating was unavoidable. When plating electrodes of lower porosity (Figure 5.3c), by decreasing the deposition rate, only slight over-plating and minimal *d/r* variation occurred. The optimum current or voltage level and plating time for each microelectrode array, neither of which scaled linearly with area, were determined empirically for each Set A device (as detailed in Table 3.2), chronopotentiometry being the most readily controllable method of deposition. It should also be noted that the platinum black electrode arrays were polarised for a longer period than the gold electrode arrays prior to acquiring chronoamperometric data, as the former did not stabilise as quickly as the latter. This was primarily due to the larger effective surface area of the platinum black electrode arrays, which resulted in higher charging and background currents.

5.2.3 Preparation of the Electrode Array Surfaces

Prior to all electrochemical recordings and electroplating procedures, removal of any passivating materials from the surface of the electrode array was essential. Various approaches to electrode preparation were considered. Cleaning the sample by oxygen plasma etching, which is frequently employed to remove organic materials from substrates, was

undoubtedly the most successful method employed. Electrode arrays were successfully regenerated by this method even after several experiments, as was previously demonstrated by Cai *et al* (2002). The results obtained when running the same experiment on different days using the same device were significantly more reproducible than when cleaning the electrode arrays with standard organic solvents alone (particularly as arrays with a SiN insulation layer could not be ultrasonicated[3] and were therefore simply soaked in solvent baths before being rinsed). Electrochemical cleaning, which relies on the electrode oxidation that occurs at positive potentials (Griffith, 1996), proved more successful than rinsing with solvents alone, though slight irreproducibility was observed from one experiment to the next. Furthermore, it is not possible to clean the resist-based electrode arrays in solvents such as acetone or to electrochemically clean them in a strong sulphuric acid solution, as the insulating resist layer will be removed. Therefore, cleaning by oxygen plasma etching was the method of choice that was carried out prior to all the electrochemical recordings detailed in this and subsequent chapters. It should be noted, however, that this method will slowly etch the resist layers employed in the nanoelectrode arrays – the etch rate for PMMA was estimated from AFM measurements to be 8.5 nm min^{-1}.

5.3 Voltammetric Studies With Microelectrode Arrays

In order to investigate the electrochemical behaviour of the sets of microelectrode arrays described in Table 5.1, cyclic voltammograms were first recorded for a model electroactive species, FMCA. Linear voltammograms, recorded in a dissolved oxygen solution, were then obtained for comparison, with both Au and platinum black electrodes being investigated.

5.3.1 Microelectrode Arrays with Constant Relative Centre-Centre Spacing (Set A)

5.3.1.1 Gold Microelectrode Arrays

Typical voltammograms obtained from the set of gold microelectrode arrays with a constant relative centre-centre spacing and varying individual electrode radii (Set A) are presented in

[3] Although the use of low-stress SiN greatly increased the durability of the insulation layer, its adhesion to the underlying gold film was still not strong enough to withstand the strong forces generated by an ultrasonic bath.

Figure 5.5. It can be seen that both the magnitude and the shape of the voltammograms vary with the individual electrode radius. As the individual microelectrode radius was increased from 1.25 μm to 25 μm, the recorded oxidation peak current, I_{pk}, decreased, whilst I_{pk} for the 50 μm array was comparable that of the 25 μm array.

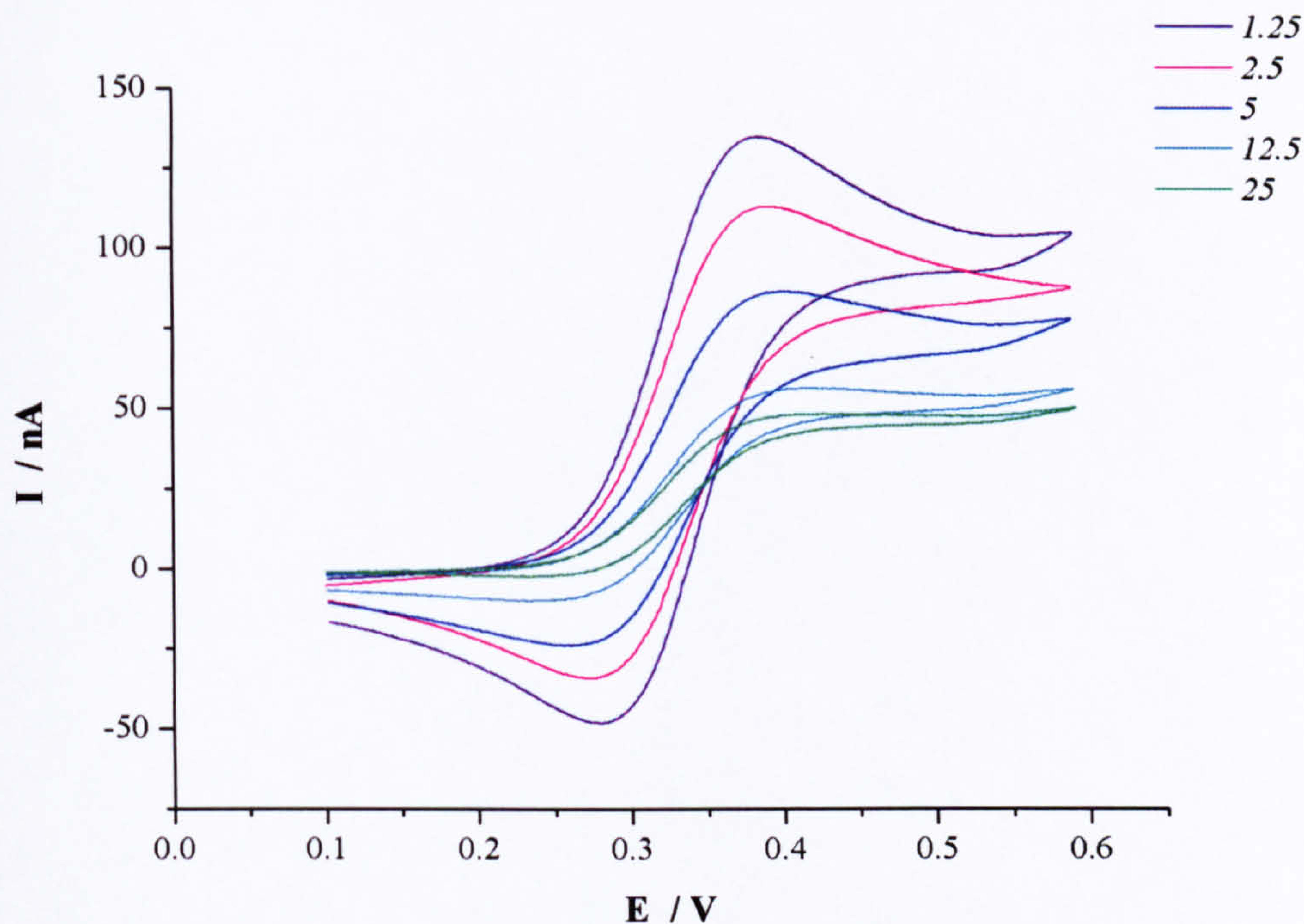

Figure 5.5 **Cyclic Voltammograms Obtained from Microelectrode Arrays with Varying Individual Electrode Radii (Set A)**

Typical cyclic voltammograms recorded in a 1 mM FMCA solution at 10 mV s^{-1}. The individual electrode radius (μm) of the corresponding array is marked for each voltammogram. For clarity, the voltammogram generated by the 50 μm electrode array is not shown.

From the FMCA voltammograms recorded, the average peak current densities were calculated for each microelectrode array (Figure 5.6) so as to normalize the data with respect to area. As expected, the 1.25 μm array generated the largest current density, more than 10 times greater than the smallest current density, which was produced by the 50 μm array. This overall trend in peak current density variation with individual microelectrode radius was observed repeatedly over a number of experiments, including the recording of linear sweep voltammograms (0V to –0.8 V vs. Ag|AgCl) in an air saturated oxygen solution (Figure 5.7).

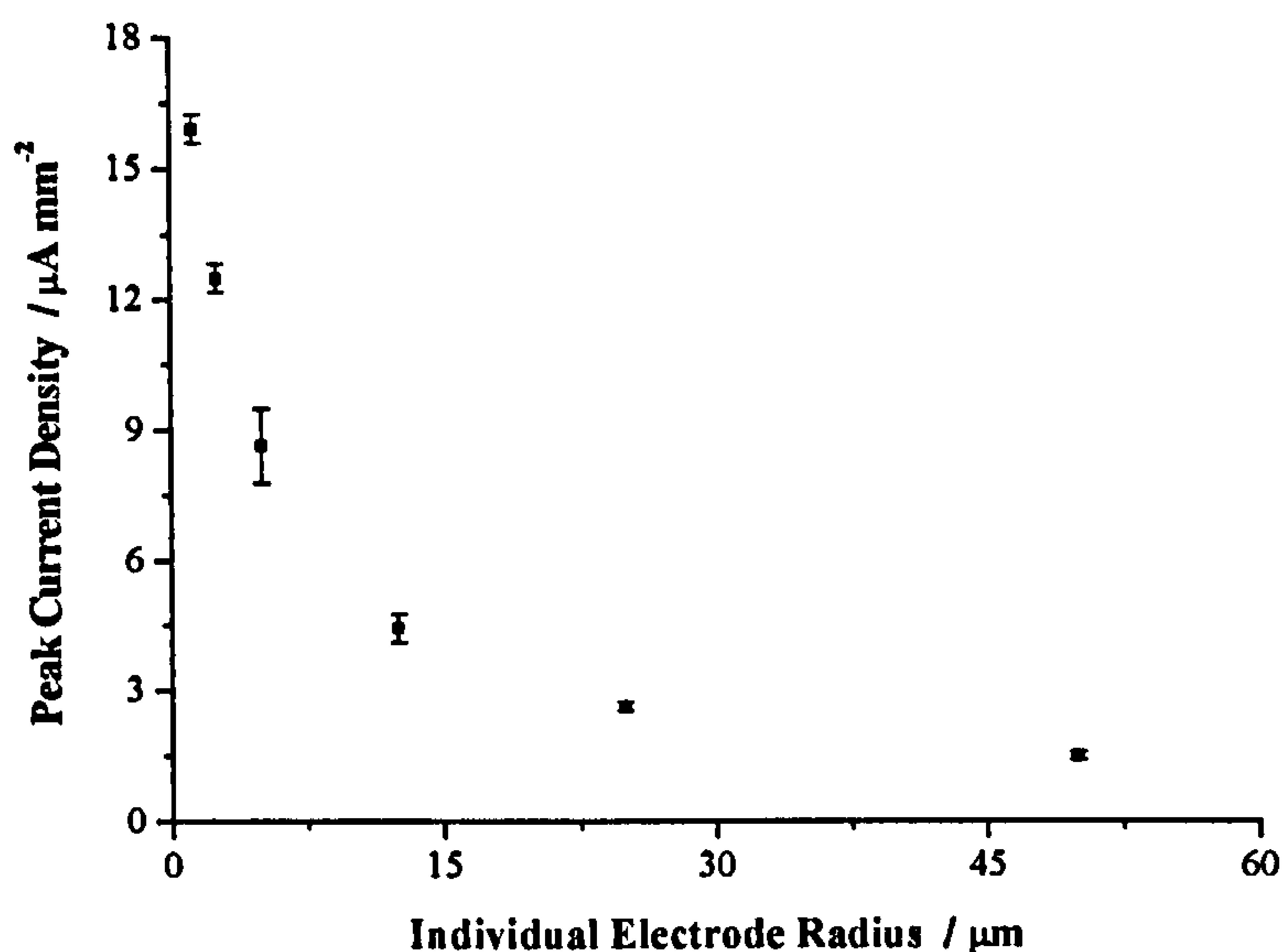

Figure 5.6 **Variation in Average Peak Current Density with Individual Electrode Radius**

Peak current densities were calculated from the cyclic voltammograms recorded at 10 mV s^{-1} in a 1 mM FMCA solution.

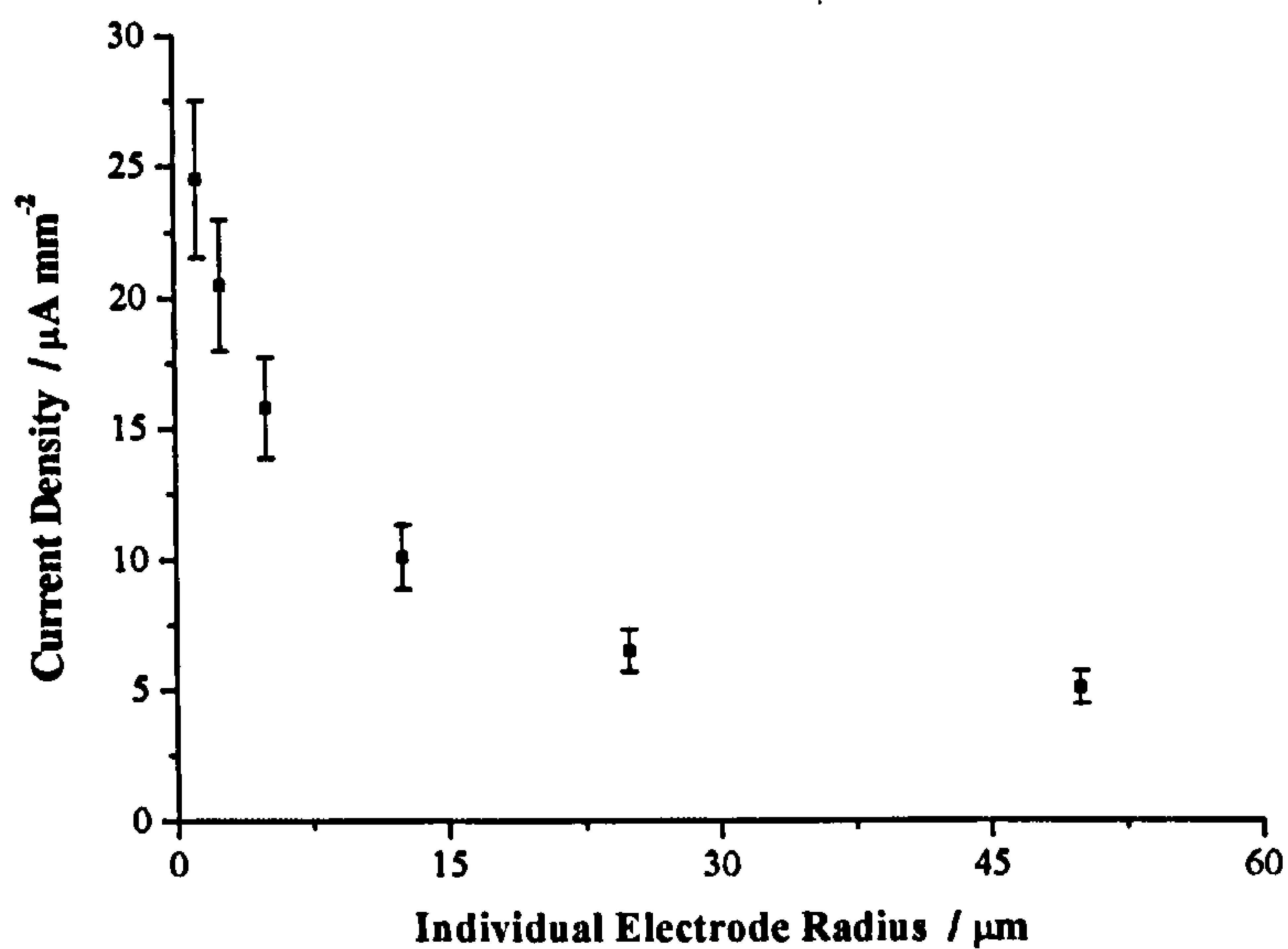

Figure 5.7 **Average Current Densities from Linear Sweep Voltammograms Recorded in an Air-Saturated Aqueous Solution**

The voltammograms were recorded from 0 to –0.8 V at a scan rate of 20 mV s^{-1} and the current densities were calculated from the values registered at –0.7 V vs. Ag|AgCl.

It can be seen from Figure 5.5 that the shape of each voltammogram is strongly dependant upon the individual microelectrode radius. The 1.25 μm array produced a strongly peaked curve, indicative of quasi-reversible linear diffusion to an electroactive site. As the individual electrode radius was increased, the current-potential curves displayed increasingly smaller peaks, the 25 μm array producing an essentially sigmoidal curve.

Individual Electrode Radius (μm)	E_{pa} (mV)	E_{pc} (mV)	Peak-Peak Separation (mV)	$\frac{i_{pa}}{i_{pc}}$	Peak Strength (nA V^{-1})
12.5	422	234	188	1.054	26.6
5.0	403	258	145	1.047	81.9
2.5	391	272	119	1.023	169
1.25	385	279	106	0.974	256

Table 5.2 **Variation in the Characteristics of a Cyclic Voltammogram with Individual Electrode Radius (Set A)**

Peak voltages, peak-peak separations, ratio of peak currents and peak strengths were calculated from the cyclic voltammograms recorded at 10 mV s^{-1} in 1 mM FMCA.

The peak-peak (E_{pk}) separation for the voltammograms produced by the 1.25, 2.5, 5 and 12.5 μm arrays (the arrays which generated peaked curves) increased with electrode radius, whilst the strength of the oxidation peak decreased and the reductive wave diminished (Table 5.2). Peak strength was defined as the magnitude of the average gradient of the curve for potential range $E_{pk}<E<(E_{pk}+80mV)$; that is, the average gradient for the region of the voltammograms where a macroelectrode would generate a current that decreases sharply from I_{pk}. As a sigmoidal voltammogram is produced when diffusion to a microelectrode array is radial, the measured peak strength of the arrays should tend towards zero as the diffusion profile becomes increasingly radial. Hence, peak strength variation may be used to estimate the smallest individual electrode radius for which radial diffusion alone would be observed. In this case (where d/r is 10 and the scan rate is 10 mVs^{-1}), as the measured peak strength tended towards zero, the individual electrode radius tended towards 25μm (Figure 5.8), for which sigmoidal behaviour was indeed observed.

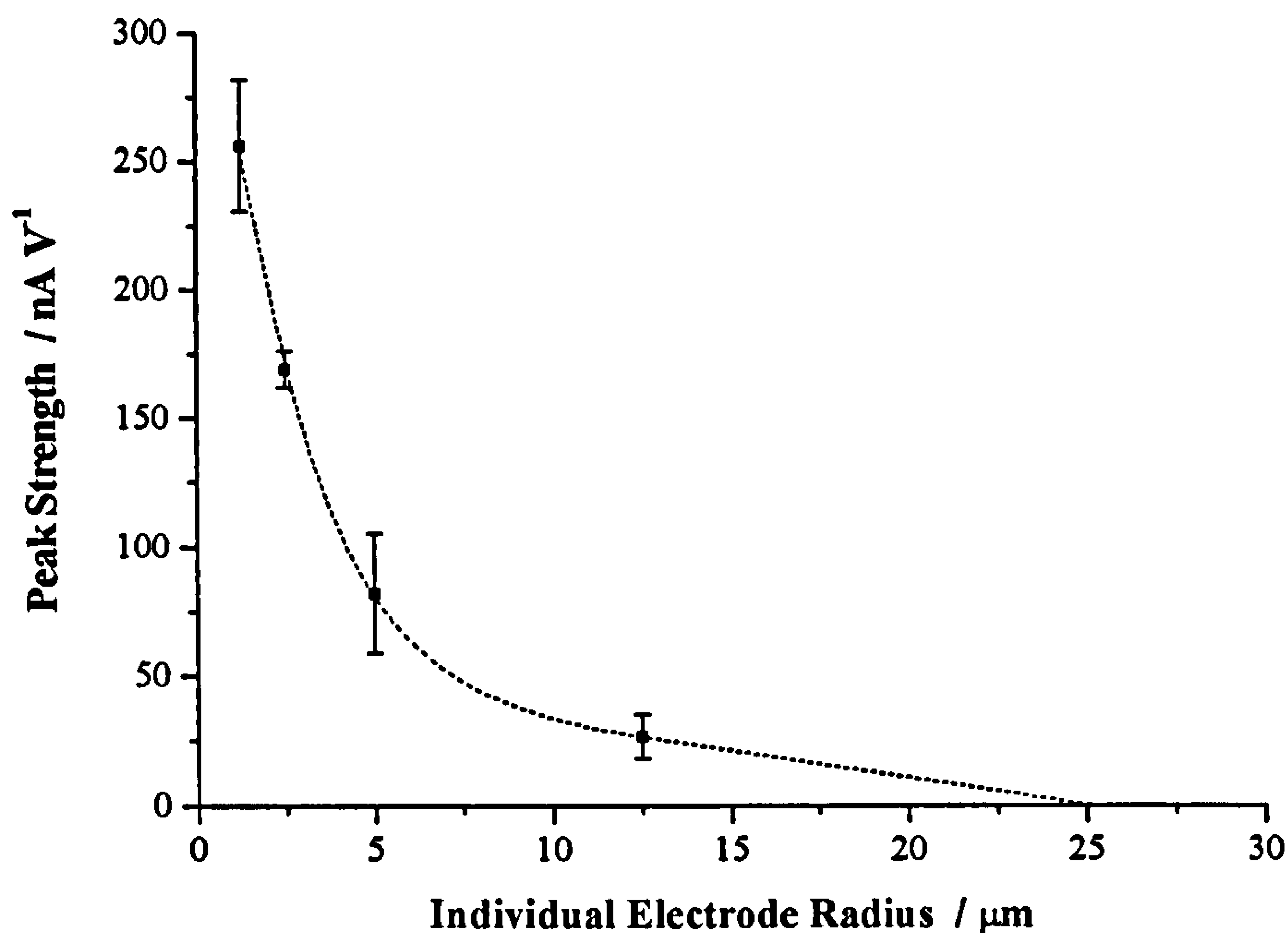

Figure 5.8 **Variation in Peak Strength with Individual Electrode Radius**
Peak strengths were calculated from the cyclic voltammograms recorded in 1 mM FMCA at 10 mV s^{-1}.

As discussed in Section 4.7, the diffusion profile of an electroactive species towards an array of microelectrodes may be either radial, when the individual microelectrodes operate independently of each other; or linear, when the diffusion fields of the individual microelectrodes merge completely; or mixed, when the individual diffusion layers partially merge. The cyclic voltammograms obtained demonstrate how, for a constant centre-centre spacing, the degree to which the diffusion layers merge is dependant upon the diameter of the individual microelectrodes. Whilst the arrays of larger microelectrodes exhibited radial diffusion behaviour, the diffusion fields of the smaller microelectrodes appeared to merge considerably, resulting in a peaked voltammogram indicative of linear diffusion.

As the electrode radius decreases, the inactive area surrounding each electrode (which has a value of $(10-\pi)r^2$ for the internal electrodes) also decreases. Thus, for a constant diffusion layer thickness, the smaller the individual electrodes, the more likely the merging of the individual diffusion layers will be, as was illustrated by the finite element simulation results presented in Section 4.8. Thus, arrays of smaller microelectrodes will not exhibit as nonlinear a diffusion profile as arrays of larger microelectrodes for a constant *d/r* ratio and timescale. Consequently, to ensure electrochemical behaviour that retains the characteristics

of a microelectrode, as the radius of the individual electrodes of an array decreases, the *d/r* value must be increased.

Furthermore, for microelectrode arrays where the individual diffusion fields overlap partially, the edge-effect phenomenon will also contribute to the increasing non-linearity of the diffusion field with increasing electrode radius. For the same geometric area and *d/r* value, arrays of large microelectrodes will have a greater perimeter-to-internal electrode ratio when compared to arrays of smaller microelectrodes; hence the overall non-linearity of diffusion to the former will be greater.

It should also be noted that, as r increases, the active area of the microelectrode array becomes progressively larger. For a finite microelectrode array, the active area can be expressed as $\pi(r+a)^2$, where $a = l/(d/r)$ and l is the centre-centre distance of the corner electrodes. Therefore, the greatest increase in active area, relative to the increase in radius, was between the 25 μm array and the 50 μm array (the arrays for which the diffusion fields of the individual electrodes remained independent). The similarity in the I_{pk} values generated by these arrays is presumed to be due to a balance between the larger active area of the 50 μm array and the increased linearity of its individual diffusion fields, due to the larger size of its electrodes.

5.3.1.2 Platinum Black Microelectrode Arrays

Linear voltammograms were also recorded in an air-saturated solution using microelectrode arrays electroplated with platinum black (Figure 5.9). Although the variation in current density with individual electrode radius was similar to that observed for the arrays of gold microelectrodes and the current densities were greatly increased, these results were not considered entirely reliable, due to the large, and often unstable, background currents that were observed. These background currents were several times larger than those recorded with the gold microelectrode arrays, as a result of the greatly enhanced effective surface area of the platinum black surface. The reason for the instability of the recorded background currents was unclear.

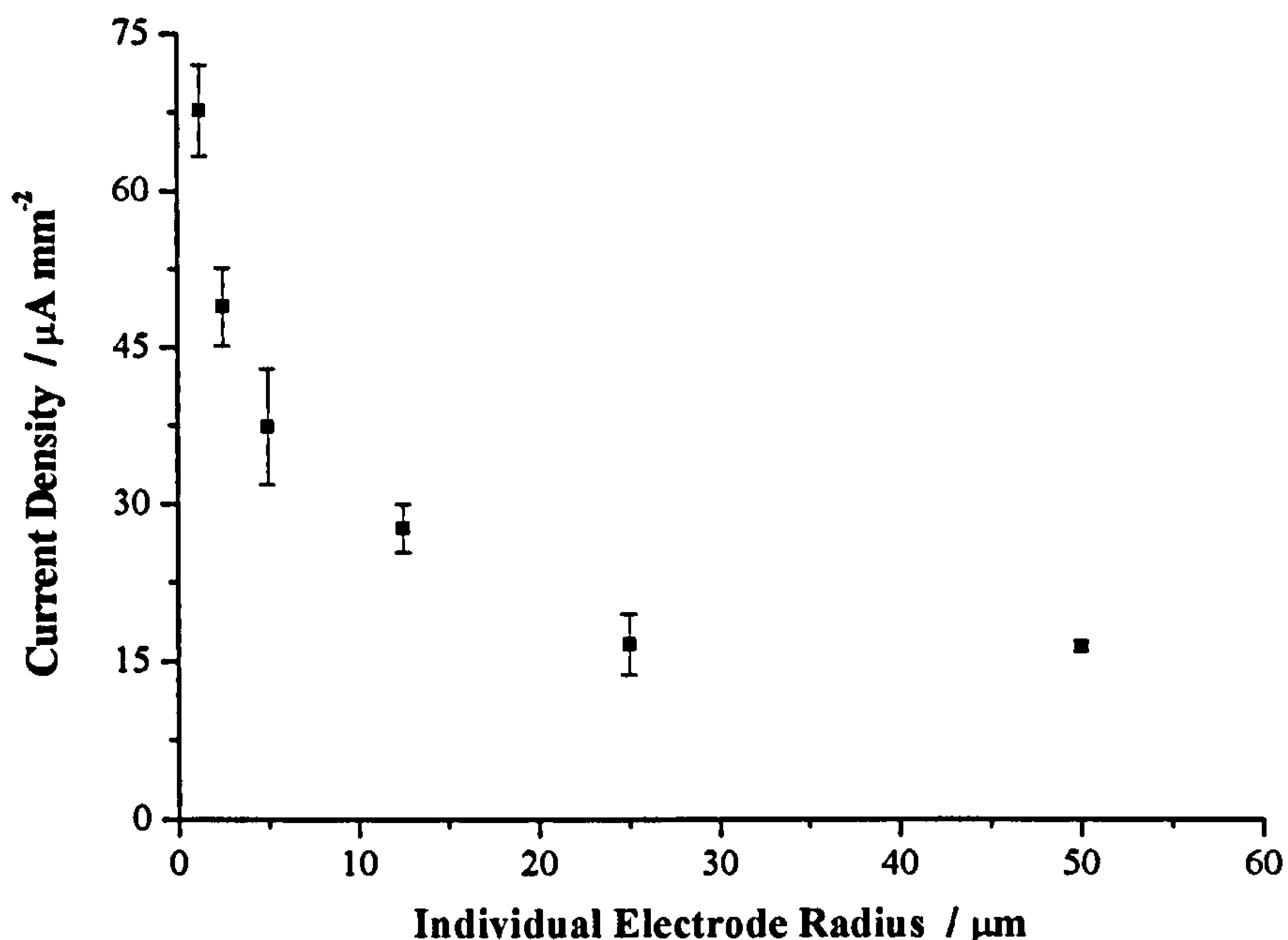

Figure 5.9 **Average Current Densities from Linear Sweep Voltammograms Recorded using Platinum Black Microelectrode Arrays**

Linear voltammograms were recorded in air-saturated water at a scan rate of 20 mV s^{-1}. Current densities were calculated from the values registered at –0.7 V vs. Ag|AgCl.

5.3.2 Microelectrode Arrays with Constant Individual Electrode Radius (Set B)

5.3.2.1 Gold Microelectrode Arrays

As characteristic microelectrode behaviour was not demonstrated by the microelectrode arrays with smaller individual electrodes, the second set of arrays (Set B), which had a constant individual electrode radius of 2.5 μm and varying relative centre-centre spacings, was investigated. Typical cyclic voltammograms recorded from the arrays in a FMCA solution are presented in Figure 5.10. As expected, the electrochemical behaviour of the microelectrode arrays varied significantly with *d/r*. A strongly peaked voltammogram was produced by the array with a *d/r* of 6, whilst the array with a *d/r* of 150 produced a sigmoidal curve, symptomatic of radial diffusion. Furthermore, the steady-state current of the latter (3.91 nA) was approximately equal to the value calculated using Equation 4.34 for 9 microelectrodes, which is 3.96 nA assuming a diffusion co-efficient of 7.2×10^{-10} m^2 s^{-1}

(Kudera *et al*, 2001), indicating that the diffusion fields of the individual microelectrodes were independent. The intermediary microelectrode arrays produced cyclic voltammograms with mixed diffusion characteristics.

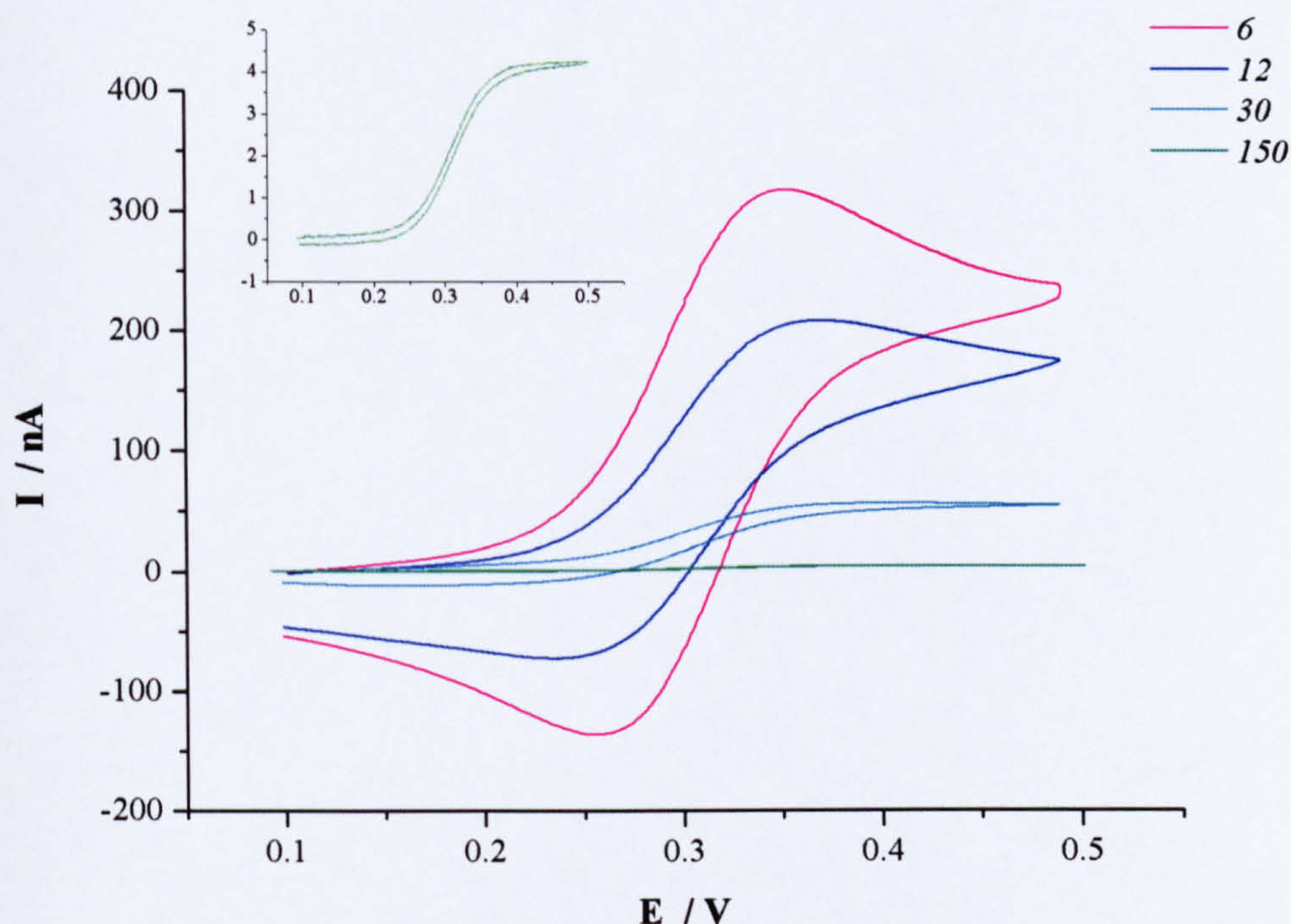

Figure 5.10 **Cyclic Voltammograms Obtained from Microelectrode Arrays with Varying Inter-Electrode Spacings (Set B)**

Typical cyclic voltammograms recorded in a 1 mM FMCA solution at 10 mV s^{-1}. The relative centre-centre spacings of the arrays employed to record each voltammogram are indicated in the legend and the voltammogram generated by the array with a *d/r* ratio of 150 is magnified for clarity.

The peak current density, the peak-peak separation and the peak strength obtained for the arrays with a *d/r* of 6, 12 and 30 are presented in Table 5.3. An increase in the centre-to-centre spacing resulted in an increase in the peak-peak separation, a decrease in the peak strength and an increase in the current density, due to the enhanced non-linearity of the diffusion profile. From the decreasing peak strength values, it can be estimated that a minimum relative centre-centre spacing of approximately 40 is required to ensure fully hemispherical diffusion to a microelectrode array with an individual electrode radius of 2.5 μm, for a potential scan rate of 10 mV s^{-1}.

Relative Centre-Centre Spacing (d/r)	Peak Current Density (µA mm^{-2})	E_{pa} (mV)	E_{pc} (mV)	Peak-Peak Separation (mV)	Peak Strength (nA m^{-1})
6	5.52	353	256	97	700
12	14.0	370	235	135	282
30	19.2	405	156	249	18

Table 5.3 **Variation in the Characteristics of a Cyclic Voltammogram with *d/r* (Set B)**

Peak current densities, peak voltages and peak-peak separations were calculated from the cyclic voltammograms recorded at 10 mV s^{-1} in 1 mM FMCA.

5.4 Chronoamperometric Studies With Microelectrode Arrays

The design for the dissolved oxygen microsensor (to be discussed in Section 6.2.1) incorporated a working microelectrode array that was to be operated at constant potential. Therefore, chronoamperometric recordings were obtained for each microelectrode array, initially to verify the electrochemical behaviour of each array when using this technique, but also to determine their signal-to-noise ratios (SNRs) and detection levels so as to assess their analytical performance. Furthermore, the behaviour of gold and platinum black microelectrode arrays could be reliably compared using chronoamperometry, unlike the voltammetric techniques employed previously.

5.4.1 Microelectrode Arrays with Constant Relative Centre-Centre Spacing (Set A)

5.4.1.1 Comparison of Gold and Platinum Black Microelectrode Arrays

Chronoamperometric recordings were obtained for each Set A microelectrode array, before and after platinisation, in water that had been equilibrated to room temperature and oxygen level. Variation in current density with electrode radius was similar to that observed previously and the current densities generated by the platinum black microelectrode arrays (calculated using the geometric areas rather than the effective surface areas) were consistently larger than those generated by the gold microelectrode arrays (Figure 5.11). However, this increase was not as large as may be expected, due to the low electrodeposition

rates that had to be employed. Furthermore, the data acquired for the microelectrode arrays with the smallest individual electrodes should be considered in light of the unavoidable but slight increase in radius during electrodeposition.

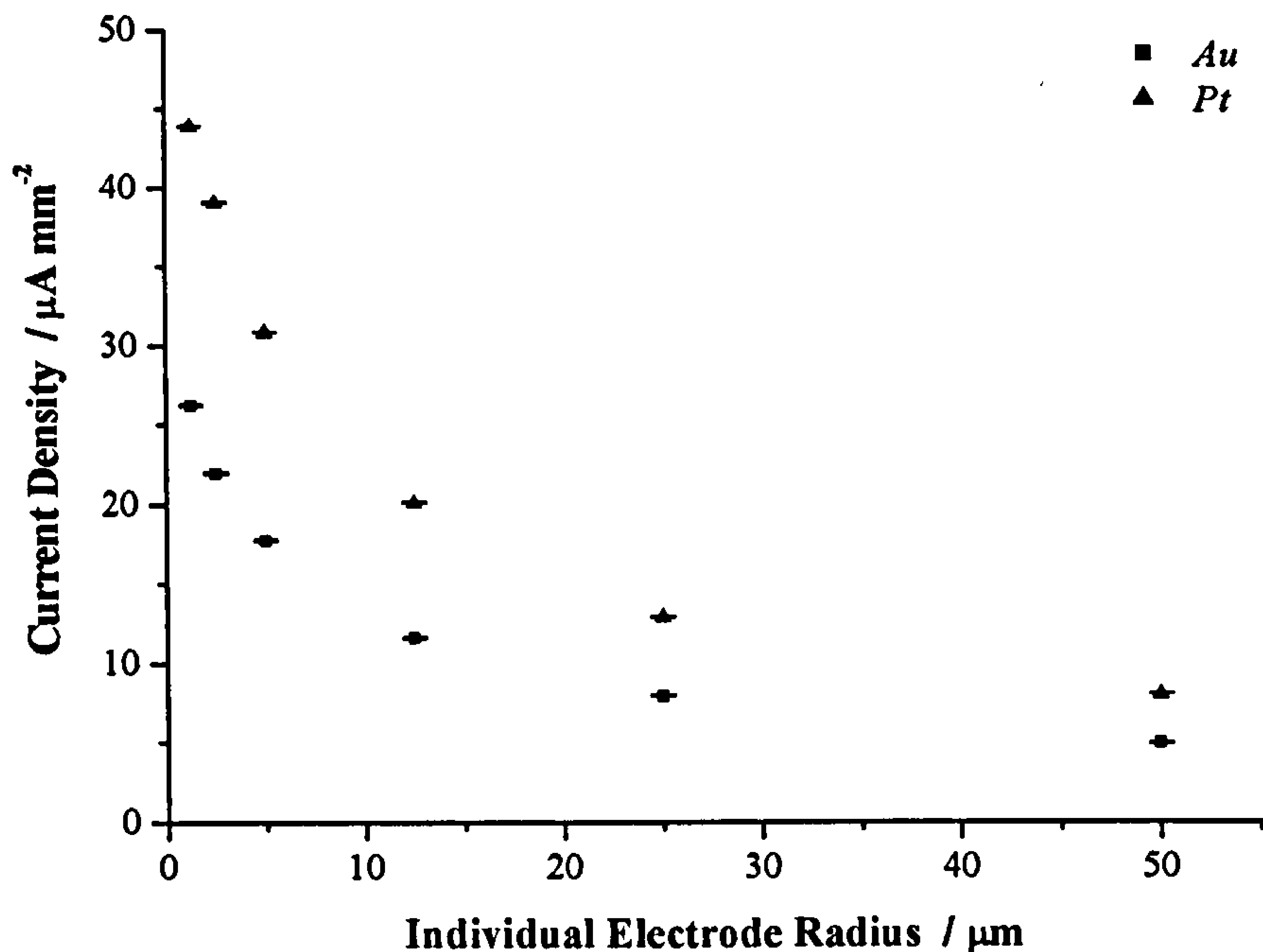

Figure 5.11 **Time-averaged Current Densities from Chronoamperometric Recordings of Dissolved Oxygen using the Set A Microelectrode Arrays**

Recordings made at -0.7 V for gold ( ) and platinum black ( ) microelectrode arrays.

When highly porous platinum black electrodes were deposited (as illustrated in Figure 5.3a), the current generated was enhanced by a factor in the region of 6-9 when compared to the initial array of evaporated gold electrodes. However, when employing such electrodes, compensation for the inevitable increase in electrode diameter would be required when designing an insulation layer for a specific electrode radius and inter-electrode spacing[4]. Furthermore, the smaller the initial electrode radius, the more hemispherical the morphology

---

[4] By decreasing the radius of the underlying gold electrodes at the perimeter of the array (with a more significant reduction for the corner most electrodes), a platinum black microelectrode array with a constant *r* and *d/r* ratio throughout the entire array could be obtained. However, the degree of reduction required would be strongly dependent upon the rate of electrodeposition and, therefore, the optimal initial electrode geometry may have to be determined by trial and error.

and the greater the surface roughness of the resulting platinum black electrodes. This would naturally enhance the current levels generated by the arrays with the smallest individual electrodes, with respect to the arrays with the largest individual electrodes, but it would also increase their background and noise levels, the upshot of which is discussed in Section 5.4.1.2.

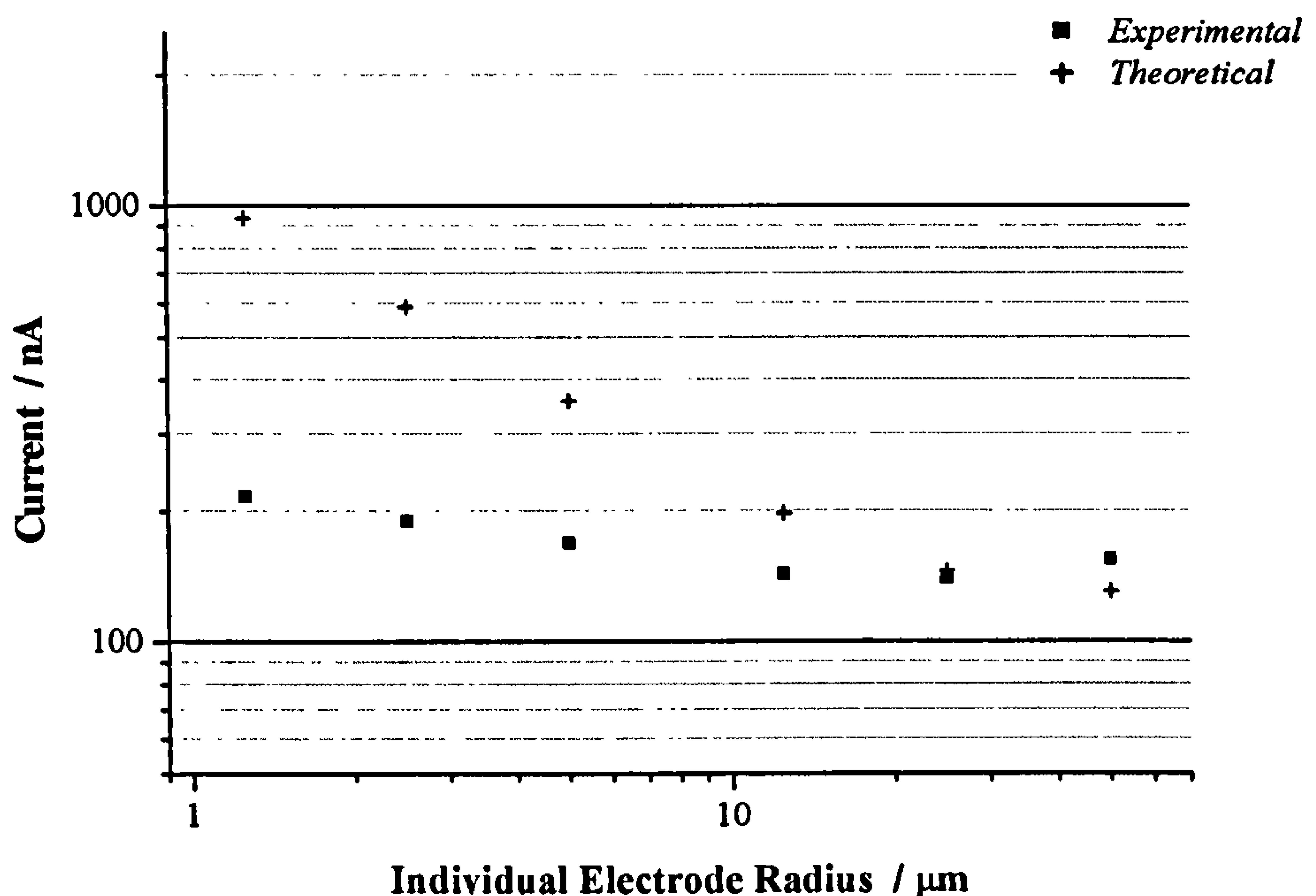

Figure 5.12 **A Comparison of Theoretical and Experimental Currents from Chronoamperometric Recordings with the Set A Microelectrode Arrays**

The theoretical values (+) were calculated by assuming radial diffusion to an array of independent microelectrodes.

A comparison of the experimental current values, for the gold microelectrode arrays, with the theoretical current that would be generated by an array of electrodes whose diffusion fields are radial and independent (using Equation 4.34 for *m* microelectrodes, a diffusion co-efficient of 2.1×10^{-9} m^2 s^{-1} and a concentration of 0.26 mM) is shown in Figure 5.12. It can be seen that the array with an individual electrode radius of 25μm did generate a current similar to the theoretical value for an array of microelectrodes exhibiting radial diffusion. However, as the individual electrode radius is decreased, the observed current becomes significantly smaller than that predicted by Equation 4.34. This confirms that, for densely

packed microelectrode arrays with the same *d/r*, the smaller the individual microelectrode, the greater the linear component of the mixed diffusion profile.

5.4.1.2 Signal-to-Noise Ratios (SNRs) and Detection Limits

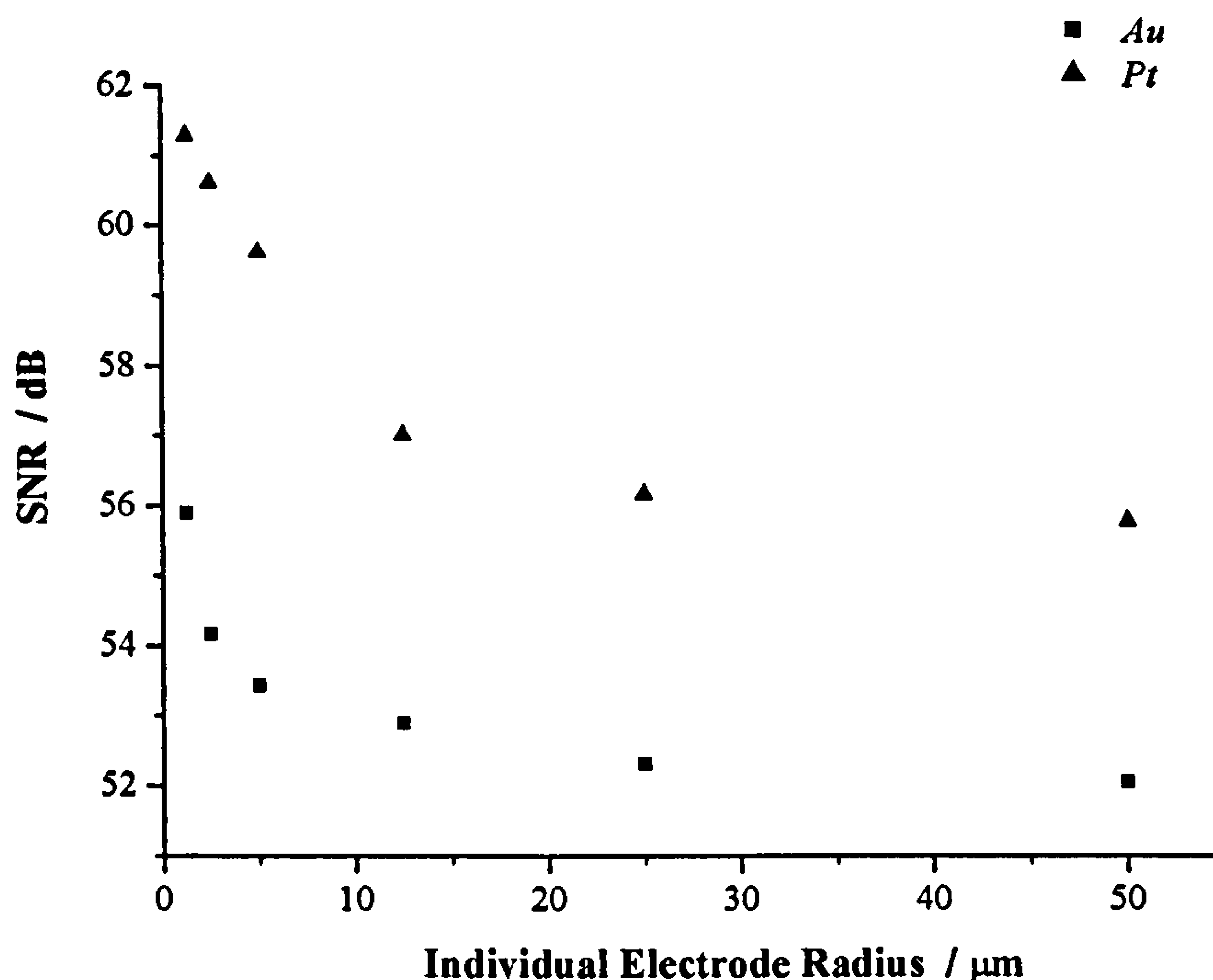

Figure 5.13 SNRs Obtained for the Set A Microelectrode Arrays
SNRs calculated in decibels from the gold ( ) and platinum black ( ) microelectrode array chronoamperometric recordings.

The signal-to-noise ratio for the system employed was determined for all Set A microelectrode arrays (Figure 5.13), the SNR being expressed in decibels:

$$SNR = 20\log_{10}\left(\frac{Signal}{Noise}\right) \tag{5.01}$$

A signal-background-ratio (SBR) may be expressed similarly, but whereas noise was defined as three standard deviations of the recorded signal for the measurement period and was mainly due to electrical instrumentation noise, the background current was simply defined as the time-averaged current recorded in an analyte-free solution. Variation with individual microelectrode radius again demonstrated a similar trend to that observed previously, with

the smallest electrodes producing the largest SNRs and platinum black microelectrode arrays producing larger SNRs than gold microelectrode arrays.

However, the average background current for the platinum black arrays (-0.44 nA) was noticeably larger than that for the gold arrays (-0.21 nA), due to the increased surface area of the platinum black. Therefore, electroplating with platinum black decreased the SBR but increased the SNR, which would produce an overall increase in the resolution of an amperometric sensor employing such a microelectrode array. The detection limit, C_m, of the system may be defined as the minimum concentration of analyte that can be detected for a given confidence level (Skoog *et al*, 1998). Assuming a minimum distinguishable signal of three standard deviations greater than the background signal, which would give a confidence level of 99%, the detection limit can be calculated as:

$$C_m = C^{\bullet}\left(\frac{3\sigma}{I_{C\bullet} - I_{back}}\right) \tag{5.02}$$

where $I_{C\bullet}$ is the time-averaged current recorded for a known bulk concentration, $C^{\bullet}$, I_{back} is the time-averaged current recorded when no analyte is present and σ is the standard deviation of the signal. The estimated detection limits for the Set A microelectrode arrays are presented in Table 5.4 (second column).

Individual Electrode Radius (μm)	Detection Limit (μM)		Low-Gain Setting with Gold Arrays	
	Platinum Black Arrays	Gold Arrays	Noise (pA)	Detection Limit (nM)
1.25	0.22	0.42	-	-
2.5	0.24	0.51	-	-
5	0.27	0.55	-	-
12.5	0.37	0.59	3.0	5.4
25	0.40	0.63	4.6	8.7
50	0.42	0.65	5.9	10.2

Table 5.4 **Detection Limits for the Set A Microelectrode Arrays**
Detection limits were calculated from the signal and background chronoamperometric dissolved oxygen recordings.

Although the detection limits, which are at trace (submicromolar) level, are improved by decreasing the individual electrode radius and electroplating with platinum black, the electrical instrumentation used limited the extent of these improvements. With the potentiostat gain setting required for these recordings, comparable noise levels were recorded for each microelectrode array, the majority of which was attributable to electronic noise (similar values were recorded when the electrochemical cell was not connected to the instrumentation). However, electrochemical noise should decrease with electrode area and, so, by reducing the electronic noise of the system to a level comparable to or below the electrochemical noise of the electrode arrays, greater improvements in the SNR with decreasing electrode radius should be observed.

When recordings were made with the gold microelectrodes in an analyte free solution at the lowest gain setting on the potentiostat employed (0.2 nA V^{-1}), which generated a background electronic noise level of approximately 2 pA, the overall noise level did decrease with the individual electrode radius (Table 5.4, third column). However, only the largest electrode arrays generated an overall noise level that was greater than the level of the electronic noise alone. Nonetheless, if low noise electronic instrumentation was employed (for example a integrated control system with a gain setting that automatically decreased as the recorded current decreased) substantially larger SNRs and lower detection limits, with a greater variation between larger and smaller individual electrode radii, could be obtained. Indeed, the detection of ultratrace (subnanomolar) concentrations of analyte should be possible, which would compare favourably to current voltammetric sensors (Bakker and Telting-Diaz, 2002). Whether or not electroplating with platinum black would increase the SNR of the system would be dependent upon the relative increase in the recorded signal with respect to the increase in the noise and background levels.

5.4.2 Microelectrode Arrays with Constant Individual Electrode Radius (Set B)

Chronoamperometric recordings were also obtained for each microelectrode array in Set B, although gold arrays alone were investigated. Variation in the recorded current density with d/r was similar to that obtained previously and a comparison of experimental and theoretical currents is presented in Figure 5.14, the theoretical values again calculated using Equation 4.34 for m microelectrodes using the parameter values noted previously. The theoretical and experimental currents for a d/r of 150 are comparable, verifying that the diffusion profile of the electroactive species is indeed radial. However, as d/r decreases, the experimental

currents progressively deviate from the theoretical values, confirming the increased linearity of diffusion to microelectrode arrays with smaller centre-centre spacings.

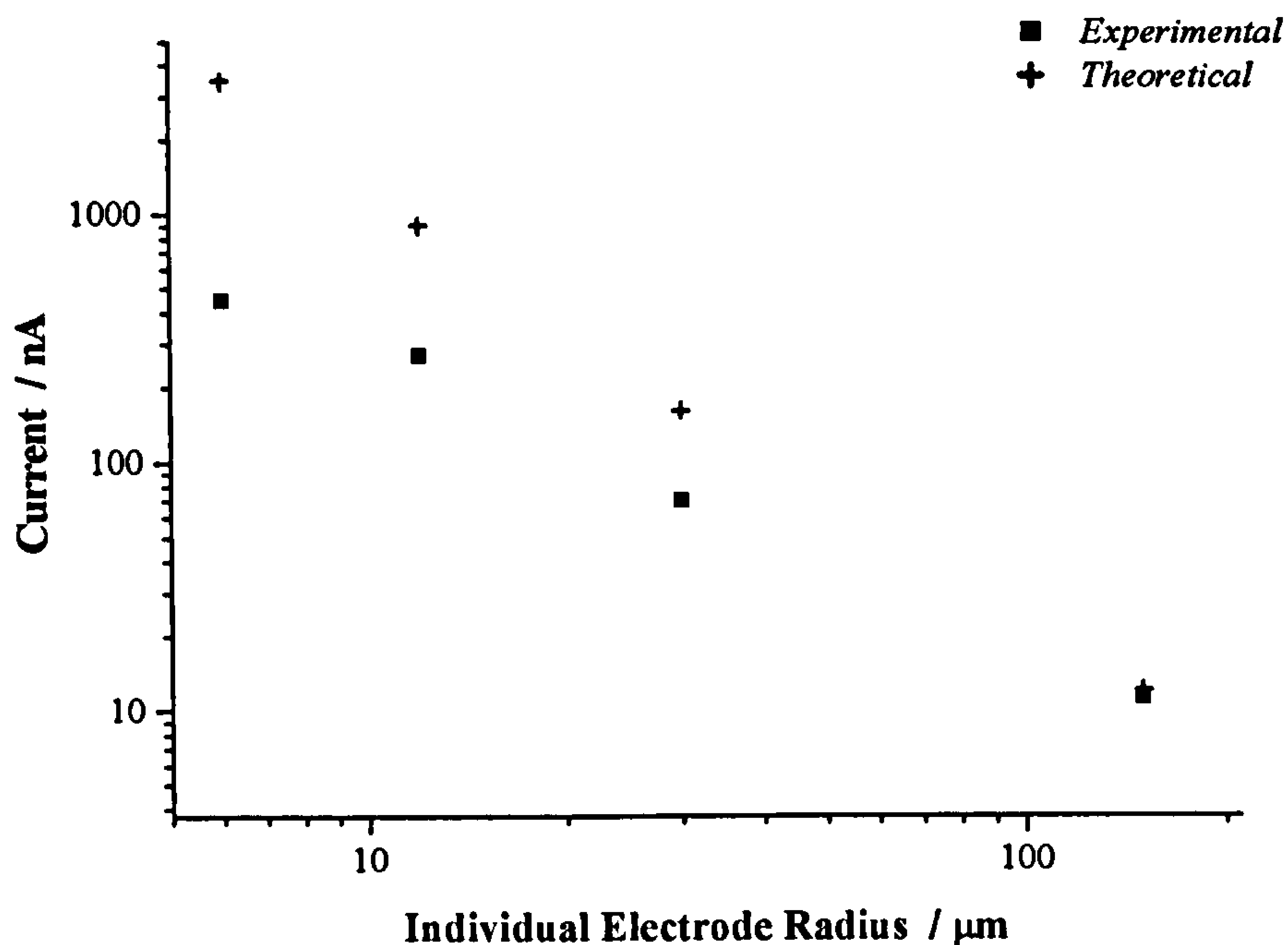

Figure 5.14 **A Comparison of Theoretical and Experimental Currents from Chronoamperometric Recordings with the Set B Microelectrode Arrays**

The theoretical values (+) were calculated assuming radial diffusion to an array of independent microelectrodes.

5.5 Characterisation of Nanoelectrode Arrays

To investigate whether the trends discussed previously for the microelectrode arrays with a constant relative centre-centre spacing continued into the sub-micron range, the nanoelectrode arrays described in Section 5.1.1 were characterised by cyclic voltammetry. Both direct-write electron-beam lithography (EBL) and nanoimprint lithography (NIL) were successfully employed to produce the insulation layer of the nanoelectrode arrays.

5.5.1 Nanoelectrode Arrays Fabricated by Direct-Write Electron Beam Lithography

5.5.1.1 Fabrication Considerations

As discussed in Section 3.3.1.5.1, exposure tests were initially carried out to determine the optimum dose for each electrode geometry. However, the first recordings with the nanoelectrode arrays generated relatively low signals and it was suspected that a thin film of resist still covered the electrode surface. Therefore, the samples were oxygen cleaned in the barrel asher for 5-15 minutes – the smaller the individual electrodes, the longer the ashing time that was required. However, oxygen plasma etching with a barrel asher is an isotropic process and, therefore, material was removed from around the perimeter of each of the holes in the insulation layer. This altered the geometry of the electrode arrays by increasing the individual electrode radii (from 500, 250, 125 and 50 nm to 550, 300, 160 and 110 nm respectively) and consequently decreasing the *d/r* ratios. Naturally, these modifications to the electrode arrays, which were determined by SEM, must be taken into account when considering their electrochemical response.

5.5.1.2 Voltammetric Studies

Cyclic voltammograms were recorded using each nanoelectrode array and the results, for arrays with a UVIII insulation layer, are presented in Figure 5.15. Similar results were obtained for the arrays employing PMMA. It can be seen that the peak current generated by the arrays continued to increase as the individual electrode radius decreased. However, the peak current generated by the 110 nm array (originally designed as an array of 50 nm electrodes) was somewhat larger than expected from the estimated trendline of the other values, as prolonged oxygen plasma etching had substantially decreased its *d/r* ratio to less than half of the intended value. It should also be noted that, as the individual electrode radius decreases, the value of the peak current obtained should tend towards the value generated by a single 500 μm square electrode. As a value of approximately 245 nA was obtained for the latter, this does appear to be the case.

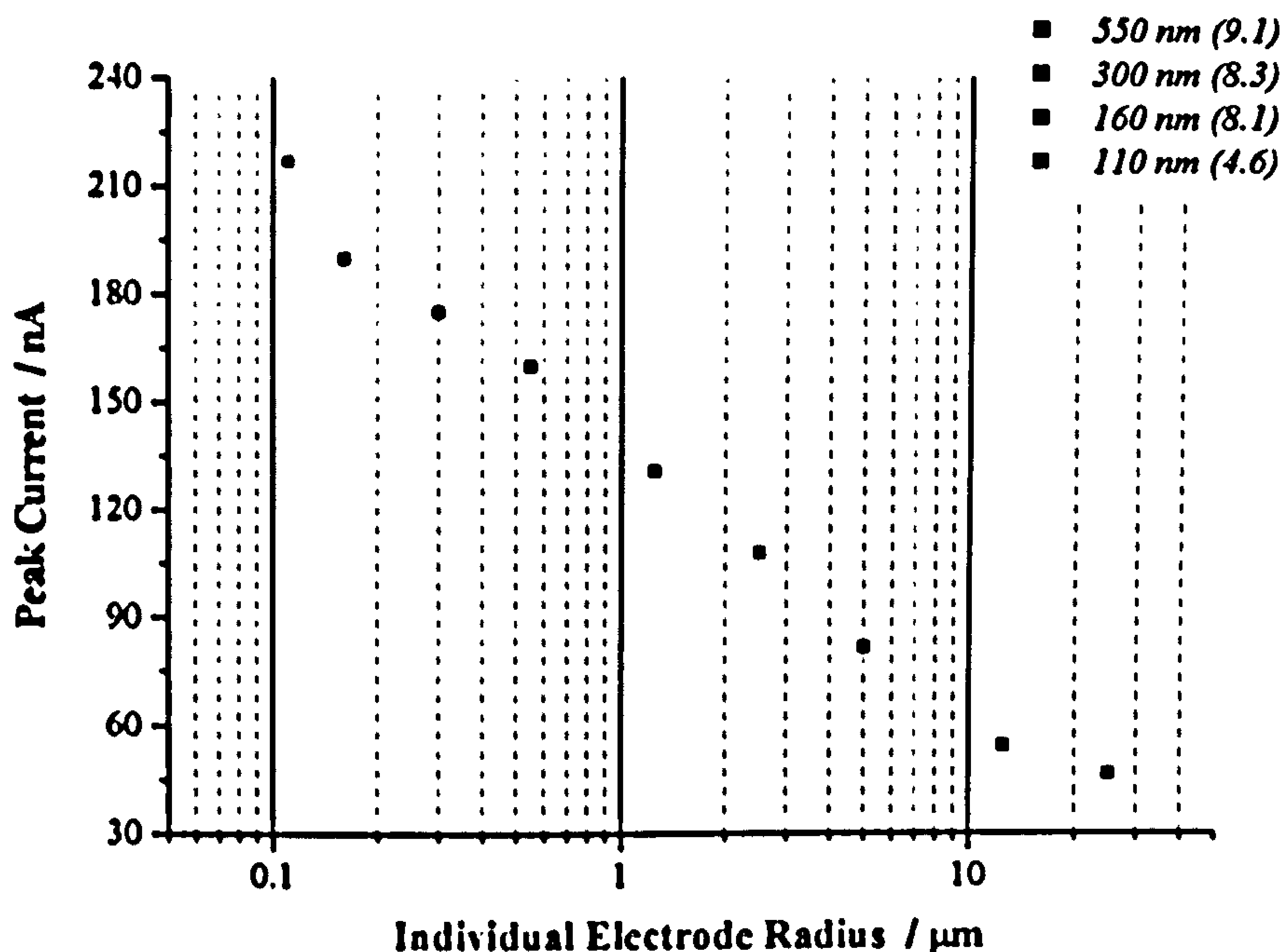

Figure 5.15 **Average Peak Currents Recorded for Nanoelectrode and Microelectrode Arrays**

Voltammograms were recorded at a scan rate of 10 mV s^{-1} in a 1 mM FMCA solution. The individual electrode radius and the *d/r* ratio are marked in the legend for each nanoelectrode array and the black points indicate the peak currents obtained for Set A microelectrode arrays that were discussed previously.

However, while the peak currents generated by the arrays were relatively stable for several trials, the characteristics of the voltammograms were not. Although the E_{pa} and ΔE_{pk} values were smaller than those obtained for the microelectrode arrays and the values obtained for the peak strength were larger, their values changed noticeably during the course of the trials. The reason for this is unclear at present, though problems with the polymer insulation layers, such as swelling or local adhesion failures, may be responsible.

5.5.2 Nanoelectrode Arrays Fabricated by Nanoimprint Lithography

5.5.2.1 Fabrication Considerations

The NIL process, which was described in Section 2.4.2.1, requires the fabrication of a nanostructured stamp. Therefore, to imprint the nanoelectrode arrays, silicon stamps that

comprised an array of pillars with a 250 nm radius and an overall geometric area and spacing equivalent to the 250 nm electrode array pattern described previously (Table 5.1) were fabricated (see Section 3.3.2.2). Figure 5.16 shows SEM images of such a silicon stamp. After imprinting 8 samples, the largest number imprinted with the one stamp, no changes in the structure of the stamp were observable when re-examining it by SEM.

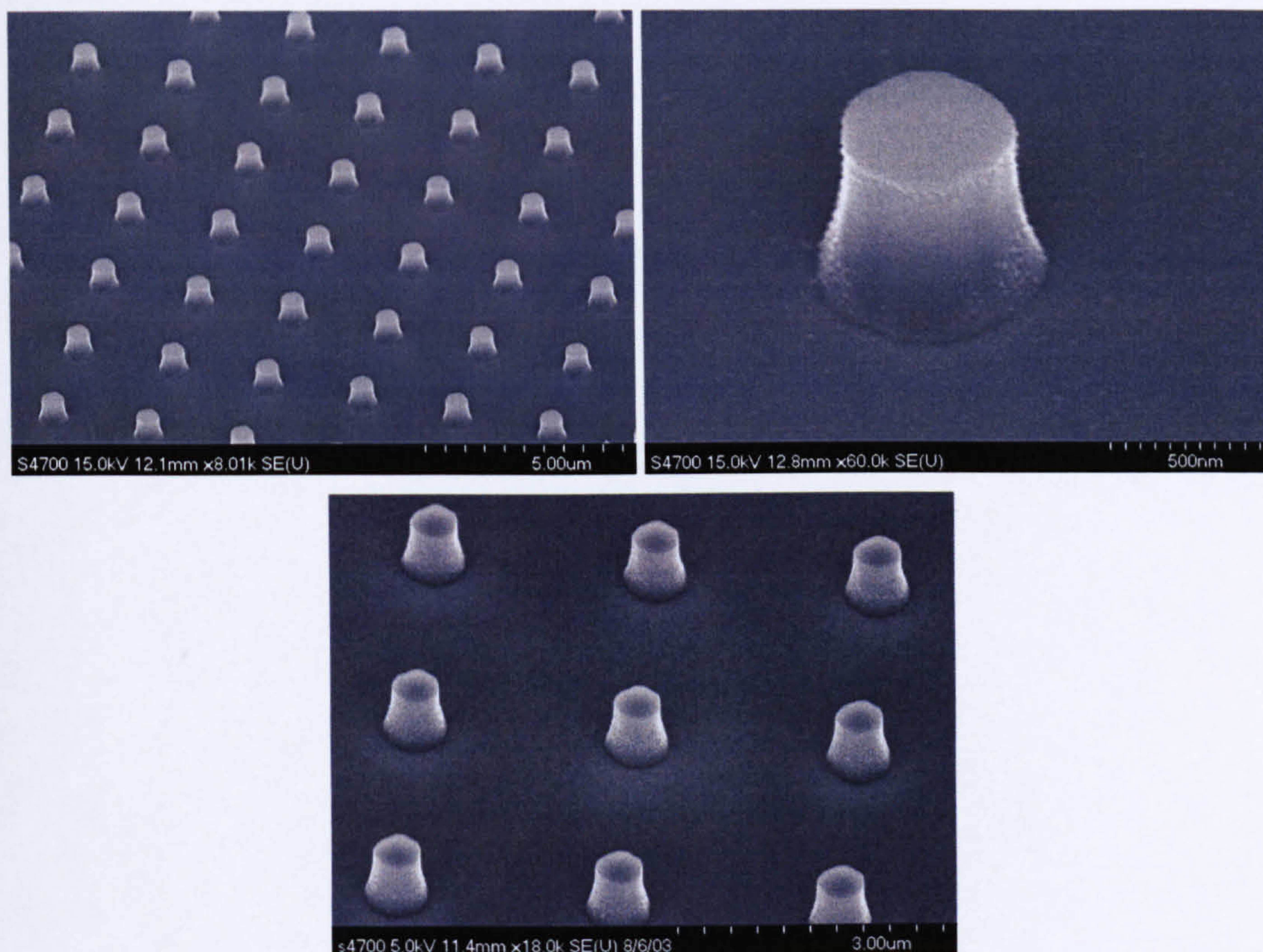

Figure 5.16 **A Silicon NIL Stamp**

An array of 250 nm radius silicon pillars. The upper two micrographs show the stamp prior to imprinting, whilst the bottom micrograph shows the stamp after 8 NIL cycles.

The patterns generated by NIL are strongly dependant upon the pressure, temperature and time parameters employed. Values similar to those found in the literature (Chen *et al*, 2002) were used when fabricating the nanoelectrode arrays. Small variations in conditions appeared to significantly change the morphology of the resulting insulation layer, as is illustrated in Figure 5.17, where an AFM image of an array patterned by direct-write EBL is also shown for comparison. Should NIL be selected as the method for patterning the insulation layer in the future, a detailed study of the effect of each of the controllable parameters would be desirable.

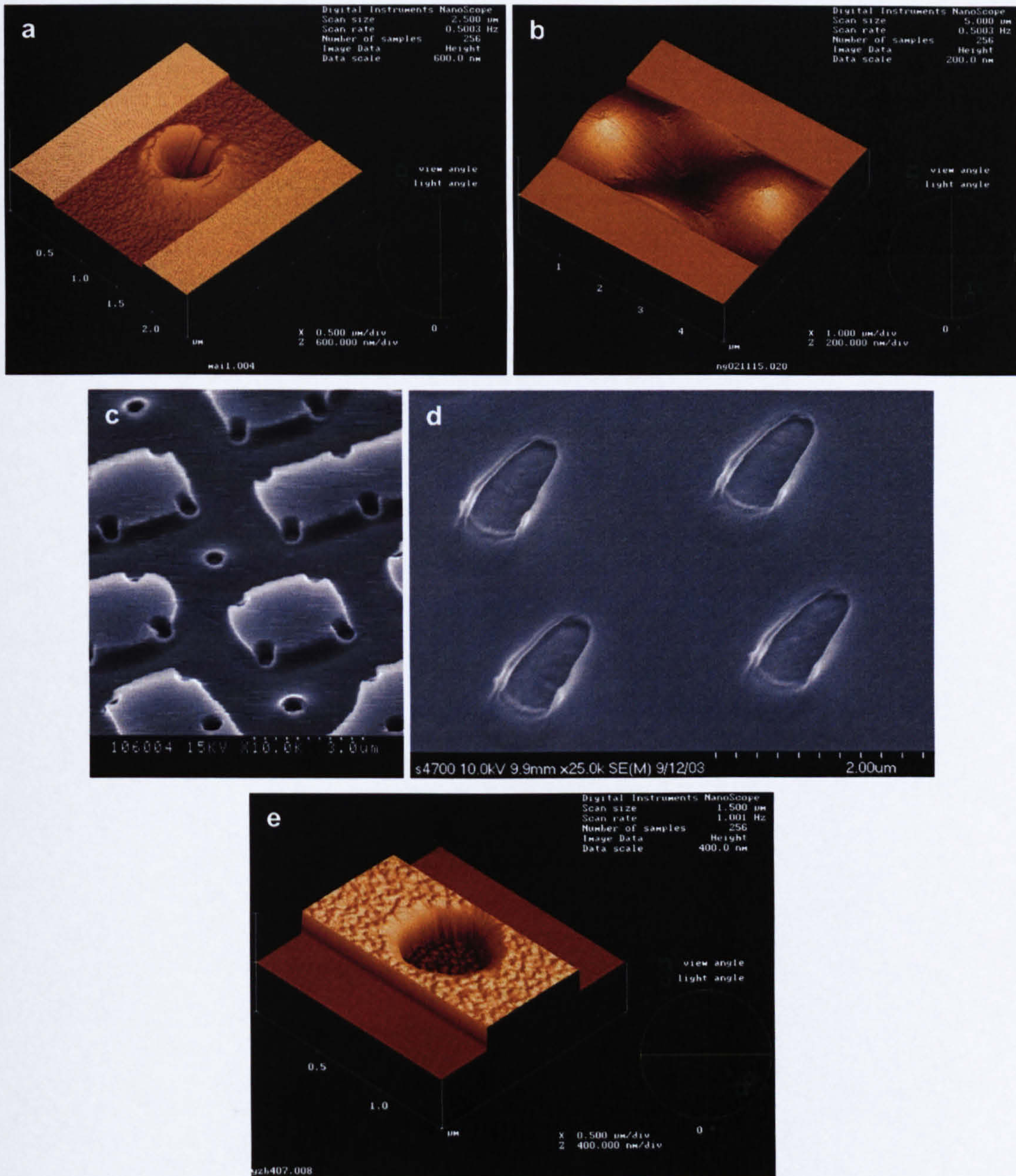

Figure 5.17 **Insulation Layers Patterned by NIL and EBL**

a. A PMMA insulation layer imprinted at 170°C and 30 Bar for 5 minutes. All the electrodes had a similar volcanic profile, attributable to a build up of the material that was forced outwards from beneath the pillar, with a flat interelectrode area. b. Another PMMA layer, imprinted at 180°C and 25 Bar for 5 minutes, with a cross-sectional profile similar to a sine wave. c. A S1805 insulation layer (the S1805 having initially been diluted 1:1 with EC solvent) imprinted at 120°C and 10 Bar for 5 minutes, which displays a large, but regular, variation in height. It is thought that this strange topography may be attributable to a surface wetting effect. d. A third

PMMA sample imprinted at 180°C and 15 Bar for 5 minutes. Here, however, the pressure was released before the sample had been adequately cooled, and lateral slippage of the stamper through the soft PMMA can be clearly seen. e. A PMMA electrode produced by direct write EBL.

After imprinting a sample, a small thickness of the resist remained at the bottom of the newly formed holes, which had to be removed by oxygen plasma etching. This was slightly problematic as the thickness of the material to be removed was unknown and, therefore, so was the appropriate etch time. Etching the sample for short periods of time in a barrel asher and then testing it until the all the resist was removed and a signal was obtained proved the most effective, if time consuming, method. The excess resist could also be removed by RIE in an Oxford Plasma Technology BP80 machine using a C_2F_6 plasma, though the etch rate for this was substantially quicker (approximately 50 nm min^{-1} for PMMA) and, thus, the samples could easily be over-etched. Nonetheless, the latter is an anisotropic procedure and is therefore preferable to the former, particularly if the thickness of the remaining resist at the bottom of the features could be monitored during the RIE process, for instance by laser reflectometry (Hicks *et al*, 1994).

5.5.2.2 Voltammetric Studies

Figure 5.18 shows a cyclic voltammogram obtained from an imprinted PMMA sample, whose average individual electrode radius, after oxygen plasma etching, was estimated by SEM to be 340 nm (with a resulting *d/r* ratio of 7.4). A voltammogram recorded with the direct-write 300 nm array (with a *d/r* ratio of 8.3) is also shown for comparison. As expected from these geometries, the peak current generated by the imprinted array is slightly larger than that generated by the directly written array.

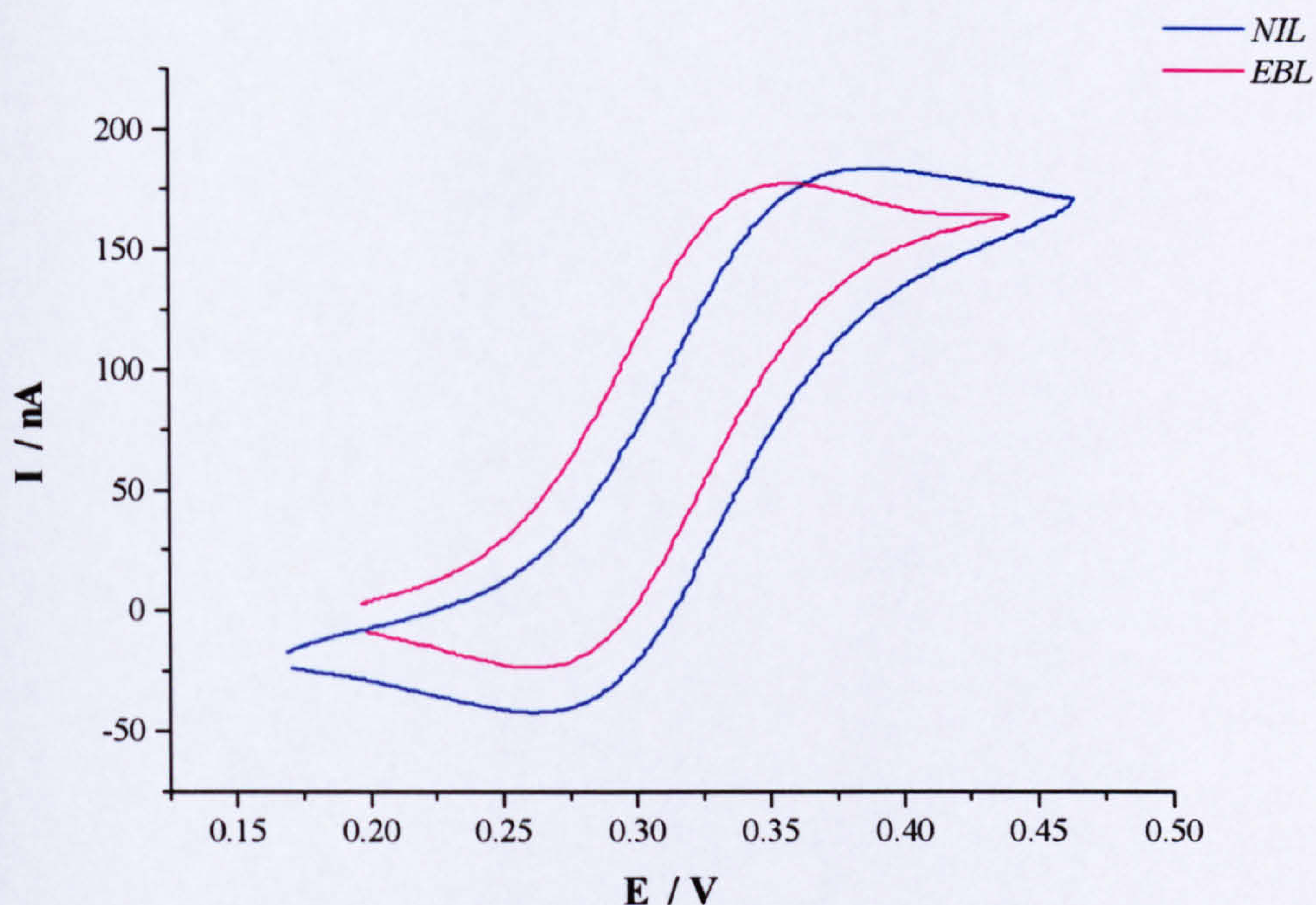

Figure 5.18 **Cyclic Voltammograms Recorded with Nanoelectrode Arrays**

Voltammograms were recorded at 10 mV s^{-1} in a 1 mM FMCA solution. The blue trace was recorded using an imprinted nanoelectrode array, whilst the pink trace was recorded using an array patterned by electron-beam lithography.

5.6 Conclusion

A range of microelectrode arrays with varying individual electrode radii and centre-centre spacings has been systematically investigated. For d/r = 10, microelectrode arrays with an individual electrode radius of 25 μm and 50 μm demonstrated sigmoidal behaviour. However, as r decreased, the recorded voltammograms became increasingly peak-shaped, due to the increased linearity of the diffusion fields. Nonetheless, the peak current densities were the largest for the microelectrode arrays with the smallest individual electrodes. To achieve radial diffusion to a microelectrode array with an individual electrode radius of 2.5 μm, an approximate centre-to-centre spacing of d/r = 40 was required. As expected from simulation work in the literature, loosely packed arrays produced significantly higher current densities than arrays with small centre-centre spacings, due to the merging of individual diffusion fields in the latter case.

When designing an electrochemical sensor that incorporates a microelectrode array, the optimum geometry of the array will depend upon the proposed application and operation of the sensor. For voltammetric microsensors, loosely packed arrays are advantageous, as it permits the acquisition of steady-state measurements and the use of very fast scan-rates. Furthermore, if a flow-independent sensor is desirable, radial diffusion will minimize the convection dependence of the sensor. In situations where radial diffusion is desirable, it has been demonstrated that the smaller the individual electrodes of an array, the greater the relative inter-electrode spacing required. For a steady-state amperometric sensor, a high SNR is generally the main concern. Small individual microelectrodes with small centre-centre spacings have been shown to produce large SNRs, with the electrodeposition of platinum black increasing the SNR further. However, if fast response times are required or the chronoamperometric sensor is to be operated continuously, a large d/r ratio and a small individual electrode radius may again be preferable, so that a steady state current may be reached in short time.

The benefits of these different diffusion regimes to a microelectrode array can be further enhanced by continuing to decrease the size of the individual electrodes. Arrays of nanoelectrodes were fabricated using conventional direct write EBL and the voltammograms obtained from them exhibited a continuing increase in the recorded peak current as the individual electrodes radius was decreased to a value of 110 nm. As EBL is a slow and costly technique that is not widely available, NIL was investigated as an alternative method of producing nanoelectrode arrays and was found to be a promising rapid fabrication technique.

CHAPTER 6

DESIGN, FABRICATION AND CHARACTERISATION OF A DISSOLVED OXYGEN AND TEMPERATURE MICROSENSOR

In Chapter 5, the electrochemical characteristics of a range of microelectrode arrays were investigated. Conclusions drawn from this study were subsequently applied to the design of a Clark-type electrochemical dissolved oxygen sensor with an integrated thermal resistor for the monitoring of freshwater environments. After presenting an overview of current dissolved oxygen sensor technologies, the design and fabrication of this microsensor will be described and the results of the calibration and stability measurements that were employed to characterise the device will be discussed.

6.1 Overview of Current Dissolved Oxygen Sensor Technologies

The measurement of oxygen levels is necessary for numerous industrial processes and for a wide range of scientific research. Current applications of oxygen sensors include (Akmal and Lauer, 1998): use in manufacturing plants (such as those involved in the production of semiconductor devices, chemical synthesis, oil refining, fermentation and the preparation of foodstuffs), combustion systems (including those in power stations and automotive engines), medical processes (for example the measurement of blood oxygen levels, the treatment of cardiovascular and respiratory disorders and the determination of aerobic fitness) and environmental monitoring (notably for the detection of pollution in aquatic systems). The dissolved oxygen sensor described in this chapter was developed for freshwater environmental analysis (as was discussed in Section 1.1.3), although it could readily be employed in a variety of other applications.

The level of dissolved oxygen in a freshwater habitat is obviously critical to the survival of the animal life that it supports. As such, the concentration of dissolved oxygen is a marker of

freshwater quality that may be monitored to highlight any variation in local environmental health. A similar marker of the general health of a freshwater ecosystem is the biological oxygen demand, BOD, which indicates the level of contamination due to organic matter (Encyclopaedia Britannica). The majority of organic pollutants are degraded by the metabolic activity of microorganisms. As the concentration of organic contaminants rises, an increase in the overall micro-organism population would be observed, with a corresponding decrease in the level of oxygen available for higher animal species (due to the increased respiratory activity of the microorganisms). Therefore, BOD is defined as the quantity of oxygen consumed by the metabolic activity of microorganisms when a freshwater sample is incubated for a specific period of time, typically five days.

The most common dissolved oxygen sensors employ an electrochemical or optical method of detection, both of which will be discussed in the following sections. Temperature compensation will also be considered, as dissolved oxygen concentrations are strongly temperature dependent, with the concentration of a saturated solution decreasing with increasing temperature. It should also be noted that an increase in the salinity, a decrease in barometric pressure or an increase in the elevation above sea level would also result in a decrease in the saturated oxygen concentration.

6.1.1 Electrochemical Microsensors

Electrochemical oxygen sensors may be categorised into three classes: galvanic, solid state electrolytic or the classical Clark-type amperometric/voltammetric sensor (Akmal and Lauer, 1998). This discussion will focus on the latter.

If a noble metal electrode is held between –(0.6-0.8) V vs. Ag|AgCl and is immersed into a sample solution, dissolved oxygen will be reduced at the electrode surface and a time-dependant current profile will be observed, as discussed in Chapter 4. At a specified time after the application of the potential step, the resulting current is then measured and compared to a calibration chart to determine the partial pressure of dissolved oxygen. If the applied potential is carefully selected, the current output of the electrode will be diffusion-limited whilst other interfering electrochemical reactions, such as hydrogen evolution, will not take place. At an appropriately polarised electrode, the reduction of dissolved oxygen occurs through a four-electron pathway (Koryta *et al*, 1993):

$$O_2 + 2H^+ + 2e^- \rightarrow H_2O_2 \quad (6.01)$$

$$H_2O_2 + 2H^+ + 2e^- \rightarrow 2H_20 \quad (6.02)$$

Many improvements to the electrochemical measurement of oxygen were made during the late 1950s, the most significant being the development of the "Clark" oxygen electrode (Clark, 1956), where both the cathode and anode were protected by a gas-permeable membrane. Hence, deactivation of the electrode by surface passivation or mechanical damage was considerably reduced. Furthermore, the reference electrode and electrolyte could be placed behind the membrane alongside the cathode and anode. Currently, membrane-enclosed electrode systems are the preferred option for the real-time measurement of dissolved oxygen.

Since the early 1980s, a variety of miniaturised Clark-type dissolved oxygen sensors have been reported in the literature. Initial examples include the work of Koudelka and Grisel (1985) who fabricated a two-electrode microsensor with a single-electrode cathode, a hydrogel electrolyte layer and silicone rubber membrane. Suzuki *et al* (1988 and 1991) developed a sensor where the anode was situated within two v-grooves that had been etched into a silicon wafer, whilst the working electrode was placed on the flat area between the two grooves. A photoresist chamber, which enclosed both the recessed anode and the cathode, was patterned onto the silicon substrate and was subsequently filled with a polyelectrolyte solution and covered with a dual photoresist-silicone rubber membrane (use of the photoresist reportedly improved the adhesion of the membrane). Although the linearity of this sensor was satisfactory for high oxygen concentrations, the response was not linear for lower concentrations, most probably due to electrochemical crosstalk.

Several dissolved oxygen sensors incorporating microelectrode arrays were reported in the 1990s (Yu-Quan and Guang, 1993; Arquint *et al*, 1994; Wittkampf *et al*, 1997). Arquint *et al* described the development of a blood gas analyser for measuring dissolved oxygen, carbon dioxide and pH levels. They employed a three-electrode Clark-type oxygen sensor that incorporated a working microelectrode array (a 9 x 8 array of 5 μm platinum electrodes with a *d/r* ratio of 40), a Ag|AgCl reference electrode, a hydrogel electrolyte and a silicone rubber membrane. Excellent linearity was achieved when calibrating this sensor (with a correlation coefficient of 0.9998), which was successfully operated for more than two months. The main difficulties concerning this sensor were related to adhesion of the membrane and variation in the chloride ion concentration of the hydrogel layer (see Section 6.1.1.1).

In recent years, the development of solid-state sensors has continued (Choi *et al*, 2001; McLaughlin *et al*, 2002). For example, McLaughlin *et al* reported the development of dissolved oxygen microsensor for biomedical and industrial applications that incorporated a solid Nafion™-based proton conductive matrix in place of an electrolyte solution or gel. The matrix also incorporated poly(vinylpyrrolidone) (PVP) to improve its adhesion to the underlying electrodes and the complete device was encapsulated with a PTFE coating. Good linearity of the sensor response (with a correlation coefficient greater than 0.96) and fast response times (where a steady state was achieved approximately 5 s after application of potential step) were obtained. However, further optimisation of the matrix composition and uniformity is required.

Dissolved oxygen microsensors may also be adapted for the determination of BOD by depositing an appropriate microbial membrane (Liu *et al*, 2000). The bacteria should metabolise any organic material in the test sample, thus reducing the output signal, relative to a standard solution, by an amount dependant upon the level of biodegradable compounds in the sample. Microorganisms that respond strongly to a wide range of organic material are most desirable. Though fast response times have been achieved (Yang *et al* (1996) acquired the relevant data within 20 minutes), BOD microsensors still present considerable difficulties for continuous, long-term monitoring applications – notably good reproducibility is extremely difficult to maintain, particularly from the mixed bacterial populations required for broad-spectrum waste-water monitoring (Tan *et al*, 1993).

However, it is not only the incorporation of microbial membranes that has presented problems: the creation of a stable, durable micro-reference electrode and the prevention of surface passivation by biofilm growth are both critical to the performance of any *in situ* electrochemical microsensor and both have proved extremely difficult to achieve.

6.1.1.1 Micro-reference Electrodes

As discussed in Section 4.1, the fundamental characteristic of a reference electrode is its non-polarisability, that is the potential at the electrode surface will remain virtually constant and will be independent of any current flowing through the electrode (assuming that the

current is relatively small) [1]. This behaviour stems from the inherently fast reaction kinetics at the electrode, which implies a large exchange current density for the system. Should an electrode structure that did not behave as a non-polarisable electrode under experimental conditions be employed as the reference, any changes in the potential at the reference electrode (as a consequence of current flowing through it) would modify the potential at the working electrode and consequently affect its output current.

One of the simplest and most widespread electrochemical reference systems is the Ag|AgCl electrode, where a silver chloride film is chemically or electrochemically grown over the surface of a silver electrode, which is subsequently immersed in a saturated solution of an alkali-chloride salt. For moderate current flows, the silver chloride layer, which is only sparingly soluble, is in equilibrium with both the silver electrode and the chloride ions and the composition of the Ag|AgCl|Cl system remains virtually constant, resulting in a stable electrode potential (Koryta *et al*, 1993). The reaction taking place at the electrode is:

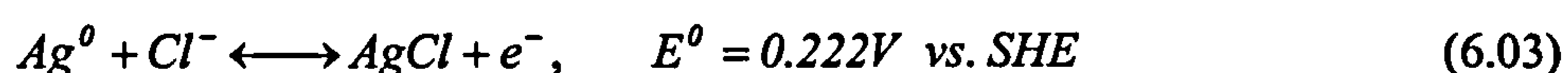

$$Ag^0 + Cl^- \longleftrightarrow AgCl + e^-, \qquad E^0 = 0.222V \;\; vs.\, SHE \tag{6.03}$$

where the rate constants for the forward and the backward reactions are both very large, giving rise to a high exchange current density. As the potential at the electrode-electrolyte interface is a function of the chloride ion concentration only, the Nernst equation for the Ag|AgCl system may be written as (Bard and Faulkner, 2001):

$$E_{Ag/AgCl} = E^0{}_{Ag/AgCl} - \frac{RT}{F} ln\left[Cl^-\right] \tag{6.04}$$

$$= 0.222 - 0.0591 log\left[Cl^-\right] \qquad (at\ 25°C) \tag{6.05}$$

Thin film Ag|AgCl electrodes can be produced by either physical deposition (evaporation or sputtering) of a silver layer followed by electrochemical growth of the silver chloride film or by electroplating both layers onto a base metal electrode. Thicker silver layers, and consequently thicker silver chloride layers, may be achieved when employing the latter, which, for the plating solutions given in Section 3.3.3.2, proceeds as follows:

---

[1] As described in Figure 4.5, negligible current should flow through the reference electrode when using a three-electrode potentiostatic system. However, in a simple two-electrode configuration, which is often sufficient for microelectrode applications, current will pass through the reference electrode.

Silver Deposition: $AgI_2^- + e^- \longrightarrow Ag_{(s)} + 2I^-$ (6.06)

Silver Chloride Growth: $Ag_{(s)} + Cl^- \longrightarrow AgCl_{(s)} + e^-$ (6.07)

As discussed by Suzuki *et al* (1999), the silver chloride layer is generated through the growth of silver chloride mounds. Therefore, the resulting film thickness is not uniform across the entire surface, particularly at the beginning of the electrodeposition process. Indeed, a thick silver chloride layer is required to ensure complete coverage of the silver electrode, which is necessary to prevent the electrolyte solution from permeating into the Ag|AgCl interface, resulting in the creation of a polarisable electrode. Furthermore, strong adhesion of the silver layer to the underlying metal is essential and both the silver and silver chloride layers should be grown in a controlled manner so as to avoid weak adhesion or high porosity. Deposition of a thick silver layer and optimisation of electroplating conditions to ensure a high transformation ratio of silver-to-silver chloride will aid the production of a durable Ag|AgCl reference electrode.

Several difficulties have been encountered when working with thin-film Ag|AgCl electrodes (Suzuki *et al*, 1998a, 1998b and 1999) including the non-negligible solubility of silver chloride, which is more problematic for the thin layers found in micro-reference electrodes than for commercial Ag|AgCl macroelectrodes - the thicker the silver chloride layer, the longer the lifetime of the reference electrode. If the Ag|AgCl electrode is in direct contact with a sample solution, the electrode potential will be subject to any variations in the chloride ion concentration of the sample, as determined by the Nernst equation. Such variations can be prevented by placing the reference electrode in a chamber with a solution of constant chloride ion concentration, which is covered with a membrane that is impermeable to chloride ions but permeable to the electroactive species (oxygen in this case).

An unavoidable liquid junction potential will then arise at the interface of the internal and external solutions, that is, across the chamber membrane. This potential will vary with any changes in the internal or external environments and will be affected by any fouling of the membrane. However, if both the working electrode and the reference electrode can be placed within the chamber, the liquid junction potential should not influence the potential at either the reference or working electrode. In that case, fouling of the chamber membrane would

only hinder the diffusion of the electroactive species from the sample solution to the electrode surface. Nonetheless, an antifouling strategy may be required to minimise such fouling.

6.1.1.2 Biofouling

Raw industrial, biomedical or environmental samples are significantly more difficult to analyse than standard laboratory test solutions. Most "real" samples will generate a significant degree of biofouling - the adsorption of proteins and other non-specific materials onto a clean surface that passivates the surface and encourages cellular attachment and the growth of a biofilm (Johnston and Ratner, 1998). As the formation of a protein layer or cellular biofilm would seriously degrade the performance of an electrochemical microsensor, and may possibly result in the complete failure of the sensor, a reliable anti-fouling strategy must be employed when analysing raw samples.

Surface modification with polymers such as poly(ethylene oxide) (PEO) and poly(ethylene glycol) (PEG) has been employed to reduce protein and cellular adsorption without altering the functionality of a device (Johnston and Ratner, 1998; Ratner, 1995). Various techniques can be used to immobilize these polymers, including RF plasma deposition, which produces a pin-hole free covering that is normally highly stable in water. (Delamination of polymer coatings in aqueous environments is a common problem for many other techniques including covalent attachment methods.) However, surface modification alone does not present a long-term solution to biofouling, as it has been demonstrated that this strategy generally only delays or limits protein adsorption (Fuhr *et al*, 1995).

Another common antifouling technique is to coat the active surface with a semi-permeable protective membrane (such as Nafion™, cellulose acetate or PTFE) that excludes any fouling materials but allows for free passage of the analyte. The groups of Buffle and Koudelka-Hep investigated the performance of a thick agarose layer as an antifouling membrane (Belmont-Hebert *et al*, 1998; Tercier *et al*, 1996). Agarose, which forms a rigid, neutral gel that is resistant to enzymatic hydrolysis, was shown to effectively prevent biofouling from raw river water samples, without reducing the sensitivity of the sensor. The diffusion coefficients of various mono- and divalent ions were shown to be approximately three times smaller within the agarose gel than in free solution. Furthermore, it was necessary to equilibrate the sensors with the sample solution prior to the acquisition of data, so as to enable the concentration of the analyte within the gel to become equal to that of the

sample solution. The required equilibration time was shown to vary linearly with the thickness of the agarose layer.

Attachment of cellular and colloidal particles can also be controlled by dielectrophoresis (DEP), a technique where non-uniform AC electric fields act upon polarisable particles to either attract them (positive DEP) or repel them (negative DEP) from regions of high field. Although there is a vast body of literature concerning dielectrophoretic behaviour and applications, very few research groups have studied its potential as an anti-fouling strategy. A silicon microfilter incorporating an array of interdigitated microelectrodes that are energised to repel microorganisms from the filter surface has been developed (Gastrock *et al*, 2000) and some initial experiments on cell repulsion using ultramicroelectrodes have been undertaken (Fuhr *et al*, 1995), yet further research into the effectiveness of this technique is required. This will be considered further in Chapter 7.

Finally, it should be mentioned that, whatever antifouling strategy proves to be the most successful for a particular application, it is likely that a combination of techniques would be required to adequately minimise the biofouling resulting from raw samples. For instance, a preliminary sedimentation or filtration chamber followed by one or more of the antifouling techniques discussed previously may be necessary for a freshwater monitoring system.

6.1.2 Optical Microsensors

Optical microsensors commonly measure dissolved oxygen levels by monitoring the quenching of an oxygen-sensitive fluorophore embedded in a transparent matrix (McEvoy *et al*, 1996; McDonagh et al, 1998; Malins *et al*, 1999). The solubility of oxygen and the diffusion co-efficient of the fluorophore within the matrix determine the quenching response of the sensor. The sol-gel process, where a silicon alkoxide undergoes hydrolysis and condensation reactions to produce a nanoporous silica film, is commonly used to entrap the oxygen-sensitive dye (for example a ruthenium complex) in an oxygen permeable matrix. Fast response times, of the order of 10 s, and a high degree of specificity may be obtained with optical microsensors. However, various fabrication and experimental concerns still need to be addressed, including optimisation of the sol-gel process, batch-to-batch reproducibility, leaching of the fluorophore and biofouling of the sensor surface.

6.1.3 Temperature Compensation

As previously mentioned, the concentration of a saturated dissolved oxygen solution decreases with increasing temperature. For a temperature range of 0-20°C, the approximate annual variation for local rivers, the saturated concentration range extends from 9.1 mg O_2 L^{-1} to 14.6 mg O_2 L^{-1} at sea level. To compensate for this substantial variation with temperature, a range of thermal sensing devices may be incorporated into a dissolved oxygen monitoring system. For example, thin-film thermocouples, which exploit the thermoelectric "Seebeck effect" [2], have been successfully employed as temperature sensors. The simplest thermocouple measurement systems incorporate two metal junctions, a reference junction and sensing junction, made from the same two metals. Thermal isolation of the reference junction, which must be at a constant temperature, is essential for accurate temperature measurement, as is the relative choice of metals. Various thin-film metal combinations have been explored including platinum/palladium (Kreider and DiMeo, 1998) and indium-tin oxide/antimony-tin oxide (Kreider, 1992). However, it is often not feasible to maintain the reference electrode at a constant temperature, for instance when the entire device is to be in contact with the test solution. Frequently used alternatives include diodes, thermistors and thermal resistors.

As the current-voltage characteristics of a diode vary with temperature, according to Equation 6.08 (where V_D is the voltage across the diode, I_D is the current and I_S is the saturation current), diodes may be employed as a temperature sensor (Johannessen, 2001):

$$V_D = \frac{kT}{q} ln\left(\frac{I_D}{I_S}\right) \qquad (6.08)$$

Thermistors are semiconductor devices, generally composed of a sintered mix of metal oxides, that possess a large, negative temperature co-efficient and a tight conformity to standard reference curves (Horowitz and Hill, 1989). However, the simplest temperature sensors are pure metal resistors, which have a positive temperature co-efficient. The chosen metal should conform strictly to a standard resistance-temperature curve, possess a large temperature co-efficient and be stable over time. Platinum thermal resistors display all these characteristics and are therefore relatively common, though somewhat expensive. Several instrumentation designs may be employed to monitor the variation in resistance with

---

[2] The Seebeck effect describes the generation of a temperature dependant voltage (typically in the mV range) that occurs at the junction of two dissimilar metals.

temperature, including a simple potential divider circuit with a fixed temperature reference (see Section 3.4.2). To avoid the need for such a reference, an alternative approach would be to employ a constant current source and to monitor the variation in the voltage across the thermal resistor with temperature.

6.2 Microsensor Design and Experimental Methods

As demonstrated in Chapter 5, high signal levels and enhanced SNRs may be obtained when using densely packed arrays of increasingly small microelectrodes. Therefore, such a microelectrode array was incorporated into an electrochemical dissolved oxygen microsensor with integrated temperature compensation. Previous experimental findings and suggestions from the literature reviewed were also taken into consideration when designing the sensor.

6.2.1 Microsensor Design

The design of the dissolved oxygen and temperature microsensor integrated a two-electrode amperometric sensor with a thin-film thermal resistor. Chronoamperometry was selected as the method of detection, as the concentration of the analyte is directly proportional to the recorded current and so no signal processing is necessary after the data has been collected and no complex instrumentation is required – indeed, a stable power supply and a precision ammeter would be sufficient. A densely packed array of microelectrodes, with a design similar to those described in Section 5.1.1, was employed as the working electrode. The centre-centre distance from one corner electrode to the next was 700 μm and an individual electrode radius of 2.5 μm and a *d/r* ratio of 5 were employed. (A slightly smaller individual electrode radius could have been employed but the yield of successfully fabricated devices would most probably have been lower.) For initial testing procedures, geometries previously used in the experimental work reported in Chapter 5 were also employed. Use of these sensors is noted alongside the appropriate experimental results.

An electroplated Ag|AgCl electrode was employed as the reference electrode, with an overlying agar electrolyte gel (containing KCl) providing both the chloride ions necessary for the operation of the reference electrode and acting as a protective barrier to limit the extent of electrode fouling. The area of the reference electrode prior to electroplating was 2.15 mm^2 (34 times larger than that of the working electrode active area). The thin-film

thermal resistor was 25 μm wide and was coiled around the sensor to increase its total length to 76 mm. All the microfabrication protocols necessary for the production of the microsensor, the construction of which is detailed in Figure 6.1, have been described in Chapter 3.

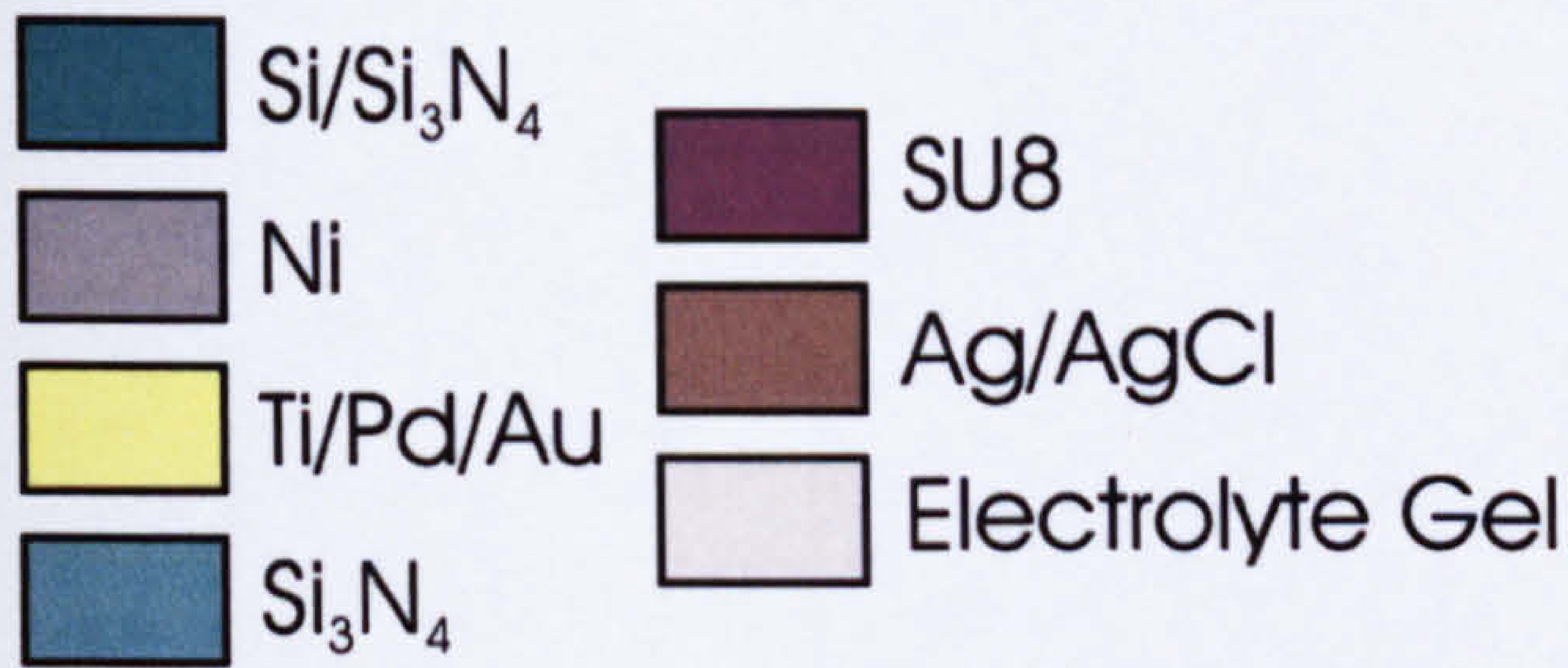

Left:
Legend for Figures 6.1a-6.1d. Figures 6.1a-6.1c are plan views of various layers within the sensor, whilst Figure 6.1d is a cross section of the completed sensor.

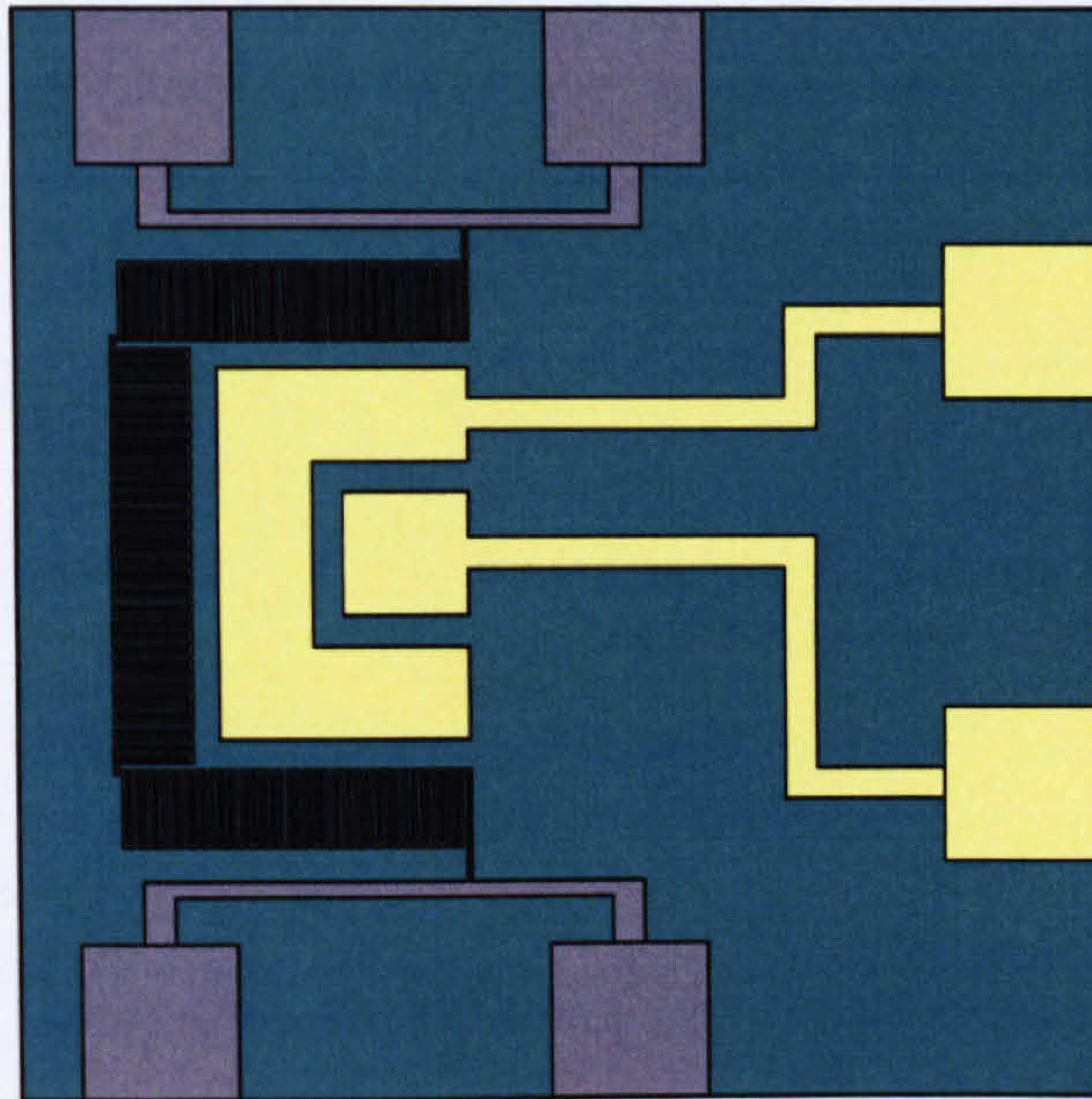

Figure 6.1a (right):
An n-type Si(100) wafer, coated on both sides with 200 nm SiN, was first cleaned with Opticlear, Acetone and Methanol. After patterning a layer of photoresist, 10 nm NiCr and 100 nm Ni were evaporated onto the substrate and lifted-off to produce a thermal resistor. Gold base electrodes were also patterned by lift-off, using a 10 nm Ti, 10 nm Pd and 100 nm Au layer.

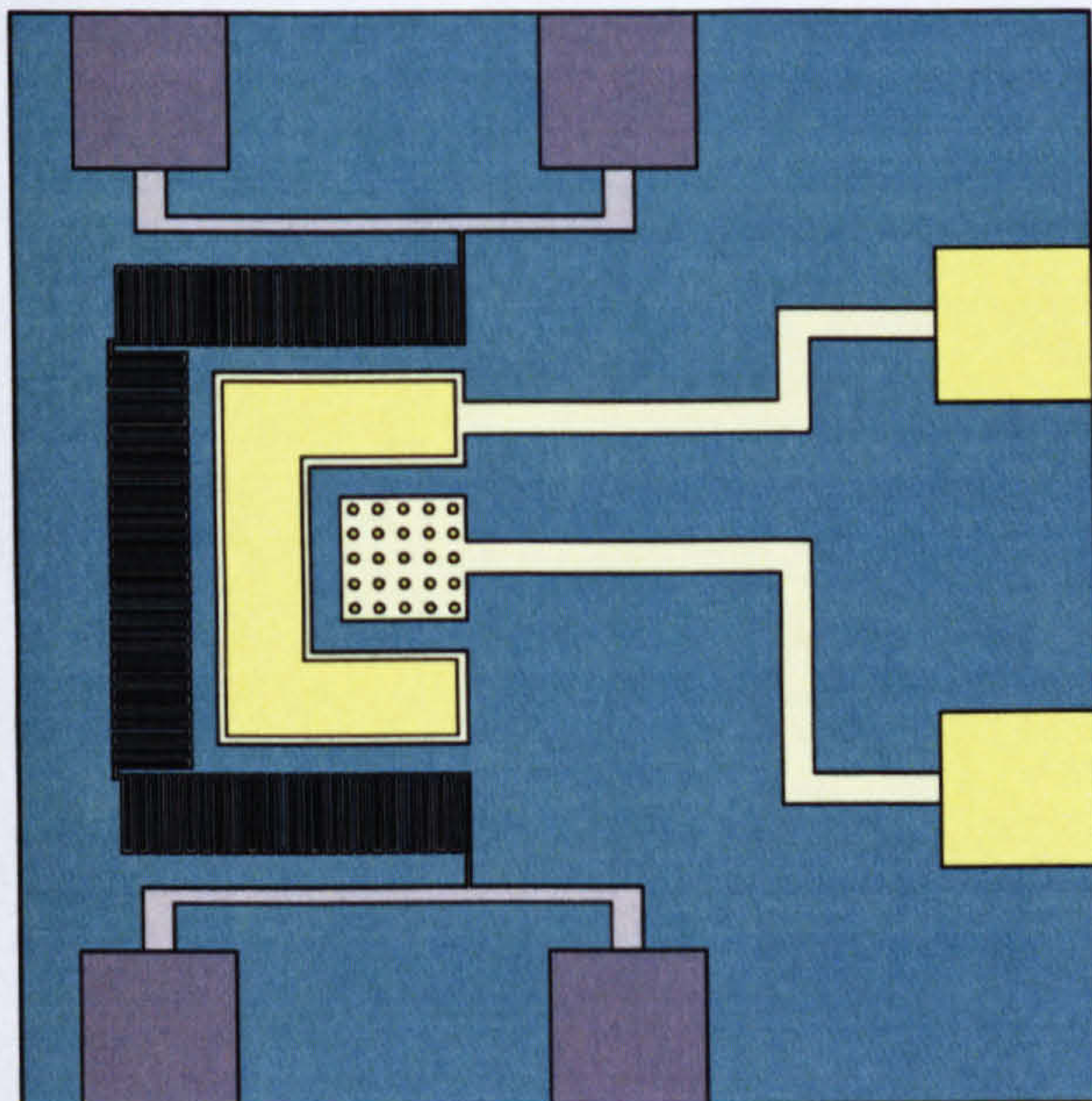

Figure 6.1b (left):
A 500 nm low-stress PECVD SiN layer was then deposited over the metal layers. RIE was employed to open up the bonding pads, the reference electrode and to create an array of microholes over the working electrode.

Figure 6.1c (right):

To contain the electrolyte gel, a 250 μm deep SU8 chamber, with a volume of 1 μl, was patterned over the SiN layer. To create the reference electrode, a layer of silver was electroplated through the SiN insulation layer and then oxidised to produce a Ag|AgCl film.

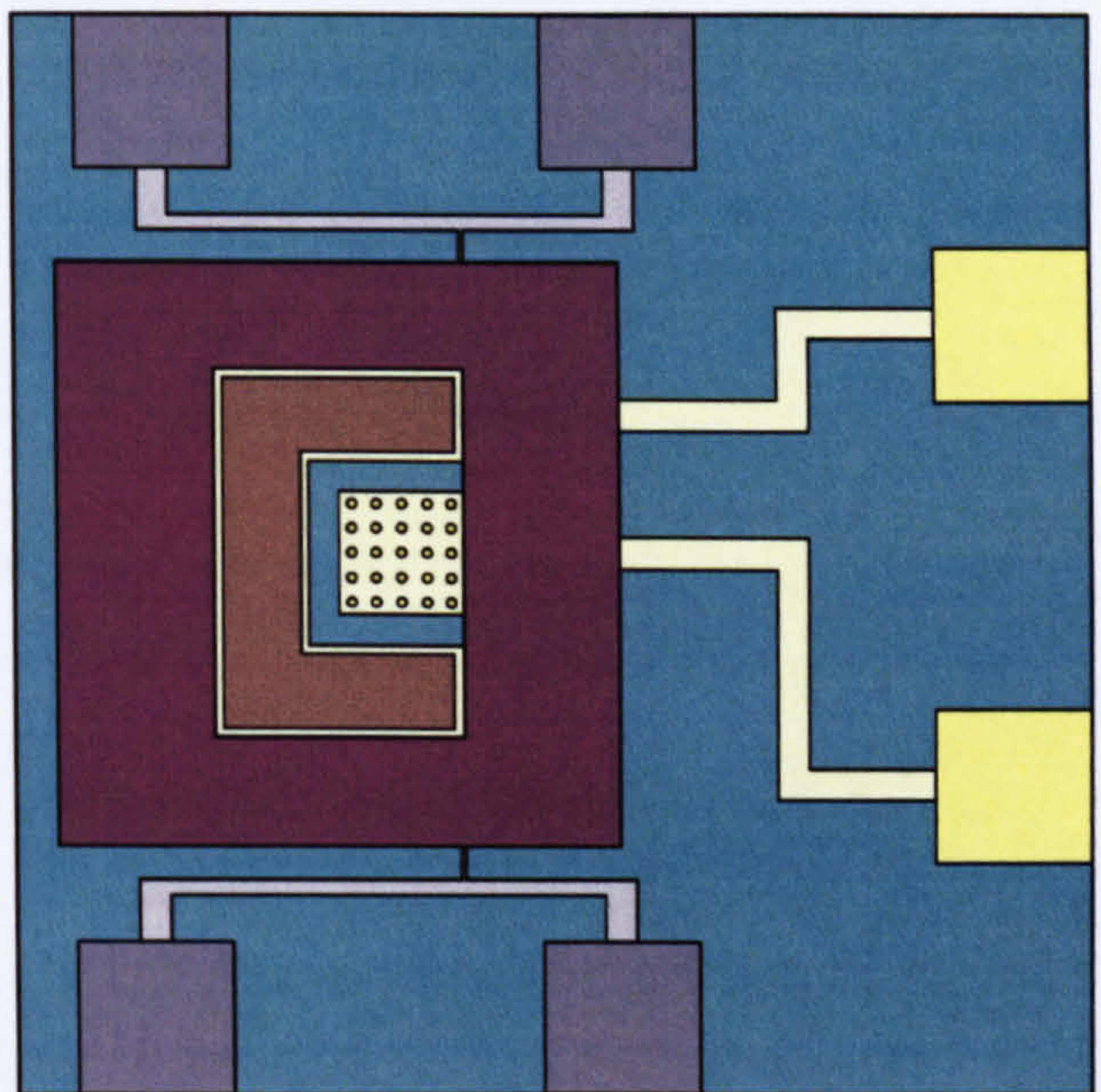

Figure 6.1d (below):

Prior to use, the chamber was filled with an agar electrolyte gel by either dip-coating or casting.

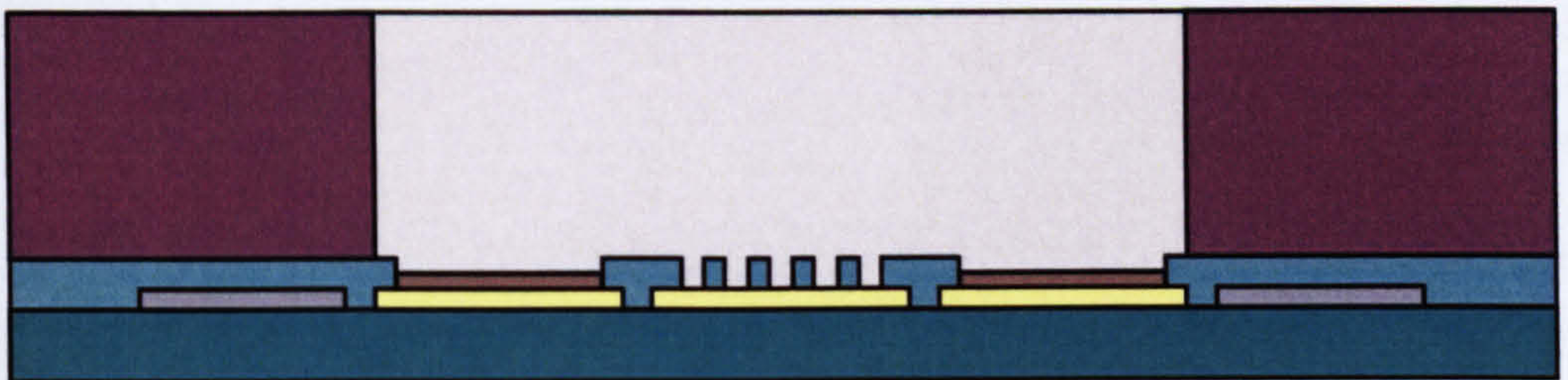

Figure 6.1 **Schematic Diagram Illustrating the Structure of the Dissolved Oxygen and Temperature Sensor**

6.2.2 Experimental Methods

To dispense the electrolyte gel into the chamber of the dissolved oxygen sensor, both dip-coating and casting were employed. In both cases, 3% w/v agarose powder was sprinkled onto a 1 M KCl solution, which was then heated on a hotplate at 100°C until the agarose had completely dissolved. When casting the gel, the sensor was placed on the hotplate, which had been cooled to below 80°C, and a small drop of the agarose was injected into the chamber using a heated needle. The sensor was then immediately removed from the hotplate. When dip-coating the sensor, the sample was simply immersed into the heated solution and then slowly removed, allowing the excess solution to overflow.

The thermal resistor was calibrated using the apparatus detailed in Section 3.4.3. As the temperature range relevant to local freshwater environments is in the region of 0-20°C [3], measurements were initially obtained by placing the device in a beaker of partially melted ice, which was placed upon the combined hot-plate and stirrer. Once the initial values of *T1*, *T2*, *V1* and *V2* had been noted, the magnetic stirrer was switched on and a series of measurements were taken as the temperature of the water rose. As the temperature of the water approached room temperature, the hotplate was employed to further heat the water.

To calibrate the dissolved oxygen microsensor, the electrochemical measurement set-up described in Section 3.4.1 was employed, along with a container of water that had one hole drilled in its lid for the gas inlet pipe and another for the microsensor connecting leads. Prior to the start of the experiment, the appropriate gas mixture was first bubbled through the water for 10 minutes and was then diverted over the surface of the water until a stable response was observed. Chronoamperometric recordings were subsequently obtained. When investigating the response time, a saturated sodium sulphite solution was injected into air-saturated water so as to rapidly de-oxygenate the water. Air was bubbled through the water until the injection of the sodium sulphite, at which point the gas inlet pipe was removed from the beaker. To estimate the potential of the micro-reference electrode with respect to a commerical Ag|AgCl electrode, cyclic voltammograms were recorded in a 1 mM FMCA, 10 mM PBS solution. Finally, the long-term stability of the micro-reference electrode was investigated using the apparatus described in Section 3.4.2 with a range of KCl solutions.

---

[3] Data obtained through correspondence with the Scottish Environmental Protection Agency (SEPA) showed an average seasonal variation in temperature from 5°C in January to 15°C in August for the River Kelvin in the year 2000. The most extreme values recorded at a single site in recent years were 0.5°C and 18°C.

6.3 Microfabrication Considerations

Various difficulties were encountered when fabricating the dissolved oxygen and temperature microsensor and the optimisation of a range microfabrication protocols was required. The following sections discuss the fabrication of each of the individual layers of the microsensor, the construction of which was outlined in Figure 6.1.

6.3.1 Metal Electrodes and Thermal Resistor

The thermal resistor was created from a 10 nm NiCr, 100 nm Ni film, as the temperature co-efficient of nickel (0.6253 % $°C^{-1}$ over the range 0-27°C) is the second largest of the metal elements, beryllium being the largest (Lide, 1993). It should be noted, however, that the variation in the resistivity of the noble metals is slightly more linear than that of nickel. The underlying metal structures for the working and reference electrodes were again created from a 10 nm Ti, 10 nm Pd, 100 nm Au film. Both lift-off (Section 3.3.1.4.1) and wet etching (Section 3.3.1.4.2) were employed to create the underlying metal electrodes and the thermal resistor. In the case of wet etching, different adhesive layers had to be used for the gold and nickel films to prevent any undercutting of the first pattern during the etching of the second. Naturally, any metal combinations could be employed when fabricating the second structure by lift-off. Furthermore, when wet etching, the nickel layer was patterned by an etchant (Table 3.1) that also slowly removed the photoresist mask, due to the inclusion of sulphuric acid. This meant that significant undercutting of the thermal resistor pattern was observed and, if the photoresist mask dissolved before the substrate had been removed from the etchant, the thickness of the resulting structure was reduced. Therefore, lift-off proved more suitable than wet etching for the patterning of the thin-film nickel resistors.

6.3.2 Insulation Layer

As discussed in Section 5.1.1, low-stress SiN proved to be the most satisfactory of the materials employed as a microelectrode array insulation layer and it was the only material available that was robust enough to withstand the subsequent fabrication steps. When removing the insulation layer covering the metal reference electrode pattern (Section 3.3.1.5.3), a band of SiN was left over the edge of the electrode structure so that none of the underlying titanium adhesive layer was exposed. Depending upon the applied voltage, titanium may be relatively easily oxidised, which would result in a shift in the potential of

the Ag|AgCl electrode and may possibly weaken the adhesion of the upper metal layers (Suzuki *et al*, 1998b).

6.3.3 SU8 Chamber

When developing a protocol for fabrication of the SU8 chamber (Section 3.3.4.1), which had a depth of approximately 250 μm and a volume of 1 μl, various difficulties were encountered, including adhesion failures, cracking of the resist and the presence of unwanted residues around the chamber walls. The processing of a thick SU8 film was therefore somewhat different to thin film processing discussed in previous chapters and the standard SU8 protocol was adapted as a result of repeated trials and information obtained from the manufacturers.

When dispensing the SU8, the sample was rotated by hand to ensure the entire surface was coated with the resist. Often the thickest SU8 formulations do not flow easily and so to enable spreading of these resists, the sample was very briefly heated on a hotplate to reduce the viscosity of the SU8. The temperature of the hotplate was relatively low (in the region of 60°C) and the sample was only placed on the hotplate for a few seconds, in order to prevent the SU8 solvent from evaporating. Prior to spinning the sample was left to relax for 1-2 hours, during which time any air bubbles, which often became trapped during the dispensing of the higher viscosity resists, rose out of the SU8 film. The spin-coating programme was comprised of three stages: firstly, the sample would be spun at a low rotational speed (300-500 rpm) when the majority of the excess resist would be thrown off the sample; secondly, the rotational speed would be slowly increased, allowing the gradual flow of SU8 across the sample surface; and finally, the sample would be held at a constant spin speed appropriate for the desired film thickness.

After spinning, the sample was again left to settle on a flat surface, so that the thickness of the edge beading was significantly reduced, resulting in a surface that was sufficiently level to achieve good contact with the mask plate during the subsequent exposure step. Similarly, when carrying out the pre-exposure softbake, the sample had to be placed on a level surface. Furthermore, to reduce the likelihood of thermal stress induced cracking and adhesion failures, the temperature of the oven was slowly ramped up and down at the beginning and end of both the softbake and post-exposure bake cycles (approximately 6°C min^{-1}). The long exposure times required were also broken down into shorter intervals to prevent any

significant heating of the sample, with a resting time between each stage equivalent to the length of each exposure period.

The development of an SU8 film is generally the most critical step for the fabrication of any structure. γ-Butyrolactone (GBL) readily solvates the uncrosslinked SU8, although care must be taken when using it. Therefore, a 1-2 minute pre-dip in GBL followed by immediate immersion of the sample into the developer solution was employed. This resulted in cleaner, more vertical walls when compared to samples that were immersed in the developer solution alone. When developing the sample, vigorous agitation was necessary to remove all the unexposed SU8 and the sample was only be rinsed with IPA once the development process was complete. Small amounts of unexposed residue were again removed by RIE with an O_2/CF_4 (90:10) plasma. However, the CF_4 etches the underlying SiN and, therefore, the maximum etching time was determined by the thickness of the SiN layer.

6.3.4 Electroplating

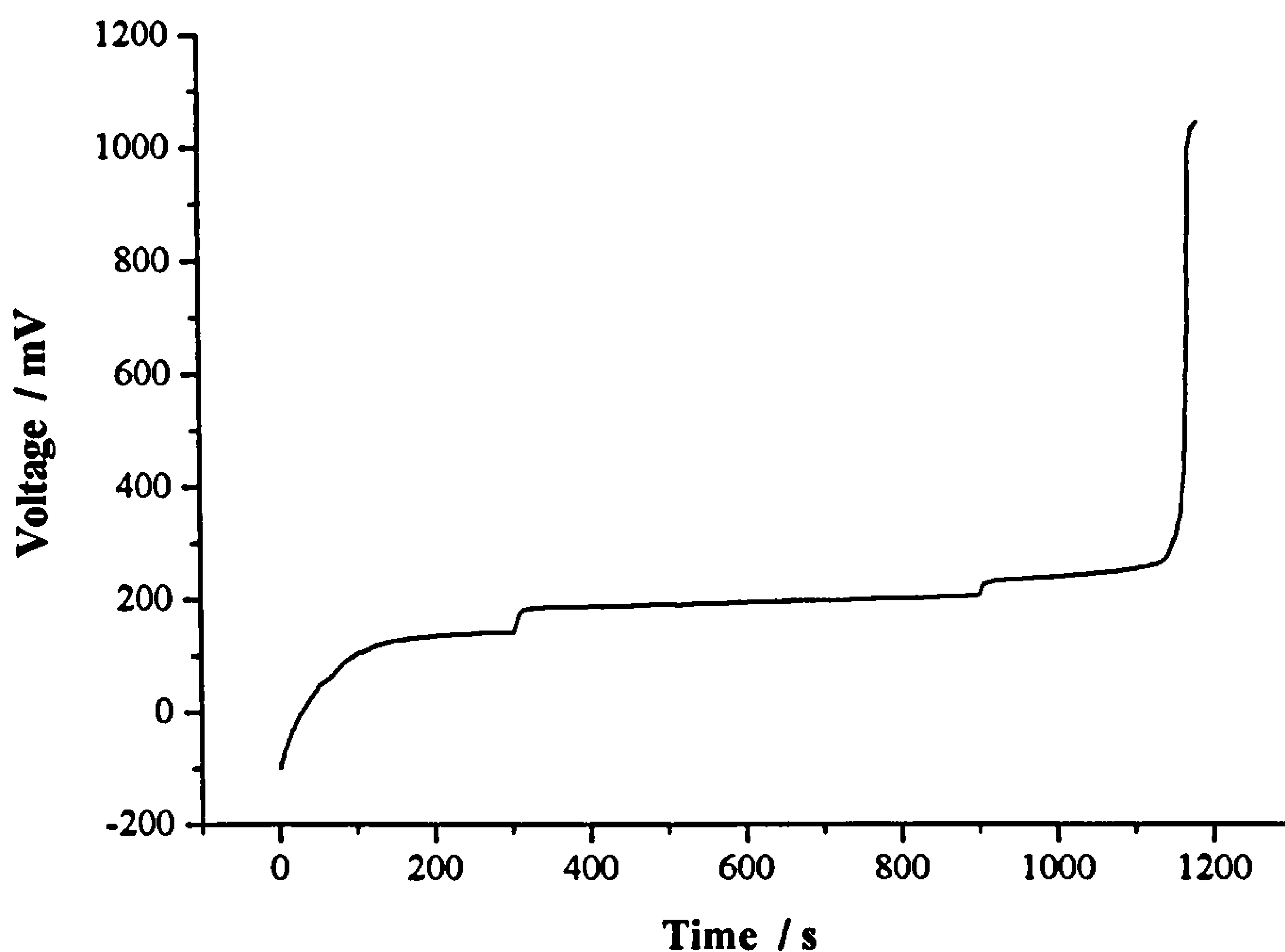

Figure 6.2 **Growth of a AgCl Layer**

The three stages in the growth of AgCl film at the surface of an electroplated silver layer. The current was stepped from 1.5 μA to 3 μA (at 300s) and finally to 5 μA (at 900s).

The electroplating process for the deposition of the Ag|AgCl reference electrode was optimised empirically (Section 3.3.3.2). Thorough cleaning of the gold surface prior to electroplating was essential and slight roughening of the surface, by cycling the electrode in an acid solution, as described in Section 3.3.3.1, aided deposition. The most durable reference electrodes were obtained when using a program of increasing voltage or current steps.

As a highly porous silver layer was undesirable, a slow initial rate of electrodeposition was employed. By progressively increasing the current and by using relatively long plating times, a thick, strongly adhered silver layer was produced. When forming the silver chloride layer, a rapid increase in the voltage (as seen in Figure 6.2) indicated that complete oxidation of the silver layer had occurred, with no more silver readily available for conversion to silver chloride. Therefore, it was attempted to halt the deposition process before this point was reached, so that a thick silver chloride layer was deposited, yet Reaction 6.03 could still proceed in either direction without a significant change in voltage.

The surface roughness (as determined by surface profiling) of the silver layer prior to growth of the AgCl film was found to be noticeably larger than that of the complete Ag|AgCl electrode. From the surface profiles of three silver and three Ag|AgCl films, the mean relative standard deviation of the silver layers (relative to the film thickness) was approximately five times greater than that acquired for the Ag|AgCl films. Using the electrode deposition processes outlined in Table 3.2, a film thickness in the order of 1 μm was obtained and the morphology of the resulting film is illustrated in Figure 6.3.

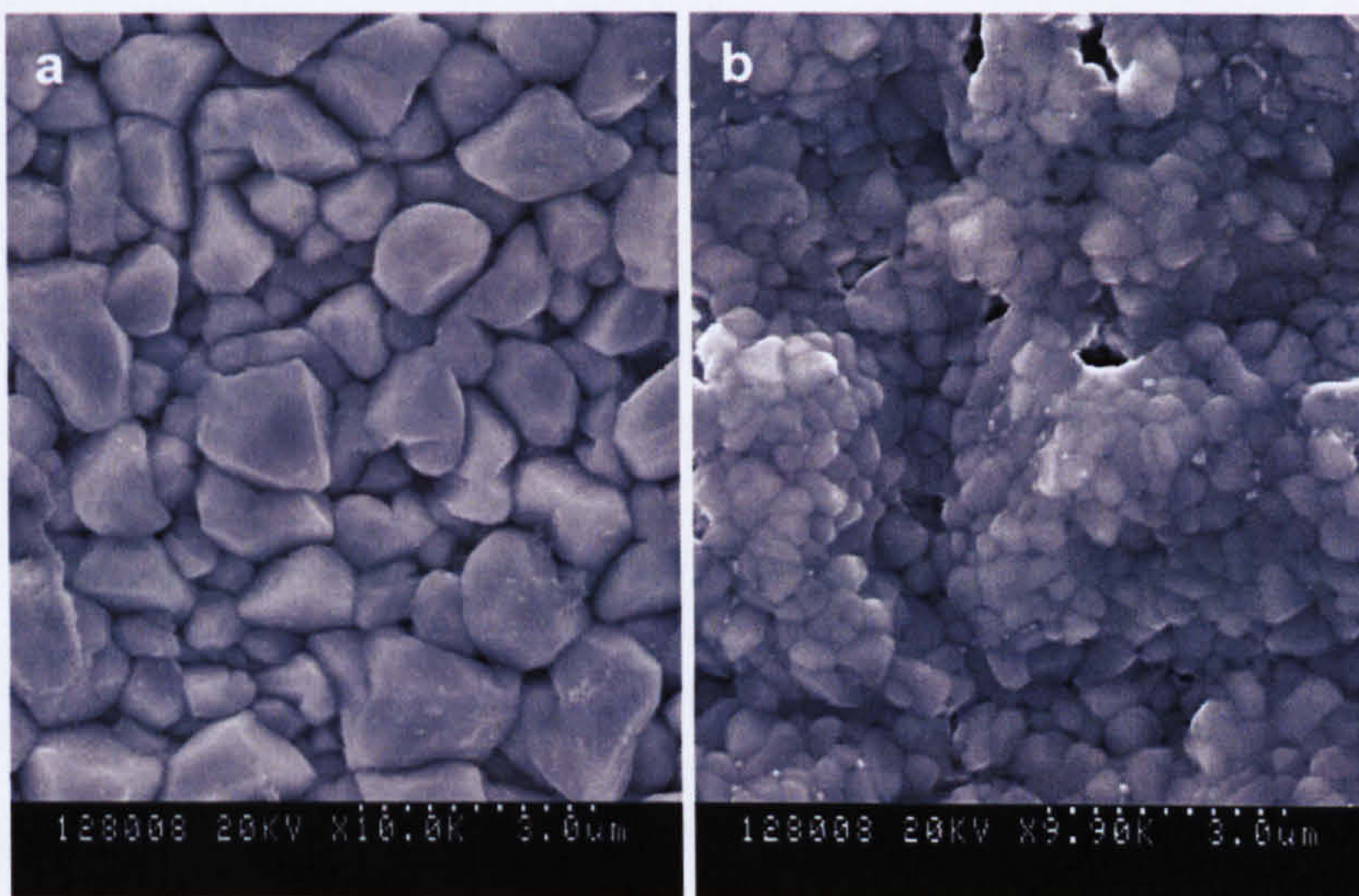

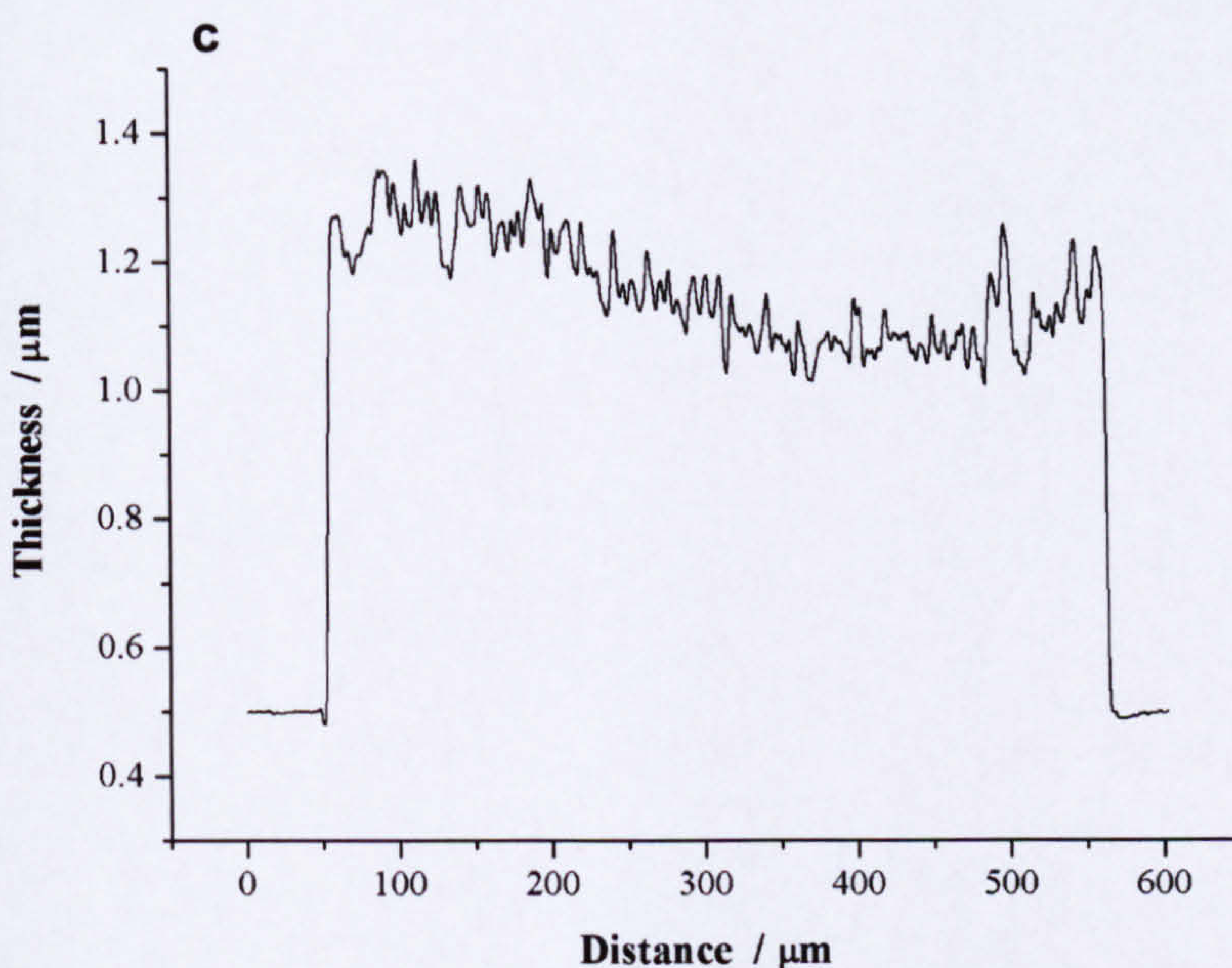

Figure 6.3 **The Morphology of an Electroplated Ag|AgCl Electrode**

a. An SEM of an electroplated silver layer. b. An SEM of an electroplated Ag|AgCl film. c. The surface profile of an electroplated Ag|AgCl film.

6.3.5 Electrolyte Gel

As detailed in Section 6.2.2, the agarose electrolyte gel was dispensed into the SU8 chamber either by casting or dip-coating. In the case of the former, it was particularly important to keep both the dispensing needle and the sample warm during the casting process and to work as quickly as possible to limit evaporation. Nonetheless for a chamber volume of approximately 1 μl, casting the electrolyte gel was somewhat awkward. Dip-coating was a

simpler process, though the gel did not always level off sufficiently. After the electrolyte gel had been dispensed, the sensor was stored in an aqueous solution, with a KCl concentration equivalent to that of the gel.

6.3.6 Completed Microsensor

A range of micrographs is presented in Figure 6.4, showing the completed microsensor structure with magnified images of the various individual components.

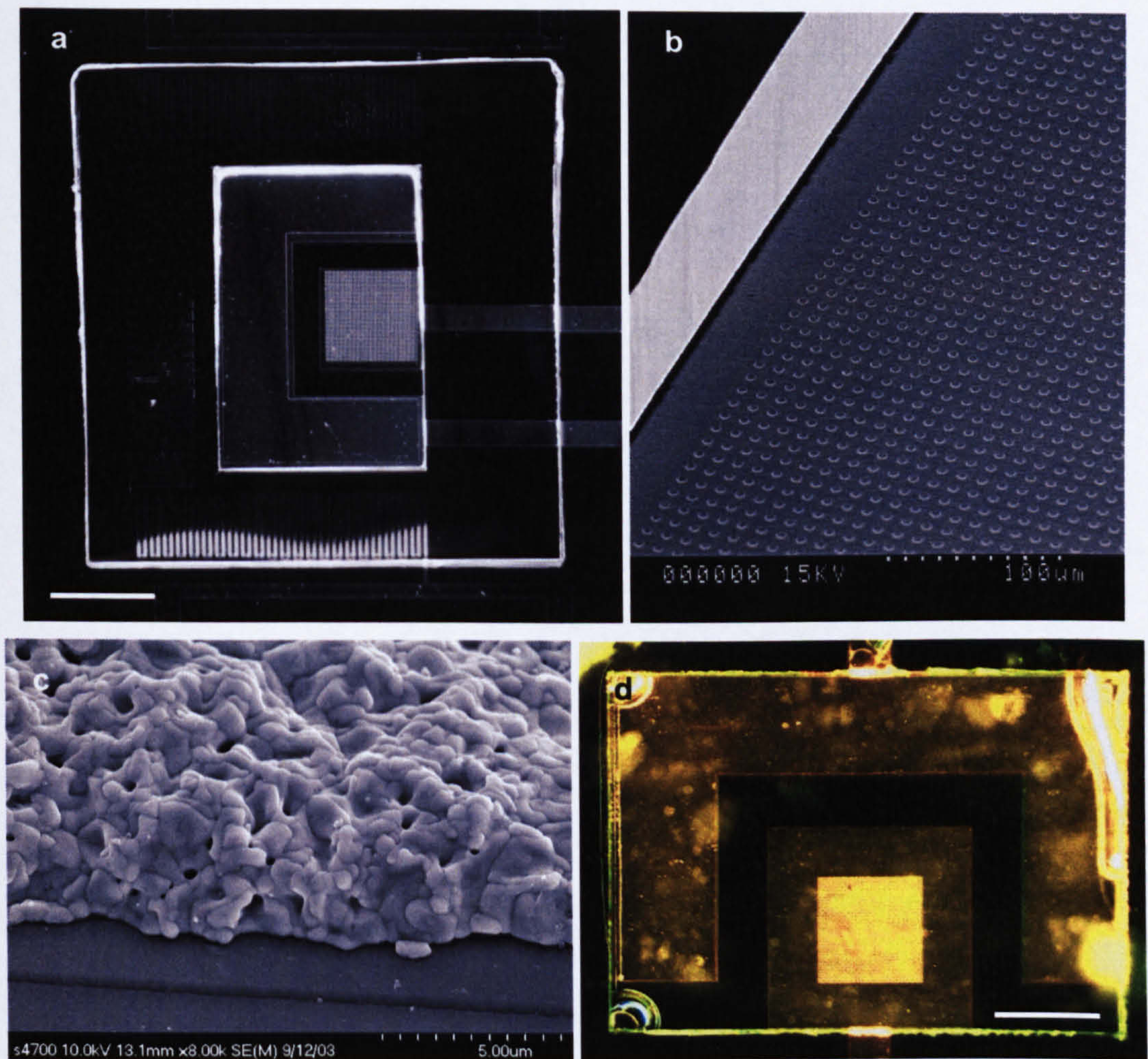

Figure 6.4 Micrographs of the Dissolved Oxygen and Temperature Sensor
a. A microsensor before the deposition of the electrolyte gel (scale bars indicates 800 μm). b. The sidewall of a SU8 chamber and a region of the microelectrode array. c. A Ag|AgCl micro-reference electrode. d. An SU8 chamber filled with the electrolyte gel (scale bar indicates 500 μm).

6.4 Performance of Dissolved Oxygen and Temperature Sensor

To assess the performance of the microsensor, calibration curves were obtained from both dissolved oxygen and temperature measurements. The potential of the thin-film Ag|AgCl electrode, relative to a commercial reference electrode, was also determined and its stability over time was monitored.

6.4.1 Calibration of Thermal Resistor

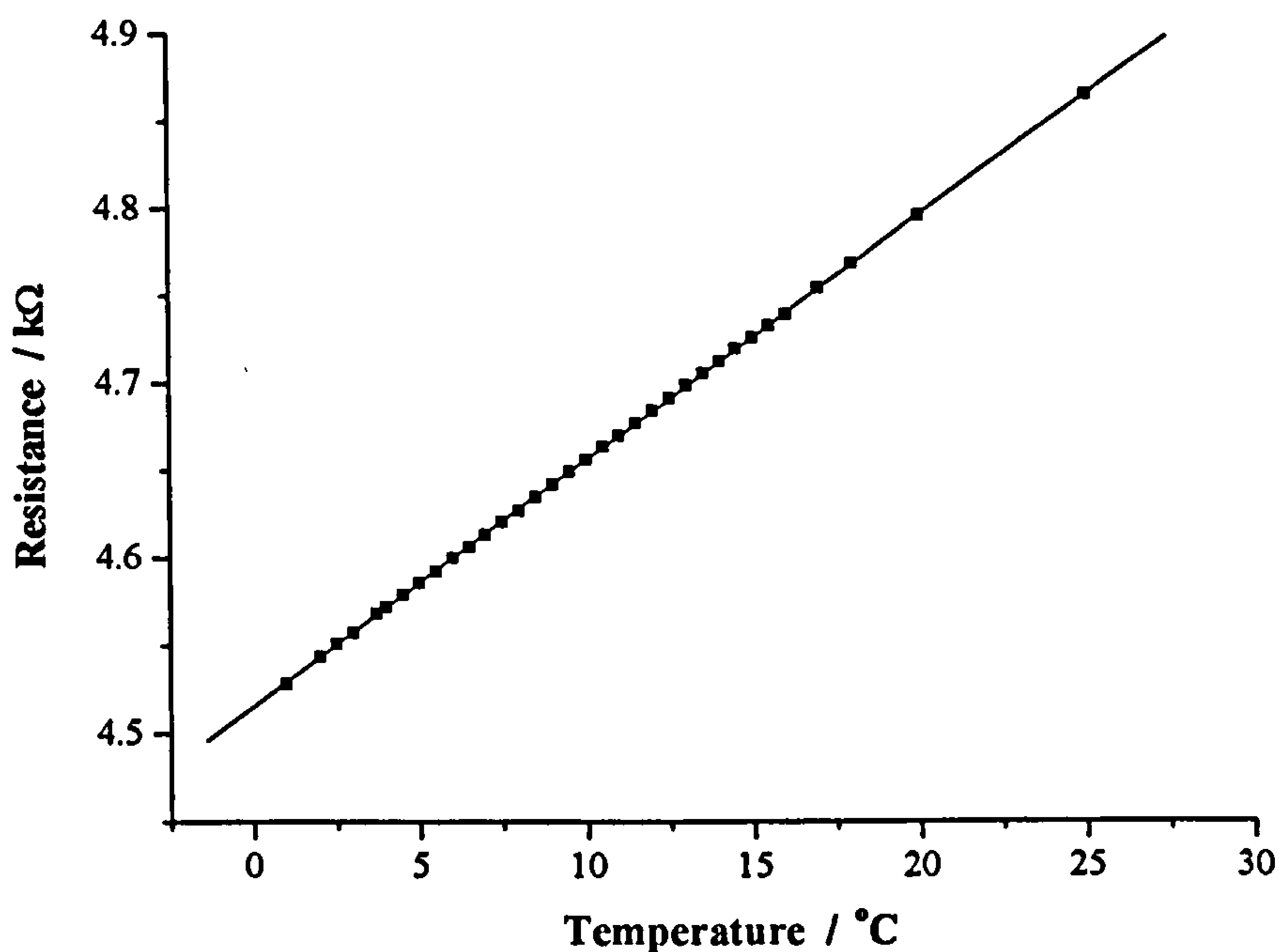

Figure 6.5 **Thermal Resistor Calibration Curve**

The response of the thin-film thermal resistor is linear throughout the temperature range of interest.

A typical calibration curve for a nickel thin film resistor is presented in Figure 6.5. The mean resistance values measured for a set of thermal resistors were significantly larger than the values calculated from the geometry of the initial design – the value at 5°C, for example, was 4.55±0.12 kΩ as opposed to 1.80 kΩ. However, all the samples tested had been patterned by wet etching, which had resulted in both undercutting of the pattern (the width of the microfabricated resistors was approximately 23.5 μm instead of 25 μm) and most probably a

reduction in the thickness of the nickel layer, as discussed in Section 6.2.2.1. Both these factors would have increased the measured resistance, as, naturally, would any pinholes or flaws in the thin-film metal layer.

Nonetheless, the thermal resistors demonstrated good linearity, with a mean correlation coefficient of 0.9996±0.002 and a temperature coefficient of 0.31±0.026 % $°C^{-1}$. The accuracy of the measurements may be estimated from three standard deviations (3σ) of the values obtained for the difference between the linear fit and the measured resistance (Skoog *et al*, 1998). For the calibration curve above, 3σ was calculated to be 0.92 Ω, which corresponds to a maximum accuracy of ±0.07°C. From these results, it can be seen that the performance of the thin-film thermal resistors is adequate for both the temperature compensation of dissolved oxygen measurements and for the direct monitoring of the temperature of river water. The stability and accuracy of the system could be improved, however, by employing a more stable power supply and by recording the data directly onto a computer.

6.4.2 Electrochemical Behaviour and Stability of Ag|AgCl Reference Electrode

Cyclic voltammograms recorded in a FMCA solution were obtained from the microsensor when using the working electrode of a sensor and either a commercial counter and Ag|AgCl reference electrode or the sensor's thin-film reference electrode, both with and without the electrolyte gel (Figure 6.6). It should be noted that, when incorporating the electrolyte gel, the microsensor was equilibrated in the FMCA solution for approximately 10 minutes prior to recording. The formal potential of the voltammogram obtained was approximated by calculating the midpoint potential, $E_{½}$, of the cathodic and anodic peaks. From these measurements, it was estimated that the potential of the micro-reference electrode vs. the commercial Ag|AgCl electrode was approximately +60 mV.

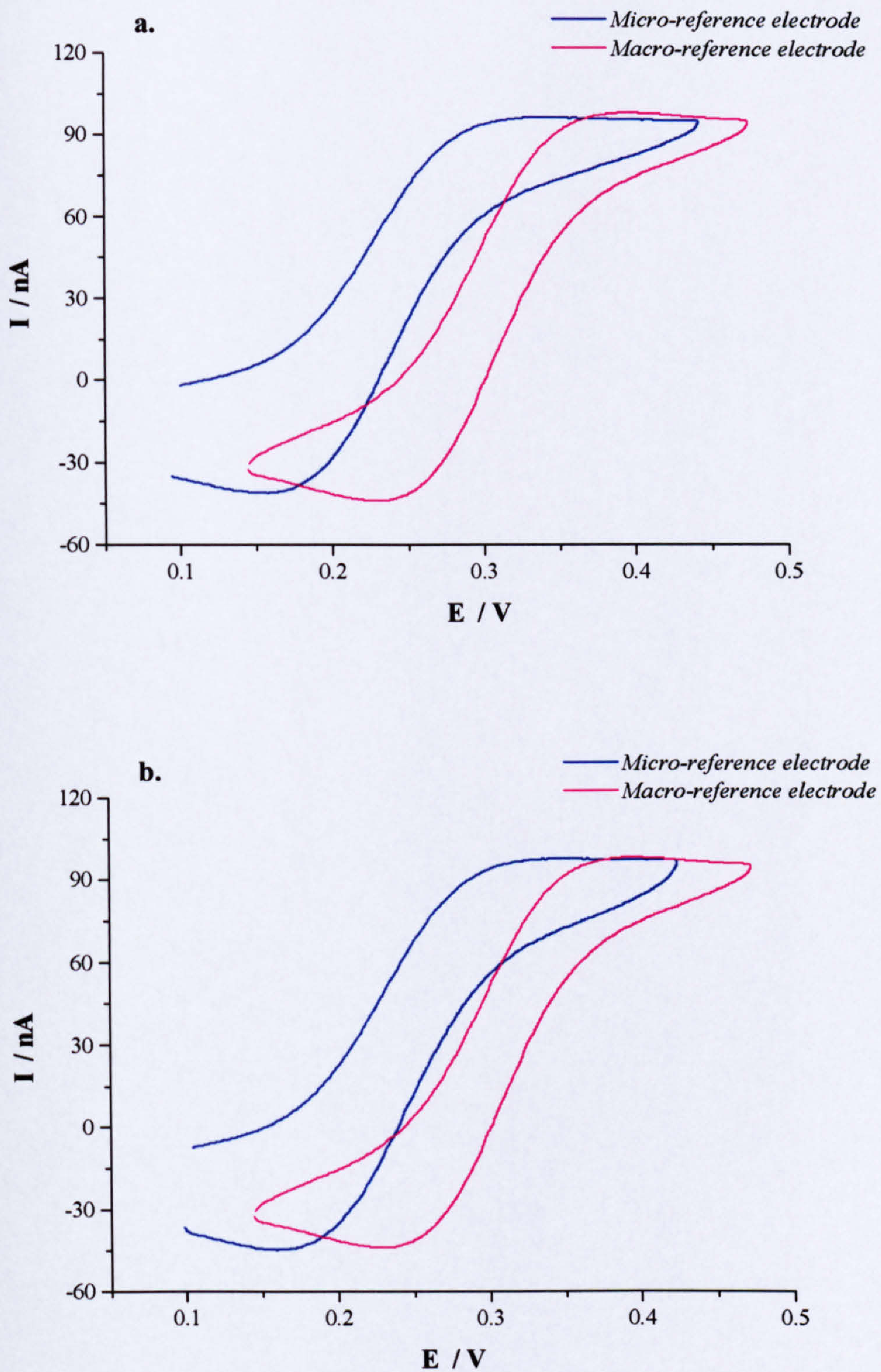

Figure 6.6 **A Comparison of the Voltammograms Obtained when Either a Micro-Reference Electrode or a Commercial Ag|AgCl Electrode was Employed**

All voltammograms were recorded at 20 mV s^{-1} in a 1 mM FMCA solution using a microsensor whose working electrode comprised an

array of 5 μm electrodes, as described in Table 5.1. No electrolyte gel layer was employed when recording with the macro-reference electrode (pink), but traces were obtained both with (b) and without (a) the electrolyte gel when employing the micro-reference electrode.

The stability of three micro-reference electrodes, with respect to a commercial Ag|AgCl electrode, with 100 nA of current flowing through each of them is shown in Figure 6.7. When immersed in a 1 M KCl solution, the micro-reference electrodes were typically stable for 25-30 hours when either +0.1 V or –0.1 V was applied, whilst a stable response was obtained for approximately 80 hours in a 0.1 M solution. This suggests that the micro-reference electrodes would be suitable for semi-continuous, long-term usage, for instance several short (15-30 minute) measurement periods per day. However, for continuous, long-term monitoring, it may be necessary to adapt the microsensor to incorporate a counter electrode (thus preventing current from flowing through the reference electrode) rather than attempting to electroplate a substantially thicker Ag|AgCl layer.

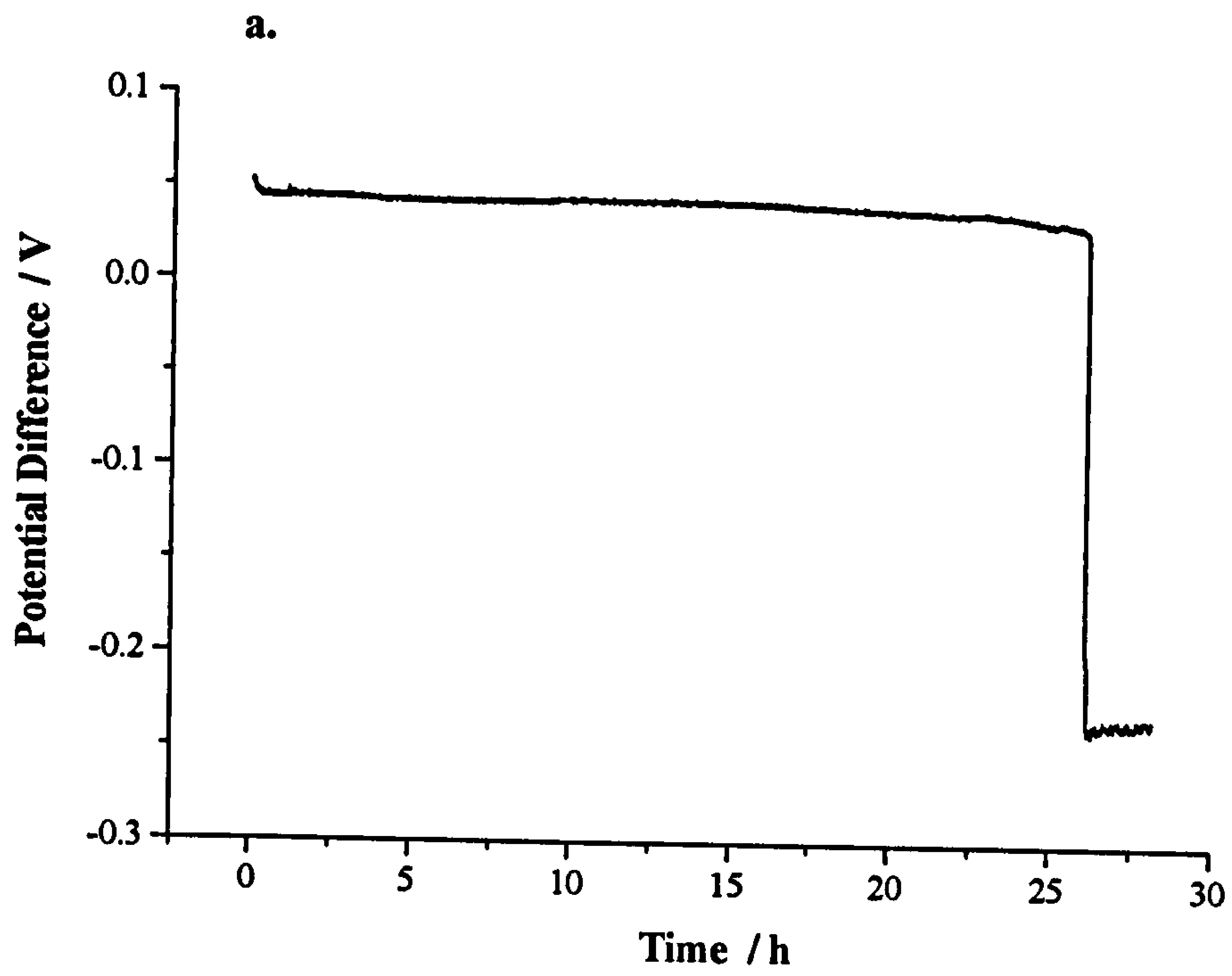
a.
0.1
0.0
-0.1
-0.2
-0.3
Potential Difference / V
0
5
10
15
20
25
30
Time / h

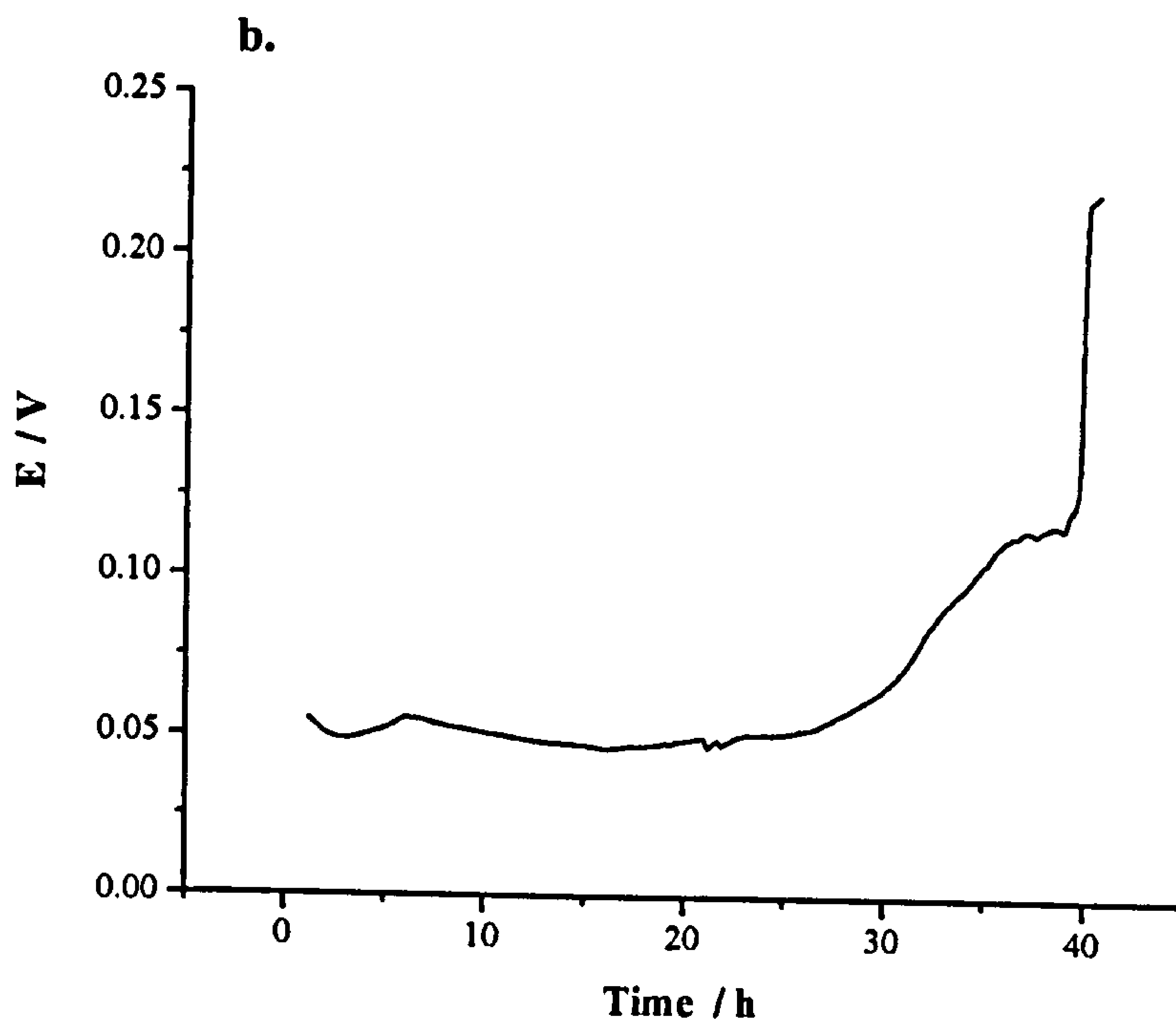
b.
0.25
0.20
0.15
0.10
0.05
0.00
E / V
0
10
20
30
40
Time / h

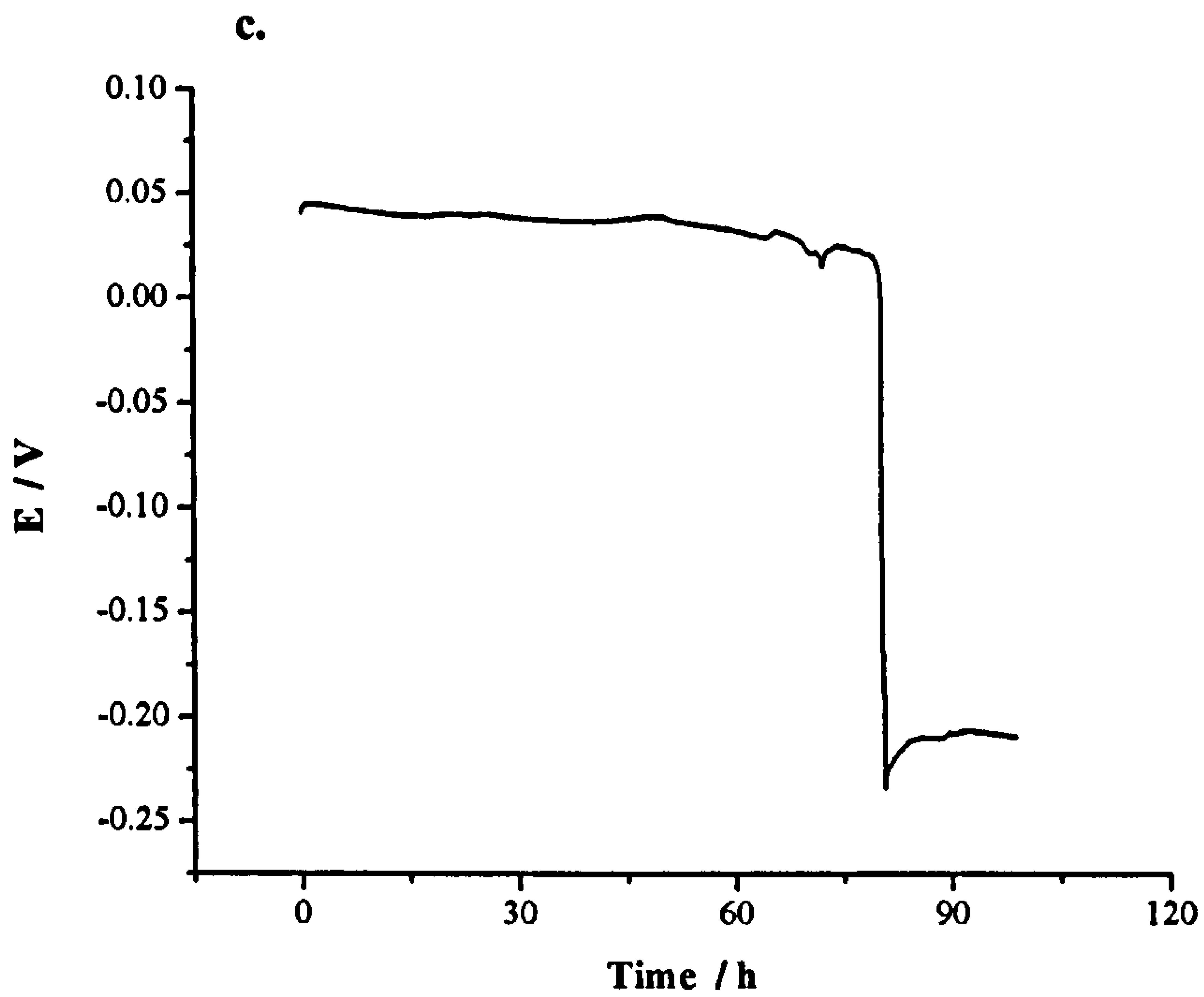

Figure 6.7 **Long-term Stability of Ag|AgCl Micro-Reference Electrode**

a. (-0.1V was applied) and b. (0.1V was applied) were recorded in 1 M KCl, whilst c. (-0.1V was applied) was recorded in 0.1 M KCl. The potentials are quoted with respect to a commercial Ag|AgCl reference electrode.

6.4.3 Calibration of Dissolved Oxygen Sensor

To select the operating potential for the working electrode of the dissolved oxygen sensor, sampled current voltammetry[4] was performed in a de-oxygenated (saturated sodium sulphite) solution. Both gold and platinum black electrode arrays, which had been used for the experiments in Chapter 5, were employed to determine the voltage at which hydrogen evolution or other interfering reactions began to occur. Similar results were obtained for all electrode arrays tested, though the current began to increase at a slightly lower potential for the platinum black arrays than for the gold arrays. In the case of the former, a very slight rise in current was observed at -0.75 V and the recorded signal increased rapidly from –0.8 V (as seen in Figure 6.8). Therefore, a potential of –0.7 V was selected for all chronoamperometric experiments.

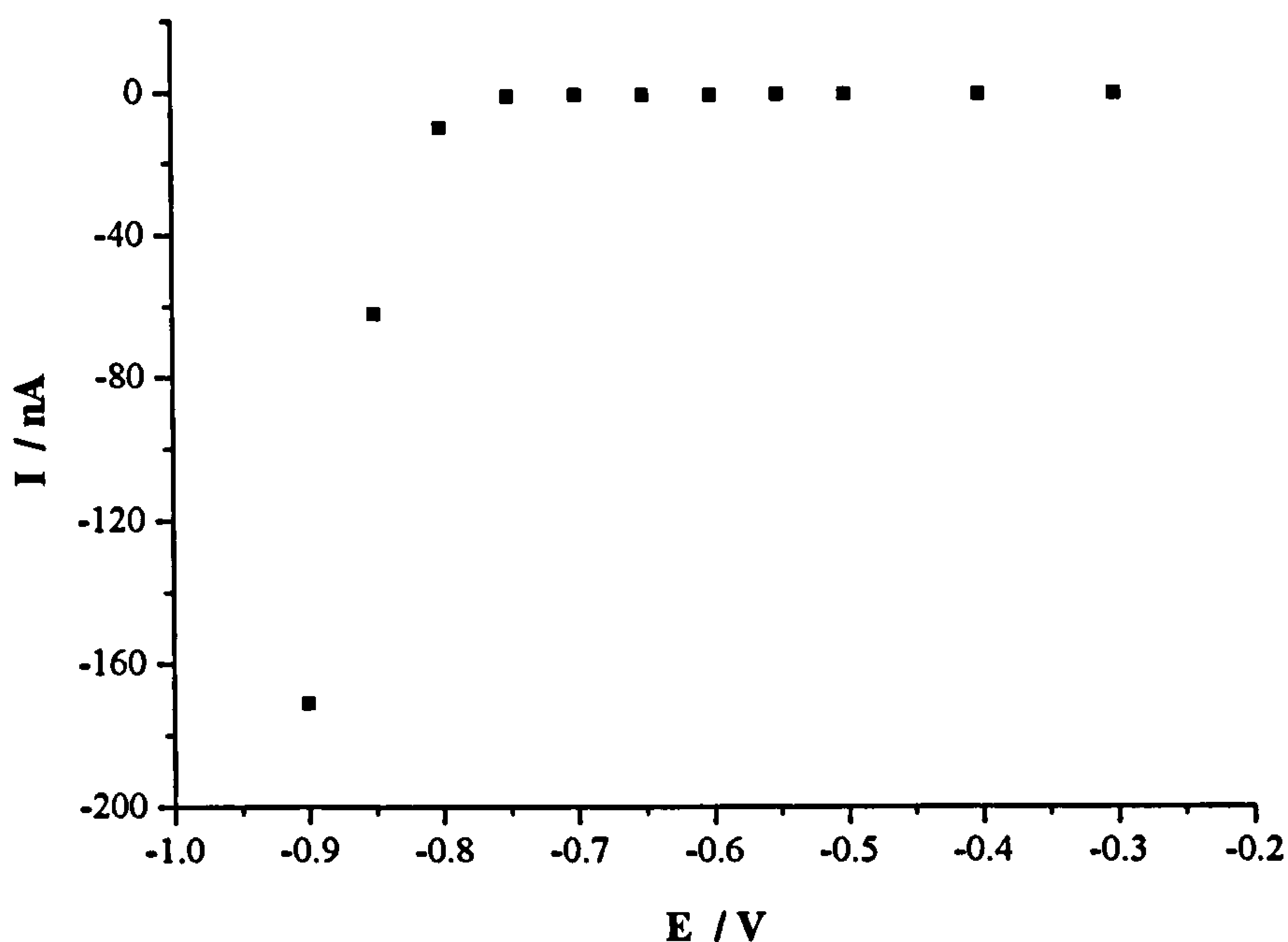

Figure 6.8 Sampled Current Voltammetry in a De-oxygenated Solution
The currents were measured 5 minutes after the application of the potential step (vs. Ag|AgCl), using a 1.25 μm platinum black electrode array (as detailed in Table 5.1).

[4] In sampled current voltammetry, a series of chronoamperometric experiments are performed using a range of applied potentials and, for each of the traces obtained, the current recorded at a specific time after the application of the potential step is noted (Bard and Faulkner, 2001).

A typical calibration curve for the dissolved oxygen microsensor is shown in Figure 6.9. It can be seen that the sensor exhibited a linear response to dissolved oxygen concentration, with a correlation coefficient of 0.997 in this example. However, fine control of the gas flow rates proved unattainable with the flow meters employed in the test rig, particularly at low flow rates, and so a certain degree of experimental error was introduced by the test rig. Therefore, to more rigorously assess the linearity of the sensors, higher precision flow meters would be required.

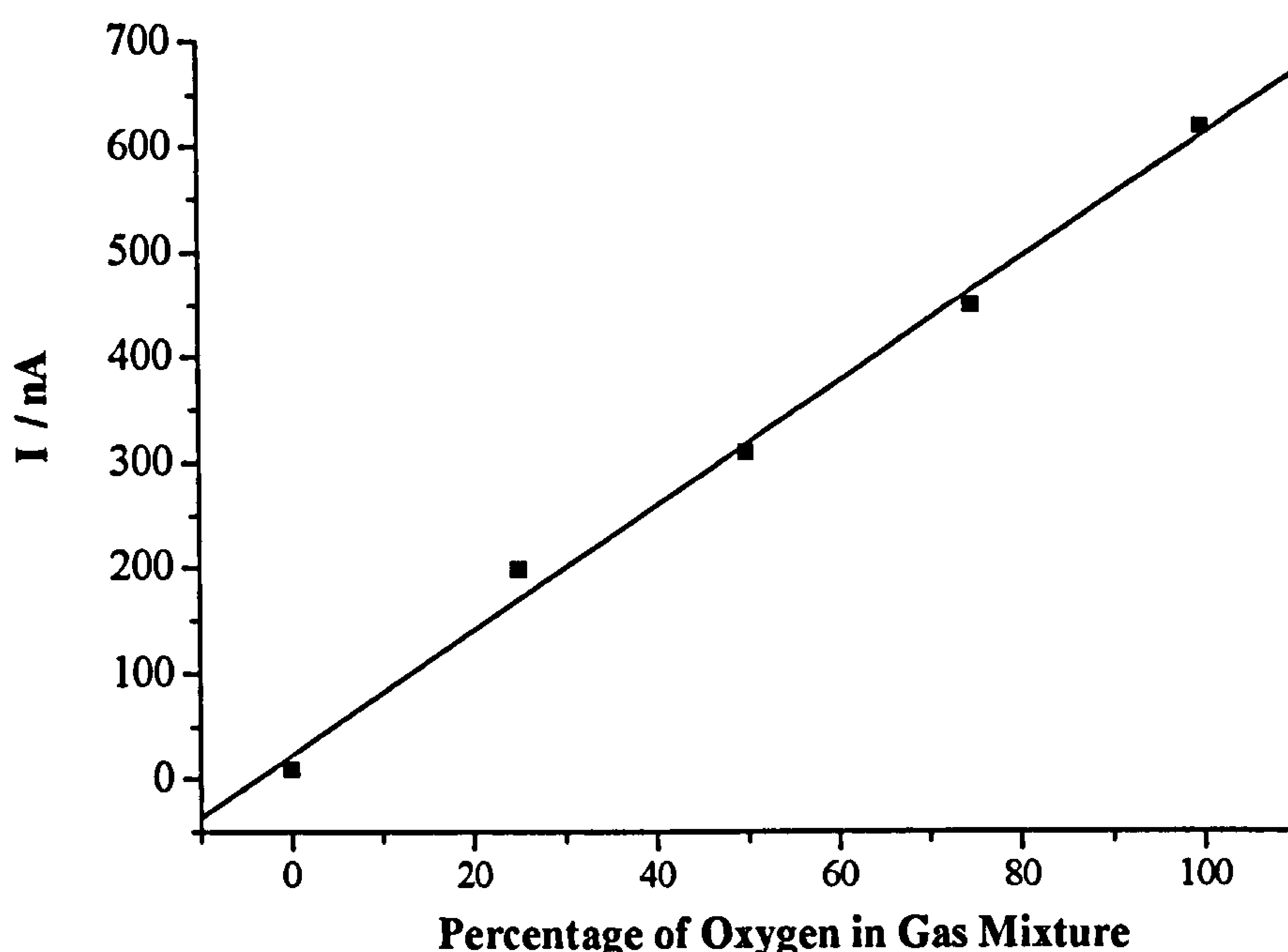

Figure 6.9 **Calibration of a Dissolved Oxygen Microsensor**
The currents were measured 10 minutes after the application of the potential step (–0.7 V vs. Ag|AgCl).

To assess the response time of the microsensor, a saturated sodium sulphite solution was injected into air-saturated water, whilst the current output of the sensor was monitored. Figure 6.10 shows the response of a microsensor, with a working electrode array of 5μm electrodes, but with no electrolyte gel, to an injection of the solution at approximately 60 s. The initial signal fluctuations were caused by the bubbling of the air through the water and the large increase in the magnitude of the signal observed after the injection of the sodium sulphite is presumed to be due to the movement of the solution. The response time of the sensor may be defined as the time, t_{95}, taken for the current to decrease by 95% from the

average value prior to the application of the potential step. For the trace shown in Figure 6.10, t_{95} was estimated to be 2.8 s. However, the microsensor response has not yet been tested with the electrolyte gel layer, the incorporation of which would presumably increase the response time.

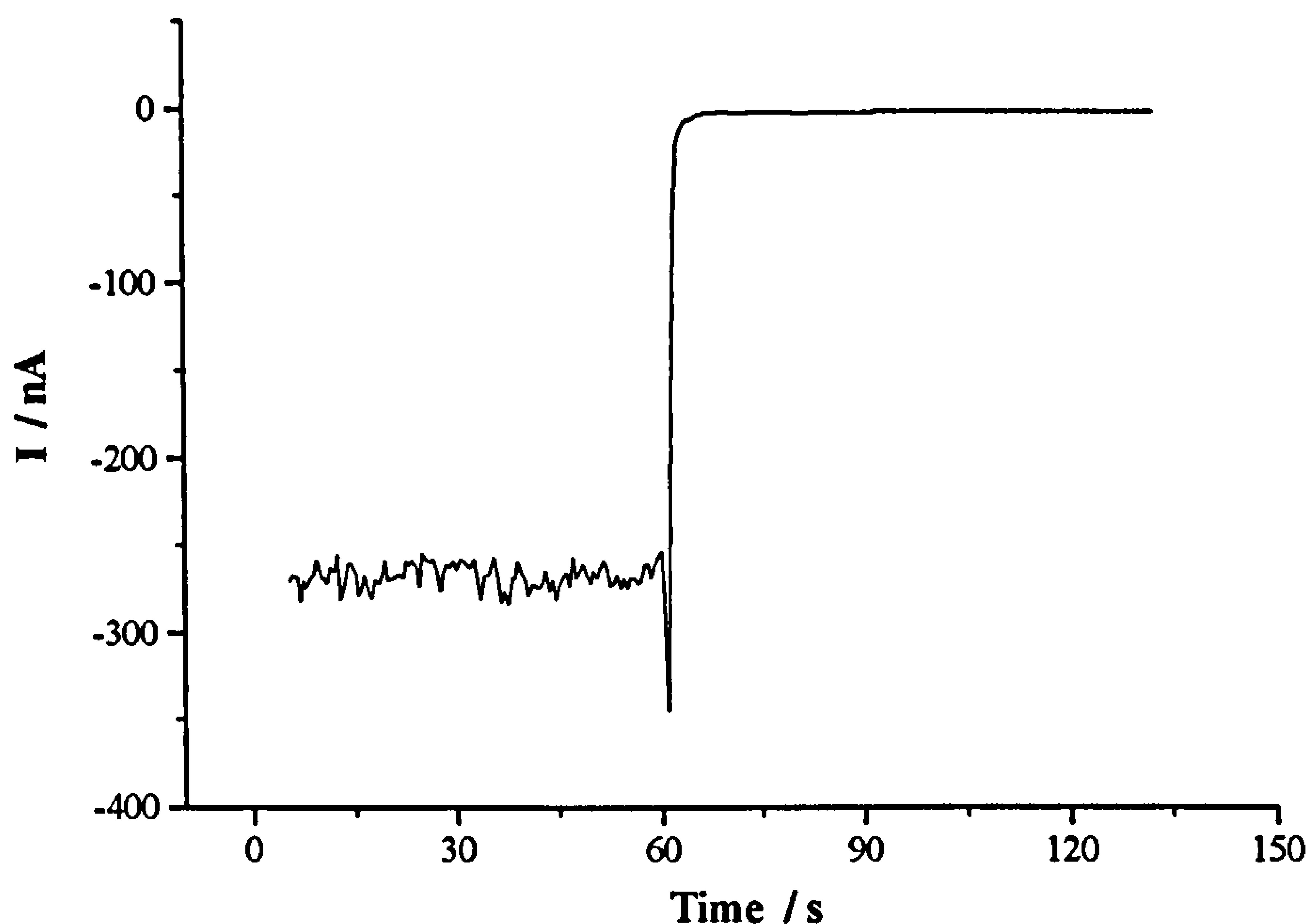

Figure 6.10: **Response of a Microsensor to the Rapid De-Oxygenation of Air-Saturated Water**

The working electrode comprised an array of 5 μm electrodes (as detailed in Table 5.1) and its potential was held at –0.7 V vs. Ag|AgCl.

6.5 Conclusion

A dissolved oxygen microsensor, with an integrated thermal resistor for temperature compensation, has been successfully designed and fabricated. Linear calibration curves were obtained from measurements of both solution temperature and dissolved oxygen concentrations, although a rigorous assessment of the latter would have required more precisely controlled gas flow rates. Fast response times (a t_{95} of 2.8 s) were also acquired for the dissolved oxygen microsensor without an electrolyte gel layer. The Ag|AgCl micro-reference electrode, which had a potential of approximately +60 mV with respect to a commercial Ag|AgCl electrode, was stable for 25-30 hours in 1 M KCl and for approximately 80 hours in 0.1 M KCl with 100 nA of current passing through it.

However, assessment of the long-term stability of the complete microsensor is still required and should be the next evaluation procedure. Furthermore, electroplating platinum black onto the working microelectrode array to increase the recorded signal; incorporating a counter electrode to prevent current from flowing through the micro-reference electrode; and use of an additional membrane that is impermeable to chloride ions should all be considered for future developments.

CHAPTER 7

THE DEVELOPMENT OF AN INTEGRATED MICROSENSOR PLATFORM: PRELIMINARY INVESTIGATIONS AND SUGGESTED FUTURE WORK

This chapter details the results of preliminary investigations concerning the development of an integrated microsensor platform. The use of dielectrophoresis as an antifouling strategy within the platform is also considered and recommendations are made for the continuation of this work.

7.1 Overview

If a microsensor, such as the dissolved oxygen and temperature sensor described in Chapter 6, is to be employed in a remote or self-contained monitoring system, integration of the microsensor and additional subunits, such as controlling electronics and fluid handling systems, will be required. From discussions with both Kodak Analytical Services and Unilever, it became apparent that a platform which enabled the integration of several sensors into a flow-through system would be desirable for several applications, particularly in environmental or biomedical monitoring systems. Therefore, a generic flow-through platform has been designed in which microsensors are integrated into the base of a flow channel.

The platform also incorporated arrays of interdigitated microelectrodes that could be employed to perform dielectrophoretic techniques, such as repelling fouling materials from the base of the channel (and therefore away from the microsensors). It is anticipated that this platform design could be employed for a variety of applications, including the monitoring of freshwater environments and the clinical analysis of blood. The design could also be simply scaled for alternative applications. In the following sections, the field of system integration

and interconnect technologies is briefly reviewed and the basic theory and relevant applications of dielectrophoresis (DEP) are discussed.

7.1.1 Integration of Microsensors

Interconnect technologies are central to the development of integrated microsystems, yet this field has not been extensively researched. Various integrated microanalytical systems have been reported in recent years, particularly in the Micro Total Analysis Systems (μTAS) conference series (Thomas *et al*, 2000; Choi *et al*, 2000; Kitamori, 2001). However, no readily interconnectable, modular systems have been reported, although several micromachined fluidic connectors designed to link individual microfluidic devices together and to the external environment have been developed (Meng *et al*, 2000; Puntambekar and Ahn, 2000; Gray *et al*, 2001; Igata *et al*, 2002).

Electrical connections from one subsystem to another could be achieved employing techniques from the semiconductor and printed circuit board (PCB) industries. For example, a range of micro-vias and plated through-holes may be produced using techniques such as precision drilling, laser ablation, wet and dry etching, use of conductive inks and electroless- or electro-deposition methods (González, 1999). Methods for connecting to bonding pads include flip-chip bonding, the use of ball grid arrays (BGAs) and flexible edge connectors (Tong, 1995).

A variety of novel, optical interconnect techniques have also been developed in recent years, which may also be exploited in microanalytical systems. These include silicon nitride micro-clips (Bostock, 1998), which position single fibres within micromachined silicon V-grooves, and the assembly techniques of "microjoinery", where standard manufacturing intersects (for instance dovetail, slot and dado joints) are miniaturised (González 1998). Nonetheless, much research is still required if fully integrated, reliable analytical microsystems are to be produced.

7.1.2 Particle Manipulation by Dielectrophoresis

As discussed in Section 6.1.1.2, the use of dielectrophoresis (DEP) as an antifouling strategy has been investigated only to a limited extent. However, DEP has been extensively researched as a particle manipulation technique and its theory has been well studied by a

number of groups. For a detailed overview of dielectrophoresis refer to Pohl (1978), Pethig (1979), Jones (1995) or Morgan and Green (2003).

7.1.2.1 *Dielectrophoresis in Microfluidic Channels*

Dielectrophoresis is an AC electrokinetic technique that induces movement in polarisable particles in non-uniform electric fields (Morgan and Green, 2003). The resulting motion of the particle is dependent upon the relative polarisabilites of the particle and of the medium in which it is suspended. When a particle is more polarisable than the medium, it will move towards a region of strong field (positive DEP), whereas a particle that is less polarisable will move away from the strong field regions (negative DEP). The polarisation of a dielectric material is dependent upon the frequency of the applied field. Particles with differing dielectric properties will have different dielectrophoretic force-frequency responses.

The effective complex polarisability, α, of a homogeneous, solid, spherical particle, may be expressed as (Jones, 1995):

$$\alpha = 3\varepsilon_m f_{CM} = 3\varepsilon_m \left(\frac{\varepsilon_p^* - \varepsilon_m^*}{\varepsilon_p^* + 2\varepsilon_m^*} \right) \tag{7.01}$$

where ε_m is the dielectric permittivity of the medium and ε_p^* and ε_m^* are the complex permittivities of the particle and the medium respectively; the complex permittivity being defined as:

$$\varepsilon^* = \varepsilon - j\left(\frac{\sigma}{\omega} \right) \tag{7.02}$$

where j is the complex operator $\sqrt{-1}$, σ is the conductivity and ω is the radial frequency. The bracketed term in Equation 7.01 is known as the Clausius-Mossotti factor, f_{CM}, the real part of which has an upper limit of 1 and a lower limit of –0.5. If $0 < Re[f_{CM}] \leq 1$, the particle will experience a positive DEP force, whilst if $-0.5 \leq Re[f_{CM}] < 0$, the will particle experience a negative DEP force. When $Re[f_{CM}] = 0$, no DEP force acts upon the particle, the frequency at which this occurs being known as the crossover frequency.

The time-averaged dielectrophoretic force is proportional to $Re[f_{CM}]$ and to the gradient of the square of the electric field, $\nabla|E|^2$ (Morgan and Green, 2003):

$$\langle F_{DEP} \rangle = \pi \varepsilon_m r^3 \, Re[f_{CM}] \nabla|E|^2 \tag{7.03}$$

where r is the radius of the particle. Using Fourier series analysis, Morgan *et al* derived an analytical solution for $\nabla|E|^2$ for an array of interdigitated microband electrodes alternately connected to two signals with identical frequency and amplitude but with a phase difference of 180° (Morgan *et al*, 2001). At heights greater than the width of the individual electrodes, d, $\nabla|E|^2$ is given by:

$$\nabla|E|^2 = -\frac{32}{\pi}\frac{V^2}{d^3} exp\left(-\frac{\pi y}{d}\right) \tag{7.04}$$

where y is the height above the electrode, V is the amplitude of the applied potential and an equal width and spacing of the electrodes is assumed. By combining Equations 7.03 and 7.04, the one-dimensional DEP force may be expressed as:

$$\langle F_{DEP} \rangle = -32\frac{V^2}{d^3}\varepsilon_m r^3 \, Re[f_{CM}] exp\left(-\frac{\pi y}{d}\right) \boldsymbol{u}_y \tag{7.05}$$

where $\boldsymbol{u}_y$ is the unit vector in the y-axis (perpendicular to the electrode array).

A range of other forces will also influence particle motion in microsystems, both externally induced forces and forces attributable to particle and fluid motion (Morgan and Green, 2003). For instance, a particle of density ρ_m and volume v in a suspending medium of density ρ_p will experience a force, $\boldsymbol{F_G}$, due to buoyancy and gravity:

$$F_G = v(\rho_M - \rho_P)g \tag{7.06}$$

where g is the gravitational acceleration (9.81 m s^{-2}). Furthermore, as the particle moves through the surrounding fluid it will experience a frictional (Stokes) drag force, $\boldsymbol{F_S}$:

$$F_S = -6\pi\eta r v \tag{7.07}$$

where η is the viscosity of the fluid and v is the velocity of the particle. In DEP microsystems, where the medium is pumped through microchannels using hydrostatic pressure gradients, the fluid flow is in the low Reynold's number regime (i.e. $Re<1$) and the fluid motion is laminar in nature. This regular, smooth fluid motion, also known as Poiseuille flow, gives rise to a characteristic parabolic flow profile defined by (Pethig, 1996):

$$v = 6\left(\frac{Q}{hl}\right)\frac{y}{h}\left[1-\frac{y}{h}\right] \tag{7.08}$$

where y is the vertical position, h is the height of the channel, l is the width of the channel and Q is the volumetric flow rate. Therefore, the velocity of the fluid at the channel walls is zero, whilst the maximum flow rate is located at the centre of the channel.

7.1.2.2 Inhibiting Adhesion of Cells and Colloids

As discussed in 6.1.1, the possibility of using negative DEP as an antifouling strategy has been considered. Fuhr *et al* (Schnelle *et al*, 1996; Fuhr *et al*, 1995) employed arrays of interdigitated nanoelectrodes (140 nm wide) to repel suspended cells from the surface of a substrate. Very high field strengths can be achieved close to the electrode surface when using nanoelectrodes, but a sharp decrease in the field strength is observed when moving away from the surface. Hence, cells close to the electrode surface would be repelled, whilst cells several micrometers away from the electrodes would be relatively unaffected by the electric fields, an important consideration for medical and biotechnological applications. In order to repel particles to a greater distance above the surface of substrate, larger electrodes would be required, although this means that the field strength at the electrode surface would be significantly decreased.

7.2 Design of the Proposed Integrated Microsensor Platform

The integrated microsensor platform was designed with a number of criteria in mind. Firstly, the platform was to facilitate the integration of three sensors into one system, where they were to be embedded within a flow-channel. Secondly, the connection of control electronic systems was to be straightforward (ideally with a row of bonding pads on the platform onto which an edge connector could be slotted) and, thirdly, the design of the platform was to be readily scaleable. Finally, an array of interdigitated electrodes that could be energised to

produce a dielectrophoretic force was to be incorporated into the design. The diameter of the electrodes employed (25-50 μm) had to be relatively wide so that the DEP force remained sufficiently strong as it extended outwards from the electrodes (see Section 7.1.2.2). A modular approach to system design was taken, so as to limit the complexities of microfabrication and to allow for the alteration of individual components without modification of the entire system becoming necessary. An overview of the integrated microsensor platform design is outlined in Figure 7.1.

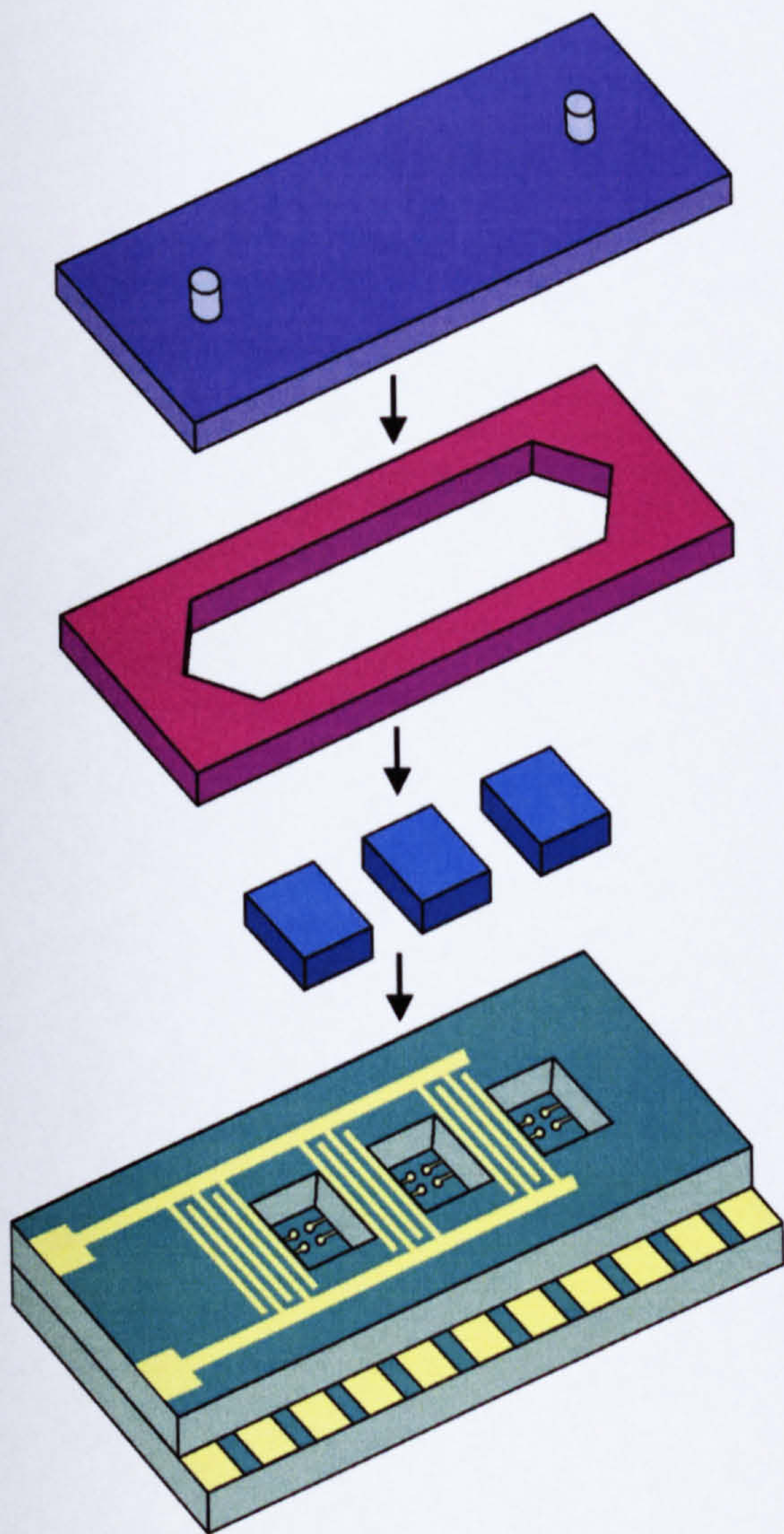

Left: The base of the platform (green) is constructed from two separate plates that are bonded together. The lower plate is patterned with several contact pads that are connected to a row of larger bonding pads, whilst the upper plate, into which a hole for each microsensor is machined, is patterned with an array of interdigitated micro-electrodes. The flow channel is defined by a polymer layer (purple) that is fixed to the upper plate and the individual microsensors (light blue) are inserted into the holes, where they are connected to the underlying contact pads. Finally, a lid with fluidic connectors is bonded onto the polymer surface to enclose the flow channel.

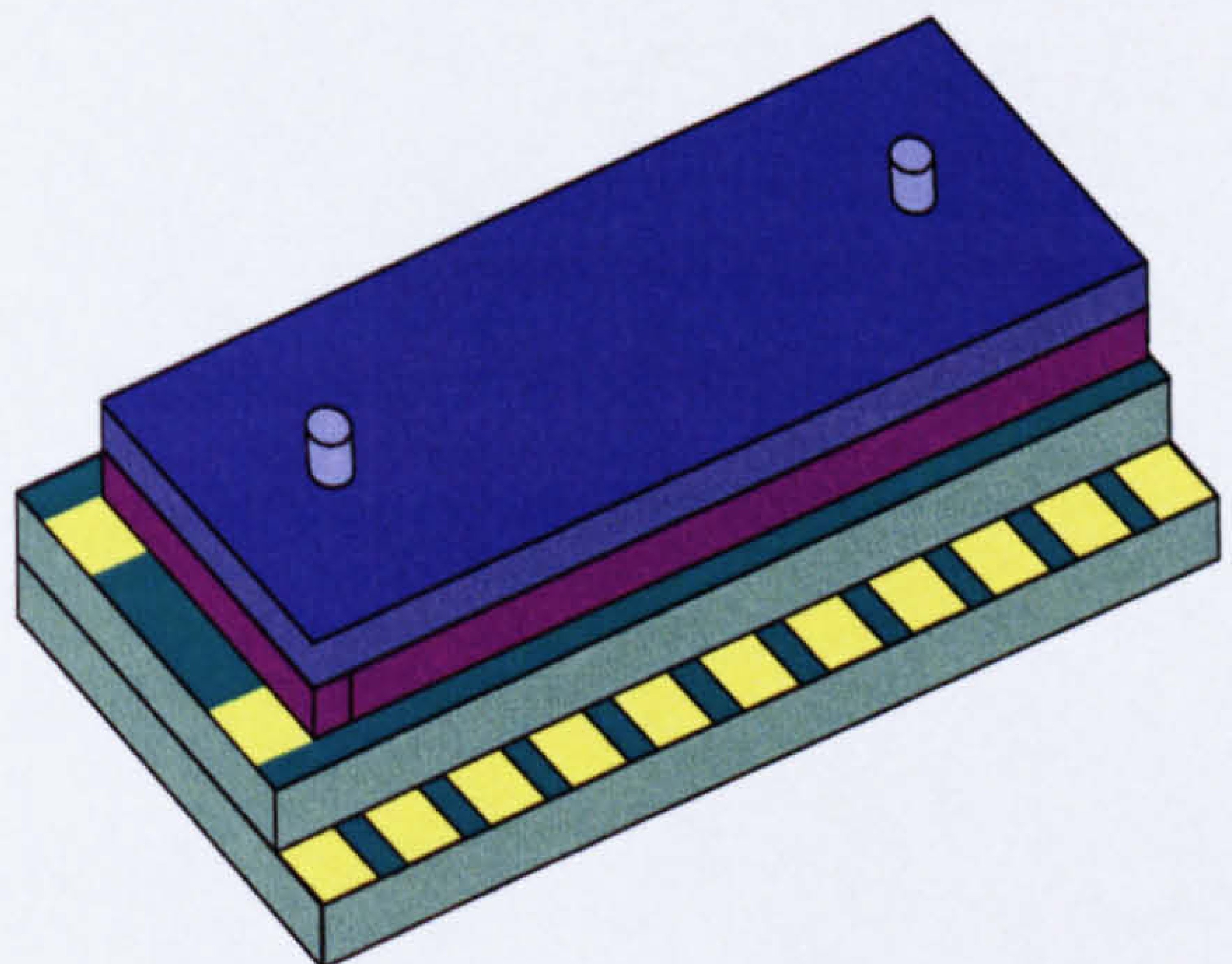

Right: The resulting flow-through system.

Figure 7.1 Schematic Illustrating the Construction of the Integrated Microsensor Platform

7.2.1 Protocols for Fabrication of the Integrated Microsensor Platform

Two different substrate materials were employed when developing the microsensor platform: an aluminium oxide ceramic and poly(ethylene terephthalate) (PET). Both materials have a low dielectric constant, are chemically durable and are relatively low cost. The ceramic is a strong, rigid material that is comparatively difficult to machine, whilst the opposite is true of the PET. Significantly different fabrication protocols were therefore required for each substrate.

As described in Figure 7.1, the construction of the platform initially involved patterning the two plates that formed the base of the system and subsequently bonding them together. When using ceramic substrates, a polyimide bonding process was employed to adhere the two plates together, whilst the PET plates were thermally bonded. Various polymers were employed to create the overlying flow channel, including a hot-melt adhesive foil and PET sheets. Fluidic connectors were created by gluing 1/16" gripper fittings over inlet and outlet holes drilled in the chamber lid.

To allow the connection of individual microsensors to the contact pads, backside contacts were required. Interconnect vias, fabricated by anisotropically wet etching through the Si substrate, were therefore integrated into the design of the dissolved oxygen microsensor. Further details of the fabrication processes employed for the production of the integrated microsensor platform and the adaptation of the microsensor are given in the following sections and the relevant microfabrication protocols can be found in Chapter 3.

7.3 Fabrication of the Integrated Microsensor Platform

Several difficulties were encountered when attempting to fabricate the microsensor platform with both ceramic and PET substrates, particularly in the case of the former. A successful prototype platform was produced using PET as the substrate material and methods for overcoming the problems encountered when using the ceramic substrates are discussed.

7.3.1 Ceramic Substrates

The surface of the ceramic substrates employed was found to be too rough to allow fine resolution patterning of the thin-film interdigitated microelectrode arrays, which had

electrode widths and gaps of either 25 μm or 50 μm. Patterning of the base plate, which had a minimum feature size of 500 μm, was however possible, as the photoresist films employed for these feature sizes were thicker than the surface roughness. From SEM images, the average surface roughness of the ceramics was estimated to be 3 μm. This could be smoothed out effectively by coating the ceramic with a 5-6 μm thick polyimide planarisation layer, such that no surface roughness could be observed with SEM imaging at a magnification of 100,000.

Processing of the planarisation layer was somewhat problematic, as the adhesion of both the polyimide to the ceramic and the metal electrode array to the polyimide layer was poor. These difficulties were overcome by silanising the ceramic plate with 3-aminopropyltriethoxysilane prior to deposition of the polyimide layer and by treating the cured polyimide film in a RIE machine with a high-pressure oxygen plasma prior to evaporation of the NiCr/Au/Ti metal layer (Nakamura *et al*, 1996).

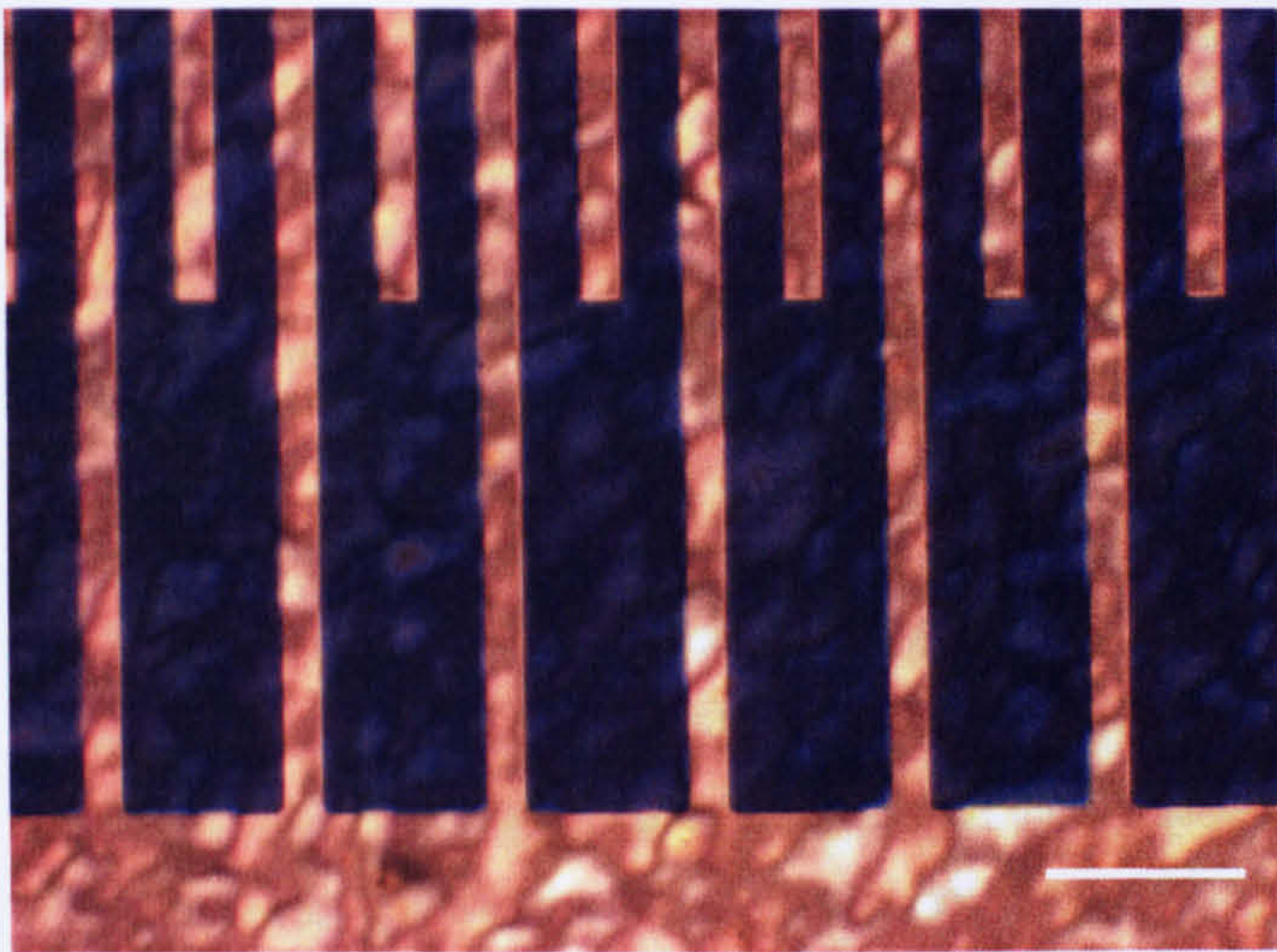

Figure 7.2 **An Array of Interdigitated Electrodes Patterned on a Polyimide Coated Ceramic Substrate**

The scale bar indicates a length of 250 μm.

It should also be noted that NiCr was employed as the adhesive layer for the interdigitated electrodes rather than Ti, as a very thin layer of the later was found to remain on the surface of the polyimide even after wet-etching the sample in a HF solution or dry etching it using a $SiCl_4$ plasma. Though the reason for this is uncertain, the thickness of the remaining film was estimated to be around 0.1 nm from resistance measurements obtained using a four-point probe. When incorporating these modifications into the microfabrication process, an

array of well-defined interdigitated microelectrodes was successfully patterned (see Figure 7.2).

As no laser profiling facilities were available to machine the required holes in the upper plate, the ceramic substrates had to be purchased pre-cut. This lead to difficulties when patterning the upper plate, as spin coating of the pre-cut substrates was not feasible (see Section 2.1.1.1). Initially, the substrates were plugged with ceramic squares, which were cut to fit tightly into each hole, and a layer of photoresist was spin coated. However, this was unsuccessful, as there were noticeable ridges around each of the ceramic plugs that generated large waves in the resist layer (see Figure 7.3).

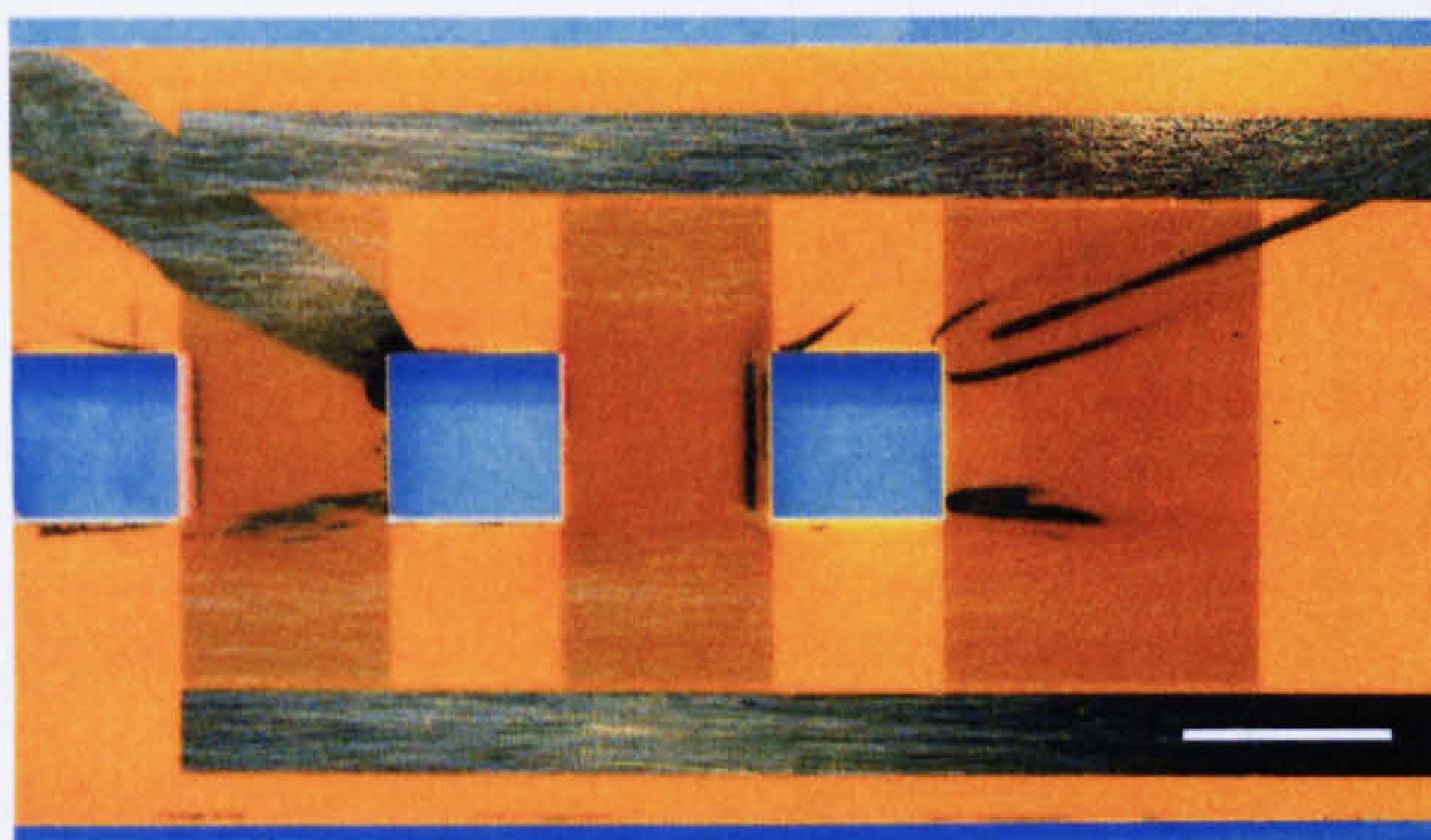

Figure 7.3 **A Pre-Cut Ceramic Substrate Patterned by Spin Coating**

The streaks of metal emanating from the holes in the substrate are the result of waves in the photoresist layer formed when spin coating the sample. These regions of thick resist were not sufficiently exposed or developed during the times that were required for the majority of the resist layer. The scale bar indicates a length of 10 mm.

Consequently, alternative methods of resist coating were investigated. These included the use of a prototyping photoresist aerosol, laminating the substrates with a film of negative-tone resist and simply pouring a diluted resist solution over the sample. Use of the photoresist aerosol was not successful as its resolution proved inadequate (by the time all the unwanted resist had been removed, the electrode pattern was seriously overdeveloped) and even coverage of the sample proved unattainable. Initially, patterning of the laminate film appeared to be relatively successful (Figure 7.4a). However, when lift-off was performed (as was necessary when using the light-field masks that had been written for the interdigitated electrode array), only narrow sections of the electrode pattern remained. It is presumed that a

thin film of resist must have remained over the unexposed areas, though immersion of the sample in the developer solution for a longer period of time would have significantly overdeveloped the pattern. Further optimisation of the lamination and exposure stages may help to create an adequate photoresist layer, though initial tests proved unsatisfactory.

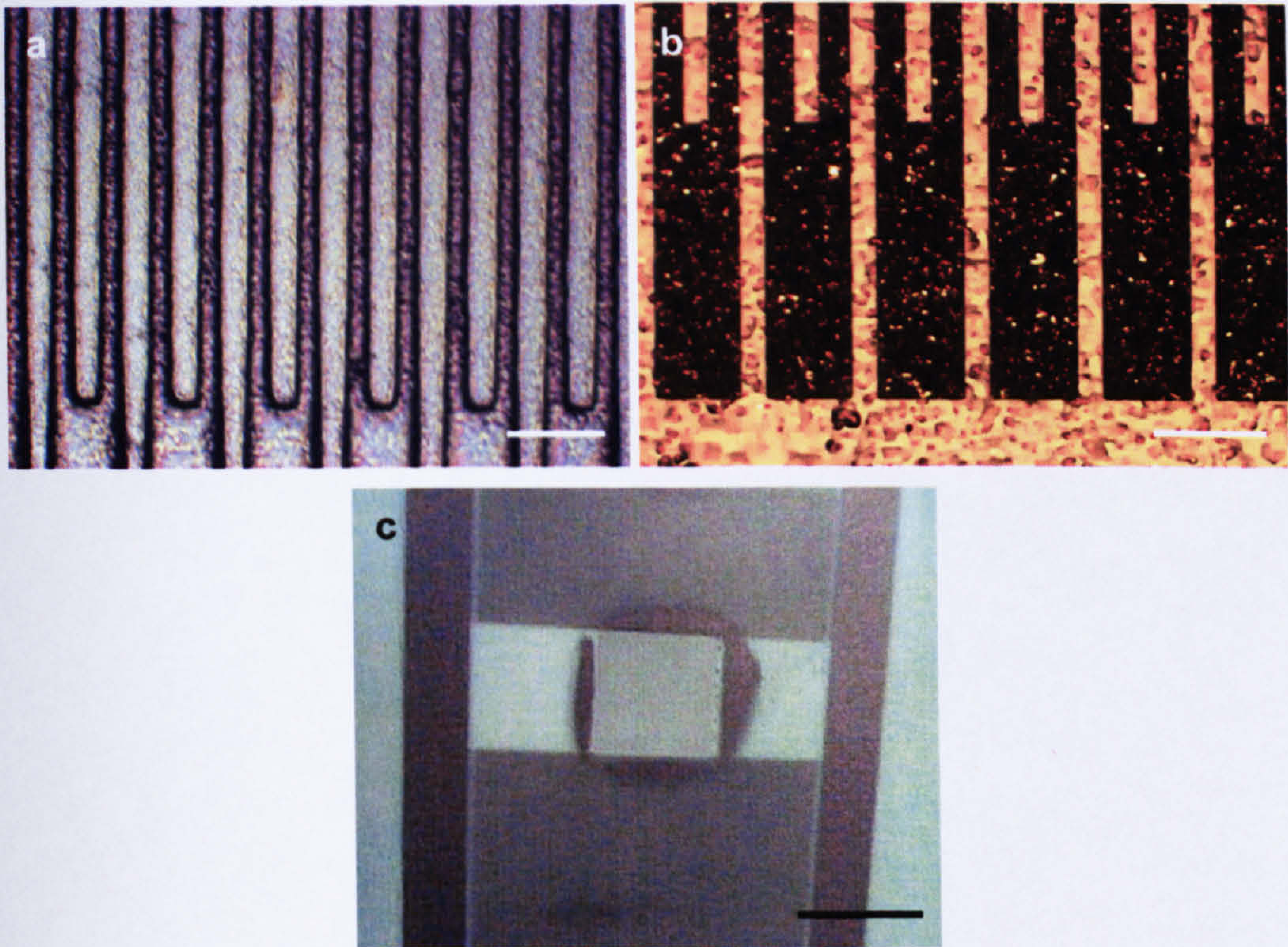

Figure 7.4 **Photoresist Deposition Techniques: Laminating and Pour Coating**

a. A patterned negative-tone laminate. b. An electrode array patterned using a pour coated resist film. c. Illustrates the results of a build-up of resist around the perimeter of the hole, which was not developed or exposed sufficiently during the time periods required for the remainder of the sample. The scale bars denote lengths of 200 μm, 200 μm and 8 mm respectively.

"Pour coating" the resist layer (Section 3.3.2.1) was relatively successful and the fabrication of the interdigitated electrode array would have been possible using this method had the electrode pattern not extended right up to the edge of the holes, where a thick layer of resist built up during the settling of sample (Figure 7.4b and 7.4c). When patterning 50 μm electrodes by this method, the resist film was sufficiently thick for the omission of the polyimide planarising layer, though the resulting electrodes were slightly rough. However,

narrower electrode structures would require the use of a resist layer thinner than the surface roughness of the ceramics and, consequently, a planarising layer would again be required.

7.3.1.1 Bonding of the Individual Layers

To bond the upper and lower ceramic plates, a polyimide layer was employed to sandwich the two together, as described in Section 3.3.4.2. Though this method proved satisfactory for the size of holes currently employed (Figure 7.5), there was a notable build up of resist around the edges of the holes which, for smaller areas, would encroach on the region where the bonding pads are situated. However, this problem could be avoided if a commercial spray coating machine was employed (see Section 2.1.1.2). Furthermore, if insulation of the connecting wires is not required, a thin adhesive layer could simply be painted onto the base of the upper plate and the two substrates clamped together to cure. The overlying flow-channel could be created straightforwardly by using a hot-melt adhesive foil to create a spacer between the base of the platform and a glass or ceramic lid. At the flow rates employed when testing the hermeticity of such channels (approximately 5-10 ml min^{-1}), no leakage was observed.

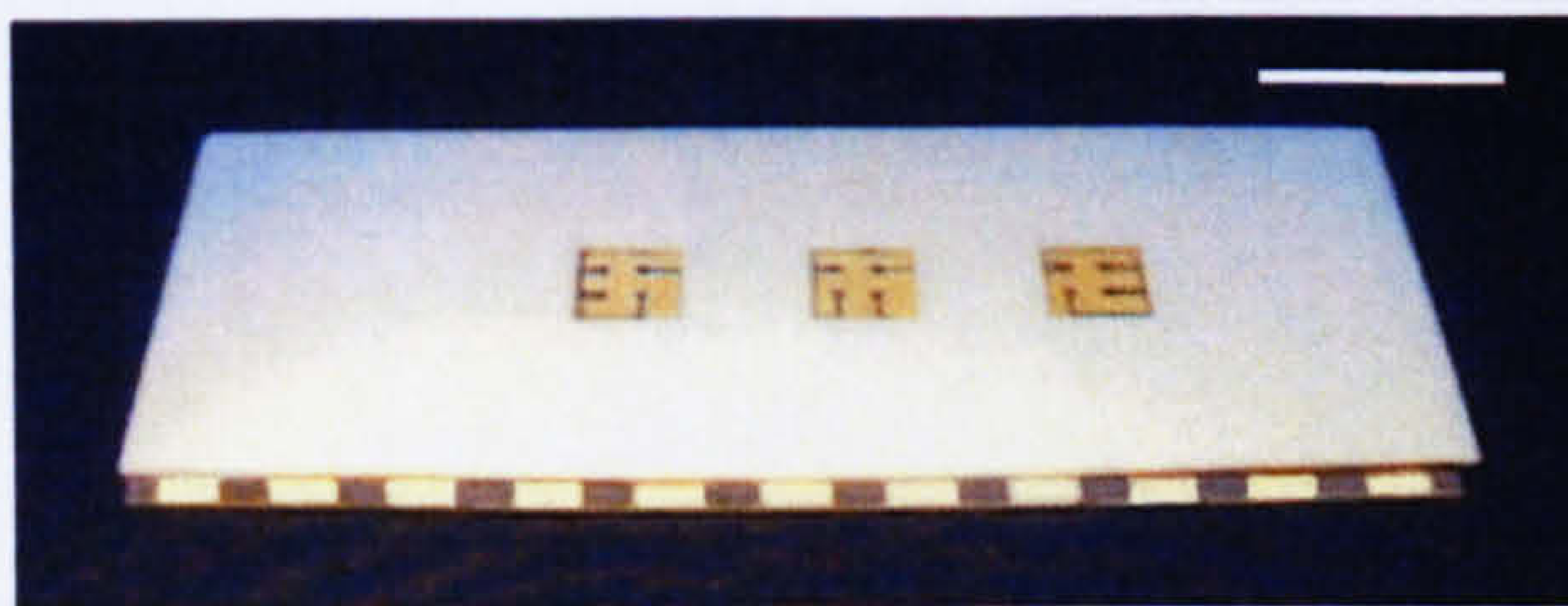

Figure 7.5 **An Example of Polyimide Bonding**
Two ceramic plates bonded together using the polyimide bonding process.

Although it was not possible to construct an integrated microsensor platform using the ceramic substrates, methods for doing so can be readily envisaged. If either a commercial spray coating machine, which could cover a pre-cut substrate with a uniform resist layer, or laser machining facilities, which would enable holes to be cut after the patterning of the substrates, were available, the upper plate of the platform base could be successfully fabricated. The upper and lower plates could then be sandwiched together using polyimide bonding (with spray coating of the photoresist mask) and a hot-melt adhesive foil could be employed to create the overlying flow-channel. Nonetheless, the cost and time required to

produce such a platform would be relatively high. Therefore, it was decided to explore the use of polymer substrates.

7.3.2 Poly(Ethylene Terephthalate) (PET) Substrates

Unlike the ceramic substrates, sheets of PET are readily machinable and, therefore, the holes for the individual sensors could be cut out after the interdigitated electrode array had been patterned; hence spin coating of the top plate was no longer problematic. The PET sheets were simple to pattern with no surface roughness or adhesion difficulties, although the samples had to be clamped flat when baking and cooling so as to prevent curling of the substrate. Also, cleaning agents had to be selected carefully, as certain solvents, including acetone, cause the surface of the PET to whiten and roughen. Nonetheless, the fabrication of an array of 2.5 μm radius dots (the smallest feature size attempted) proved both successful and straightforward using this substrate.

For the prototype microsensor platform shown in Figure 7.6a, holes were drilled through the upper plate after patterning the interdigitated electrode array, the surface of which was protected with a film of photoresist. Alternatively, square holes may be produced by simply clamping and heating the sample to 100-110°C on hotplate and then cutting out the squares of material using a suitable cutting tool.

Optimisation of the thermal bonding of the upper and lower plates and the overlying flow channel is still required. Although successful bonding was achieved using a clamp protected with Mylar films (to prevent sticking of the PET) at a temperature of 110-115°C, slightly too much pressure caused the PET plates to be crushed, whilst too high a temperature produced a white, more brittle structure. Conversely, when the temperature or pressure employed was too low, the plates and the flow channel could be easily peeled apart and were not sufficiently watertight. Access to a hydraulic press, for example, with accurate temperature and pressure control would allow for optimisation of the process.

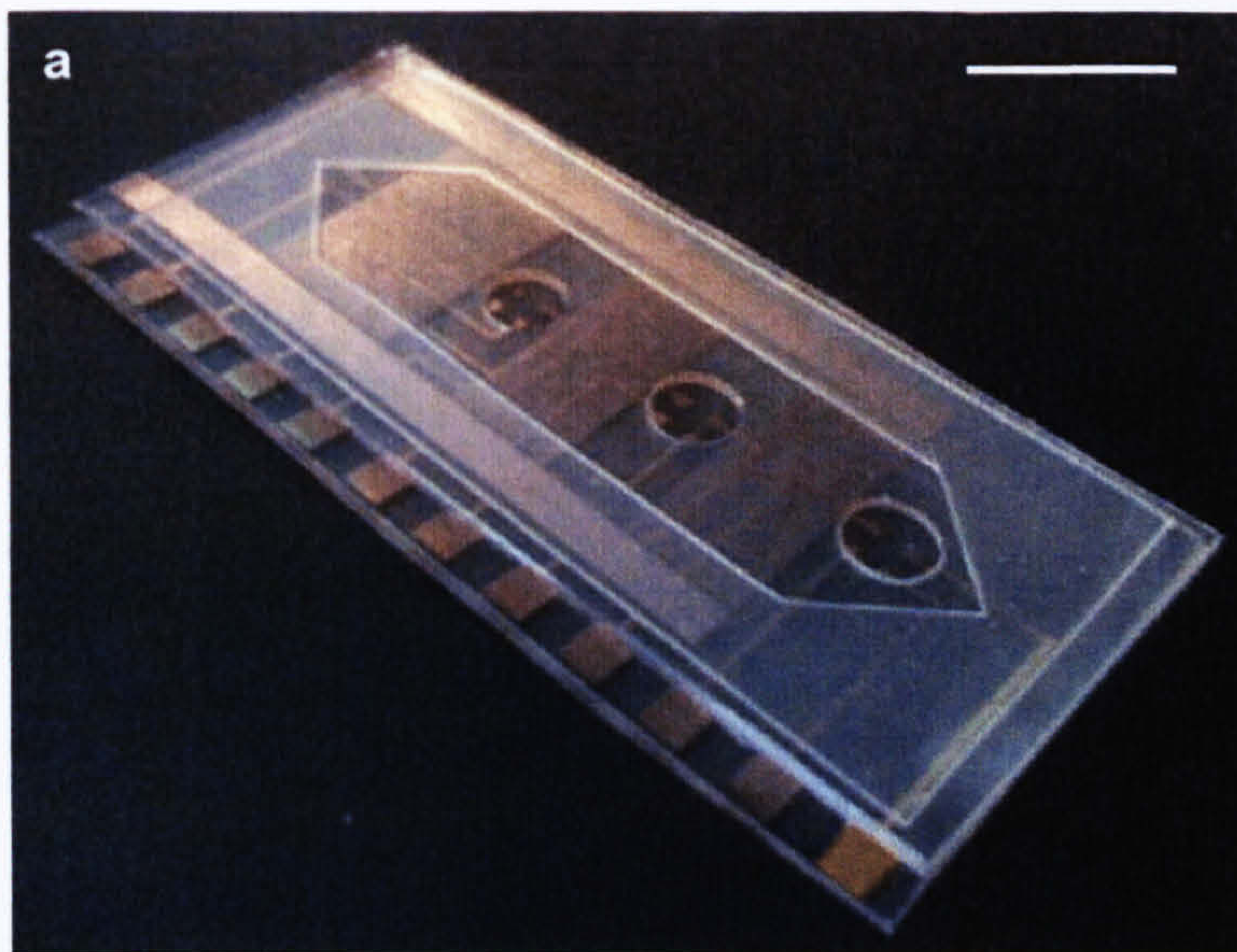

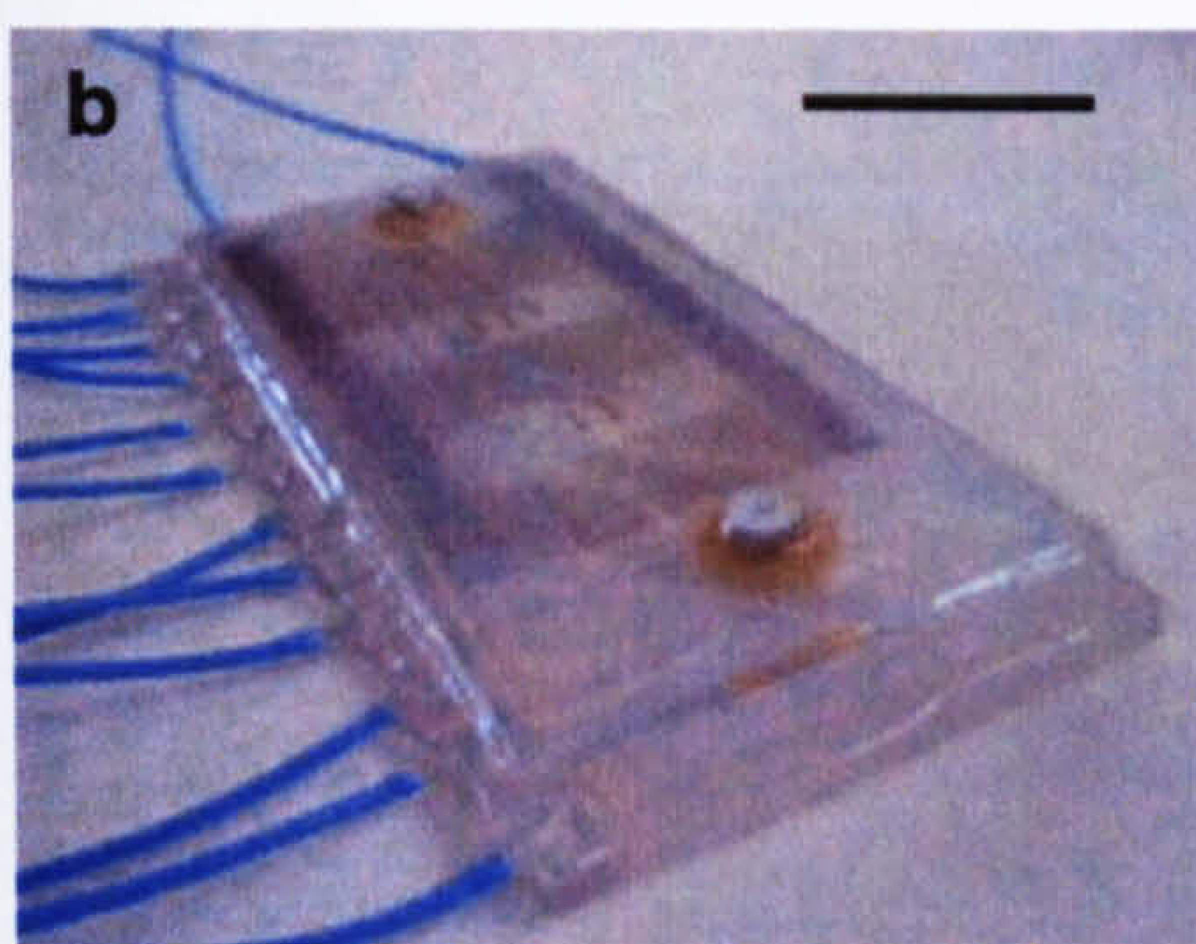

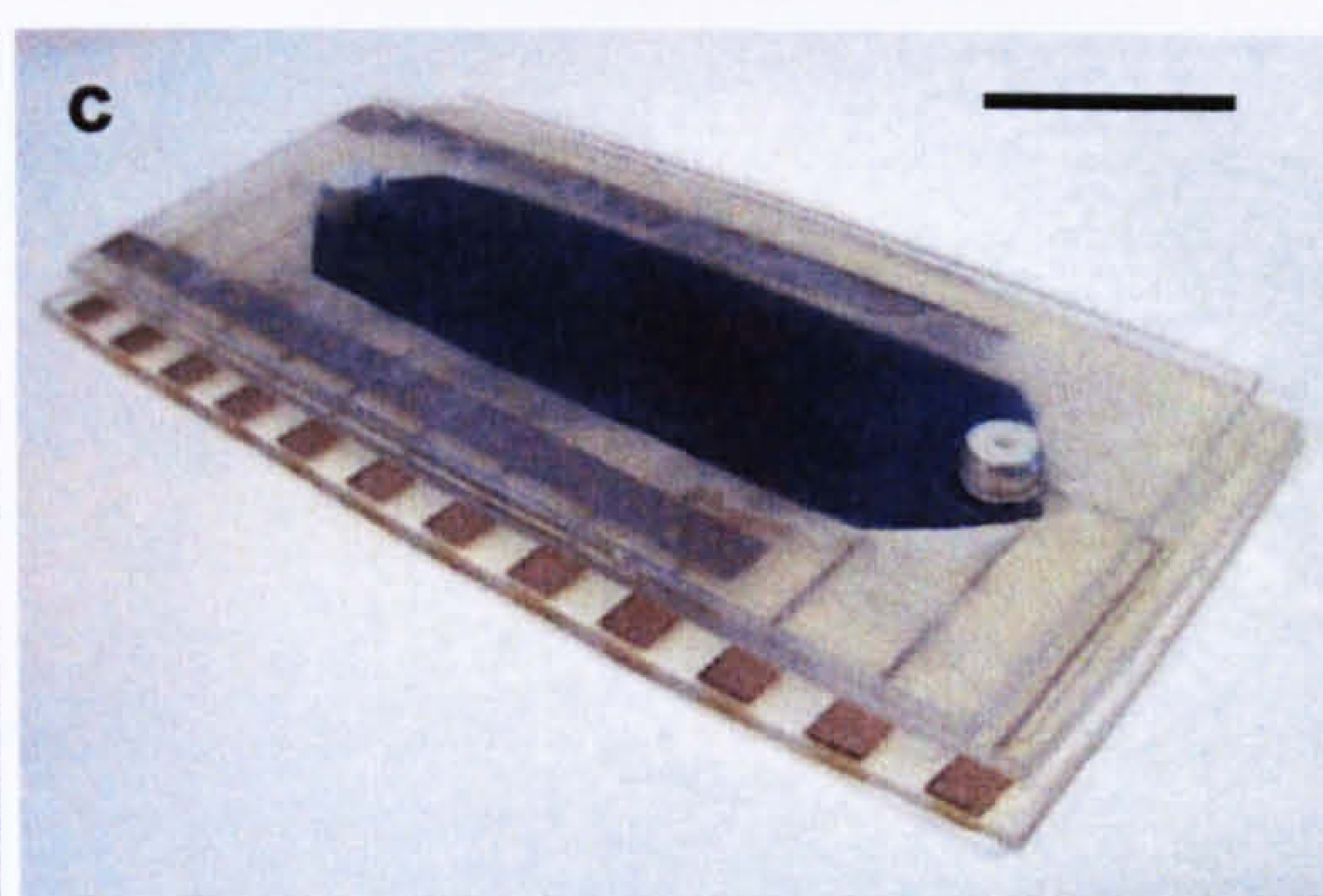

Figure 7.6 **Photographs of a PET Integrated Microsensor Platform**

a. The lower plate, upper plate and flow channel walls of a platform after thermal bonding. b. A platform encapsulated with PDMS. c. Testing the hermeticity of the flow-channel. The scale bars indicate a length of approximately 20 mm.

Fluidic connectors were attached to the inlet and outlet ports using a commercial epoxy and, after soldering a wire to each of the bonding pads, the entire device was encapsulated with PDMS (Figure 7.6b), though ideally use of an insulated edge connector would be preferable. The hermeticity of the system was again checked by injecting a dye solution at rate of 5-10 ml min^{-1} and no leakage was observed, although in the future more rigorous testing would be desirable. Nonetheless, it appears that PET can be employed to simply produce a low-cost, flow-through analytical system.

7.3.3 Microsensor Interconnect Vias

The creation of an interconnect via through a silicon substrate (Figure 7.7a) is a relatively straightforward task, where the substrate is anisotropically wet-etched through a silicon nitride or silicon oxide mask. However, the presence of such vias complicates any subsequent microfabrication steps, due to the effect on the spin coating process.

For the dissolved oxygen and temperature sensor described in Chapter 6, it was necessary to create six interconnect vias prior to all other fabrication steps. Nevertheless, the layout of the microsensor meant that waves emanating from the vias only affected the outside of the sample, away from the critical areas in the centre of the design. Spin coating was therefore employed, with the backside of the sensors fixed to a coverslip. However, this proved relatively problematic, as there was generally inadequate coverage of the sharp edges of each via and, after exposure and development, areas of unwanted resist remained at the edges of the sample. Injecting small quantities of resist into each via, so that the level of resist rose to slightly over the boundaries of each via, solved the first of these problems, whilst removing the unwanted resist from around the edges of the sample with a cotton bud soaked in acetone resolved the second.

Nonetheless this was a time consuming process, so the "pour coating" procedure was employed once more. Unfortunately, injection of resist into each of the vias was again required to ensure no breaks between the connecting wires and the metal-coated vias. These problems could again be avoided by employing a commercial spray coating machine, which should enable the creation of a uniform resist film over the entire sample surface.

It should be noted here that no difficulties were encountered when patterning the SU8 chamber, as the SU8 employed was significantly thicker than the photoresist formulations and, therefore, a more uniform coverage was obtained, particularly when the sample was left to settle after spinning. Furthermore, only the central area of sample was patterned with SU8 – the SU8 covering all other areas was washed away when the sample was developed. A dissolved oxygen and temperature microsensor with interconnect vias is shown in Figure 7.8.

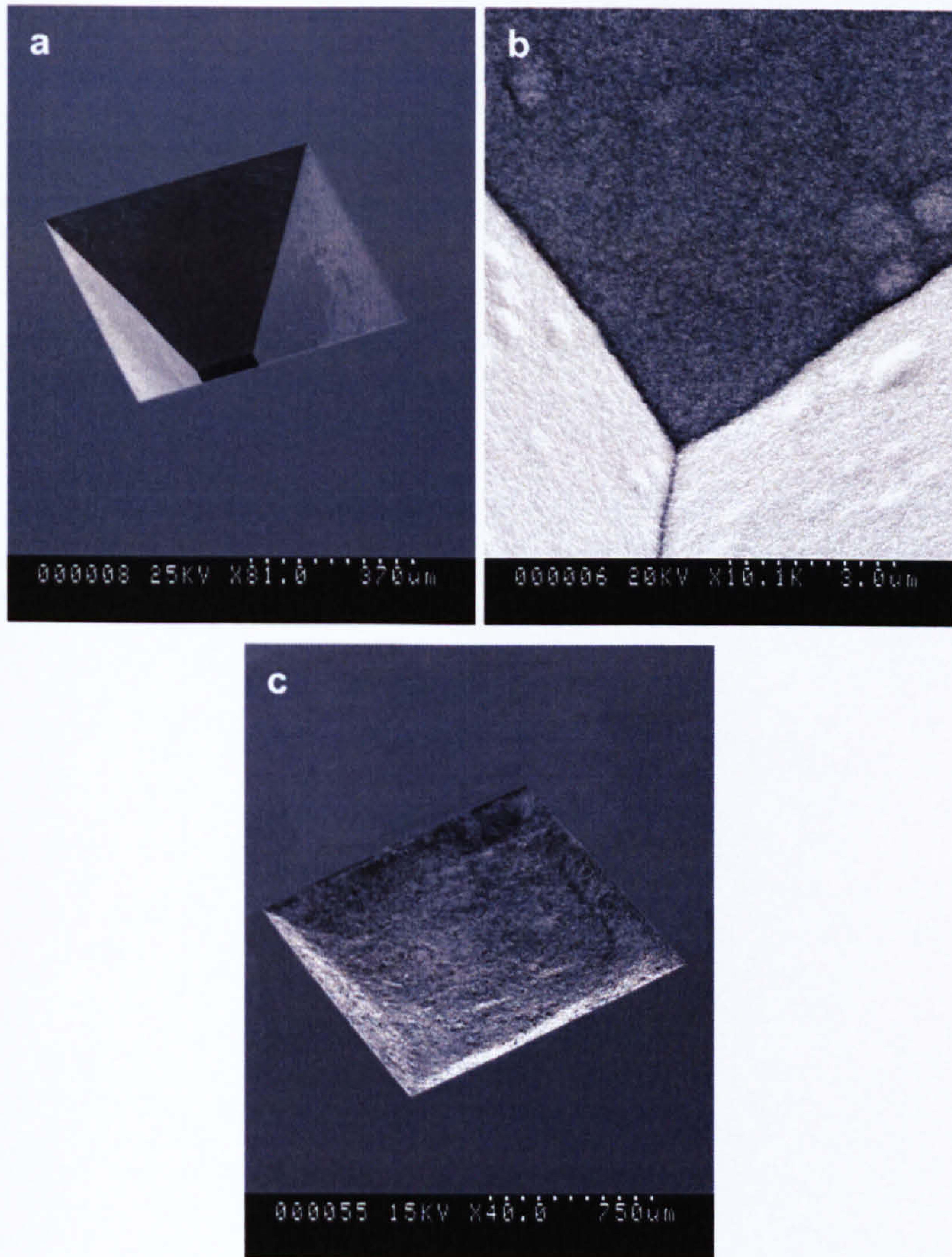

Figure 7.7 **SEMs of Microfabricated Interconnect Vias**

a. A via created by wet etching through a Si(100) wafer. b. A via, with a silicon nitride membrane on the backside, after electroplating gold for 1.5 hours. c. A via filled with conductive adhesive.

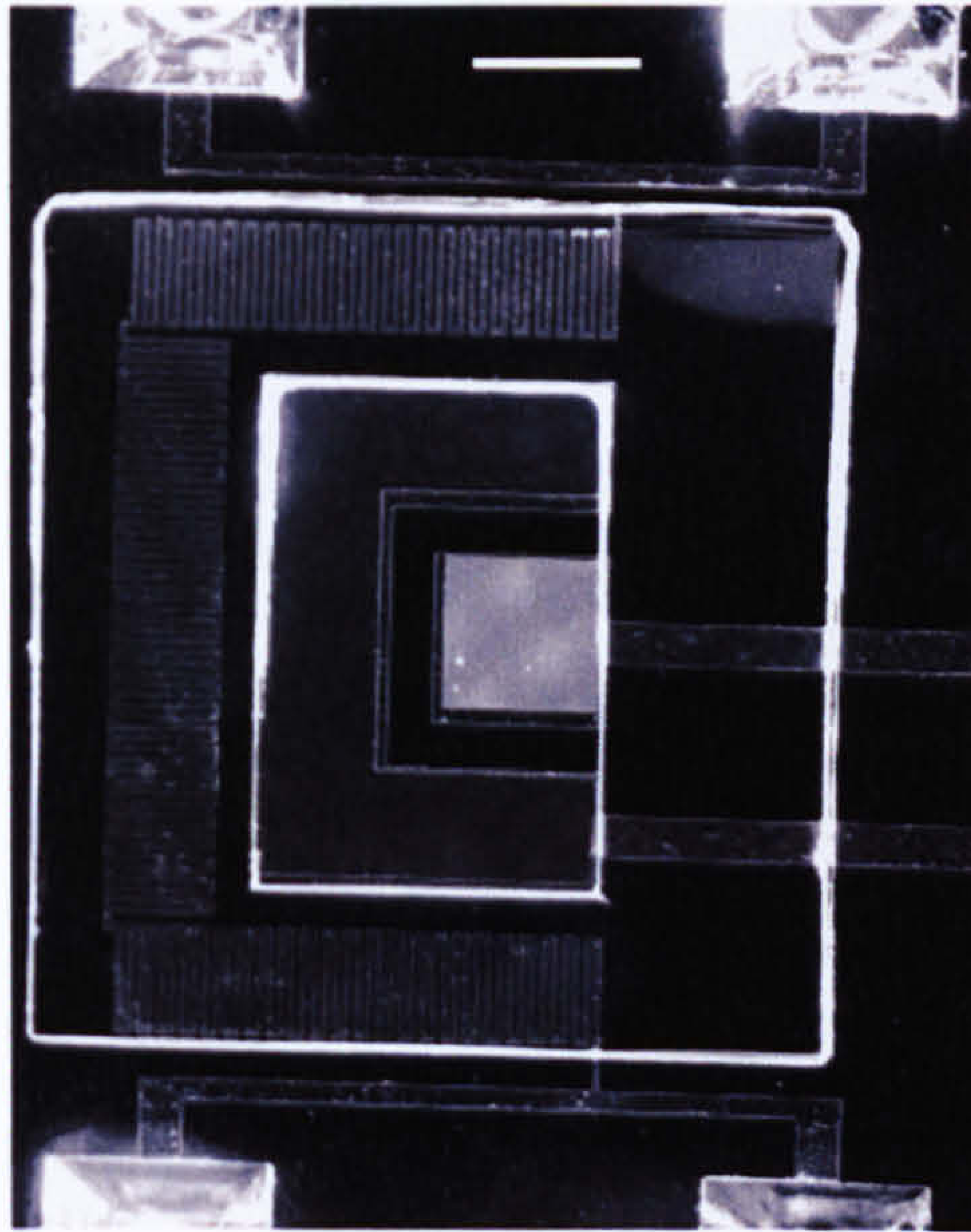

Figure 7.8 **A Dissolved Oxygen and Temperature Microsensor with Interconnect Vias**

The scale bar denotes a length of 800 μm.

7.3.3.1 Connection of the Microsensors to the Integrated Microsensor Platform

Two methods were considered for bonding the sensors to the platform: flip-chip bonding and the use of a conductive adhesive. In the case of the former, it was necessary to electroplate a thick metal onto to the surface of the vias, so as to ensure a good connection between the base of the via and the contact pad on the platform. However, electroplating the vias proved to be a time consuming process – after 1.5 hours of electroplating, using the parameters given in Table 3.2, the thickness of the electroplated gold layer obtained was estimated (from SEMs) to be 25 μm. Furthermore, so as to maintain a flat surface on the backside of the sensor after electroplating, it was necessary to ensure that the fragile silicon nitride membrane created when wet-etching through the silicon wafer remained intact (Figure 7.7b). This membrane would then have to be removed by RIE after electroplating the vias. As incorporation of these procedures would significantly increase the overall complexity of the microsensor fabrication process and as the flip-chip bonding process itself required much optimisation, it became apparent that an alternative, more straightforward, approach was required.

It was therefore decided to employ a conductive adhesive, with a high silver content, to bond the sensors to the platform. The backside silicon nitride membrane was simply removed with

a cotton bud and the sensor was then positioned over the contact pads whilst the conductive adhesive was injected into each via by hand (Figure 7.7c). This technique proved both simple and effective, though a more controllable injection system would be required if the width of the vias was decreased to below 500 μm.

7.4 Simulation and Experimental Methods

7.4.1 Matlab Simulations

Simulations of the negative DEP antifouling system employed the dimensions of the integrated microsensor platform structure, as seen in Figure 7.6. To illustrate the dimensions more clearly, a schematic drawing of the structure, the main features of which are to scale, is shown in Figure 7.9. Only the inlet region (the inlet port being marked by the circle towards the left of the flow channel), the large initial electrode array and the first sensor region were described in the Matlab script.

The trajectories of latex beads moving through the platform were simulated, as these were used as model particles for the preliminary experimental work. Variation in the value of f_{CM} with ε_m, σ_m and ω was plotted using Equations 7.01 and 7.02. The value employed for σ_p was calculated using:

$$\sigma_p = \frac{2K_s}{r} \tag{7.09}$$

where K_s is the surface conductance, which was estimated by Cui *et al* (2001) to be 0.67 nS for a 2.02 μm latex bead. A value of 2.56 (the value for bulk latex) was assumed for ε_p.

Particle trajectories were simulated by successively resolving the horizontal and vertical forces acting on a particle and from this estimating its path over time. To achieve this, an initial position was defined for each particle. The program then evaluated the forces acting on each particle and, from the resulting values, the horizontal and vertical velocities were obtained. These velocities were then multiplied by a time step value, so that the new positions could be calculated for each particle. This sequence of calculations was repeated for each new position until the simulation ended at a specified time point. Naturally, the results of the simulation were influenced by the value of the time step employed.

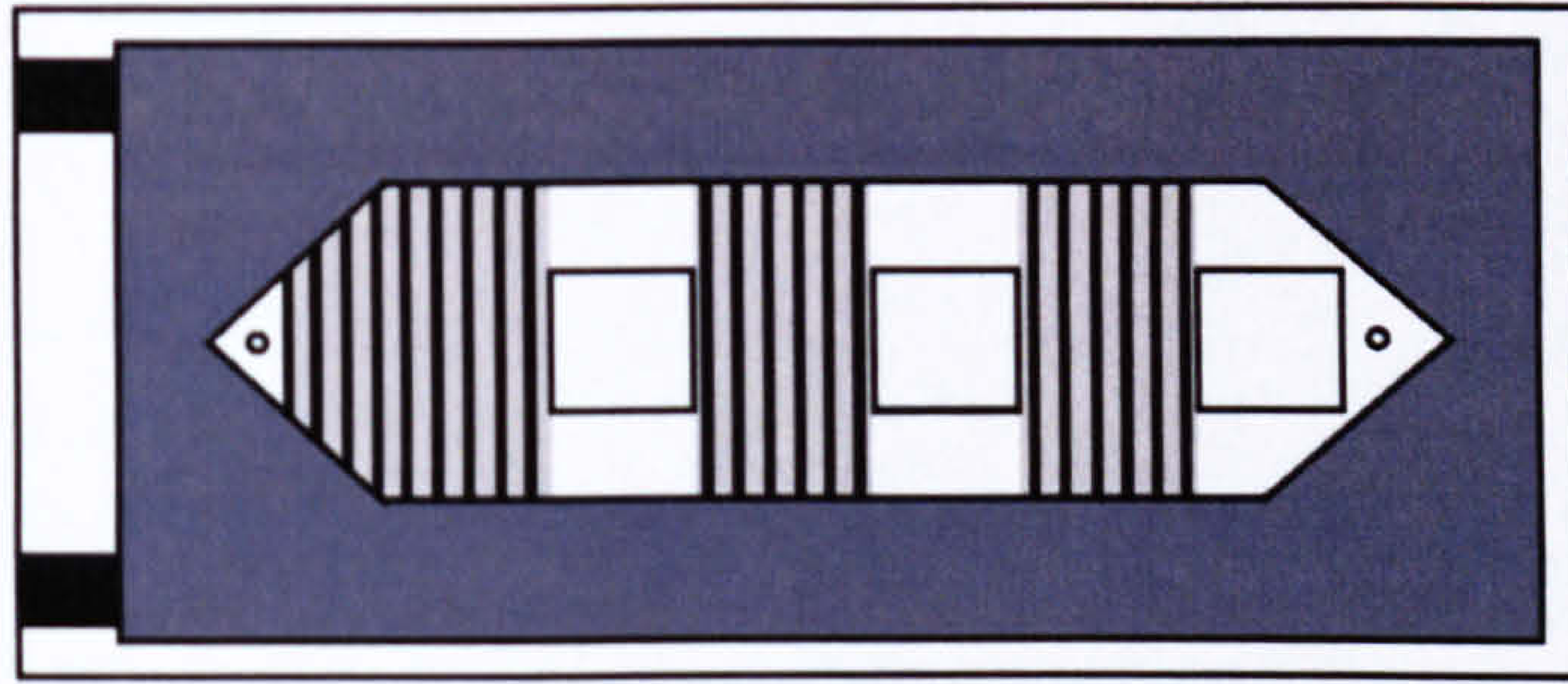

Figure 7.9 **Schematic Diagram of the Simulated Integrated Microsensor Platform**

The dark grey area represents the flow channel, whilst the light grey areas (with black line electrodes) represent the interdigitated microelectrode arrays. The three square sensor regions have dimensions of 8 mm x 8 mm and the inlet and outlet ports are marked by two circles.

In the vertical dimension, the forces due to viscous drag, gravity, buoyancy and negative DEP (Section 7.1.2.1) were combined to obtain a formula for the steady state velocity:

$$v = \frac{F_{DEP} + F_G}{6\pi\eta r} \tag{7.10}$$

The velocity in the horizontal direction was calculated using Equation 7.08. It should be noted that the Matlab programme accounted for the shape of the flow-channel employed in the microsystem design by applying a linearly increasing channel width throughout the inlet region (increasing to 18 mm wide) and assuming a F_{DEP} value of zero directly beneath the sample inlet. Naturally, a F_{DEP} value of zero was also employed in the sensor region.

7.4.2 Experimental Methods

The device employed for preliminary experiments comprised an interdigitated array of 10 nm Ti, 100 nm Au, 20 nm Ti electrodes fabricated on a glass microscope slide by wet-etching (Section 3.3.1.4.2). The width of the electrodes and the inter-electrode spacing was 50 µm. A hot-melt adhesive flow channel, which covered the edges of the individual microelectrodes, was subsequently thermally bonded onto the microscope slide (Section

3.3.4.3). A second glass slide, into which two holes had been drilled for the inlet and outlet ports, was then bonded onto to the surface of the flow-channel.

Preliminary experimental investigations were performed by flowing a solution containing latex beads through the interdigitated microelectrode array device. 2.02 μm and 4.66 μm diameter carboxylated latex beads were washed twice and then re-suspended in a 30 mS m^{-1} solution of phosphate buffered saline (PBS) in RO water. The frequency of the signal applied to the electrode arrays was swept (from approximately 1 kHz to 20 MHz) to determine the frequencies at which positive and negative DEP occurred. For the later, measurements of the levitation height of the particles were made for a range of voltages at a set frequency (2 MHz), with the height above the microelectrodes being measured using the calibrated focus control on a Nikon Microphot microscope (using a x10 magnification lens in brightfield mode).

7.5 Preliminary Simulation and Experimental Results

7.5.1 Simulation of the Dielectrophoretic Antifouling Strategy

Before running the particle trajectory simulations it was necessary to determine the value of f_{CM} for the relevant conductivities and permittivities. Figure 7.10a illustrates the variation in f_{CM} with frequency for a range of medium conductivities (0.1 mS m^{-1} to 10 mS m^{-1}) for a 2.02 μm latex bead, assuming a relative medium permittivity of 84, a relative particle permittivity of 2.56 and a particle surface conductance of 0.67 nS. The strong dependence of f_{CM} on the conductivity of the medium employed can be clearly seen and, for conductivities greater than 1.3 mS m^{-1}, only negative values of f_{CM} were obtained.

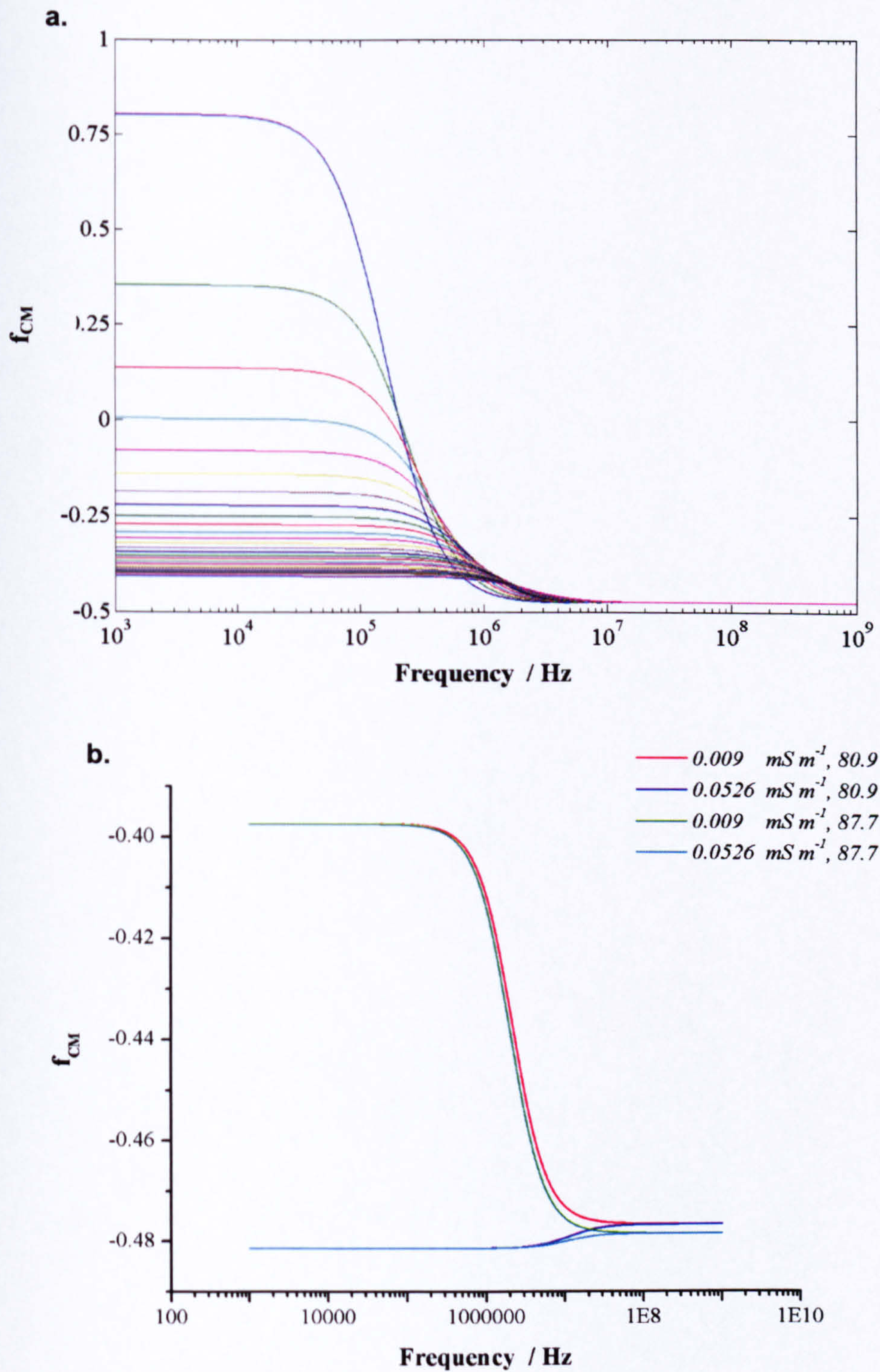

Figure 7.10 **Variation in the Clausius-Mossotti Factor (f_{CM}) with Variation in Frequency, Medium Conductivity and Temperature**

a. Moving downwards from the blue trace at the top left of the graph, the medium conductivity employed for each trace increases from 0.1 mS m^{-1} to 10 mS m^{-1} in steps of 0.4 mS m^{-1}. b. The legend details the medium permittivity and conductivity employed for each

trace. 87.7 corresponds to the relative permittivity of water at 0.5°C, whilst 80.9 corresponds to the relative permittivity at 18°C (Lide, 1993).

If negative DEP was to be used as an antifouling technique in a system analysing freshwater samples, a variety of conductivities may be encountered. Annual data for the conductivity and the temperature (which will affect medium permittivity) of the River Kelvin was obtained from the Scottish Environmental Protection Agency (SEPA). For the year 2000, the average values of the conductivity and temperature of the river were 31.7 mS m^{-1} and 9.5°C respectively, whilst the most extreme values recorded were 9 and 52.6 mS m^{-1} and 0.5 and 18°C. The variation in f_{CM} with frequency for the latter values is shown in Figure 7.10b. At 2 MHz (the frequency employed for the preliminary levitation experiments), the smallest negative value of f_{CM} obtained was –0.435.

Figure 7.11 shows simulated trajectories for 2.02 μm latex beads flowing through the system from three starting heights (assuming an applied voltage of 4 V, a relative medium permittivity of 80.9, an f_{CM} of –0.435, a medium viscosity of 0.9 g m^{-1} s^{-1}, a volumetric flow rate of 4.2 mm^3 s^{-1} (15 ml h^{-1}), a medium density of 1000 kg m^{-3} and a particle density of 1050 kg m^{-3}). As the lower two particles move over the microelectrode array, negative DEP causes them to move upwards towards the faster flow streams at the centre of the channel (which is 500 μm high). Therefore, the particles flow more quickly over the microsensor region, with little sedimentation occurring. The height of uppermost particle is seen to continuously decrease, as F_{DEP} is weaker at these heights than F_G and, hence, the particle will descend towards a steady-state levitation height, where F_{DEP} and F_G are balanced. With this simulation, a levitation height of 101 μm was obtained, which agrees with theory for the values employed. The time step used between successive velocity calculations was 10 ms, as the variation in the results obtained with smaller time steps was minimal (a 0.03% difference between 10 ms and 1ms), whilst the computational time was significantly longer.

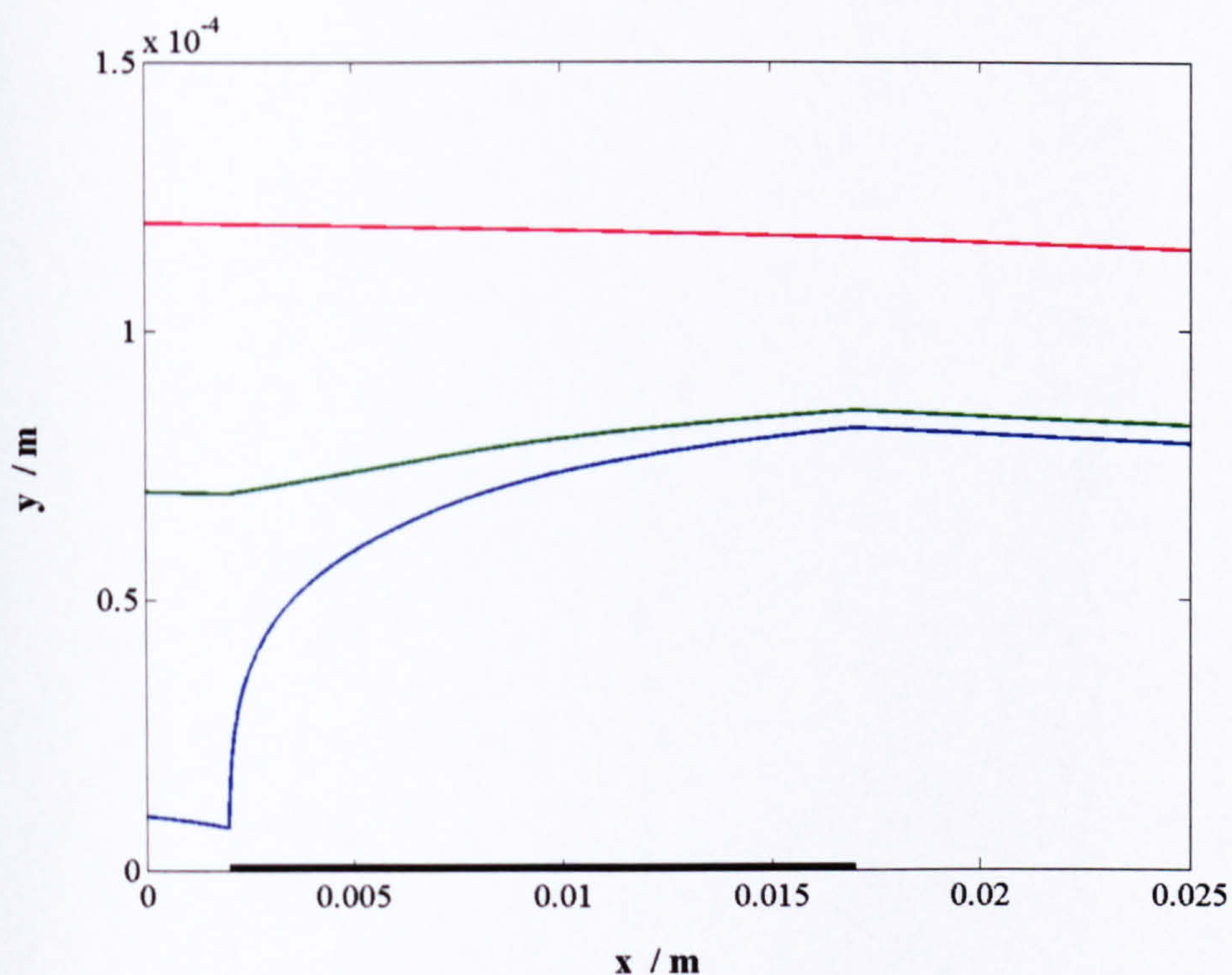

Figure 7.11 **Simulated Trajectories of a 2.02 μm Latex Bead Flowing Through the Integrated Microsensor Platform**

For both the platform structure shown in Figure 7.6 and the Matlab programme employed for these simulations, no electrodes were situated directly beneath the sample inlet. However, 2 mm after the inlet, a 15 mm long interdigitated electrode array began (the position of which is marked by the thick black line on the x-axis), after which there was an 8 mm space for a microsensor.

7.5.2 Experimental Results for the Dielectrophoretic Antifouling System

For experiments employing arrays of interdigitated microelectrodes to generate a dielectrophoretic force, a glass device with a hot-melt adhesive flow-channel was fabricated so that the motion of the particles could be easily monitored using a microscope (see Figure 7.12).

Initial experiments employed suspensions of 2.02 and 4.66 μm latex beads. A 2 MHz signal was applied so as to generate a strong negative dielectrophoretic force. When a suspension of beads was passed through the glass device, the height of the beads could be seen to gradually increase as they flowed over the initial electrode array and no beads were observed on or near the glass surface in the regions without microelectrodes. Measurements of the levitation

height of a suspension of beads (Figure 7.13) were made in a quiescent solution to ascertain the heights obtained for different applied voltages. The results are displayed in Figure 7.14.

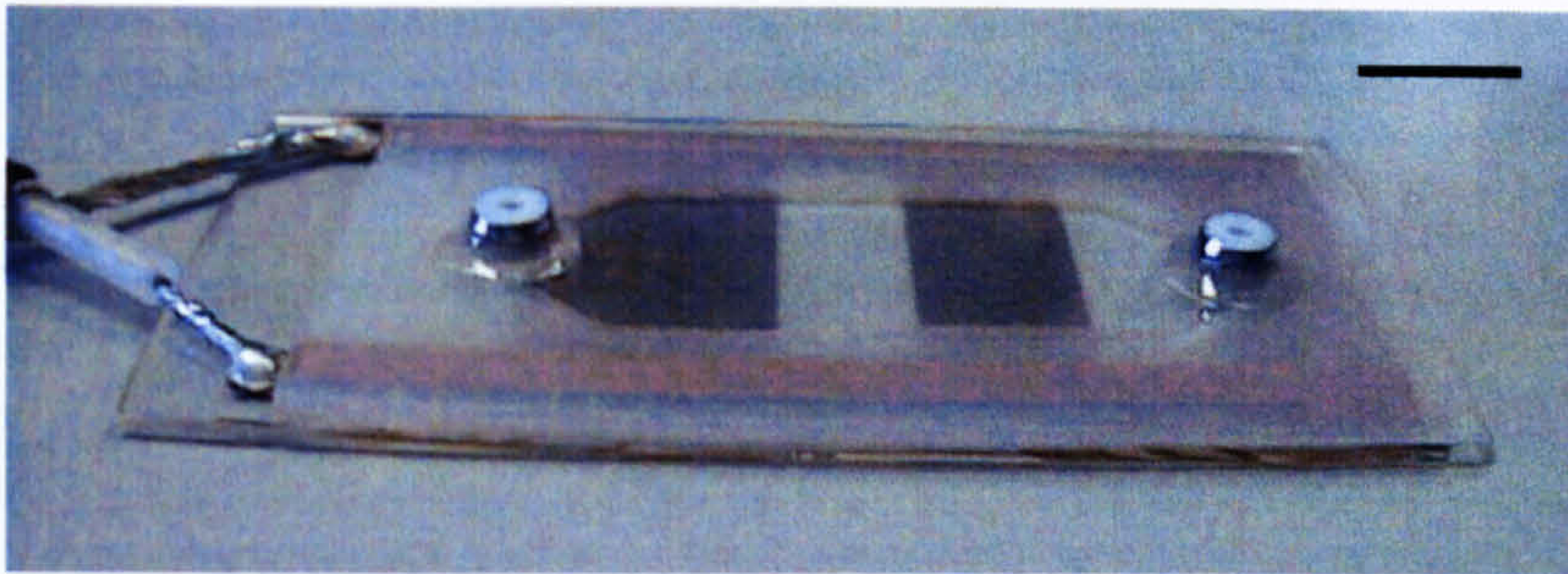

Figure 7.12 **The Interdigitated Microelectrode Array Device Employed For DEP Experiments**

Samples were injected through the inlet at the left of the device. They then flowed over the large electrode array, across a blank "sensor" region and then across the smaller electrode array and the second "sensor" region. The scale bar indicates a length of approximately 10 mm.

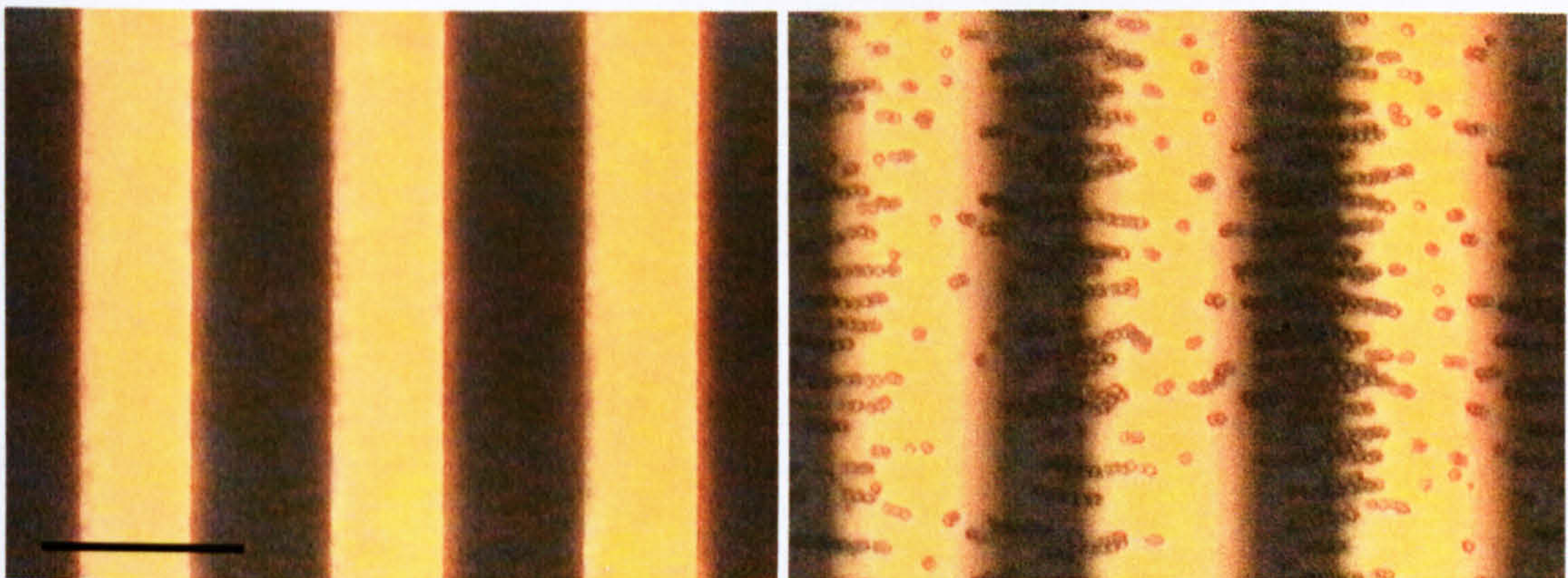

Figure 7.13 **Latex Beads Levitating Above a Microelectrode Array**

When focussing on the surface of the microelectrodes no beads could be seen (a) as they were levitating above the electrode surface (b). So-called pearl chain formation was observed amongst the levitating beads (caused by the local distortion of the electric field surrounding the individual particles, which results in mutually attractive forces between the particles (Markz and Davey, 1999). The scale bar indicates 80 μm.

It can be seen that, as expected, the experimental measurements follow a logarithmic trend and that similar values were obtained for the experimental and theoretical levitation heights at low voltages. However, the experimental values deviate somewhat from the theoretical

values at higher voltages. Probable reasons for this are twofold. Firstly, refractive index mismatches at the air/glass/water interfaces cause an "apparent depth" effect (Shaw, 1999), leading to a discrepancy between the movement of the focal plane of the sample with respect to the movement of the microscope stage. Secondly, due to the size of the electrode arrays, an appreciable voltage drop could potentially occur along the length of the electrodes. This would result in a reduction of the strength of the electric field within the fluid and consequently a reduction in the DEP force acting on the particles, which would reduce the levitation height.

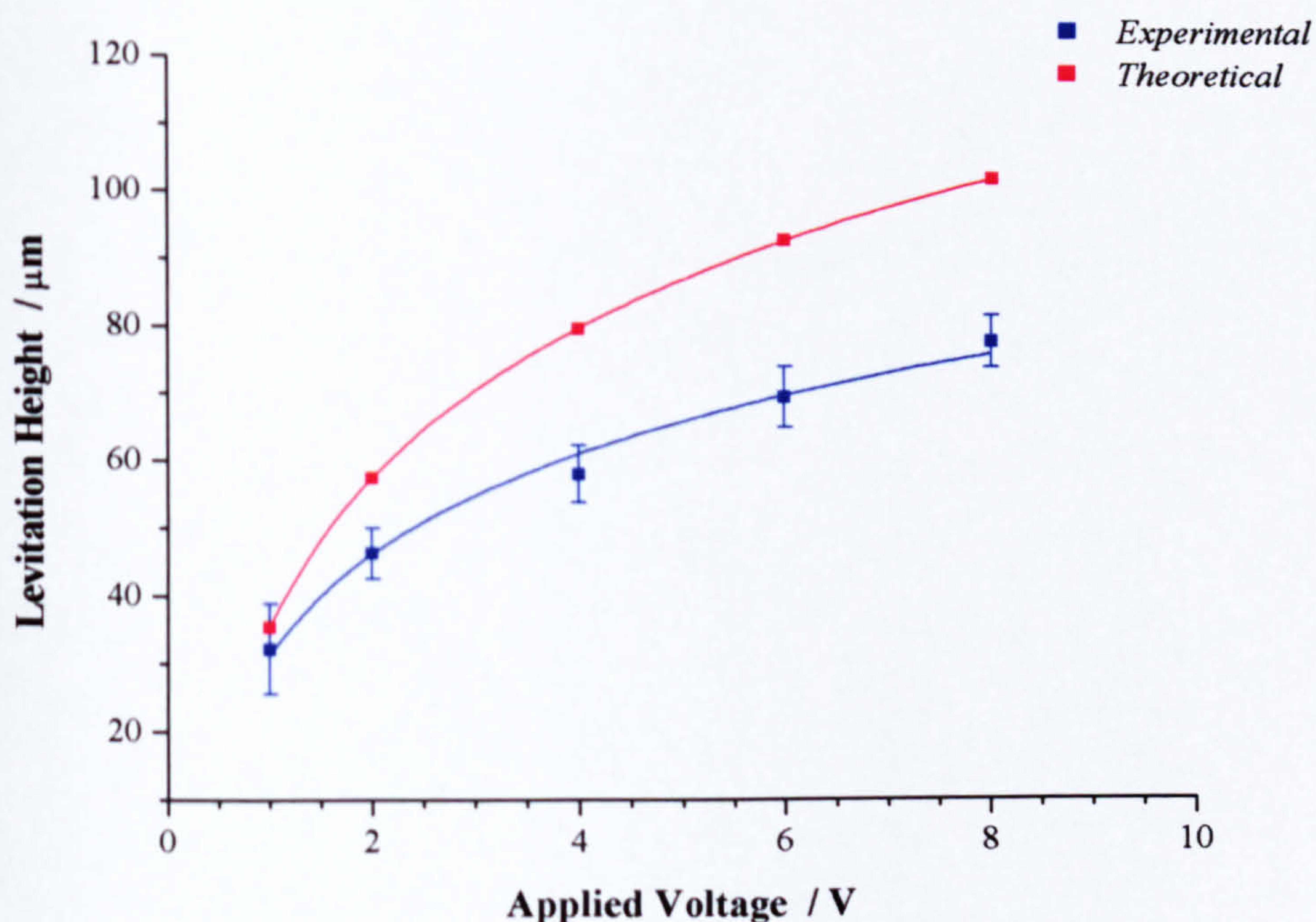

Figure 7.14 **Variation in Levitation Height with Voltage**

The theoretical levitation heights for latex beads in a 30 mS m^{-1} solution were calculated by equating Equations 7.05 and 7.06 (assuming values of 78.7, -0.468, 1000 kg m^{-3} and 1055 kg m^{-3} for ε_m, f_{CM}, ρ_m and ρ_p respectively).

7.6 Conclusions and Suggestions for Future Investigations

A microsensor platform which enables the integration of several sensors with a negative DEP antifouling strategy has been designed and fabricated. The principle of operation of the DEP antifouling strategy has been demonstrated through simulation and experimental work

using model latex particles. Experimental results for the levitation height of the beads were in broad agreement with theoretical predictions. However, further product engineering would be required to realise a practical, simply constructed device and it may be necessary to combine the antifouling strategy with a traditional macroscopic filter or a sedimentation chamber for the removal of large debris.

To simplify the microfabrication process and to facilitate the miniaturisation or modification of both the integrated microsensor platform and the modified sensors, use of a spray-coating machine would be desirable. Optimisation of the thermal bonding of the PET substrates, or of alternative polymeric materials, would also be required. The performance of the current dissolved oxygen and temperature sensor should be assessed within the platform before additional sensors are incorporated into the system (in case any alternations to the design are necessary). For the monitoring of freshwater environments, additional sensors could include ion-sensitive field effect transistor (ISFET) based devices, such as pH, Ca^{2+} or Mg^{2+} sensors.

To optimise the antifouling strategy for the analysis of freshwater samples, measurement of the dielectric properties of a range of native freshwater organisms would be required, as there is little information concerning these species in the literature. The organisms measured should include common protozoa, such as ciliates; bacteria, including cyanobacteria; and algae, for instance the diatoms *A. Minutissima* and *N. Gregaria* (which were the most commonly observed diatoms in the River Kelvin in the year 2000[1]). Discussions (with Morgan and Holmes) have suggested that, for typical river water conductivities, it should be possible to simultaneously generate negative DEP in the majority of these organisms, although this may require the use of high frequency signals (in the order of 10^8 Hz). At these high frequencies, modifications to the electrode array design may be required to ensure efficient coupling of the signal into the device

The effectiveness of negative dielectrophoresis as antifouling strategy could also be assessed using clinical samples, as the integrated microsensor platform could be employed, for instance, as a blood gas analyser. Negative dielectrophoresis has previously been used to manipulate blood cells and could be employed to repel them from the base of the platform. Holmes and Morgan (2001 and 2002) have previously demonstrated the focussing of white blood cells in the centre of a fluidic channel, using a 20 MHz signal and a medium conductivity of 10 mS m^{-1}.)

[1] According to data obtained from the Scottish Environmental Protection Agency.

Alternative dielectrophoretic strategies could also be investigated for use in the integrated microsensor platform. A combination of both nano- and micro-scale electrodes could be employed to simultaneously repel particles with a range of sizes (both cells and macromolecules for instance) (Schnelle *et al*, 1996). It may also be possible to exploit electrohydrodynamic flow as an anti-fouling mechanism (Morgan and Green, 2003). Furthermore, several uses could be envisaged for a DEP system that could selectively enrich or position particles of interest with a microfluidic analytical system. This could be achieved by applying positive instead of negative DEP, although the optimum electrode design and layout would depend upon the specific application.

CHAPTER 8

CONCLUSION

This chapter summarises the research presented in this thesis, restating the main results and achievements and making recommendations for the continuation of this work.

8.1 Summary of Thesis

The research presented in this thesis was primarily concerned with microelectrode arrays and their use in electroanalytical microsensors. After reviewing current micro- and nanofabrication technologies, the electrochemical characteristics of macroelectrodes, microelectrodes and microelectrode arrays were discussed. Simulations of the diffusion fields generated by microelectrodes and microelectrode arrays were performed and the results obtained were shown to be in general agreement with theory.

Results from the electrochemical characterisation of two sets of microelectrode arrays were presented in Chapter 5: one with a constant relative centre-centre spacing (d/r) and another with a constant individual electrode radius (r). For the first set of devices, diffusion of the electroactive species to the surface of the electrode array became increasingly linear as r was decreased and, hence, the cyclic voltammograms obtained became increasingly peak-shaped. Peak current densities were found to be largest for the microelectrode arrays with the smallest individual electrodes, with these arrays also generating the highest signal-to-noise ratios (SNRs). For the second set of microelectrode arrays (those with a constant individual electrode radius), loosely packed arrays of microelectrodes were found to produce significantly higher current densities than arrays with smaller d/r ratios, as was expected from theory.

Electron-beam lithography (EBL) and nanoimprint lithography (NIL) techniques were employed to further decrease the radius of the individual electrodes. The peak currents

generated by these nanoelectrode arrays continued to increase with decreasing electrode radius and comparable voltammograms were obtained from nanoelectrode arrays produced by both the EBL and NIL methods. The NIL technique is of particular interest, as it enables the rapid production of low-cost, nano-scale electrode structures.

Chapter 6 details the design and fabrication of a dissolved oxygen and temperature microsensor, which incorporates a densely packed working microelectrode array. Dissolved oxygen was measured amperometrically by a two-electrode cell, comprising the microelectrode array and a Ag|AgCl micro-reference electrode. Both of these electrodes were situated within a SU8 chamber, which was filled with an electrolyte gel. A nickel thermal resistor was also integrated into the microsensor to allow for temperature compensation of the dissolved oxygen measurements. Linear calibration curves were obtained for dissolved oxygen and temperature measurements and the reference electrode was stable for approximately 80 hours in a 0.1 M KCl solution (when a fixed current of 100 nA was passing through it).

Lastly, an integrated microsensor platform, which was developed in order to integrate several microsensors and a dielectrophoretic antifouling strategy into a flow-through system, was successfully designed and fabricated (as detailed in Chapter 7). Preliminary simulations and experimental work were performed in order to demonstrate the principle of operation, using latex beads as model particles. The experimental values obtained for the levitation heights of the beads were in close agreement with theory. Further developmental work is, however, required before a practical device is realised.

8.2 Suggestions for Future Work

A range of possibilities may be considered for the continuation of this work, many of which would have been pursued but for time constraints. To continue the research into nanoelectrode array structures, it would useful to fabricate, by EBL, a set of devices with SiN insulation layers. Unlike the lithographic resist insulation materials employed, which were slowly etched by oxygen, SiN insulation layers could be oxygen cleaned without the geometries of the arrays being affected. Optimisation of the NIL process for the production of nanoelectrode arrays could then be carried out and electrochemical recordings from the imprinted arrays could be compared to those obtained using the EBL devices. The imprinting

of a polymeric material that may be hard-baked to withstand repeated oxygen cleaning (such as a polyimide precursor) could also be investigated.

The long-term stability of the complete dissolved oxygen and temperature microsensor in freshwater samples has not yet been quantified and this should be assessed before any modifications are made to the design of the sensor. Such modifications could include the use of a membrane that is impermeable to chloride ions and the incorporation of a counter electrode, to increase the lifetime of the Ag|AgCl reference electrode.

As regards the development of the microsensor platform, a range of directions may be considered. For use as a freshwater analytical system, measurements of the dielectric properties of relevant freshwater organisms would be necessary. The antifouling system could then be tested with artificial suspensions of common organisms and with filtered and unfiltered freshwater samples. It would also be necessary to assess the performance of the dissolved oxygen microsensor within the microsensor platform. In addition, the application of the platform as a blood gas analyser could also be investigated.

REFERENCES

Akmal, N. and J. Lauer (1998). Electrochemical Oxygen Sensors: Principles and Applications. Polymers in Sensors, Theory and Practice. N. Akmal and A. M. Usmani. Washingon DC, USA, American Chemical Society.

Allsopp, D. W. E., K. R. Milner, et al. (1999). "Impedance technique for measuring dielectrophoretic collection of microbiological particles." Journal of Physics D-Applied Physics 32(9): 1066-1074.

Arnost, R. (2000). "Imaging with polymers, how it all began." The Spectrum Spring: 9-11.

Arquint, P., M. Koudelka-Hep, et al. (1994). "Micromachined Analyzers on a Silicon Chip." Clinical Chemistry 40(9): 1805-1809.

Arundell, M. (2000). Miniaturised glass devices for the on-line analysis of phenols in surface water. Department of Chemistry. London, UK, Imperial College, University of London.

Auroux, P. A., D. Iossifidis, et al. (2002). "Micro total analysis systems. 2. Analytical standard operations and applications." Analytical Chemistry 74(12): 2637-2652.

Backstrom, G. (2002). Fields of Physics by Finite Element Analysis – An Introduction. Malmo, Sweden, GB Publishing.

Bakker, E. and M. Telting-Diaz (2002). "Electrochemical sensors." Analytical Chemistry 74(12): 2781-2800.

Baldwin, R. P. (2000). "Recent advances in electrochemical detection in capillary electrophoresis." Electrophoresis 21(18): 4017-4028.

Bard, A. J. and L. R. Faulkner (2001). Electrochemical methods : fundamentals and applications. New York, USA, John Wiley & Sons.

Bard, A. K. and C. G. Zoski (2000). "Voltammetry retrospective." Analytical Chemistry 72(9): 346A-352A.

Becker, E. W., W. Ehrfeld, et al. (1986). "Fabrication of microstructures with high aspect ratios and great structural heights by synchrotron radiation lithography, galvanoforming, and plastic moulding (LIGA process)." Microelectronic Engineering 4(1): 35-56.

Becker, H. and U. Heim (2000). "Hot embossing as a method for the fabrication of polymer high aspect ratio structures." Sensors and Actuators a-Physical 83(1-3): 130-135.

Belmont-Hebert, C., M. L. Tercier, et al. (1998). "Gel-integrated microelectrode arrays for direct voltammetric measurements of heavy metals in natural waters and other complex media." Analytical Chemistry 70(14): 2949-2956.

Beriet, C., R. Ferrigno, et al. (2000). "Simulation of the chronoamperometric response of a regular array of micro-disc electrodes." Journal of Electroanalytical Chemistry 486(1): 56-64.

Bertsch, A., H. Lorenz, et al. (1999). "3D microfabrication by combining microstereolithography and thick resist UV lithography." Sensors and Actuators a-Physical 73(1-2): 14-23.

Bockris, J. O'M. and A. K. N. Reddy (1970). Modern electrochemistry : an introduction to an interdisciplinary area. New York, USA, Plenum Press.

Bone, S. and B. Zaba (1992). Bioelectronics. New York, USA, John Wiley & Sons.

Bostock, R. M. (1998). "Silicon nitride microclips for the kinematic location of optic fibres in silicon V-shaped grooves." Journal of Micromechanics and Microengineering 8: 343-360.

Bozeat, R. J. (1998). Stress control in low-temperature PECVD silicon nitride for highly manufacturable micromechanical devices. 9th Micromechanics Europe Workshop, Oslo, Norway, 3rd-5th June.

Cai, X., N. Klauke, et al. (2002). "Ultra-Low-Volume, Real-Time Measurements of Lactate from the Single Heart Cell Using Microsystems Technology." Analytical Chemistry 74(4): 908-914.

Campanella, L., P. Cipriani, et al. (1995). "New Enzyme Sensor for Sulfite Analysis in Sea and River Water Samples." Analytica Chimica Acta 305(1-3): 32-41.

Campbell, S. A. (1996). The science and engineering of microelectronic fabrication. New York, USA, Oxford University Press.

Chang, T. H. P. (1975). "Proximity effect in electron beam lithography." Journal of Vacuum Science & Technology 12(6): 1271-1275.

Chen, X. H., Y. B. Hu, et al. (2002). "Glucose microbiosensor based on alumina sol-gel matrix/electropolymerized composite membrane." Biosensors & Bioelectronics 17(11-12): 1005-1013.

Chen, Y., D. Macintyre, et al. (2002). "Fabrication of high electron mobility transistors with T-gates by nanoimprint lithography." Journal of Vacuum Science & Technology B 20(6): 2887-2890.

Choi, J.-W., A. Wijayawardhana, et al. (2000). Development and Characterization of a Generic Microfluidic Subsystem Toward Portable Biochemical Detection. Fourth International Symposium on Micro Total Analysis Systems, Enschede, The Netherlands, 14-18 May, Kluwer Academic Publishers.

Choi, S. H., J. Ha, et al. (2001). "Planar amperometric oxygen sensor with improved preconditioning property." Analytica Chimica Acta 431(2): 261-267.

Choi, W. B., B. K. Ju, et al. (1997). "Experimental analysis on the anodic bonding with an evaporated glass layer." Journal of Micromechanics and Microengineering 7(4): 316-322.

Chou, S. Y., P. R. Krauss, et al. (1996). "Nanoimprint lithography." Journal of Vacuum Science & Technology B 14(6): 4129-4133.

Clark, L. C., Jr. (1956). "Monitor and control of blood and tissue oxgen tensions." Transactions of the American Society of Applied Physiology **2**: 41-48.

Clark, L. C., Jr. and C. Lyons (1962). "Electrode systems for continuous monitoring in cardiovascular surgery." Annals of the New York Academy of Sciences **102**: 29-45.

Clerc, P. A., L. Dellmann, et al. (1998). "Advanced deep reactive ion etching: a versatile tool for microelectromechanical systems." Journal of Micromechanics and Microengineering **8**(4): 272-278.

Cobbold, R. S. C. (1974). Electrodes for the measurement of bioelectric potentials: Transducers for biomedical measurements: principles and applications (Chapter 10). New York, USA, John Wiley & Sons.

Creager, S. E. and P. T. Radford (2001). "Electrochemical reactivity at redox-molecule-based nanoelectrode ensembles." Journal of Electroanalytical Chemistry **500**(1-2): 21-29.

Cui, L., D. Holmes, et al. (2001). "The dielectrophoretic levitation and separation of latex beads in microchips." Electrophoresis **22**(18): 3893-3901.

Cumming, D. R. S., S. Thoms, et al. (1996). "Fabrication of 3 nm wires using 100 keV electron beam lithography and poly(methyl methacrylate) resist." Applied Physics Letters **68**(3): 322-324.

Dayton, M. A., J. C. Brown, et al. (1980). "Faradaic Electrochemistry at Microvoltammetric Electrodes." Analytical Chemistry **52**: 946-950.

Dentinger, P. M., W. M. Clift, et al. (2002). "Removal of SU-8 photoresist for thick film applications." Microelectronic Engineering **61-2**: 993-1000.

Duffy, D. C., J. C. McDonald, et al. (1998). "Rapid prototyping of microfluidic systems in poly(dimethylsiloxane)." Analytical Chemistry **70**(23): 4974-4984.

Duffy, D. C., O. J. A. Schueller, et al. (1999). "Rapid prototyping of microfluidic switches in poly(dimethyl siloxane) and their actuation by electro-osmotic flow." Journal of Micromechanics and Microengineering 9(3): 211-217.

Effenhauser, C. S., G. J. M. Bruin, et al. (1997). "Integrated capillary electrophoresis on flexible silicone microdevices: Analysis of DNA restriction fragments and detection of single DNA molecules on microchips." Analytical Chemistry 69(17): 3451-3457.

Elliott, J. M., P. R. Birkin, et al. (1999). "Platinum microelectrodes with unique high surface areas." Langmuir 15(22): 7411-7415.

Elwenspoek, M. and H. V. Jansen (1999). Silicon Micromachining. Cambridge, UK, Cambridge University Press.

Encyclopaedia Britannica (2003). Biochemical Oxygen Demand.

Faircloth, B., H. Rohrs, et al. (2000). "Bilayer, nanoimprint lithography." Journal of Vacuum Science & Technology B 18(4): 1866-1873.

Faβbender, F., G. Schmitt, et al. (2000). "Optimization of passivation layers for corrosion protection of silicon-based microelectrode arrays." Sensors and Actuators B-Chemical 68(1-3): 128-133.

Feeney, R. and S. P. Kounaves (2000). "Microfabricated ultramicroelectrode arrays: Developments, advances, and applications in environmental analysis." Electroanalysis 12(9): 677-684.

FEI Company Manual for the FEI Tecnai 12 Transmission Electron Microscope. Eindhoven, The Netherlands.

French, P. J., P. M. Saro et al. (1997). "Optimization of a low-stress silicon nitride process for surface-micromachining applications." Sensors and Actuators A – Physical 58(2): 149-157

Feynman, R. (1992). "There's plenty of room at the bottom." Journal of Microelectromechanical Systems 1(1): 60-66.

Fisher, A. C. (1996). Electrode Dynamics. Oxford, UK, Oxford University Press.

Fojta, M. (2002). "Electrochemical sensors for DNA interactions and damage." Electroanalysis 14(21): 1449-1463.

Frebel, H., G. C. Chemnitius, et al. (1997). "Multianalyte sensor for the simultaneous determination of glucose, L-lactate and uric acid based on a microelectrode array." Sensors and Actuators B-Chemical 43(1-3): 87-93.

Freund, M. S. and A. Brajtertoth (1991). "Determination of Ultramicroelectrode Array Dimensions at Graphite and One-Dimensional Organic Conductor Electrodes Using Simulations, Chronocoulometry and Chronoamperometry." Journal of Electroanalytical Chemistry 300(1-2): 347-363.

Frost, M. C. and M. E. Meyerhoff (2002). "Implantable chemical sensors for real-time clinical monitoring: progress and challenges." Current Opinion in Chemical Biology 6: 633-641.

Frye, R. C. and K. L. Tai (1995). "Silicon Multichip Modules - Evolving a High-Performance Technology From Low-End Applications." Materials Chemistry and Physics 40(4): 230-235.

Fuhr, G., A. Voigt, et al. (1995). "Electric-Field-Mediated Inhibition of Cell and Microparticle Adhesion - a New Way to Create Bio-Repellent Surfaces." Sensors and Actuators B-Chemical 27(1-3): 468-470.

Gastrock, G., S. Kunze, et al. (2000). Negative dielectrophoresis prevents surfaces from blocking. Micro Total Analysis Systems 2000, Proceedings. Dordrecht, Kluwer Academic Publishers: 91-94.

Goater, A. D., J. P. H. Burt, et al. (1997). "A combined travelling wave dielectrophoresis and electrorotation device: applied to the concentration and viability determination of Cryptosporidium." Journal of Physics D-Applied Physics 30(18): L65-L69.

González, C. (1998). "Microjoinery: concept, definition and application to microsystem development." Sensors and Actuators A 66: 315-332.

Gonzalez, C. G., R. A. Wessel, et al. (1999). "Epoxy-based aqueous-processable photodielectric dry film and conductive ViaPlug for PCB build-up and IC packaging." IEEE Transactions on Advanced Packaging 22(3): 385-390.

Gray, B. L., S. D. Collins, et al. (2001). Interlocking Mechanical and Microfluidic Interconnections Fabricated by Deep Reactive Ion Etching. Fifth Symposium on Micro Total Analysis Systems, Monterey, California, USA, Kluwer Academic Publishers.

Greef, R., R. Peat, et al. (1985). Instrumental Methods in Electrochemistry. New York, USA, Halsted Press.

Green, N. G., A. Ramos, et al. (2000). "Fluid flow induced by nonuniform ac electric fields in electrolytes on microelectrodes. I. Experimental measurements." Physical Review E 61(4): 4011-4018.

Griffith, A. W. (1996). Applications of microfabrication in biosensor technology. Faculty of Engineering. Glasgow, UK, University of Glasgow.

Handa, S. (1998). Technology of reactive ion etching (Chapter 5). Plasma Etching: Fundamentals & Applications. M. Sugawara. Oxford, UK, Oxford University Press: 180-211.

Heinze, J. (1993). "Ultramicroelectrodes in Electrochemistry." Angewandte Chemie-International Edition in English 32(9): 1268-1288.

Herdan, J., R. Feeney, et al. (1998). "Field evaluation of an electrochemical probe for in situ screening of heavy metals in groundwater." Environmental Science & Technology 32(1): 131-136.

Hicks, S. E., W. Parkes, et al. (1994). "Reflectance Modeling for in-Situ Dry Etch Monitoring of Bulk SiO_2 and III-V Multilayer Structures." Journal of Vacuum Science & Technology B 12(6): 3306-3310.

Hirai, Y., M. Fujiwara, et al. (2001). "Study of the resist deformation in nanoimprint lithography." Journal of Vacuum Science & Technology B **19**(6): 2811-2815.

Holmes, A. S. (2001). "Laser fabrication and assembly processes for MEMS." Proceedings of SPIE **4274**: 297-306.

Holmes, D. and H. Morgan (2001). Particle focussing and separation using dielectrophoresis in a microfluidic device. Fifth Symposium on Micro Total Analysis Systems, Monterey, California, USA, Kluwer Academic Publishers.

Holmes, D. and H. Morgan (2002). "Cell positioning and sorting using dielectrophoresis." European Cells and Materials 4(2): 120-122.

Hoole, A. C. F., M. E. Welland, et al. (1997). "Negative PMMA as a high-resolution resist - the limits and possibilities." Semiconductor Science and Technology **12**(9): 1166-1170.

Horowitz, P. and W. Hill (1989). The Art of Electronics. Cambridge, UK, Cambridge University Press.

Hulme, J. P., S. Mohr, et al. (2002). "Rapid prototyping for injection moulded integrated microfluidic devices and diffractive element arrays." Lab On a Chip **2**(4): 203-206.

Igata, E., M. Arundell, et al. (2002). "Interconnected reversible lab-on-a-chip technology." Lab on a Chip **2**(2): 65-69.

Ito, T. and S. Okazaki (2000). "Pushing the limits of lithography." Nature **406**: 1027-1031.

Jin, P., A. Yamaguchi, et al. (2001). "Glucose sensing based on interdigitated array microelectrode." Analytical Sciences **17**(7): 841-846.

Johannessen, E. A. (2001). Nanocalorimetric measurements of heat from biological systems. Department of Human Anatomy and Cell Biology. Liverpool, UK, University of Liverpool.

Johannessen, E. A., T. B. Tang, et al. (2002). An ingestible electronic pill for real time analytical measurements of the gastrointestinal tract. Sixth Symposium on Micro Total Analysis Systems, Nara, Japan, Kluwer Academic Publishers.

Johnston, E. and B. D. Ratner (1998). Protein adsorption: friend or foe? Immobilized Biomolecules in Analysis: A Practical Approach. T. Cass and F. S. Ligler, Oxford University Press: 79-94.

Jones, T. B. (1995). Electromechanics of Particles. Cambridge, UK, Cambridge University Press.

Judy, J. W. (2001). "Microelectromechanical systems (MEMS): fabrication, design and applications." Smart Materials & Structures 10(6): 1115-1134.

Kim, M. A. and W. Y. Lee (2003). "Amperometric phenol biosensor based on sol-gel silicate/Nafion composite film." Analytica Chimica Acta 479(2): 143-150.

Kissinger, P. T. and W. R. Heineman (1983). "Cyclic Voltammetry." Journal of Chemical Education 60(9): 702-706.

Kitamori, T. (2001). Continuous Multi Chemical Processing in 2D and 3D Microchannel Networks on Chip. Fifth Symposium on Micro Total Analysis Systems, Monterey, California, USA, Kluwer Academic Publishers.

Klaassen, E. H., K. Petersen, et al. (1996). "Silicon fusion bonding and deep reactive ion etching: A new technology for microstructures." Sensors and Actuators a-Physical 52(1-3): 132-139.

Kleps, I., A. Angelescu, et al. (2002). "Measurement systems based on metal/dielectric nanostructures for electrochemical analyses." Materials Science & Engineering C-Biomimetic and Supramolecular Systems 19(1-2): 219-223.

Kořyta, J., J. Dvořak, et al. (1993). Principles of Electrochemistry. Chichester, UK, John Wiley & Sons Ltd.

Koster, O., W. Schuhmann, et al. (2001). "Quality control of ultra-microelectrode arrays using cyclic voltammetry, electrochemical impedance spectroscopy and scanning electrochemical microscopy." Sensors and Actuators B-Chemical 76(1-3): 573-581.

Koudelka, M. and A. Grisel (1985). Minaturized "Clark-type" oxygen sensor. Transducers '85 - The 1985 International Conference on Solid State Sensors and Actuators, IEEE New York.

Kovacs, G. T. A. (1994). Introduction to the theory, design, and modeling of thin-film microelectrodes for neural interfaces. Enabling Technologies for Cultured Neural Networks. D. A. Stenger and T. McKenna. London, UK, Academic Press: 121-65.

Kovacs, G. T. A. (1998). Micromachined transducers sourcebook. New York, USA, McGraw-Hill Science.

Kreider, K. G. (1992). "Thin-film transparent thermocouples." Sensors and Actuators A 34: 95-99.

Kreider, K. G. and F. DiMeo (1998). "Platinum/palladium thin-film thermocouples for temperature measurements on silicon wafers." Sensors and Actuators A 69: 46-52.

Kudera, M., H. A. O. Hill, et al. (2001). "Electrochemical characterisation and application of multi microelectrode array devices to biological electrochemistry." Sensors 1: 18-28.

Kutchoukov, V. G., J. R. Mollinger, et al. (2000). "New photoresist coating method for 3-D structured wafers." Sensors and Actuators a-Physical 85(1-3): 377-383.

Kyser, D. F. and N. S. Viswanathan (1975). "Monte Carlo simulation of spatially distributed beams in electron-beam lithography,." Journal of Vacuum Science & Technology 12(6): 1305-1308.

Layson, A. R. and M. R. Columbia (1997). "The morphology of platinum black electrodeposited on highly oriented pyrolytic graphite studied with scanning electron microscopy and scanning tunneling microscopy." Microchemical Journal 56(1): 103-113.

Le Drogoff, B., M. A. El Khakani, et al. (2001). "Effect of the Microelectrode geometry on the diffusion behavior and the electroanalytical performance of Hg-electroplated iridium microelectrode arrays intended for the detection of heavy metal traces." Electroanalysis 13(18): 1491-1496.

Lee, H. J., C. Beriet, et al. (2001). "Cyclic voltammetry at a regular microdisc electrode array." Journal of Electroanalytical Chemistry 502(1-2): 138-145.

Lee, K. Y., N. LaBianca, et al. (1995). "Micromachining applications of a high resolution ultrathick photoresist." Journal of Vacuum Science & Technology B 13(6): 3012-3016.

Lee, S. (2002). "Fabrication of an array of surface mount device 32.768 kHz quartz tuning fork-type crystals: photolithography and selective etching of an array of quartz tuning fork resonators with subsequent photoresist spray coating." Vacuum 65(2): 161-168.

Lenigk, R., H. X. Zhu, et al. (1999). "Recessed microelectrode array for a micro flow-through system allowing on-line multianalyte determination in vivo." Fresenius Journal of Analytical Chemistry 364(1-2): 66-71.

Levinson, H. J. and W. H. Arnold (1997). Optical Lithography (Chapter 1). Handbook of Microlithography, Micromachining, and Microfabrication. Volume 1: Microlithography. P. Rai-Choudhury. Bellingham, Washington, USA, SPIE Press.

Li, W. J., J. D. Mai, et al. (1998). A MEMs fabrication technique for non-planar substrates. The Eleventh Annual International Workshop on Micro Electro Mechanical Systems (MEMS '98), Heidelberg, Germany, January 25-29.

Lide, D. R. (1993). CRC Handbook of Chemistry and Physics. Florida, USA, CRC Press.

Liu, J., L. Bjornsson, et al. (2000). "Immobilised activated sludge based biosensor for biochemical oxygen demand measurement." Biosensors and Bioelectronics 14: 883-893.

Liu, J. J., H. Berg, et al. (1995). "Plastic Ball Grid Array (PBGA) Overview." Materials Chemistry and Physics 40(4): 236-244.

Liu, Z. X. and D. L. DeVoe (2001). "Micromechanism fabrication using silicon fusion bonding." Robotics and Computer-Integrated Manufacturing 17(1-2): 131-137.

Long, J. T. and S. G. Weber (1988). "Noise At Microelectrodes and Microelectrode Arrays in Amperometry and Voltammetry." Analytical Chemistry 60(20): 2309-2311.

Lorenz, H., M. Despont, et al. (1997). "SU-8: a low-cost negative resist for MEMS." Journal of Micromechanics and Microengineering 7(3): 121-124.

Lorenz, H., L. Paratte, et al. (1996). "Low-cost technology for multilayer electroplated parts using laminated dry film resist." Sensors and Actuators a-Physical 53(1-3): 364-368.

Luxbacher, T. and A. Mirza (1999). "Spray coating for MEMs, interconnect and advanced packaging applications." HDI Magazine 2(5): 36-41.

Mack, C. A. (1994). "Photoresist development." Microlithography World, Autumn Issue: 22-24.

Madou, M. J. (1997). Fundamentals of Microfabrication. New York, USA, CRC Press.

Madou, M. J., L. J. Lee, et al. (2001). "Design and fabrication of CD-like microfluidic platforms for diagnostics: microfluidic functions." Biomedical Microdevices 3(3): 245-254.

Malins, C., S. Fanni, et al. (1999). "The preparation of a sol-gel glass oxygen sensor incorporating a covalently bound fluorescent dye." Analytical Communications 36(1): 3-4.

Manz, A., N. Graber, et al. (1990). "Miniaturized Total Chemical-Analysis Systems - a Novel Concept for Chemical Sensing." Sensors and Actuators B-Chemical 1(1-6): 244-248.

Markx, G. H. and C. L. Davey (1999). "The dielectric properties of biological cells at radiofrequencies: Applications in biotechnology." Enzyme and Microbial Technology 25(3-5): 161-171.

Martynova, L., L. E. Locascio, et al. (1997). "Fabrication of plastic microfluid channels by imprinting methods." Analytical Chemistry 69(23): 4783-4789.

McCord, M. A. and M. J. Rooks (1997). Electron Beam Lithography (Chapter 2). Handbook of Microlithography, Micromachining, and Microfabrication. Volume 1: Microlithography. P. Rai-Choudhury. Bellingham, Washington, USA, SPIE Press.

McDonagh, C., B. D. MacCraith, et al. (1998). "Tailoring of sol-gel films for optical sensing of oxygen in gas and aqueous phase." Analytical Chemistry 70(1): 45-50.

McEvoy, A. K., C. M. McDonagh, et al. (1996). "Dissolved oxygen sensor based on fluorescence quenching of oxygen-sensitive ruthenium complexes immobilized in sol-gel- derived porous silica coatings." Analyst 121(6): 785-788.

McLaughlin, G. W., K. Braden, et al. (2002). "Microfabricated solid-state dissolved oxygen sensor." Sensors and Actuators B-Chemical 83(1-3): 138-148.

Meng, E., S. Wu, et al. (2000). Micromachined Fluidic Couplers. Fourth International Symposium on Micro Total Analysis Systems, Enschede, The Netherlands, 14-18 May, Kluwer Academic Publishers.

Menon, V. P. and C. R. Martin (1995). "Fabrication and Evaluation of Nanoelectrode Ensembles." Analytical Chemistry 67(13): 1920-1928.

Menz, W., J. Mohr, et al. (2001). Microsystem Technology. Weinheim, Germany, Wiley-VCH.

Metz, S., R. Holzer, et al. (2001). "Polyimide-based microfluidic devices." Lab on a Chip 1(1): 29-34.

Michel, B., A. Bernard, et al. (2001). "Printing meets lithography: Soft approaches to high-resolution printing." Ibm Journal of Research and Development 45(5): 697-719.

Monaghan, P. B., A. Manz, et al. (2000). Microbiology on-a-chip. Fourth International Symposium on Micro Total Analysis Systems, Enschede, The Netherlands, 14-18 May, Kluwer Academic Publishers.

Morf, W. E. (1996). "Theoretical treatment of the amperometric current response of multiple microelectrode arrays." Analytica Chimica Acta **330**(2-3): 139-149.

Morf, W. E. (1997). "Theoretical treatment of the current vs. time response of microelectrode arrays to changes of potential, concentration, or flow." Analytica Chimica Acta **341**(2-3): 121-127.

Morf, W. E. and N. F. de Rooij (1997). "Performance of amperometric sensors based on multiple microelectrode arrays." Sensors and Actuators B - Chemical **44**: 538-541.

Morgan, H. and N. G. Green (2003). AC Electrokinetics: Colloids and Nanoparticles. Baldock, UK, Research Studies Press.

Morgan, H., D. Holmes, et al. (2003). *Personal Communication.*

Morgan, H., A. G. Izquierdo, et al. (2001). "The dielectrophoretic and travelling wave forces generated by interdigitated electrode arrays: analytical solution using Fourier series." Journal of Physics D-Applied Physics **34**(10): 1553-1561.

Mucha, J. A., D. W. Hess, et al. (1994). Plasma Etching (Chapter 5). Introduction to Microlithography. L. F. Thompson, C. G. Wilson and M. J. Bowden. Washington DC, USA, The American Chemical Society.

Nakamura, E. Y., Y. Suzuki, et al. (1996). "Effect of oxygen plasma etching on adhesion between polyimide films and metal." Thin Solid Films **209-291**: 367-369.

Nese, M. and A. Hanneborg (1993). "Anodic Bonding of Silicon to Silicon-Wafers Coated with Aluminum, Silicon-Oxide, Polysilicon or Silicon-Nitride." Sensors and Actuators a-Physical **37-8**: 61-67.

Neumann, E., K. Tonsing, et al. (2000). "Perspectives for microelectrode arrays for biosensing and membrane electroporation." Bioelectrochemistry 51(2): 125-132.

Niwa, O., T. Horiuchi, et al. (1996). "Determination of acetylcholine and choline with platinum-black ultramicroarray electrodes using liquid chromatography with a post-column enzyme reactor." Analytica Chimica Acta 318(2): 167-173.

Nomura, Y., K. Ikebukuro, et al. (1998). "Application of a linear alkylbenzene sulfonate biosensor to river water monitoring." Biosensors & Bioelectronics 13(9): 1047-1053.

Percin, G., T. S. Lundgren, et al. (1998). "Controlled ink-jet printing and deposition of organic polymers and solid particles." Applied Physics Letters 73(16): 2375-2377.

Pethig, R. (1979). Dielectric and electronic properties of biological materials. Chichester, UK, John Wiley & Sons.

Pethig, R. (1996). "Dielectrophoresis: Using inhomogeneous AC electrical fields to separate and manipulate cells." Critical Reviews in Biotechnology 16(4): 331-348.

Pham, N. P., P. M. Sarro, et al. (2001). Spray Coating of AZ4562 photoresist for MEMS applications. Semiconductor Advances for Future Electronics (SAFE 2001), Veldhoven, The Netherlands, November 28-29.

Pohl, H. A. (1978). Dielectrophoresis. Cambridge, UK, Cambridge University Press.

Puntambekar, A. and C. H. Ahn (2000). Self-Aligning Microfluidic Interconnects with Low Dead Volume. Fourth International Symposium on Micro Total Analysis Systems, Enschede, The Netherlands, 14-18 May, Kluwer Academic Publishers.

Qin, D., Y. Xia, et al. (1998). Microfabrication, microstructures and microsystems. Microsystem Technology in Chemistry and Life Sciences. A. Manz and H. Becker. Berlin, Germany, Springer-Verlag. 194.

Ratner, B. D. (1995). "Surface Modification of Polymers - Chemical, Biological and Surface Analytical Challenges." Biosensors & Bioelectronics 10(9-10): 797-804.

Reyes, D. R., D. Iossifidis, et al. (2002). "Micro total analysis systems. 1. Introduction, theory, and technology." Analytical Chemistry 74(12): 2623-2636.

Schmitt, G., J. W. Schultze, et al. (1999). "Passivation and corrosion of microelectrode arrays." Electrochimica Acta 44(21-22): 3865-3883.

Schnelle, T., T. Muller, et al. (1996). "Adhesion-inhibited surfaces. Coated and uncoated interdigitated electrode arrays in the micrometer and submicrometer range." Langmuir 12(3): 801-809.

Schulz, H., H. C. Scheer, et al. (2000). "New polymer materials for nanoimprinting." Journal of Vacuum Science & Technology B 18(4): 1861-1865.

Sharp, D. J. (1979). "Corrosion inhibition in sputter-deposited thin-film systems using an intermediary layer of palladium." Journal of Vacuum Science and Technology 16(2): 204-207.

Shaw, P. J. (1999). Introduction to Confocal Microscopy. Light Microscopy in Biology. A. J. Lacey. Oxford, UK, Oxford University Press: 45-71.

Skoog, D. A., F. J. Holler, et al. (1998). Principles of Instrumental Analysis. Florida, USA, Harcourt Brace & Company.

Strong, T. D., H. C. Cantor, et al. (2001). "A microelectrode array for real-time neurochemical and neuroelectrical recording in vitro." Sensors and Actuators a-Physical 91(3): 357-362.

Štulík, K., C. Amatore, et al. (2000). "Microelectrodes. Definitions, characterization and applications." Pure and Applied Chemistry 72(8): 1483-1492.

Suzuki, H., T. Hirakawa, et al. (1998a). "Micromachined liquid-junction Ag/AgCl reference electrode." Sensors and Actuators B-Chemical 46(2): 146-154.

Suzuki, H., A. Hiratsuka, et al. (1998b). "Problems associated with the thin-film Ag/AgCl reference electrode and a novel structure with improved durability." Sensors and Actuators B-Chemical 46(2): 104-113.

Suzuki, H., H. Shiroishi, et al. (1999). "Microfabricated liquid junction Ag/AgCl reference electrode and its application to a one-chip potentiometric sensor." Analytical Chemistry 71(22): 5069-5075.

Suzuki, H., A. Sugama, et al. (1991). "A minature Clark-type oxygen electrode using a polyelectrolyte and its application as a glucose sensor." Biosensors and Bioelectronics 6: 395-400.

Sze, S. M. (2002). Semiconductor Devices, Physics and Technology. New York, USA, John Wiley & Sons.

Tan, T. C., F. Li, et al. (1993). "Measurement of BOD by initial rate of response of a microbial sensor." Sensors and Actuators B 10: 137-142.

Tercier, M. L. and J. Buffle (1993). "Insitu Voltammetric Measurements in Natural-Waters - Future- Prospects and Challenges." Electroanalysis 5(3): 187-200.

Tercier, M. L. and J. Buffle (1996). "Antifouling membrane-covered voltammetric microsensor for in situ measurements in natural waters." Analytical Chemistry 68(20): 3670-3678.

Thomas, N., A. Ocklind, et al. (2000). Integrated Cell Based Assays in Microfabricated Disposable CD Devices. Fourth International Symposium on Micro Total Analysis Systems, Enschede, The Netherlands, 14-18 May, Kluwer Academic Publishers.

Tong, H. M. (1995). "Microelectronics Packaging - Present and Future." Materials Chemistry and Physics 40(3): 147-161.

Tsutsui, K., E. L. Hu, et al. (1993). "Controlling the profile of nanostructures." Journal of Vacuum Science and Technology B 11(6): 2233-2236.

Uhlig, A., U. Schnakenberg, et al. (1997). "Highly sensitive heavy metal analysis on platinum- and gold- ultramicroelectrode arrays." Electroanalysis 9(2): 125-129.

Vogt, K. W., P. A. Kohl, et al. (1994). "Characterization of thin titanium oxide adhesion layers on gold: resistivity, morphology and composition." Surface Science **301**: 203-213.

Wallis, G. and D. I. Pomerantz (1969). "Field assisted glass-metal sealing." Journal of Applied Physics **40**: 3946-3950.

Wang, J. (1999). "Amperometric biosensors for clinical and therapeutic drug monitoring: a review." Journal of Pharmaceutical and Biomedical Analysis **19**(1-2): 47-53.

Wang, J. (2001). "Glucose biosensors: 40 years of advances and challenges." Electroanalysis **13**(12): 983-988.

Wang, J. (2002). "Electrochemical detection for microscale analytical systems: a review." Talanta **56**(2): 223-231.

Willson, C. G. (1994). Optical Lithography (Chapter 2). Introduction to Microlithography. L. F. Thompson, C. G. Willson and M. J. Bowden. Washington DC, USA, The American Chemical Society.

Willson, C. G., R. A. Dammel, et al. (1997). "Photoresist materials: a historical perspective." Proceedings of SPIE **3051**: 28-41.

Wittkampf, M., G. C. Chemnitius, et al. (1997). "Silicon thin film sensor for measurement of dissolved oxygen." Sensors and Actuautors B **43**: 40-44.

Wittstock, G., B. Grundig, et al. (1998). "Evaluation of microelectrode arrays for amperometric detection by scanning electrochemical microscopy." Electroanalysis **10**(8): 526-531.

Xia, Y. N., J. A. Rogers, et al. (1999). "Unconventional methods for fabricating and patterning nanostructures." Chemical Reviews **99**(7): 1823-1848.

Xia, Y. N. and G. M. Whitesides (1998). "Soft lithography." Annual Review of Materials Science **28**: 153-184.

Xiao, P. F., N. Y. He, et al. (2002). "In situ synthesis of oligonucleotide arrays by using soft lithography." Nanotechnology 13(6): 756-762.

Yang, Z., H. Suzuki, et al. (1996). "Disposable sensor for biochemical oxygen demand." Applied Microbiology and Biotechnology 46: 10-14.

Yu-Quan, C. and L. Guang (1993). "An autocalibration miniature microhole cathode array sensor system for measuring dissolved oxygen." Sensors and Actuators B 10: 219-222.

Zhou, H., B. K. Chong, et al. (2000). "Lithographically defined nano and micro sensors using "float coating" of resist and electron beam lithography." Journal of Vacuum Science & Technology B 18(6): 3594-3599.

Zhu, H. X., T. C. Lo, et al. (1998). "Fabrication of a novel oxygen sensor with CMOS compatible processes." Sensors and Actuators B 46(2): 155-159.

Zhu, J., A. S. Holmes, et al. (1996). "Laminated dry film resist for microengineering applications." Microelectronic Engineering 30(1-4): 365-368.

Ziler, I., J. E. F. Frost, et al. (1996). "Crosslinked PMMA as a high-resolution negative resist for electron beam lithography and applications for physics of low- dimensional structures." Semiconductor Science and Technology 11(8): 1235-1238.

PUBLICATIONS ARISING FROM THIS WORK

M. E. Sandison, N. Anicet, A. Glidle, J.M. Cooper, "Optimisation of the Geometry and Porosity of Microelectrode Arrays for Sensor Design", *Analytical Chemistry*, **2002**, **74**, 5717-5725

M. E. Sandison, J.M. Cooper, "Optimisation of an Electrochemical Dissolved Oxygen Microsensor for an Environmental Monitoring System", *Sensors for Environmental Control*, Editor P. Siciliano, World Scientific Publications, April **2003**

Conference Proceedings

M. E. Sandison, J.M. Cooper, "Nanoelectrode Arrays for Electroanalytical Sensing", Nanotech2002: The 6th Annual European Conference on Micro and Nanoscale Technologies for the Biosciences, 26-28 November 2002, Montreaux, Switzerland

M. E. Sandison, J.M. Cooper, "Optimisation of an Electrochemical Dissolved Oxygen Microsensor for an Environmental Monitoring System", *ENVSENS: The International Workshop on New Developments on Sensors for Environmental Control*, 27-29 May 2002, Lecce, Italy, **Oral Presentation**

M. E. Sandison, J.M. Cooper, "Negative Dielectrophoresis as an Antifouling Strategy in an Environmental Microsensor System", *Electrokinetics and Electrohydrodynamics in Microsystems*, 6-7 September 2001, Glasgow, U.K.

M. E. Sandison, D. Cumming, J.M. Cooper, "Development of an Integrated Microsensor Array for Remote Environmental Monitoring", *SmallTalk (the Microfluidics, Microarrays, and BioMEMS conference)*, 27-31 August 2001, San Diego, U.S.A.

M. E. Sandison, D. Cumming, J.M. Cooper, "Development of an Integrated Microsensor Array for Remote Environmental Monitoring", *2nd France-Israel Workshop (with an International Participation): Bioanalytical Sensors, Biochips and Nanobiotechnologies*, 11-16 December 2000, Autrans, France

M. E. Sandison, D. Cumming, J.M. Cooper, "Development of an Integrated Microsensor Array for Environmental Monitoring", *SET for Britain: Special Presentations by Britain's Younger Scientists, Engineers and Technologists at the House Of Commons*, 19 March 2001, London, U.K.

PUBLICATIONS PRIOR TO THIS WORK

M. E. Sandison, A.S.G. Curtis, C.D.W. Wilkinson, "Effective Extra-cellular Recording from Vertebrate Neurons in Culture Using a New Type of Microelectrode Array", *Journal of Neuroscience Methods*, **2002**, 114, 63-71

GLASGOW
UNIVERSITY
LIBRARY